(5)

TELESEISMIC STUDY OF RUPTURE PROCESSES WITH LONG DURATION

by

PIERRE FRÉDÉRIC IHMLE

Diplom als Naturwissenschafter, Eidgenössische Technische Hochschule, Zürich, 1989

Submitted to the Department of
Earth, Atmospheric, and Planetary Sciences
in partial fulfillment of the requirements for the degree of

DOCTOR OF PHILOSOPHY

at the

MASSACHUSETTS INSTITUTE OF TECHNOLOGY

May 1994

Signature of Author_____
Department of Earth, Atmospheric, and Planetary Sciences
May 10, 1994

Certified by_____
Thomas H. Jordan
Thesis Supervisor

Accepted by_____
Thomas H. Jordan
Department Head

Lindgren

To my wife, Isabelle.

TELESEISMIC STUDY OF RUPTURE PROCESSES WITH LONG DURATION

by

PIERRE FRÉDÉRIC IHMLE

Submitted to the Department of
Earth, Atmospheric, and Planetary Sciences
in partial fulfillment of the requirements for the degree of
Doctor of Philosophy

MAY 1994

ABSTRACT

Slow earthquakes are events with anomalously long durations compared to ordinary earthquakes of similar moment, which implies that they have anomalously low characteristic velocities. Although the dynamics of slow earthquakes is still poorly understood, it has been observed that they are commonly located along oceanic transform faults. To obtain more information about this interesting class of teleseisms, we have undertaken a systematic survey of oceanic transform fault earthquakes using normal-mode techniques. Accelerograms from the IDA network have been processed for 68 events with $M_w > 6.2$ on the world-wide ridge systems from 1978 to 1992. Integrals of the complex Fourier spectra centered on the fundamental spheroidal modes were used to recover the source mechanisms and phase spectra over 1-mHz bands in the frequency range 1-11 mHz, and integrals of the power spectra were used to recover their total-moment spectra over the same ten disjunct bands. From these quantities we estimated the zero-frequency seismic moments, centroid times, characteristic durations, and (less reliably) skewnesses of the source time functions.

Our results indicate that most events in this population are slow ($v_c < 1$ km/s). Moreover, we observe a number of cases where the low-frequency properties of the source time function cannot be explained if all of the moment is released after the high-frequency origin time, implying that some events on oceanic transform faults have slow precursors. We hypothesize that these earthquakes are compound events, with an episode of slow moment release preceding—and presumably nucleating—a fast, brittle rupture at shallow depth.

Waveform fitting techniques are routinely employed to infer the time history of rupture of large earthquakes. However, inversion of body waves for source time functions has poor resolution at low frequencies, which makes it difficult to study events with large time constants, such as slow earthquakes. Similarly, deconvolution of surface waves using empirical Green's functions lacks spectral resolution below 4-5 mHz. To overcome these limitations, we have developed methods for obtaining and inverting broad-band, network-averaged source spectra in overlapping frequency intervals from a combination of normal-mode (1-10 mHz), surface-wave (2-20 mHz) and body-wave (10-50 mHz) data. The spectral recovery procedures employ synthetic seismograms corrected for low-degree aspherical structure using recent tomographic models. The combination of data in overlapping bands and from different instrumental components allows us to

assess the effects of uncorrected propagation bias, which tends to be most severe in the 10-20 mHz band. From an analysis of a global set of earthquakes, it appears, for example, that the spherically symmetric earth model PREM is slow for Rayleigh waves in this band. The amplitude and phase-delay spectra are inverted by minimizing a weighted combination of a chi-squared measure of spectral misfit and a quadratic form that measures the smoothness of moment release. We impose a positivity constraint on the source time functions, and we also assume that the source mechanism is constant. Errors of the solution are estimated using both a delete-one jackknife algorithm and a Monte-Carlo simulation of the error process of the spectral data.

These spectral techniques have been applied to a number of earthquakes recorded on global networks of high-performance digital stations. For example, we obtain compact source time functions of about 10 sec duration for both the 1994 Northridge event (M_W=6.6) and 25 s duration for the 1992 Landers (M_W=7.2) earthquake. The inversion method is particularly suited to study events with long duration and we will present events from a variety of tectonic settings, such as slow earthquakes on oceanic transform faults, as well as the tsunamigenic Sept 2, 1992 Nicaragua event. The 14 Mar 1994 Mid-Atlantic Ridge event provides us with a unique opportunity to study the nucleation of a large earthquake. Spectra for this event require a slow precursor, whereas tiny preshocks mark the onset of high-frequency radiation for this event. A low-frequency ramp, emerging from the noise about 20 s before the main shock may be related to the time-domain signature of a slow precursor Evidence for the existence of slow precursors, such as in the case of the great 1989 Macquarie Ridge earthquake, will be discussed, and we will offer some speculations on the nature of slow, infraseismic motion (10-100 m/s) on faults and its implication for the short-term prediction of some classes of earthquakes.

Thesis committee:

Dr. Thomas H. Jordan, Professor of Geophysics (thesis supervisor)
Dr. Bradford H. Hager, Professor of Geophysics
Dr. Chris J. Marone, Professor of Geophysics
Dr. Leigh H. Royden, Professor of Geology/Geophysics
Dr. Göran Ekström, Professor of Geophysics, Harvard University

ACKNOWLEDGMENTS

There are very many people that deserve my deepest thanks, people who made my stay at MIT a rich and unique experience, and it is nearly impossible to thanks them all.

But let's try.

First of all, Tom Jordan was a remarkable advisor. Aside from his tremendous scientific insight and leadership, I was most impressed by his scientific generosity. I feel particularly lucky and privileged to have been involved in such a fruitful environment.

Over the years, my fellow graduate students and friends, helped me, in the course of numerous conversations, to build up a broad view of geophysics, from seismology to geodynamics. I am thinking of Greg Beroza, Nicolas Fiszman, Jim Gaherty, Lind Gee, Mamoru Kato, Peter Puster, Steve Shapiro, Ann Sheehan, Mark Simons, and many others. In my early days at MIT, Paolo Harabaglia shared with me his knowledge of scientific programming, and was a very enjoyable friend and collaborator in many projects. My understanding of seismology and earthquake mechanics profited from many discussions with Renata Dmowska, Göran Ekström, Chris Marone, Jeff Park, Jim Rice, Peter Shearer, Paul Silver, and John Vidale. Bob Cicerone was very supportive in the final stages of this work, was always game for an espresso at Toscanini's, and patiently straightened up my English. This work would not have been possible without the constant commitment of people at the IRIS data management center, and those of the GEOSCOPE and IDA networks, to the distribution of high quality seismological data.

David Krowitz and Linda Meinke, our systems managers, are kindly acknowledged for introducing me into the arcane world of computers and for making things run so smoothly. Also, I would like to express my gratitude to the administrative staff of the department and, in particular, Beverly Kozol-Tattlebaum, Libby Kurten, Marie Senat and Katherine Ware, who helped make bureaucratic matters go like a breeze.

My parents, as well as my family-in-law, were very supportive, both financially and morally, and I thank them warmly to have stood by our side for the many years of my graduate career. "We" is of course my wife, Isabelle, and my daughters, Delphine and Ariane, who brought to me the invaluable joy of family life. Will I ever be able to give back what I owe to you, Isabelle ?

This work was funded by the National Science Foundation under grants EAR-9018690 and EAR-9305081, and by NASA under grant NAG5-1905. I express also my thanks to the Sunburst Fonds and the Hans-Kudlich Stiftung of the Swiss Federal Institute of Technology in Zurich for additional financial support.

Table of contents

CHAPTER 1

Introduction

Ordinary earthquakes are usually understood as shear instabilities or as elastodynamic cracks propagating at an appreciable fraction of the shear wave speed. The total duration of the source process lasts for a few seconds for small events, and up to several minutes for great earthquakes. The definition of a slow earthquake is mainly empirical. Slow earthquakes represent events with observed characteristic velocities of less than 1 km/sec, and hence have anomalously long durations. As ordinary events, slow earthquakes may show one or more periods of fast rupture, radiating broadband teleseismic energy. They are, however, enriched in energy at low frequencies (Kanamori and Stewart, 1976; Kanamori and Stewart, 1979).

This type of seismic event is most commonly observed to occur on oceanic transform faults (e.g. Beroza and Jordan, 1990; Kanamori and Stewart, 1976; Ihmlé and Jordan, 1991; Okal and Stewart, 1982). Oceanic transform faults appear in general to have a seismic deficit that can be accounted for if part of the plate motion is accommodated aseismically (Davies and Brune, 1971; Burr and Solomon, 1978; Kawasaki et al., 1986). Slow earthquakes have also been observed on the Eltanin fracture zone (Beroza and Jordan, 1990; Okal and Stewart, 1982). Other tectonic settings also show this type of seismic behavior; for example, the February 21, 1978 Banda-sea and the October 22, 1977 Argentina events (Silver and Jordan, 1983), the April 12, 1983 Peru-Ecuador earthquake (Jordan, 1991), and the September 2, 1992 Nicaragua event (Kanamori and Kikuchi, 1993). The June 6, 1960 aftershock of the great Chilean earthquake ruptured the source region for more than one hour (Kanamori and Stewart, 1979). Slow moment

release has been suggested for a subevent of the 1988 Armenia earthquake (Kikuchi et al., 1993). A sequence of earthquakes in February-March 1981 in the Gulf of Corinth region display low stress drops and long rise times, and are thought to represent slow energy release (Kim, et al., 1984). Some slow events have been shown to produce tsunamis (Abe, 1973; Kanamori, 1972; Pelayo and Wiens, 1992; Kanamori and Kikuchi, 1993).

Very slow deformation that does not give rise to teleseismically detectable energy has been documented from near-field borehole strainmeters; for example the series of strain events following the Izu-Oshima 1978 earthquake (Sacks, et al., 1981). This type of strain release has been reported as one of numerous precursory phenomena to seismic ruptures. Its role in strain accumulation and stress redistribution in the focal region has been postulated for the Japan Sea earthquake of May 1983 (Linde and Silver, 1989) and for the May 1974 Izu peninsula earthquake (Sacks et al., 1978). Since only a small number of the world's major destructive faults are well instrumented in the near-field, it would be of considerable interest to devise far-field methods to recognize precursory behavior. Strain events do not possess recordable far-field signatures. However, it is possible to observe slow seismic precursors to ordinary fast ruptures. Jordan (1991) reports the anomalous spectra of the 12 Apr 1983 Peru-Ecuador intermediate depth event and Ihmlé et al. (1993) describe in detail the spectral observation of a slow precursor to the great 1989 Macquarie Ridge earthquake. Other examples are the slow precursor to the great Chilean earthquake of 1960 (Cifuentes and Silver, 1989; Kanamori and Cipar, 1974) and the still controversial behavior of the July 31, 1970 Colombian earthquake (Dziewonski and Gilbert, 1974). Except for the work of Beroza & Jordan (1990), no systematic study has been attempted to characterize this type of anomalous seismic source in the far-field.

We present a systematic teleseismic study of earthquakes known to yield slow earthquakes and discuss evidence that some of them may have slow precursors (Chapter 2). In order to retrieve the low-frequency source spectra (1-11 mHz), we employ techniques that aim at reducing the scattering effects due to unmodeled lateral heterogeneity of the earth (Silver and Jordan, 1982, 1983; Riedesel et al, 1986; Jordan, 1991). We discuss at length possible sources of bias that might affect our spectral recovery procedures and conclude that our averaging procedures appear to be robust in that respect. Most events occuring on the mid-oceanic ridge systems are found to be slow earthquakes (see also Kanamori and Stewart, 1976; Beroza and Jordan, 1990; Ihmlé and Jordan, 1991). We apply Jordan's (1991) formalism to detect short-term slow precursors and find that almost half of the events seem to require a slow precursor at a high confidence level. These earthquakes appear to be compound events comprising an ordinary seismic rupture preceded, and presumably initiated, by an episode of slow, smooth (infraseismic) deformation. The great 1989 Macquarie Ridge earthquake belongs to this group and is the subject of a detailed study in Chapter 5 (see also Ihmlé et al., 1993). Some speculations about possible physical mechanisms of infraseismic slow motion on faults are presented.

In Chapter 3, we focus on expanding the spectral recovery method to higher frequencies. We develop a narrow-band cross-correlation technique, similar to Gee and Jordan's (1992) approach, that allows to us to recover network-averaged source spectra from first orbit surface waves (2-20 mHz), and from long-period body waves (10-50 mHz). The spectral recovery procedures employ synthetic seismograms corrected for low-degree aspherical structure using recent tomographic models. The combination of data in overlapping bands and from different instrumental components allows us to assess the effects of uncorrected propagation bias , which tend to be most severe in the band 10-20 mHz. In general, the agreement is good between the normal modes and the traveling

wave methodologies in the band 1-10 mHz, indicating that the averaging procedures efficiently reduce various types of scattered signals.

We develop an algorithm to invert network-averaged spectra (1-50 mHz) for the source time function of an event. In contrast to time domain methods, which have poor resolution at low frequencies (e.g., Ekström, 1989; Nabelek , 1984; Ruff, 1989; Kikuchi and Kanamori, 1982, 1986, 1991; Das and Kostrov, 1990), our spectral inversion procedure is well suited to study events with long duration. The spectral techniques are applied to a number of earthquakes that are well recorded on global networks of high-performance stations. For examples, we find compact source time functions for the 1992 Landers and the 1994 Northridge events, that compare well with time-domain waveform inversions (Kanamori et al., 1992; Wald and Heaton, 1994; Wald et al., unpublished abstract). Details of the inversion procedure and of its properties, as well as a jackknife and a Monte Carlo error analysis of the solution, are illustrated in Appendix A.

The tools developed previously are used in Chapter 4 to study the rupture process of the slow, tsunamigenic Nicaragua earthquake of 2 September 1992. The spectral inversion method takes full advantage of the low-frequency information contained in network-averaged spectra of this event. For example, time-domain inversion of body-waves severely underestimates its scalar moment (Ide et al., 1993; Satake et al., 1993). Our approach allows for the correct distribution of that part of the moment release function missing from body wave studies. We determine the very-low frequency long-period body-wave centroids of the event, and relocate its aftershocks. The spatial pattern and rupture history of the 1992 Nicaragua earthquake suggest that slow moment release occurred in shallow subducted sediments, possibly in a velocity strengthening regime (see also Kanamori and Kikuchi, 1993).

The spectral techniques are applied to the 1989 Macquarie Ridge earthquake (Chapter 5), which is one of the first great earthquakes to be well recorded on global networks of high-performance digital stations. The low-frequency radiation of both the vertical and

the transverse components require that the earthquake's main shock was initiated by a slow, smooth precursor with significant moment release more than 100 s to prior the event's high-frequency origin time. The source time function satisfies observations from normal modes, surface waves and long period body waves . In particular, it satisfies the lack of an observable precursor in front of *P* waves at nearby, high-gain stations. The location of the slow precursor relative to the main rupture is not constrained by our data, but we speculate that it involves a region of transitional frictional behavior at the base of the seismogenic layer in the oceanic lithosphere.

In Chapter 6, we study the rupture initiation of the 14 Mar 1994 Romanche transform earthquake. The spectra of this event cannot be satisfied if all the moment is released after the onset of brittle rupture. Separate inversion of spectra obtained from vertically and transversely polarized seismograms indicates a slow precursor for this event starting about 200 s before the onset of high-frequency radiation. Inspection of broad-band seismograms reveals a ramp, emerging from the noise 20 s before the onset of the main shock, which suggests that we may be observing the time domain signature of a slow precursor.

Chapter 7 summarizes the main results obtained in this work and points to a number issues that may lead to interesting and exciting new directions of research.

CHAPTER 2

Slow earthquakes on mid-ocean ridge systems: a reconnaissance study

2.1 Introduction

In this chapter, we analyze the low-frequency source characteristics of an earthquake population known to yield slow earthquakes. We process long-period vertical seismograms for 130 events larger than $M_W = 6.1$ that were located on the world-wide ridge systems from 1978 to 1992. Most of them possess a strike-slip transform mechanism. These events provide an ideal data set, in the sense that most events occur in a similar tectonic regime, at shallow depth, and over a limited range of magnitudes. Phase-sensitive and power-spectral techniques are employed to recover the source time-shift and total scalar moment spectra in 10 disjoint frequency bands from 1 to 11 mHz and 1 to 20 mHz, respectively (Jordan, 1991; Riedesel, et al., 1986; Silver and Jordan, 1983). Our results show that the oceanic population is composed mainly of slow events. We discuss in detail the sources of bias on the retrieved total scalar moment and time-shift spectra. We use Jordan's (1991) formalism to detect short-term slow precursors, and we observe several significant positive detections. Some speculations are presented concerning the physical mechanism of slow motion on faults that could account for the inferred low rupture velocities of slow earthquakes and slow precursors.

2.2 Moment tensor inversion techniques

In this section, we review the techniques used to recover the moment tensor and the total scalar moment of an event. Backus & Mulcahy (1976) and Backus (1977) introduce the concept of the stress-glut tensor $\Gamma(\mathbf{r},t)$, which represents the stress difference between the stress predicted by linear elasticity theory and that due to the seismic source. In the long-wavelength approximation (i.e., source radius << wavelength), the Fourier transform of the moment rate tensor, $\mathbf{M}(\omega)$, is defined as the zeroth spatial moment of the stress-glut rate tensor:

$$\mathbf{M}(\omega) = \int_V \dot{\Gamma}(\mathbf{r},\omega)\, dV(\mathbf{r}), \tag{2.1}$$

In the normal mode formalism, the moment tensor occurs as a linear term in the expression for ground motion excited by an indigenous source (Gilbert, 1970). For large source dimensions and long source durations, higher spatial, temporal, and mixed spatial-temporal moments are necessary to describe the source process (Backus, 1977a; Backus, 1977b). We consider here synchronous point sources (Silver and Jordan, 1982) where

$$\mathbf{M}(\omega) = |\mathbf{M}(\omega)|\exp(i\phi(\omega)). \tag{2.2}$$

and $\phi(\omega)$ is the source phase. Such a moment rate tensor describes a source where all six elements share the same temporal centroid. A source where all the components of the moment rate tensor share the same time history is a special case of a synchronous source. The squared total seismic moment can be written as

$$M_T^2(\omega) = \frac{1}{2}\mathbf{M}^*(\omega):\mathbf{M}(\omega), \tag{2.3}$$

Defining the mechanism tensor with unit Euclidean norm $\widehat{\mathbf{M}}$, one obtains

$$\mathbf{M}(\omega) = \sqrt{2} M_T(\omega) \left| \hat{\mathbf{M}}(\omega) \right| \exp(i\phi(\omega)), \tag{2.4}$$

Riedesel and Jordan (1989), and Jordan (1991) have developed low frequency techniques for moment tensor retrieval that allow for the determination of the mechanism spectrum $\hat{\mathbf{M}}$, the source phase spectrum $\phi(\omega)$, and their related errors in 10 disjoint frequency bands from 1 to 11 mHz. Their matching filter formalism leads to a standard least squares inversion for the moment tensor elements

$$u_p(\omega) = \mathbf{G}_p(\omega) : \mathbf{M}(\omega), \tag{2.5}$$

where $u_p(\omega)$ is the Fourier transform of the vertical ground motion at the p^{th} station and $\mathbf{G}_p$ represents the theoretical Green's function that incorporates source-receiver geometry, earth structure, and instrument response. In order to account for the effect of lateral heterogeneity, which produces path dependent shifts in eigenfrequencies and hence apparent phase shifts (Dahlen, 1979; Jordan, 1978), and for other unmodeled effects, Jordan (1991) applies a non-linear phase adjustment procedure that compensates for the phase mismatch between data and synthetics. To reduce the effect of attenuation and splitting, the data functionals used in this phase-sensitive technique are integrals of the acceleration spectra over narrow frequency bands. In the original form of the algorithm, these integrals are centered on the degenerate eigenfrequencies $\overline{\omega}_\nu$ of fundamental spheroidal or toroidal modes (Gilbert, 1973). We modify the procedure in order to make the analysis path dependent by replacing the center frequencies for a spherically symmetric earth by their great circle average values for a given 3D earth model (Jordan, 1978; Woodhouse and Dziewonski, 1984). Because the method integrates over individual modes, it is not applied at frequencies above 11 mHz, where the mode spectrum becomes densely populated and the fundamental-mode resonance peaks begin to overlap considerably.

The inverse Fourier transform of the product of observed and theoretical integrals is summed over 10 fundamental mode peaks in each 1-mHz band. The maximum of the correlation function determines the time-shift that best equalizes the phase of the data relative to the synthetics. Although individual measurements show a large scatter, averaging over many stations allows for a satisfactory determination of the source time-shift spectrum $\Delta t(\omega)$. In order to recover zero frequency parameters of the source time function, we follow Jordan (1991) and parametrize the time-shift spectrum with the functional form :

$$\Delta t(\omega) = (1-\alpha)t_1 + \frac{\alpha}{\omega}\arctan(\omega t_1), \quad 0 \le \omega \le \omega_{max} \tag{2.6}$$

where α is a dimensionless parameter related to the skewness of the source time function and t_1 represents the zero frequency intercept of the time-shift spectrum, i.e., the source centroid time.

Riedesel and Jordan (1989), and Jordan (1991) have shown that the above techniques are well suited for the recovery of the mechanism spectrum and the time-shift spectrum and we will show in a subsequent chapter the excellent agreement between time-shift spectra obtained with this modal technique and those recovered using a traveling wave approach (Gee and Jordan, 1992; Ihmlé et al., 1993). However, scattering of modal energy through high-wavenumber lateral heterogeneity reduces the correlation between data and synthetics, which can bias the total scalar moment towards low values, especially at the higher end of the 1 to 11 mHz frequency band.

To obtain unbiased estimates of the total moment spectrum, we employ the method of Silver & Jordan (1982, 1983). Their algorithm is based on integrals of the cross acceleration spectrum over 1-mHz bands from 1 to 11 mHz. We use a modified version that requires only the integrated power spectra of the seismograms (Riedesel et al., 1986). This version has the advantage of rendering the results of the inversion insensitive to both

incorrect centroid time of the event and unmodeled elastic structure of the Earth. Moreover, we extend the validity of the analysis out to 20 mHz. Bias due to noise, error in the theoretical transfer functions, errors due to unmodeled aspherical structure of the Earth, and modeling errors due to incomplete knowledge of the source mechanism are all explicitly taken into account. This leads to expressions for the total bias and variance that allow for determination of optimal estimates of the scalar moment $M_T(\omega)$. Following Silver & Jordan (1983), we derive the total static moment at zero frequency, $M_T(0) \equiv M_T^0$ and the characteristic duration

$$\tau_c = 2 \cdot \mathrm{var}(f(t))^{1/2} \tag{2.7}$$

from the total moment spectra, where $f(t)$ represents the source time function of the event. The total moment spectrum is parametrized as

$$M_T(\omega) = M_T^0 \left(1 + \frac{\omega^2 \tau_c^2}{8} \right)^{-1} \tag{2.8}$$

The above parametrization extracts the smooth properties of the total moment spectrum, assuming the seismic source is localized in space, but not in time. The roll-off of the spectrum with increasing frequency is interpreted as an interference effect due to the finite duration of the source. Silver & Jordan (1983) discuss the role of higher spatial and temporal moments of the stress-glut tensor $\Gamma(\mathbf{r},t)$ on τ_c. They found that the spatial extent of the source has only a relatively small effect on the estimation of τ_c. We discuss in a following chapter other sources of frequency dependent bias on $M_T(\omega)$, notably seismic noise, incorrect radial attenuation models, and mode-mode coupling (Park, 1986). The choice of the functional forms (eq's 2.6 and 2.7) used to extrapolate the spectra at zero-

frequency is not unique, but the modeling errors will be small as long as the time constant of the source process is smaller than the considered characteristic periods (Jordan, 1991).

2.3 Theoretical transfer functions

Two basic ingredients are needed for the moment tensor inversion: an earth model to compute theoretical transfer functions and knowledge of the earthquake's source including mechanism, origin time, and location. Both modal techniques rely on differential measurements and require synthetic seismograms to model the source geometry and propagation effects. All synthetics are calculated by normal-mode summation using the spherically symmetric, non-rotating, anisotropic, anelastic structure of PREM (Dziewonski and Anderson, 1981) and the aspherical, elastic structure of SH8/WM13 (Woodward et al., 1993) or S12_WM13 (Su et al., 1994). The latter two are tomographic models derived from the inversion of waveform and travel-time data out to spherical-harmonic degree and order eight and twelve, respectively. We also use Rayleigh wave phase maps recently obtained by Ekström and Tromp (unpublished material) in the range 8-20 mHz. These maps allows us to reduce the variance of our time-shift measurements and to correct for PREM's bias toward large negative time-shifts in this frequency range. Aspherical corrections to the eigenfrequencies and eigenfunctions are based on the asymptotic theory of Woodhouse and Dziewonski (1984) and corrections for hydrostatic ellipticity are also computed (Dahlen, 1968, 1976). The source mechanism and centroid are obtained from the Centroid Moment Tensor (CMT) catalog published by Harvard University (Dziewonski et al., 1981; Dziewonski and Woodhouse, 1983). For our purposes, the CMT solution represents an adequate low frequency point source. The CMT solution is estimated from long period body waves recorded in the frequency range 15-20 mHz. Mantle waves centered around 5-6 mHz are used for larger events.

2.4 Data selection at low-frequencies

We use the very long period channel, which is sampled at 10-second intervals (20 seconds for older data), and we compare all seismograms from the IDA (International Deployment of Accelerometers, Agnew et al., 1986), GEOSCOPE (Romanowicz, et al., 1984), CDSN (Chinese Digital Seismic Network), and IRIS (Smith,1986) stations with synthetic seismograms calculated for the CMT source model. We reject those data with egregious timing or amplitude problems, non-linearities due to instrument saturation, large data gaps, or poor signal-to-noise ratios. The tides are subsequently removed, using a matched filtering algorithm. Events corrupted by energy from preceding earthquakes are rejected from the analysis. After processing, we retain 68 events from our original data set of more that 130 earthquakes for further analysis. All these events have shallow hypocenters. Figure 2.1 shows the epicenters of our set of earthquakes. Our data set comprises 57 strike-slip transform events, 8 dip-slip and 3 compensated linear vector dipole events (Appendix B, Table B.1)

The data set of events covers the period from 1978 to 1992. We also include the recent 14 Mar 1994 Central Mid-Atlantic event in our analysis. This unusual earthquake will be the subject of a separate study in a subsequent chapter. In the late 70s and mid 80s, the IDA global network, which comprised about 20 stations, was the workhorse of low-frequency seismology. Due to the low dynamic range of its instruments (Lacoste-Romberg gravimeters with a feedback system), shallow focus events larger than about $M_W > 6.6$ often saturated the first arriving Rayleigh waves (R1), which had to be removed prior to processing. Also, these instruments recorded only the vertical component of motion. In the mid-80s, GEOSCOPE stations with 3-component, high-dynamic range instruments (Wielandt and Streckeisen, 1982) brought great improvement in the low-frequency study of large

earthquakes. It is, however, only since 1989 that global networks have reached maturity and record data of high quality for many stations. There are, however, problems with azimuthal coverage and data quality, especially for events prior to 1989. For historical reasons, and because of high noise levels on the horizontal component, we concentrate in this study on the vertical component of motion. The processing techniques are, however, not restricted to the vertical component.

2.5 Time shift spectrum

As a first stage in processing, the focal mechanism $\hat{\mathbf{M}}$ and the time shift spectrum $\Delta t(\omega)$ are determined using the technique described above (Riedesel et al., 1986). The first arriving Rayleigh wave packets (R1, R2) contain the most useful information about the seismic source. Later arriving Rayleigh waves tend, because of their multiple orbits around the Earth, to accumulate the effect of lateral heterogeneity. In order to minimize such effects, the length of the time series was taken to be 6 hours, starting from the first good data point. Shorter time series were used in the case of a following event, but never were less than 2 hours of data processed. The moment rate tensor is constrained to be deviatoric. The low-frequency spectrum of shallow events is dominated by fundamental-mode energy. For shallow sources, $M_{r\phi}$ and $M_{r\theta}$ cannot be adequately resolved from surface wave data (Kanamori and Given, 1981) and, in most cases, are projected out of model and data spaces (Riedesel, 1985). The moment rate tensor is then constrained to have two horizontal principal axes, yielding either strike-slip, dip-slip or compensated linear vector dipole mechanisms. As previously noted by Riedesel (1985) and Riedesel et al., (1986), very few of the retrieved mechanism spectra show any frequency dependence.

We use a variance reduction criteria to reject stations that cannot be adequately fit by the phase adjustment procedure. At this stage, seismograms exhibiting poor variance reduction

in several bands are removed. Reasons for this misfit include low signal to noise ratio, signal generated noise, incorrect station timing, improper calibration of the seismometers, and signal corruption by local earthquakes. This culling also eliminates time series corresponding to nearly nodal positions in the surface-wave radiation patterns where Coriolis coupling between fundamental spheroidal and toroidal modes, as well as other scattering effects not built into the synthetics, are most commonly observed (Park, 1986). Coriolis coupling generates pseudo-Love waves on the vertically polarized component of displacement, or pseudo-Rayleigh waves on the transverse component (Park, 1986). This effect is strongest in the band 2-5 mHz for nodal stations on near-polar paths and can be easily recognized when the data are appropriately band-pass filtered. Since Coriolis coupling is not included in our synthetics, this could potentially bias our spectral estimates in this band. We find the phase equalization technique also suited in identifying stations that show strong coupling between spheroidal and toroidal modes. Our choice here is to eliminate affected stations, although at higher frequencies there would be no *a priori* reason to reject the data.

2.6 Total moment spectrum

The second stage in data processing involves the retrieval of the total moment spectrum using the modified version of Silver & Jordan's (1982,1983) power spectral algorithm. Again, we take the CMT mechanism as the starting solution and the covariance matrix is constructed from results of the moment tensor inversion in the previous processing stage.

Events in the range of 2.5 to 10.0 x10^{18} Nm can show pronounced noise corruption that affects power-spectral estimates. We have made an extensive study of the low-frequency noise at stations of the IDA network by measuring more than 8000 band-averaged noise spectral densities from 6 hours of clean records. For a given station, noise histograms

display similar characteristics in each of the 1-mHz band from 1-11 mHz, approaching in many cases a log-normal distribution. Although order of magnitude fluctuations are observed, this type of distribution allows the definition of "noise reference curves" for each station. A median estimate is chosen to determine these noise reference curves. As previously observed (Agnew and Berger, 1978; Beroza and Jordan, 1990), the low-frequency noise decreases rapidly from 1 to 3 mHz and then stays at a constant level up to 11 mHz. Typically, the station RAR (Rarotonga) in the Cook Island is the noisiest due to coastal edge waves (Agnew and Berger, 1978). Noise reference curves are used to calibrated noise estimates made from 6 hours of data preceding an event. At every station, a bias correction is applied based on the SNR in each 1-mHz band.

2.7 Assessment of propagation bias

Time-shift spectrum

Estimates of $\Delta t(\omega)$ are most sensitive to inaccuracies of the radial elastic structure used to compute synthetics. From a global study of shallow focus earthquakes, we find that PREM+S12_WM13 is slow on average for vertically polarized surface waves from 7 to 20 mHz, leading to large negative time shifts (Fig 3.1, Chapter 3). Although time-shift spectra will be shown here, we defer a thorough analysis of propagation biases to the next chapter, where we introduce a narrow-band cross-correlation method to retrieve $\Delta t(\omega)$. One of the two most important parameters considered in this chapter is the centroid time-shift of events. Figure 2.2 shows a comparison of the centroid time-shifts Δt_1 obtained using the normal modal procedure with those listed in the CMT catalog. We find in general a good agreement between the two, except in the South Pacific and Atlantic, where our values are often less than the CMT centroid, especially for earlier events in the data set. The cause of

the regional discrepancy is somewhat unclear and may have to do with poor station coverage. Also, there is no guarantee that Δt_1 from the CMT solution is a zero-frequency quantity. The CMT processing corrects for source process time by assuming a boxcar function, and hence assumes that the time-shift spectrum is a constant function of frequency. Although this is often true at low-frequencies, the shape of the time-shift spectrum needs to be taken into account when extrapolating to zero-frequency (eq 2.6).

Amplitude spectrum

We find that estimates of $M_T(\omega)$ are most sensitive to depth and to the choice of the radial attenuation structure, but that they are affected little by Coriolis coupling. Near-source structure can potentially affect $M_T(\omega)$, mostly at frequencies higher than 10 mHz. Source directivity can bias the average amplitude spectrum towards low values, depending on source mechanism, azimuthal averaging, and the type of wave considered, leading to an apparent duration larger than the characteristic duration of the event. Silver & Jordan (1983) find that the positive bias in τ_c can reach up to 20% for a "fast" event with horizontal slip on a vertical fault (strike-slip mechanism). For a slow earthquake (rupture velocity on the order of 1 km/s), the bias is greatly reduced. Strong directivity effects can be recognized in the seismograms as a broadening or sharpening of body wave phases. A comparison of spectra obtained from R1 (G1) and R2 (G2) that leave the source at opposite azimuths can also diagnose directivity of the source process. At the present stage of the spectral averaging techniques, special care should be exerted in the interpretation of spectra from such events. Future work will include spatial effects (primarily directivity) in the recovery of average spectra for large earthquakes.

Silver & Jordan (1983) describe sources of bias related to the use of an improper spatial centroid. Numerical experiments show that epicentroid mislocation on the order of 100 km

would produce a decrease of moment of no more than 10% over the 1-11 mHz band. This is less than the observational errors of about 20% that are typical for scalar moment recovery procedures. Systematic centroid mislocations do not appear to be a significant source of bias.

In Silver & Jordan's (1982,1983) total moment recovery , an inadequate model for the radial anelastic structure of the earth can introduce a non-negligible source of frequency dependent bias in $M_T(\omega)$ which to first order, is given by : $\Delta M_T / M_T \cong -1/2\,\Delta Q / Q$, where Q is the seismic quality factor. Figure 2.3 shows total moment spectra for the 28 June 1992, Landers California earthquake that have been obtained using QM1, a recent radial attenuation model (Widmer et al, 1991), and PREM's radial Q model. The characteristic duration[1] τ_c^{PREM} is 22±2 s, which is somewhat large considering a source process time of 25 sec obtained by teleseismic and strong motion data (Wald and Heaton, 1994). As expected, τ_c^{QM1}=28±2 s is larger and in this example, QM1 leads to an estimate of τ_c, which is too large. From a global study of earthquakes whose time history of rupture is known, we find that the spheroidal fundamental mode Q values predicted by QM1 are too high by 5-10% in the band 4-10 mHz (Ihmlé et al., 1993). This fact has been confirmed by Durek et al., (1993). Therefore, we prefer to use PREM's attenuation structure.

3D variations in Q are not well resolved, because fluctuations of long-period surface wave amplitudes have many causes, such as source effects, focusing/defocusing of wavefronts, multi-pathing due to lateral variations in the elastic structure, and lateral variations in Q. This is in contrast to 3D variations in the elastic structure that are well known at low-frequencies and can be constrained by phase measurements alone. Variations in Q between continents and oceans have been reported by Dziewonski and Steim (1982) from surface wave measurements, and by Sipkin and Jordan (1980) from the measurement

---

[1] The characteristic duration is obtained from amplitude spectra in the range 1-11 mHz. In Fig 2.4 however, a smaller value of τ_c =15 s is obtained from spectra up to 20 mHz.

of ScS attenuation. Recent work on the low-order, even degree (2-6) spherical harmonic expansion of Q in the upper mantle (Durek et al., 1993; Romanowicz, 1990) implies lateral variation in Q^{-1} of about 30% at 5 mHz, which leads to amplitude perturbations on the order of those produced by lateral heterogeneity. Therefore, until better Q models are available for the calculation of synthetic seismograms, we will rely on the averaging of amplitude measurements to eliminate these unmodeled effects. Residual biases cannot be entirely ruled out, but a comparison between observed spectra with those predicted from known earthquakes indicates that network averaging is effective in this respect (see Figure 2.4).

Reference events

The modal techniques outlined here have been empirically validated by applying them to a variety of earthquakes studied by other methods. For example, the spectra recovered for the 1992 Landers earthquake (M_W = 7.4), the 1989 Loma Prieta earthquake (M_W = 7.0) shown in Figure 2.4, and other large strike-slip California events are consistent with the source mechanisms and moment-rate functions determined from near-field data. This precludes these events from having slow precursors observable at teleseismic distances (Johnston et al, 1990; Takemoto, 1991; Wald and Heaton, 1994). The spectra for the recent 1994 Northridge thrust event (M_W = 6.6) shown in Figure 2.4 display a nearly flat spectrum, consistent with source time functions obtained from broad-band P wave inversions (Ihmlé and Bennett, unpublished material). In Figure 2.4, we note the excellent agreement between M_0 from the Harvard CMT and our values of $M_T{}^0$. Similarly, the centroid time shift obtained by the extrapolation to zero frequency (eq. 2.6) is very similar to the CMT centroid time. In this analysis, time is always referenced to the high-frequency origin time of the event taken from the NEIC catalog. The amplitude and phase-delay spectra derived for high-stress-drop, deep-focus events are observed to be flat, as expected

for sources with compact time functions, and to have static moments and centroid time shifts in good agreement with the Harvard CMT values (Harabaglia, 1993).

2.8 Slow earthquakes on ridge systems

Amplitude spectra for the California events do not display any structure out to 20 mHz. Their continuous roll-off with increasing frequency indicates that these events are dominated by source time functions with a single time constant on the order of tens of seconds or less. Their time-shift spectra are equally structureless out to 10 mHz. This is in contrast to the behavior of events occurring on mid-ocean ridges. Figure 2.6 shows total moment spectra of four events that occurred on the Romanche and Chain transform faults in the central Mid-Atlantic. Except for the 5 Aug 1990 event, which rolls off smoothly up to 15 mHz, amplitude spectra show a kink between 6-9 mHz. In the latter part of this section, we will discuss possible causes for the bimodal behavior of this population of earthquakes. In order to account for the two time constants involved by the spectra, we determine M_T^0 and τ_c by extrapolating the spectra to zero-frequency with the functional form (2.8) in two different bands, from 1-9 mHz and 10-20 mHz. Some variation in these bounds exists from event to event.

Our results for the ridge events are summarized in Figure 2.5, where we show a comparison of M_T^0 and τ_c . In Appendix B, time-shift and amplitude spectra for all the events used in Figure 2.5 are shown. For reference, scaling curves are indicated on the figure for different values of the characteristic velocity of an event $v_c = L_c/\tau_c$, where L_c represents a characteristic spatial dimension of faulting. The total scalar moment is proportional to fault area and average slip. A L^3 scaling has been shown to hold for small events, i.e., events that do not rupture the entire width of the seismogenic zone (Scholz,

1990). After a cut-off at about 7.5 10^{18} Nm, the moment of large earthquakes is thought to scale with L^2 (Scholz,1982,1994; Shimazaki, 1986). A debate has been initiated on the scaling of large earthquakes by Romanowicz (1992), who argues that a L-scaling is more appropriate for interplate strike-slip events larger that ~ 7 10^{19} Nm. In Figure 2.5, however, we assume that L_c is proportional to $M_0^{1/3}$ and we compute v_c using a scaling constant calibrated by Kanamori and Given (1981),

$$\tau_c = \frac{1.7523 \cdot 10^{-5}}{\sqrt{3} \cdot v_c} M_0^{1/3} \qquad (2.9)$$

The $\sqrt{3}$ factor accounts for the fact the Kanamori and Given use the total, rather than characteristic durations, assuming a boxcar time function. v_c is in km/s, M_0 in Nm. An L^3 scaling assumes that the rupture is free to grow in two orthogonal directions on the faulting surface. In the case of an elongated fault rupture, where the width of faulting is controlled by the depth of the brittle-ductile transition , L^2 or even L scaling is more appropriate, and the rupture grows in only one direction. At a given value of the scalar moment, L or L^2 events last longer that L^3 events. We consider here mainly strike-slip events for which L and L^2 scaling is more appropriate, and in Figure 2.5, we probably underestimate v_c for events having scalar moments greater than about 7.5 10^{18} Nm.

Between 10-20 mHz, amplitude spectra are flat and resemble those of regular events with characteristic rupture velocities around 2-3 km/s, such as the California events. Between 1-9 mHz, we find that a large proportion of oceanic earthquakes have velocities v_c lower than 1 km/s or lie in the vicinity of the 1 km/s scaling curve. For example, on Figure 2.6, the 26 Dec 1992 event has τ_{c1} = 48±2 s (v_c = 0.6 km/s) and τ_{c2}= 14±1 s (v_c = 1.7 km/s) and the 28 Aug 1992 event has τ_{c1} = 31±2 s (v_c = 1.0 km/s) and τ_{c2}= 2±8 s (v_c = 2.7 km/s for the upper bound on τ_{c2}) .

We find that the slowness is not correlated with mechanism, i.e., dip-slip events show identical features as strike-slip events, and it appears that slow earthquakes occur on all ridge systems. Some intraplate events, in the vicinity of plate boundaries, are large enough to be included in our population. They do not depart from the behavior of interplate events. Spreading rates, determined from the plate model NUVEL-1 (DeMets, et al., 1990) range from about 10 to 160 mm/yr and do not appear to be correlated with characteristic velocities obtained from our set of events.

The above observations call for two general hypotheses:

1) On the one hand, source time functions of oceanic events are "compound events" dominated by a bimodal distribution of time constants, leading to the bimodal character of the total moment spectra, with: a) a regular type of faulting that ruptures the oceanic crust and adjacent mantle in short bursts of moment release; b) a long duration process with characteristic time constant around 50-200 sec.

2) On the other hand, measurements of τ_c might be systematically biased for oceanic locations. The latter point will be addressed in the following discussion that focuses first on the effect of using an incorrect centroid on the computation of transfer functions. We will discuss the possible effect of the assumed attenuation structure in the source region on τ_c. The discussion finally involves a comparison between surface wave magnitude and scalar moment for oceanic events.

The CMT solution (Dziewonski et al., 1981; Dziewonski and Woodhouse, 1983) is used to compute theoretical transfer functions. The inversion algorithm, essentially a power-spectral technique, is insensitive to errors in the temporal centroid. An incorrect centroid depth however, does affects the total moment spectra. The CMT depths for the events in this study range from 10 km (the minimum value allowed by the CMT inversion

procedure) to 15 km, and are typically in good agreement with values reported in the ISC and NEIC bulletins. They are also consistent with Bergman & Solomon's (1988) centroid depths of 7-10 km below the seafloor for large earthquakes on transform faults in the North Atlantic. Systematic centroid mislocations do not appear to be a significant sources of bias.

Consider the total moment spectra displayed on Figure 2.6. Two alternative sources of bias can be proposed to explain their bimodal character. The first alternative argues that low-frequency estimates (1-9 mHz) are biased towards higher amplitudes. Coriolis coupling, which is strongest on near-polar paths, produces pseudo-Love waves on vertically polarized seismograms and, if unaccounted for, can be a cause of positive bias in the frequency band 2-5 mHz. The spectra on Figure 2.6 are from near equatorial events on the Mid-Atlantic ridge, for which rotational effects are expected to be lowest. To highlight this point, Figure 2.8 displays amplitude spectra from events in the Southern Pacific and South-East Indian ocean. The 7 Apr 1985 and the 31 Mar 1992 Easter Island Cordillera earthquakes have $\tau_c = 8\pm3$ s and $\tau_c = 11\pm2$ s, respectively in the band 1-20 mHz. For the 4 Nov 1992 Balleny Island event, $\tau_c = 9\pm1$ s. These have the flattest spectra of all the events analyzed, even though they should be among the most affected by a rotational coupling bias. This is consistent with a numerical experiment in which we generated synthetic seismograms for the great 1989 Macquarie Ridge earthquake using a non-asymptotic code that incorporates along-branch aspherical coupling among the fundamental modes and Coriolis coupling between fundamental spheroidal and toroidal modes[2]. Experiments with these synthetics demonstrate that these types of mode coupling have a negligible effect on the spectra recovered by the normal-mode analysis (Ihmlé et al., 1993).

The second alternative is to consider a negative bias between 10-20 mHz. As frequency increases, fundamental spheroidal modes, which produce the dominant waveforms for

---

[2] The code for computing the coupled-mode synthetics was written by J. Park and modified by P. Puster, based on the first-order subspace projection approximation of Park (1987) and Dahlen (1987).

shallow focus events, sample the earth at shallower depth. One could hypothesize that a shallow low-Q zone could give rise to low-values of $M_T(\omega)$. The abrupt change in slope in the spectra of Figure 2.6 is inconsistent with that hypothesis, because the depth sensitivity of fundamental modes is a smooth function of frequency (see also Figure 2.2). In addition, the centroid locations of the four events of Figure 2.6 are close together, whereas the frequency location and intensity of the slope break varies from event to event: 10 mHz for the 26 Dec 1992 event, 8 mHz for the 28 Aug 1992 event, 12 mHz for the 5 Aug 1990 event, and 6 mHz for the 7 Jul 1981 earthquake. This observation is again inconsistent with the hypothesis that the slope breaks are related to propagation effects.

Comparisons between surface wave magnitude M_S and M_W for oceanic events gives independent evidence of the anomalous character of events on the global ridge system. M_S is measured from the amplitude of 50 mHz surface waves. M_0, in the CMT inversion, is determined from 15-20 mHz body waves (in the case of larger events, weighted with 5-6 mHz mantle waves), and is then extrapolated to zero frequency using a rupture velocity of about 2.5 km/s. M_W is obtained from M_0 using the empirical scaling relationship given in Kanamori (1977), which is based on an analysis of global seismicity. Most of the oceanic events have larger M_W than predicted from their surface wave magnitude, especially at low magnitudes (Figure 2.9). For comparison, the same diagram is shown for events from a continental environment with centroid depths less than 50 km. The latter events scatter on both sides of the empirical linear fit. Based on a similar observation, Ekström and Dziewonski (1987) discuss regional variations of the M_S-M_0 scaling, and proposed a modified scaling relationship for oceanic events. They point out that, although propagation related bias can play a role, the most likely explanation for the M_S-M_0 discrepancy is the longer than average source process of oceanic events. The M_0-M_S discrepancy for oceanic events is best explained in terms of long source durations that produce strong roll-off of spectral amplitudes with increasing frequency, i.e. a slow event.

Figure 2.10 shows a comparison between M_0 (Harvard CMT) and M_T^0 obtained from the zero-frequency extrapolation of both the 1-9 mHz and the 10-20 mHz bands. M_T^0 from the 1-9 mHz band is systematically larger than M_0 , whereas M_T^0 from the 10-20 mHz band is comparable to M_0 . From a global study of other events, we find in general good agreement between M_T^0 and M_0. Replacing M_0 with M_T^0 on Figure 2.9 makes the M_S-M_0 discrepancy even larger.

In conclusion, with our present knowledge of the earth's structure, the discrepancy of M_0 and τ_c estimates in the 1-9 and 10-20 mHz bands cannot be explained by any pathological propagation effects. On the contrary, our data suggest that the bimodal character of the total moment spectra of ridge system events, as summarized in Figure 2.5, is due to a type of moment release dominated by a very slow component of long duration and a regular component with comparatively short duration. This is what we call the "compound event" hypothesis. In the following section, we will focus on the frequency dependence of time-centroids of the source time functions and will test the hypothesis that the low-frequency spectra are consistent with the presence of precursory moment release.

2.9 A formalism for the detection of short-term slow precursors

If all the moment released during an earthquake occurs after the high-frequency origin time, one expects slow earthquakes to have large centroid time-shifts. Unless the source time function is strongly skewed towards the origin, an event with a large τ_c and a small Δt_1 will have some sort of moment release prior to the high-frequency origin time. We observe that several oceanic events have small Δt_1 compared to their large τ_c (Figure 2.11). We apply Jordan's (1991) formalism to search for short-term slow precursors.

Conceptually, such a precursor is characterized by smooth moment release with a time constant on the order of tens to hundreds of seconds. By definition, a slow precursor is not an impulsive source, and possesses no broad-band time domain signature in seismograms. The existence of slow precursors has been postulated by Jordan et al., (1988). Fault zones in continental regions are known to experience essentially two types of deformation: fast seismic rupture with characteristic velocities v_c around 3 km/s and stable transient creep with rates on the order of 1 mm/s. Rupture velocities intermediate to these values have not been unequivocally observed, and deformation velocities on the order of 10-100 m/s are still speculative.

Following Jordan (1991), we express the low-frequency parameters τ_c, Δt_1 and α in terms of the lower-order polynomial moments μ_p of the source time function $f(t)$[3]. $\widehat{\mu_p}$ are the central moments, with $\mu_0 = 1$. In this notation, $\tau_c = 2\,\widehat{\mu_2}^{1/2}$ and $t_1 = \mu_1$. t_1 is the centroid time of the event. We denote t_0, the high-frequency origin time of an event and t_*, the start time of stress glut release. In the case of an ordinary earthquake, $t_* = t_0$ and the dimensionless skewness parameter can be written as $\alpha = 1/2\,\widehat{\mu_3}/\mu_1^3$. At this point, it is convenient to introduce the null hypothesis

$$H_0 \equiv \{\text{the earthquake is ordinary}\} \equiv \{\, t_* = t_0 \,\}$$

and the alternative

$$H_1 \equiv \{\text{ the earthquake has a short term slow precursor}\} \equiv \{\, t_* < t_0 \,\}$$

In order to test the above hypothesis, we note that the polynomial moments of a one-sided, positive-valued function obey a number of constraints. The latter can be expressed in terms of the observed parameters (Jordan, 1991):

---

[3] To simplify the algebra, the moment release rate is here normalized to unity $\int f(t)dt = 1$. In other cases, for example in Chapter 3, $\int f(t)dt = M_T^0$. The context will make the distinction obvious.

$$\Delta t_1 > 0 \tag{2.10}$$

$$\tau_c < \tau_c^{max}(H_0) = \Delta t_1 \sqrt{2(1+\sqrt{1+8\alpha})} \tag{2.11}$$

$$\alpha > -1/8 \tag{2.12}$$

where $\Delta t_1 = t_1 - t_0$. Without loss of generality one sets t_0 = 0, so that, under H_0, Δt_1 is equal to t_1. Equation (2.11) imposes an upper bound on the characteristic duration of an event. Note that (2.11) depends on $\alpha^{1/4}$, so that the upper bound on τ_c depends only weakly on α. In contrast to the amplitude spectrum, the time-shift spectrum can have downward curvature ($\alpha > 0$) and upward curvature ($\alpha < 0$). The causality condition that the group delay $d\phi(\omega)/d\omega$ be positive for $\omega < \omega_{max}$ determines an upper bound for α. Provided that the functional form (2.6) is an adequate representation, one obtains after differentiation:

$$\alpha < 1 + (\omega_{max} \Delta t_1)^{-2} \tag{2.13}$$

Each of the inequalities (2.10), (2.11), (2.12), and (2.13) is an independent condition. If our observational data fail any one of them, one rejects H_0 in favor of H_1. Jordan (1991) applied this test to the 18 Oct 1989, Loma Prieta earthquake, and was unable to reject H_0. On the other hand, H_0 was rejected at the 99% level for the 12 Apr 1983, Peru-Ecuador event.

As an example, we apply the inequality constraints to the 26 May 1984, Prince Edwards Island earthquake (Figure 2.13). Δt_1 = 7.8±1.0 s, but α = -6.5±1.4 is less than the lower bound (2.11). Therefore, H_0 is rejected. Keeping the lower bound for α and using (2.11), we have an upper bound of τ_c^{max} = 13 s at the 99% confidence level, smaller than the observed value of $\tau_c = 44 \pm 2$ sec. Again, H_0 is formally rejected in favor of H_1.

We apply the formal test (2.11) to our data set at the 99% confidence level. The result is displayed on Figure 2.12, where solid symbols are events for which 10 or more stations were used. Symbol size is proportional to event magnitude. The shaded field indicates the region where H_0 is not rejected, i.e. events do not require a precursor (Table 2.3). In equation 2.11, τ_c^{max} depends linearly on Δt_1 and the null hypothesis is rejected primarily because characteristic durations are much larger than centroid time-shifts. The two largest events in this group are the 25 May 1981, Macquarie Ridge event (M_W=7.7) and the 30 Nov 1983 Chagos Archipelago event (M_W=7.8). Of the 68 events in our data set, 30 lie in the field where H_0 is rejected in favor of the alternative that they require a slow precursor. For 12 of these events, spectra are obtained from 10 or more stations. The more notable element of this set is the 23 May 1989 Great Macquarie event (M_W=8.2) for which Ihmlé et al. (1993) inferred the existence of a slow precursor, based on the inversion of normal mode, surface-wave and body-wave data. This event will be analyzed in more detail in a later chapter.

Figure 2.13 displays four examples of potentially precursive events. All of these events display a kink in the amplitude spectra. Table 2.1 lists all precursive events with 10 stations or more and Table 2.2 lists those with less than 10 stations. Except for 5 events, the 30 events in this group have strike-slip mechanisms. They sample all of the ridge systems, but predominantly in the Pacific and Indian Oceans (Figure 2.14). In particular, many events lying on the East Pacific Rise and the Chile Rise seem to require a slow precursor. These ridges are characterized by large spreading rates of about 16 cm/y, and are thought to have large seismic deficits (see discussion in next section). The missing part of the seismic budget of these transforms could possibly be accommodated by aseismic slip, a type of deformation not inconsistent with the existence of slow precursors. This is to be contrasted with slow-spreading ridges, like the Mid-Atlantic Ridge, that show few events requiring

slow precursors (Figure 2.14) and for which the seismic budget is nearly complete (see next section).

In testing at the 99% level, we define that the probability of a Type-I error (false rejection of H_0) be small. In order to assess the robustness of the detector, we carried out the same experiment for 4 well-studied shallow focus earthquakes (Table 2.4). They constitute our reference set of events, for which near-field instruments did not detect any premonitory strain above the instrumental sensitivity (Johnston, et al., 1990; Johnston, et al., 1987; Takemoto, 1991). Results indicate no evidence for slow precursors. Δt_1 might be systematically biased for ridge system events, but even adding a considerable positive shift of several seconds to the centroid time shift leaves some events in the precursive field (Table 2.1 and 2.2).

The probability of a Type-II error (false negative) is difficult to assess. The detection of short term slow precursors rests on fundamental inequalities interrelating the observed parameters, τ_c, Δt_1, and α (Jordan, 1991). The retrieval of these quantities depends on the zero-frequency extrapolation of measurements made at discrete frequencies. There exists a fundamental non-uniqueness in the choice of the functional forms required to perform these extrapolations. However, the errors introduced by an incorrect choice will be small as long as the time constant of the source process is smaller than the considered characteristic periods (Jordan, 1991). Zero-frequency quantities are smoothly extrapolated from the spectra, and details, such as the 6-12 mHz kink of the amplitude spectra, are not taken into account. If the time-shift spectra were structureless out to 20 mHz, we see heuristically that it would be difficult to accommodate both short and long time constants for an even greater proportion of events in our data set. A downward curvature of the time-shift spectrum ($\alpha > 0$) indicates a moment release function with a short rise time and long decay time. A flat time-shift spectrum with a small centroid time-shift requires a symmetric distribution of moment release around its centroid, both for the short-duration and the long-duration components, hence the necessity of a slow precursor. A time-shift spectrum with an upward

curvature ($\alpha < 0$), as for the Great 1989 Macquarie event, necessitates a type of moment release with long rise and short decay times, raising the suspicion that the event has a slow precursor. In order to resolve some of these uncertainties, one needs to consider the shape of phase-delay spectra out to shorter periods. The next chapter will bridge this interpretative gap and will focus on expanding the spectral recovery method to higher frequencies. An algorithm to invert network-averaged spectra (1-50 mHz) for the source time function of an event will be presented.

2.10 Discussion

Transform faults accommodate a wide range of slip rates: from 1.7 cm/yr on the Arctic Ridge up to 18.0 cm/yr on the Southern East Pacific Rise. The transform fault boundary is affected by a complex thermal structure (Fox and Gallo, 1986) and juxtaposes rocks of various composition and mechanical behavior. The topography of slow-slipping transform faults in the North Atlantic is dominated by a 10 to 30 km wide central trough depressed by several hundred to a few thousands meters relative to the adjacent lithosphere of the same age. Dredging of transform valley material reveals the presence of serpentinized peridotite near the surface, as well as serpentinite diapirs (Fox and Gallo, 1986). Due to hydrothermal circulation in the fractured, hot, olivine bearing crust and mantle, serpentine is a likely mineral to be found as gouge material in transform faults. Seismological investigations indicate an anomalous velocity structure across and along the fracture zone (Purdy and Ewing, 1986), with an anomalously thin crust of about 2 km thick. The principal transform displacement zone accommodates most of the relative motion across the transform. It is located at the bottom of the transform fault valley within a zone of recent tectonism, called the transform fault zone, which consists of numerous short fault strands parallel to the principal transform displacement zone (Fox and Gallo, 1986). Fast-slipping transform

faults of the East Pacific ocean are less well studied, but appear to be less localized, defining 20 to 150 km wide shear zones, with complex en-echelon structures (Fox and Gallo, 1989). Although thermal structure is likely to differ from slow to fast slipping transforms, anomalously thin crust and heterogeneous rock assemblages seem to be distinctive features of transform faults in general.

Seismic budget of oceanic transform faults

Oceanic transform faults seem to be in general deficient in seismic moment (Davies and Brune, 1971; Kawasaki et al., 1986), and there appears to be a negative correlation between spreading rate and seismic budget. For example, large earthquake seldom occur on the ridge systems in the East Pacific, where spreading rates reach 18 cm/y (DeMets, et al, 1990), and seismicity is low. The seismic coupling coefficient (or seismic budget) is defined as the ratio of slip rate released by earthquakes divided by geologically measured slip rate on faults or, in case of plate boundaries, the slip rate predicted by plate motion (e.g. Scholz, 1990). The seismicity of oceanic transform faults is dominated by events with strike-slip mechanism where one of the focal planes is parallel to the transform's strike. In that case, an appropriate expression for seismic slip rate is

$$\dot{u}_s = \frac{1}{\mu A T} \sum M_0 \qquad (2.14)$$

where μ is the shear modulus, A the average fault surface and T is the period of time considered. M_0 is the total moment of individual events in the sum. Typically, seismic coupling calculations are dominated by the few largest events occurring in a region of interest.

Seismic slip rates calculated for transform faults are inversely proportional to the assumed depth of faulting. This parameter is uncertain, and is related to the thermal structure and the rheological stratification of transform faults. Ordinary shallow focus earthquakes are usually interpreted as being caused by shear instabilities rupturing the brittle part of the lithosphere (e.g. Scholz, 1990). The brittle-plastic transition is thought to coincide with the transition from a velocity weakening to a velocity strengthening frictional behavior. This transition marks the limiting depth of faulting in the lithosphere. Depending on the local geothermal and tectonic regime, the transition occurs in a quartz controlled rheology at a depth of about 10 to 15 km, in the temperature range of 300 to 450 °C. In an oceanic environment, the flow laws of olivine govern this behavior. Centroid depths of transform fault earthquakes suggest that the depth extent of faulting is limited by the 600-900 °C isotherms (Bergman and Solomon, 1988). The authors report centroid depths of 7-10 km for North-Atlantic transforms, consistent with results from a microearthquake survey of the Rivera Fracture Zone (Prothero and Reid, 1982).

Kanamori and Stewart (1976) found the Gibbs transform faults are fully coupled seismically to that depth. We computed the seismic budget of the Romanche transform fault using eq 2.14 for events in the CMT catalog, covering the period from 1977 to 1992. Assuming a depth of faulting of 10 km and current plate motion rate of 3.2 cm/y, the 940 km long Romanche transform fault has a seismic budget of 71%. In this chapter, we show that the CMT moment underestimates the scalar moment of oceanic transform fault events by about 20%. Considering this additional factor, the seismic budget for the Romanche transform fault is nearly complete. It is interesting to note that few events on the Mid-Atlantic ridge require a slow precursor (Figure 2.14). This is consistent with earlier studies that observe the lack of seismic deficit of the Romanche, as well as of other transforms on the Mid-Atlantic ridge (Burr and Solomon, 1978; Kawasaki et al., 1985). There is no evidence that aseismic slip on these transforms contributes to their seismic budget. And yet, many earthquakes on these transforms are slow earthquakes (this study; Kanamori and

Stewart, 1976). Clearly, the physical mechanism of slow motion on faults needs to be investigated, as well as the rheological stratification of oceanic lithosphere.

Transform faults on fast spreading ridges, such the East Pacific Rise and the Pacific-Antarctic Ridge, appear to be far from fully coupled seismically, and that the missing part of the plate motion across the transform may occur aseismically. For example, the Eltanin fracture zone, which is actually composed of three transform faults, has a seismic budget of 30%, assuming a limiting depth of faulting of 5 km. Many events on the fast spreading East Pacific Rise and the Chile Rise require slow precursors at the 99% confidence level (Figure 2.14). Nevertheless, there is an uncertainty of a factor of two in seismic budget calculations for oceanic transform faults, because the number of seismic cycles recorded by current seismicity catalogs may not be sufficient, and because the depth extent of faulting is not well known. However, the issue of the seismic budget of oceanic transform faults deserves to be addressed more thoroughly. The availability of the CMT catalog and the new findings from this study will allow for a more detailed study to be done.

Possible physical mechanisms of slow ruptures

Ordinary earthquakes have rupture velocities that approach the shear wave speed of the medium. Because inspection of seismograms in front of first arrival *P* waves does not reveal any precursory signal above the noise level, we interpret the inferred slow precursors in terms of quiet earthquakes (Beroza and Jordan, 1990), i.e. events with appreciable moment release and long characteristic duration of at least several hundred seconds. These non-impulsive sources might result from a smooth rupture process, with characteristic velocities on the order of 10-100 m/s (Beroza and Jordan, 1990). We hypothesize that slow earthquakes are compound events, resulting from the temporal superposition of a quiet earthquake with episodes of fast brittle rupture. Such quiet earthquakes might in some

cases precede and nucleate an ordinary event (Ihmlé et al., 1993). The reverse situation is also plausible, where a quiet earthquake is driven by brittle rupture of the lithosphere.

Although research focused on understanding the physics of slow motions on faults would assuredly keep researchers busy for many years to come, we present here some possible mechanisms for the stabilization of slip at low or very low rupture velocities.

In the context of state and rate (single) variable friction (Dieterich, 1986; Marone et al., 1991; Rice and Gu, 1983), the coefficient of friction varies, over a characteristic distance D_c, from its static value at rest to its dynamic value during sliding. The velocity dependence of steady state friction is controlled by the so called (a-b) factor. The parameter a describes the immediate effect of a velocity step and b accounts for the decay of the coefficient of friction as time evolves. If (a-b) >0, one speaks of velocity strengthening and stable slip ensues. Instability requires (a-b) < 0 (velocity weakening). Laboratory data show that the passage from a velocity weakening to a velocity strengthening behavior is temperature dependent (e.g. Lockner and Byerlee, 1986), but also depends on fluid pressure at hydrothermal conditions (Blanpied et al., 1991). Numerical simulation of the seismic cycle suggest that such a transition occurs in the crust at about the same depth at the brittle-plastic transition (Tse and Rice, 1986). A large D_c implies that friction on the fault needs a longer time (or displacement) to reach its steady-state value (long-rise time), yielding slow or even quiet earthquakes. Values of D_c for natural faults are speculative. Dieterich (1986) indicates that the nucleation radius for instability grows as D_c becomes larger. Critical nucleation patches will therefore depend on heterogeneity of the fault surface.

To address the quiet earthquake question, one is faced with the apparent paradox of 1) nucleating an event, which necessitates a velocity weakening environment and 2) stabilizing this event and releasing appreciable moment before a catastrophic instability sets in. One could postulate that a large-D_c instability could develop at depth on a patch with subcritical nucleation radius, thus yielding slow stable slip. Nucleation of an ensuing small-D_c instability would depend on the available strain energy, the pre-stress on the fault and the

stress change imposed by the initially large-D_c instability. However, it is not obvious how rupturing in the quasi-static regime could generate large moment release. Numerical experiments with state and rate friction laws indicate a small amount of slip in this regime (Dieterich, 1992). On the other hand, there may exists a transition zone at depth where (a-b) becomes very gradually positive (neutral) and where slip is marginally stable, allowing both nucleation and stable slipping. Both scenarios, alone or in conjunction, could lead to low rupture velocities. A third possibility is that material at nucleation depth undergoes a rapid transition from velocity weakening to velocity strengthening when slip velocities exceed a relatively low threshold value (Ihmlé et al., 1993). This behavior is in qualitative agreement with laboratory data on halite (Shimamoto and Logan, 1986) and granite (Blanpied et al., 1987) at low normal stress, although serpentine, a major consistuent of the upper-mantle in a ridge environment, behaves in the opposite sense. Laboratory experiments on the frictional properties of serpentine indicate that this mineral would creep at loading rates typical of plate motion and that it could lead to earthquakes if forced to slide at higher rates (Reinen, et al., 1991, 1992; Tullis and Weeks, 1990,).

Further interpretations of slow rupture velocities invoke visco-elastic relaxation processes at depth following an ordinary earthquake (Bonafede, et al., 1983), interacting shear cracks (Yamashita, 1982), rupture of an asperity on a weak fault (Das and Kostrov, 1986), frictional instability on a strongly heterogeneous fault (Mikumo, 1981), and localized plastic instabilities at depth with thermal runaway (Hobbs, et al., 1986). Precursory stable sliding has been observed in laboratory stick-slip experiments (Scholz et al., 1972), with rupture velocities one order of magnitude lower than the medium shear wave speed (Ohnaka, et al., 1986). Stable sliding in the brittle or frictional regime on a natural fault appears to be achievable, and may radiate enough energy at very low-frequency to be analyzed in the far-field.

2.11 Conclusion

We systematically survey the low-frequency characteristics of ridge-system events. We confirm the slowness of transform events and quantify them in terms of the characteristic duration and the total moment of the event. In most cases, rupture velocities of 1 km/s or less are observed, and these velocities are independent of geographical location and focal mechanism. In addition, almost half (44%) of the events appear to have significant low-frequency energy release prior to the high-frequency origin time.

We discuss extensively some possible sources of observational bias. τ_c appears to be a robust estimate of the characteristic duration of an event. We present in the next chapter a traveling wave method to measure Δt_1 from first orbit surface waves. In most cases, excellent agreement exists between the modal and time-domain methods, indicating that any residual bias must be small. The moment tensor retrieval procedures can be modified to incorporate the spatial dependence of the stress-glut release into the inversion scheme. Although this might prove impractical considering the long wavelength of normal mode oscillations, a test of the compound event hypothesis can be set up in an attempt to differentiate the spatial and spectral contributions of quiet and fast subevents. Laboratory experiments and numerical modeling of rate and state variable friction on a fault with depth dependent properties should be carried out to evaluate possible scenarios for smooth and slow short-term precursory behavior. From a geodynamic point of view, the seismic budget of transform faults should be reassessed in order to better understand seismic moment deficit on transform faults (Burr and Solomon, 1974; Kawasaki et al., 1985).

TABLE 2.1: EVENTS FOR WHICH H_O IS REJECTED AT THE 99% CONFIDENCE LEVEL
10 OR MORE STATIONS ARE USED

M_T^0 and its standard deviation are in units of 10^{18} Nm. τ_c^{max} is from inequality (2.11) and is computed at the 99% confidence level. τ_c , the characteristic duration of the event is obtained between 1-9 mHz from a fit to the amplitude spectrum. The centroid time-shift Δt_1 is in seconds and is referenced to the NEIC high-frequency origin time. α is the skewness parameter (see section 2.9 of the text). α_{max} is the upper bound on α given by eq. 2.13. # is the number of stations used in the normal mode techniques. M is the mechanism of the event, where S stands for strike-slip, N for normal faulting, T for thrust and C for events with a large non-double component, i.e. $\varepsilon > 0.25$, where ε is the ratio of smallest to largest eigenvalue of the moment tensor (in absolute value).

Event	Region	M_T^0	τ_c^{max}	τ_c	Δt_1	α_{max}	α	#	M
84/01/16	Easter Island Region	4.2 ± 0.6	10.8	38.7 ± 6.4	1.3 ± 1.6	161.0	0.0 ± 0.0	11	C
84/05/25	South Pacific Cordillera	5.7 ± 0.5	9.9	26.2 ± 6.8	5.6 ± 0.5	9.1	-33.2 ± 0.2	10	S
84/05/26	Prince Edward Is. Region	16.3 ± 0.6	13.4	44.0 ± 1.8	7.8 ± 0.7	5.2	-6.5 ± 1.4	10	S
85/11/12	Southern Pacific Ocean	4.8 ± 0.4	6.5	38.6 ± 4.3	2.1 ± 1.0	57.7	-10.6 ± 0.1	10	S
87/07/08	Easter Island Region	7.4 ± 0.4	26.6	39.0 ± 2.8	5.4 ± 1.1	9.7	-0.3 ± 0.9	13	N
89/05/23	Macquarie Islands Region	2070.0 ± 137.0	24.1	53.4 ± 4.0	14.8 ± 0.8	2.2	-8.9 ± 1.8	18	S
89/08/29	Off Jalisco, Mexico Cst	7.9 ± 0.5	3.0	36.9 ± 3.3	-2.6 ± 1.5	37.9	0.0 ± 0.1	21	S
91/03/11	South of Africa	5.6 ± 0.3	8.3	41.2 ± 2.7	4.0 ± 0.7	16.8	-13.5 ± 0.3	10	S
91/06/10	North Atlantic Ridge	4.4 ± 0.3	2.8	7.8 ± 12.9	0.7 ± 0.5	254.3	-20.4 ± 1.8	12	S
91/12/11	Easter Island Cordillera	6.0 ± 0.4	7.6	25.1 ± 4.7	3.9 ± 0.6	17.8	-26.4 ± 0.2	22	N
92/03/31	Easter Island Cordillera	4.3 ± 0.4	9.6	29.4 ± 6.5	5.3 ± 0.6	10.0	-14.9 ± 0.5	17	S
92/06/22	SW Atlantic Ocean	5.0 ± 0.4	6.6	35.4 ± 4.6	1.0 ± 0.5	239.3	1.0 ± 0.0	20	S

TABLE 2.2: EVENTS FOR WHICH H_0 IS REJECTED AT THE 99% CONFIDENCE LEVEL
LESS THAN 10 STATIONS ARE USED

See Table 2.1 for explanations.

Event	Region	M_T^0	τ_c^{max}	τ_c	Δt_1	α_{max}	α	#	M
78/05/29	Off Coast Southern Chile	6.5 ± 0.5	8.7	27.7 ± 5.1	4.3 ± 0.7	14.5	-16.2 ± 0.2	6	S
78/08/10	South Atlantic Ridge	4.6 ± 0.3	35.8	40.0 ± 3.4	4.1 ± 1.2	16.2	36.5 ± 7.9	8	S
78/12/25	Off Coast of Mexico	14.3 ± 0.7	10.5	41.6 ± 2.4	2.2 ± 2.0	54.4	-2.8 ± 0.0	6	S
79/02/18	Prince Edward Is. Region	5.4 ± 0.3	9.7	27.0 ± 4.4	5.0 ± 0.7	11.1	-11.4 ± 0.4	6	S
80/11/01	Off Coast Jalisco Mexico	5.7 ± 0.4	9.4	46.2 ± 2.8	2.6 ± 1.5	37.9	-4.6 ± 0.1	7	S
81/04/27	West of Macquarie Isl.	9.0 ± 0.4	6.8	14.8 ± 5.0	1.5 ± 1.3	111.6	-6.6 ± 0.1	6	S
81/10/28	Easter Island Region	5.7 ± 0.5	15.5	36.8 ± 4.7	2.1 ± 1.7	58.3	0.2 ± 0.0	7	S
83/04/08	Arabian Sea	6.7 ± 0.4	8.8	51.2 ± 2.1	2.7 ± 1.4	36.9	-19.9 ± 0.4	8	S
85/01/31	Off W. Cst South Is.,n.z.	3.3 ± 0.3	53.6	56.9 ± 2.1	7.3 ± 2.4	5.7	5.8 ± 2.0	7	C
85/07/08	West of Macquarie Island	4.8 ± 0.3	11.5	43.2 ± 2.7	4.8 ± 1.3	11.9	-8.9 ± 0.3	9	S
86/10/14	Prince Edward Is. Region	2.2 ± 0.1	7.5	31.6 ± 3.2	3.5 ± 0.7	21.1	-24.9 ± 0.1	9	S
86/12/25	Off Southern Chile Coast	5.9 ± 0.6	7.0	35.3 ± 6.1	1.9 ± 1.2	70.7	-2.6 ± 0.0	9	S
86/12/28	Mid-Indian Rise	3.8 ± 0.3	10.3	28.8 ± 5.3	0.9 ± 1.2	254.3	0.4 ± 0.0	7	S
88/03/21	Laptev Sea	5.4 ± 0.4	47.1	41.8 ± 3.7	7.8 ± 1.7	5.2	12.4 ± 1.8	8	N
88/05/05	Easter Island Cordillera	3.9 ± 0.3	7.9	24.0 ± 6.2	3.1 ± 0.9	26.7	-10.7 ± 0.1	8	S
88/10/01	Easter Island Cordillera	4.1 ± 0.3	7.8	30.4 ± 4.3	3.0 ± 1.0	28.9	-14.6 ± 0.1	8	S
90/07/14	N. of Ascension Island	10.7 ± 0.8	45.6	29.9 ± 4.8	9.1 ± 1.3	4.0	11.5 ± 2.0	8	S
90/09/17	Macquarie Islands Region	5.9 ± 0.5	9.4	41.4 ± 3.9	5.4 ± 0.4	9.5	-24.3 ± 0.4	8	S

TABLE 2.3: EVENTS FOR WHICH H_O IS NOT REJECTED

See Table 2.1 for explanations.

Event	Region	M_T^0	τ_c^{max}	τ_c	Δt_1	α_{max}	α	#	M
79/05/16	South Atlantic Ridge	8.0 ± 0.6	32.1	25.4 ± 5.7	4.9 ± 1.6	11.5	2.1 ± 0.5	8	S
80/06/08	Macquarie Islands Region	2.8 ± 0.2	81.7	35.7 ± 3.7	15.4 ± 3.9	2.1	-0.6 ± 1.9	8	S
80/06/21	S'western Atlantic Ocean	6.6 ± 0.5	77.6	44.4 ± 3.8	14.0 ± 3.7	2.3	5.8 ± 1.7	6	S
81/03/06	Off Coast Centrl. Amer.	17.9 ± 1.5	42.6	32.8 ± 4.8	2.7 ± 3.7	36.8	3.1 ± 0.1	6	S
81/05/25	W. Coast, S. Isl.,n. Z.	431.0 ± 18.3	105.6	55.7 ± 1.7	26.1 ± 3.6	1.4	-1.1 ± 1.1	7	S
81/07/07	Cntr Mid-Atlantic Ridge	28.5 ± 2.4	75.5	55.0 ± 3.9	17.0 ± 2.7	1.9	1.2 ± 0.8	9	S
81/08/19	Mid-Indian Rise	4.0 ± 0.2	74.7	41.5 ± 2.5	10.5 ± 4.1	3.3	5.4 ± 1.9	7	S
82/01/03	Centr Mid-Atlantic Ridge	72.9 ± 5.5	83.1	47.7 ± 3.5	20.1 ± 2.7	1.6	1.4 ± 0.3	7	C
82/05/07	Sw Atlantic Ocean	50.4 ± 4.4	57.0	39.8 ± 4.6	9.3 ± 2.4	3.9	5.7 ± 1.8	11	S
82/06/06	North Atlantic Ridge	6.0 ± 0.5	66.8	48.9 ± 3.5	13.8 ± 2.5	2.3	1.9 ± 0.9	8	S
82/07/07	North of Macquarie Is.	89.4 ± 6.9	88.6	45.9 ± 3.5	16.9 ± 4.3	1.9	1.1 ± 1.2	6	S
83/09/01	South of Africa	4.3 ± 0.4	81.4	36.5 ± 4.0	18.3 ± 3.0	1.8	0.9 ± 0.6	6	S
83/11/30	Chagos Archipelago	549.0 ± 43.0	92.8	40.7 ± 4.1	24.7 ± 2.4	1.4	0.0 ± 0.6	10	N
83/12/03	Chagos Archipelago Reg.	4.1 ± 0.4	44.7	32.2 ± 6.0	6.7 ± 1.6	6.6	3.4 ± 1.7	8	N
84/01/02	South Pacific Cordillera	6.6 ± 0.6	44.0	40.2 ± 4.2	9.6 ± 1.2	3.7	-2.1 ± 1.9	11	S
84/05/17	South Indian Ocean	33.3 ± 1.5	60.6	53.3 ± 2.1	12.8 ± 2.0	2.5	0.9 ± 1.2	10	S
84/06/22	Southwestern Atlantic O.	4.9 ± 0.4	62.5	34.9 ± 5.0	9.6 ± 3.0	3.8	5.4 ± 1.9	8	S
84/09/17	Mascarene Islands Region	3.6 ± 0.2	95.3	55.4 ± 2.3	17.9 ± 4.8	1.8	3.3 ± 0.9	6	S
84/11/01	Cent. Mid-Atlantic Ridge	53.3 ± 3.0	50.4	25.6 ± 4.5	9.8 ± 1.6	3.7	0.8 ± 1.9	9	S
85/04/07	Easter Island Cordillera	6.4 ± 0.6	39.3	28.9 ± 6.5	4.8 ± 1.7	11.9	6.5 ± 0.7	11	S
85/05/16	Mid-Indian Rise	5.3 ± 0.4	42.0	41.7 ± 3.6	5.6 ± 1.7	9.1	4.9 ± 1.2	10	N
85/06/06	Cent. Mid-Atlantic Ridge	8.4 ± 0.4	56.0	47.0 ± 2.1	8.7 ± 2.4	4.3	2.8 ± 1.9	9	S
85/10/12	Cent. Mid-Atlantic Ridge	7.3 ± 0.4	76.3	54.5 ± 2.1	14.5 ± 3.5	2.2	1.1 ± 1.4	8	S
85/11/16	Mid-Indian Rise	7.6 ± 0.7	58.7	34.1 ± 5.4	11.0 ± 2.3	3.1	5.1 ± 1.2	9	S
86/07/07	Carlsberg Ridge	5.1 ± 0.4	73.9	27.4 ± 6.0	16.4 ± 2.7	1.9	-1.3 ± 1.4	8	T
88/02/26	Atlantic-Indian Rise	20.9 ± 1.5	48.5	32.2 ± 4.6	9.2 ± 1.6	4.0	1.9 ± 1.9	27	T
88/03/23	North Atlantic Ridge	3.0 ± 0.2	54.8	36.3 ± 3.8	8.1 ± 2.4	4.8	7.3 ± 1.9	7	S

TABLE 2.3: CONT.

Event	Region	M_T^0			τ_c^{max}	τ_c			Δt_1			α_{max}	α			#	M
88/06/18	Gulf of California	14.8	±	0.9	41.0	28.5	±	4.3	4.2	±	1.6	15.7	32.0	±	9.8	16	S
90/08/05	N. of Ascension Island	6.0	±	0.4	59.4	26.4	±	5.0	12.0	±	2.1	2.8	4.8	±	1.0	10	S
91/01/18	South of Australia	4.3	±	0.4	59.9	14.9	±	12.9	11.6	±	2.3	2.9	1.3	±	1.5	8	S
91/11/05	Mascarene Islands Region	11.5	±	0.9	54.8	34.8	±	4.6	11.3	±	1.7	3.0	0.8	±	1.5	14	S
92/07/20	Svalbard Region	16.0	±	0.8	63.3	34.7	±	2.8	14.0	±	2.1	2.3	3.1	±	0.6	23	S
92/08/28	N. of Ascension Island	27.1	±	1.0	46.6	31.1	±	2.4	6.8	±	1.8	6.5	9.7	±	2.0	28	S
92/11/04	Balleny Islands Region	6.1	±	0.2	33.8	14.4	±	3.6	7.2	±	1.0	5.9	-1.1	±	1.6	21	S
92/12/26	Cntrl Mid-Atlantic Ridge	23.3	±	0.8	86.0	47.8	±	1.6	23.6	±	2.0	1.5	0.6	±	0.3	26	S
94/03/14	Cntrl Mid-Atlantic Ridge	48.3	±	1.5	79.5	42.6	±	1.5	22.6	±	2.0	1.5	0.1	±	0.4	26	S

TABLE 2.4: REFERENCE EVENTS

M_T^0 and its standard deviation are in units of 10^{18} Nm. τ_c^{max} is from inequality (2.11) and is computed at the 99% confidence level. τ_c , the characteristic duration of the event is obtained between 1-11 mHz from a fit to the amplitude spectrum. The centroid time-shift Δt_1 is in seconds and is referenced to the NEIC high-frequency origin time. α is the skewness parameter (see section 2.9 of the text). α_{max} is the upper bound on α given by eq. 2.13. More than 10 stations are used in the normal mode techniques.

Event	Region	M_T^0	τ_c^{max}	τ_c	Δt_1	α_{max}	α
87/11/24	Superstition Hills	8.3 ± 0.5	56.7	17.9 ± 5.4	12.3 ± 1.7	2.7	-0.3 ± 1.6
89/10/18	Loma Prieta	29.6 ± 2.7	41.1	11.9 ± 11.8	8.6 ± 1.1	4.4	-1.3 ± 2.0
92/06/28	Landers	106.0 ± 4.3	58.5	22.3 ± 2.0	13.6 ± 1.6	2.4	-1.4 ± 1.4
94/01/17	Northridge	11.6 ± 0.3	21.5	11.3 ± 1.3	4.0 ± 1.0	17.0	1.0 ± 0.4
92/09/02	Nicaragua	450.0 ± 46.3	172.5	68.5 ± 2.7	52.2 ± 3.8	1.1	0.7 ± 0.1

Figure captions

FIGURE 2.1. Location map of the 68 ridge systems events retained in this study (solid diamonds). Current plate boundaries are indicated with the solid line. Mollweide projection.

FIGURE 2.2. A comparison between Δt_1 obtain from the zero-frequency extrapolation (using 2.7) of the 1-10 mHz time-shift spectra and Δt_1 taken from the CMT catalog.

FIGURE 2.3. *Top*: Frequency dependence of fundamental spheroidal mode attenuation up to 12 mHz for two radial Q-models. Solid line: PREM (Dziewonski and Anderson, 1981). Open circles are a subset of the observations used to derive this model. Dashed line: QM1 (Widmer et al., 1992) and observations (open squares). *Bottom*: Inversion for the total moment spectrum using PREM (solid circles) and QM1 (shaded squares) for the 28 June 1992 California Landers earthquake. We obtain $\tau_c^{PREM} = 22 \pm 2$ s (solid line) and a larger value $\tau_c^{QM1} = 28 \pm 2$ s (dashed line). Total scalar moments are very similar in both cases. The moment from the CMT catalog is indicated as a zero-frequency intercept.

FIGURE 2.4. Amplitude and phase-delay spectra for three California events, the 18 Oct 1989 Loma Prieta, the 28 June 1992 Landers and the 17 Jan 1994 Northridge earthquakes. Solid lines are fits of the functional form described in the text from 1-20 mHz for the total moment spectra and 1-10 mHz for the time-shift spectra. τ_c and α for each event are given on the diagrams. Zero-frequency intercepts of the curve yield M_T^0 and Δt_1. The CMT values are also given on the abscissa.

FIGURE 2.5. M_T^0 versus τ_c diagram. *Top*: Total moment spectra fit with an Aki-type spectrum (eq. 2.8) from 1 to 9 mHz. *Bottom*: 10-20 mHz fit. 68 events are shown that satisfy the quality criteria described in the text. Error bars are one-standard deviation. Solid lines are an empirical calibration between moment and event duration (Kanamori and Given, 1981) scaled for the ruptures velocities indicated on the figures. Most events in the band 10-20 mHz have small characteristic durations, in contrast to their long apparent duration between 1-9 mHz. This dichotomy is the basis for the "compound" event hypothesis.

FIGURE 2.6. Amplitude spectra for four strike-slip events of the central Mid-Atlantic ridge. The 26 Dec 1992 and 07 July 1981 events occurred on the Romanche transform; the 28 Aug 1992 and the 05 Aug 1990 earthquakes were on the Chain transform. Solid line: fit of the total moment spectrum between 1-9 mHz, yielding τ_{c1} ; dashed line, 10-20 mHz fit yielding τ_{c2}. Note the prominent kinks in the spectra around 6-12 mHz and the large discrepancies in moment and characteristic durations for the two bands. The CMT moment is given on the abscissa.

FIGURE 2.7. Phase-delay spectra for the same events in Figure 2.6. The plotting convention is the same as in Figure 2.4. Except for the 28 Aug 1992 event, all have large centroid time-shifts. Note the good agreement between the CMT and our own estimates of Δt_1.

FIGURE 2.8. Amplitude and phase-delay spectra for three events of the Southern Pacific and South-Western Indian ridge systems. Same plotting convention as in Figure 2.4. In contrast to Figure 2.6, all three earthquakes have flat total moment spectra.

FIGURE 2.9. M_w versus M_s diagrams for oceanic and shallow (< 50 km) continental earthquakes. Only events larger that M_w=6.1 have been considered. M_w is obtained from the relation $M_w = 2/3 \log M_0 - 6.06$ (Kanamori, 1977). Relative to the Eurasian events, the ridge system population has systematically larger M_w compared to M_s. Data are from the CMT catalog from 1977 to 1992.

FIGURE 2.10. A comparison between M_T^0 and M_0 from the Harvard CMT catalog for the 68 selected events of the text. *Left panel:* M_T^0 from 1-9 mHz amplitude spectra are consistently larger that M_0. *Right panel*: M_T^0 from 10-20 mHz amplitude spectra show good agreement with M_0.

FIGURE 2.11. Δt_1 versus τ_c diagrams. *Top*: τ_c is estimated from the 1-9 mHz band. The solid line is from inequality 2.11, where α is set to its maximum bound given by the group delay inequality in 2.10. As Δt_1 becomes larger ($\alpha \rightarrow 1$), the curve approaches the asymptote with slope $2\sqrt{2}$. The dashed line has a slope of 1/2. In this Figure, we set the curvature α to its maximum allowable value and do not use the full information in the time-shift spectra. However, heuristically, we see that events lying to the left of the solid line can be considered as having a potentially precursory behavior.

FIGURE 2.12. A plot of τ_c versus τ_c^{max} for the set of ridge systems events. Circle size is proportional to event magnitude. Filled circles are events where 10 or more very-long period seismograms were used for the spectral analysis; open circles are events with less than 10. τ_c^{max} is the upper bound on the right-hand side of inequality (2.11), calculated at the 99% confidence level. The 38 points in the shaded lower triangle of the diagram correspond to events where the hypothesis that $t_* = t_0$ (no slow precursor) could not be rejected by this test. The 28 points in the white upper triangle fail this test, and they are potential candidate for having slow precursors. The large event at τ_c = 53 s is the great 1989 Macquarie Ridge earthquake, which appears to have a large slow precursor (Ihmlé et al., 1993).

FIGURE 2.13. Amplitude and phase-delay spectrum of four oceanic events for which H_0 is rejected at 99% confidence level (see also Figure 2.12). Same plotting conventions as in Figure 2.6 and 2.7.

FIGURE 2.14. Location map of ridge systems events for which H_0 is rejected at the 99% level: black diamonds (10 stations or more could be used), gray shaded diamonds (less that 10 stations). Events for which H_0 is not rejected are shown with lightly shaded circles. Current plate boundaries are indicated with the solid line. Mollweide projection.

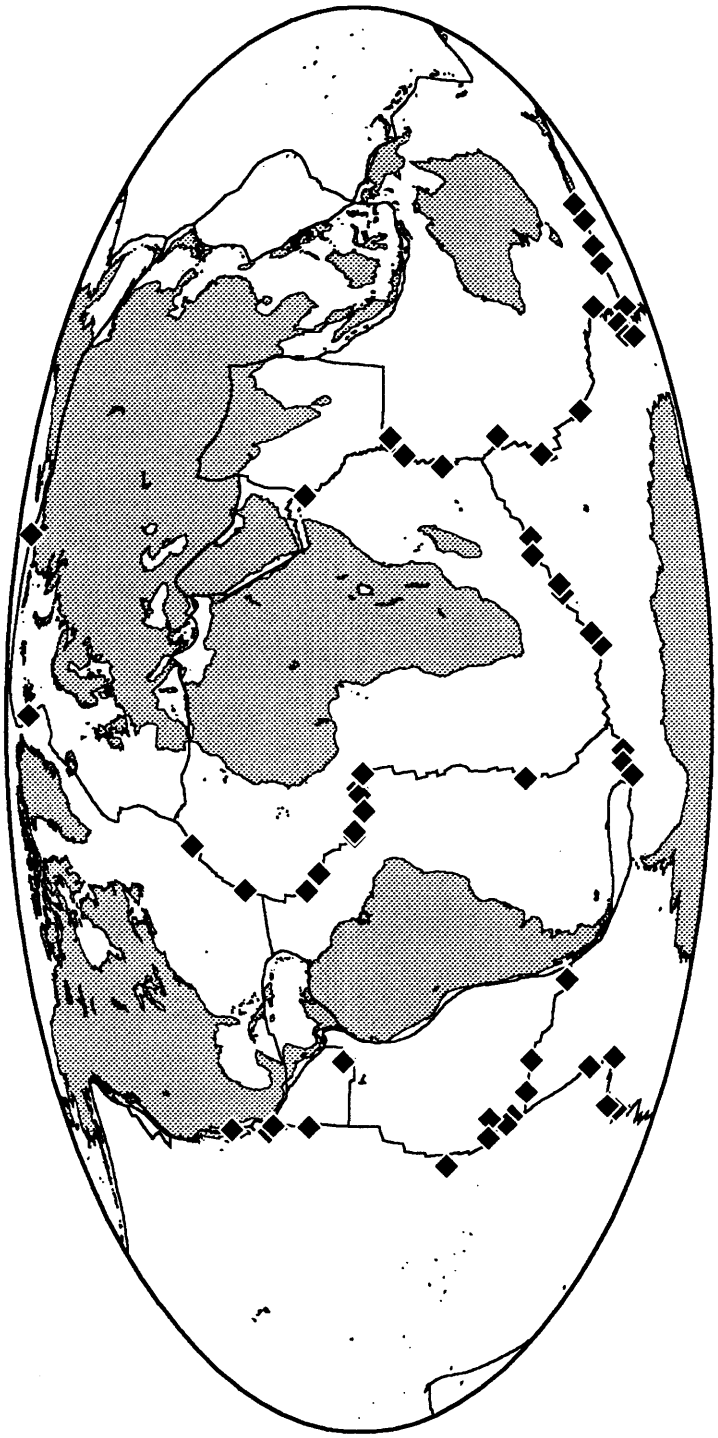

Figure 2.1

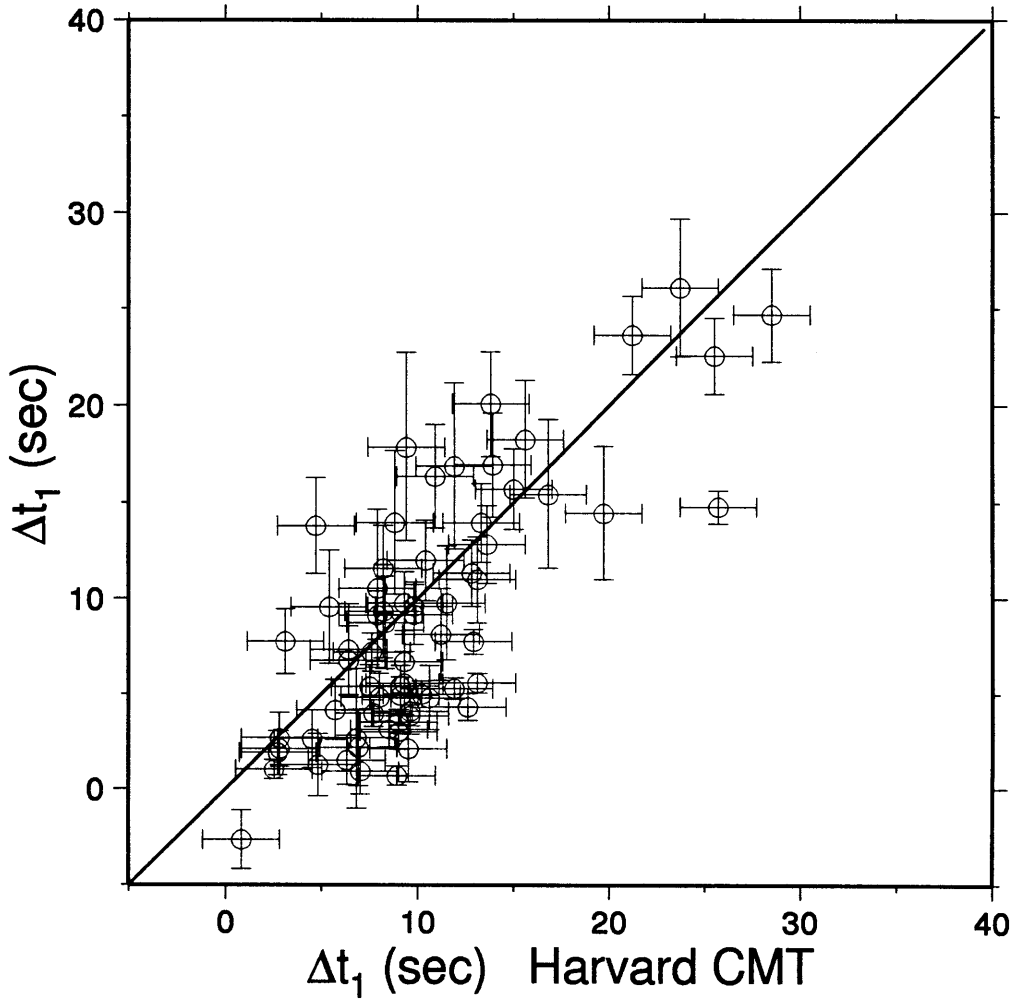

Figure 2.2

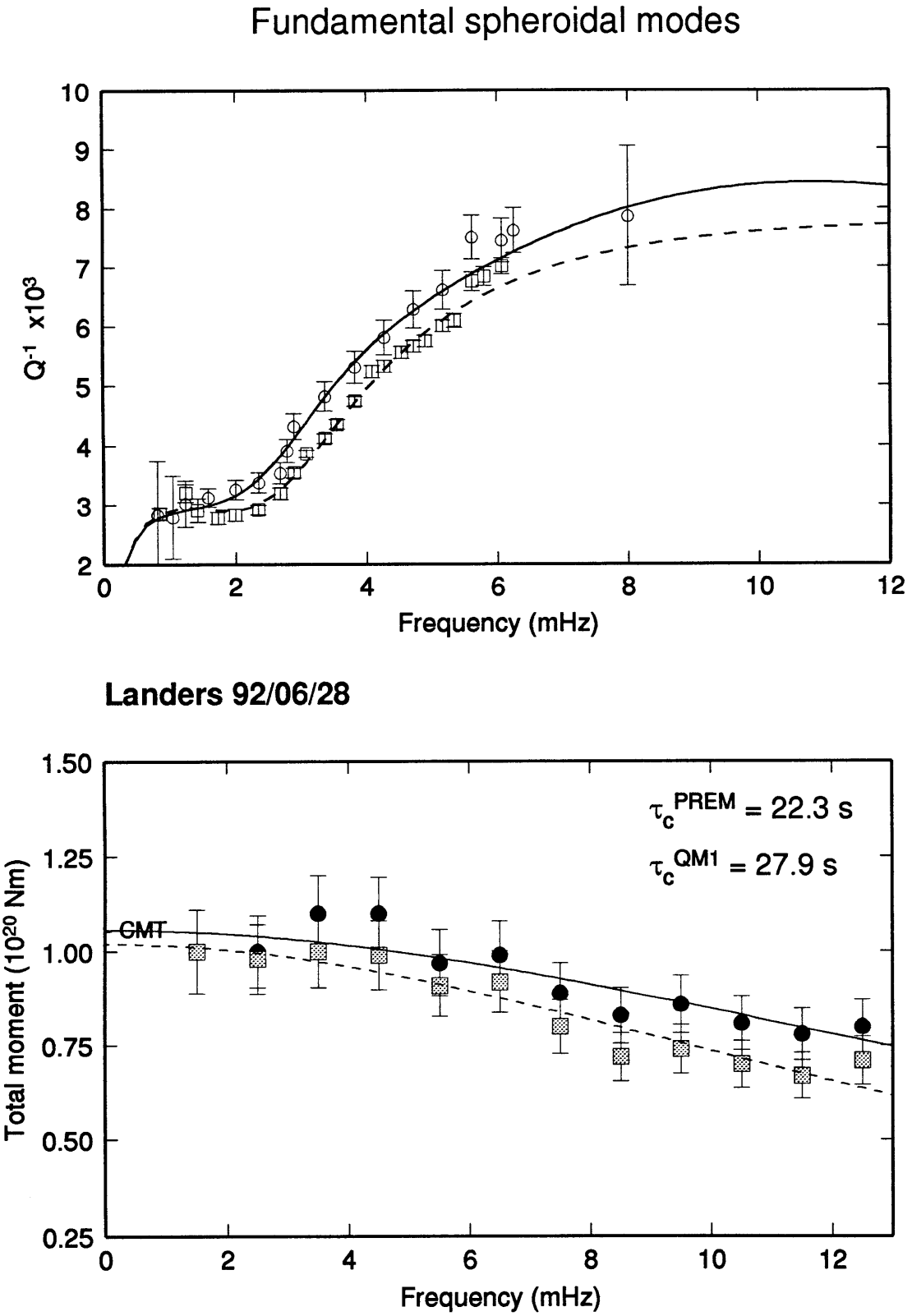
Fundamental spheroidal modes
Q-1 x10³
Frequency (mHz)
Landers 92/06/28
Total moment (10²⁰ Nm)
CMT
τc PREM = 22.3 s
τc QM1 = 27.9 s
Frequency (mHz)

Figure 2.3

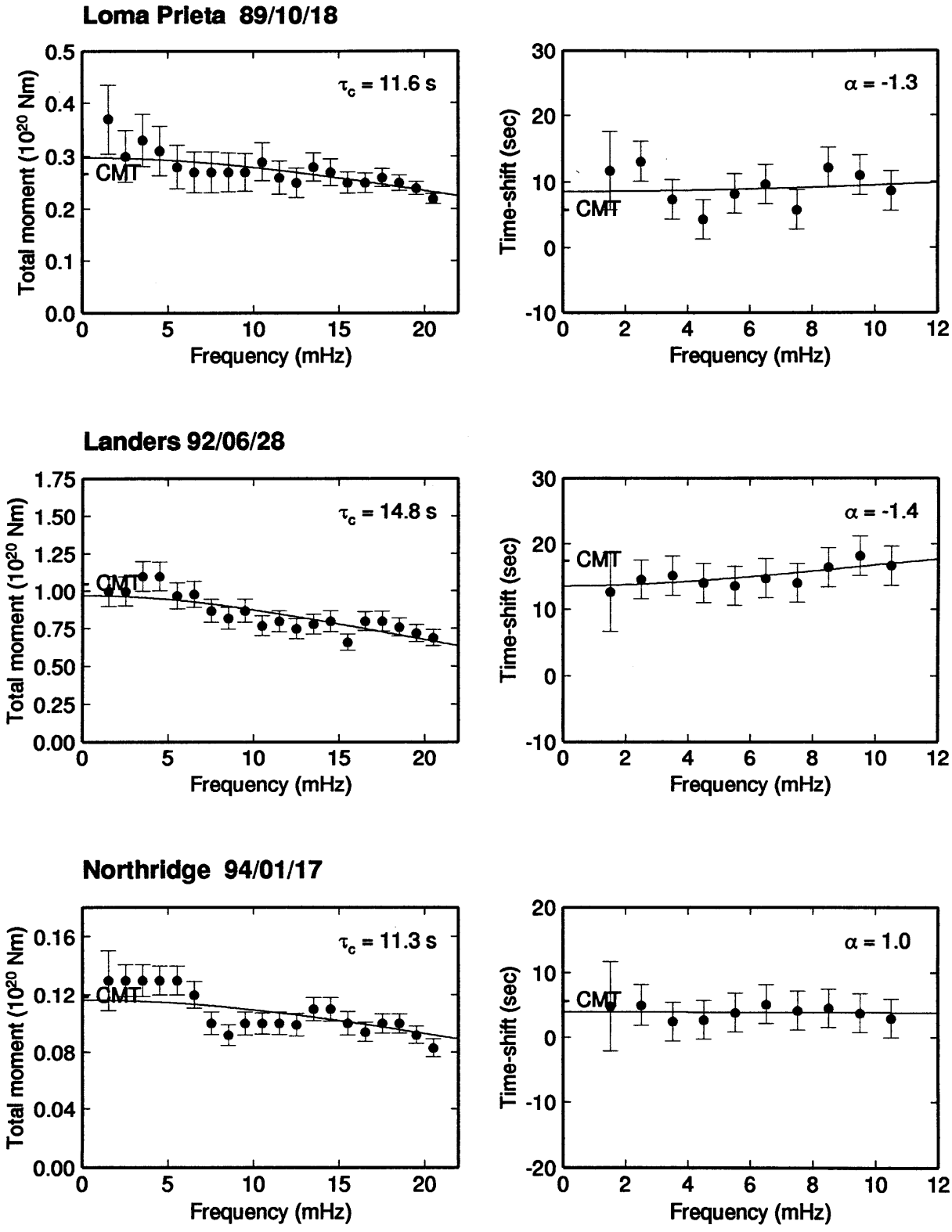
Loma Prieta 89/10/18
Total moment (10^20 Nm)
τc = 11.6 s
CMT
Frequency (mHz)
Time-shift (sec)
α = -1.3
CMT
Frequency (mHz)
Landers 92/06/28
Total moment (10^20 Nm)
τc = 14.8 s
CMT
Frequency (mHz)
Time-shift (sec)
α = -1.4
CMT
Frequency (mHz)
Northridge 94/01/17
Total moment (10^20 Nm)
τc = 11.3 s
CMT
Frequency (mHz)
Time-shift (sec)
α = 1.0
CMT
Frequency (mHz)

Figure 2.4

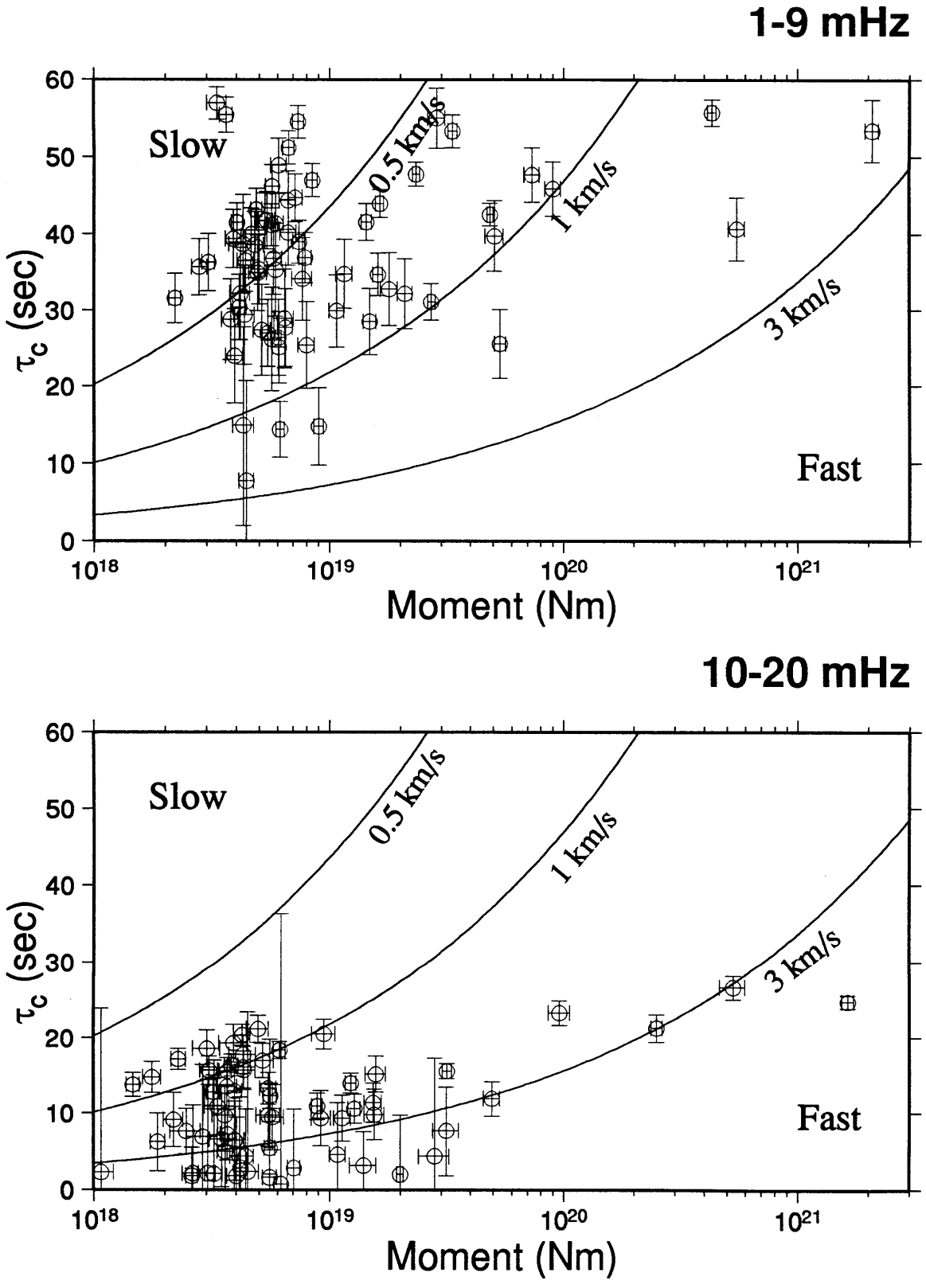
1-9 mHz
Slow
Fast
0.5 km/s
1 km/s
3 km/s
τc (sec)
Moment (Nm)
10-20 mHz
Slow
Fast
0.5 km/s
1 km/s
3 km/s
τc (sec)
Moment (Nm)

Figure 2.5

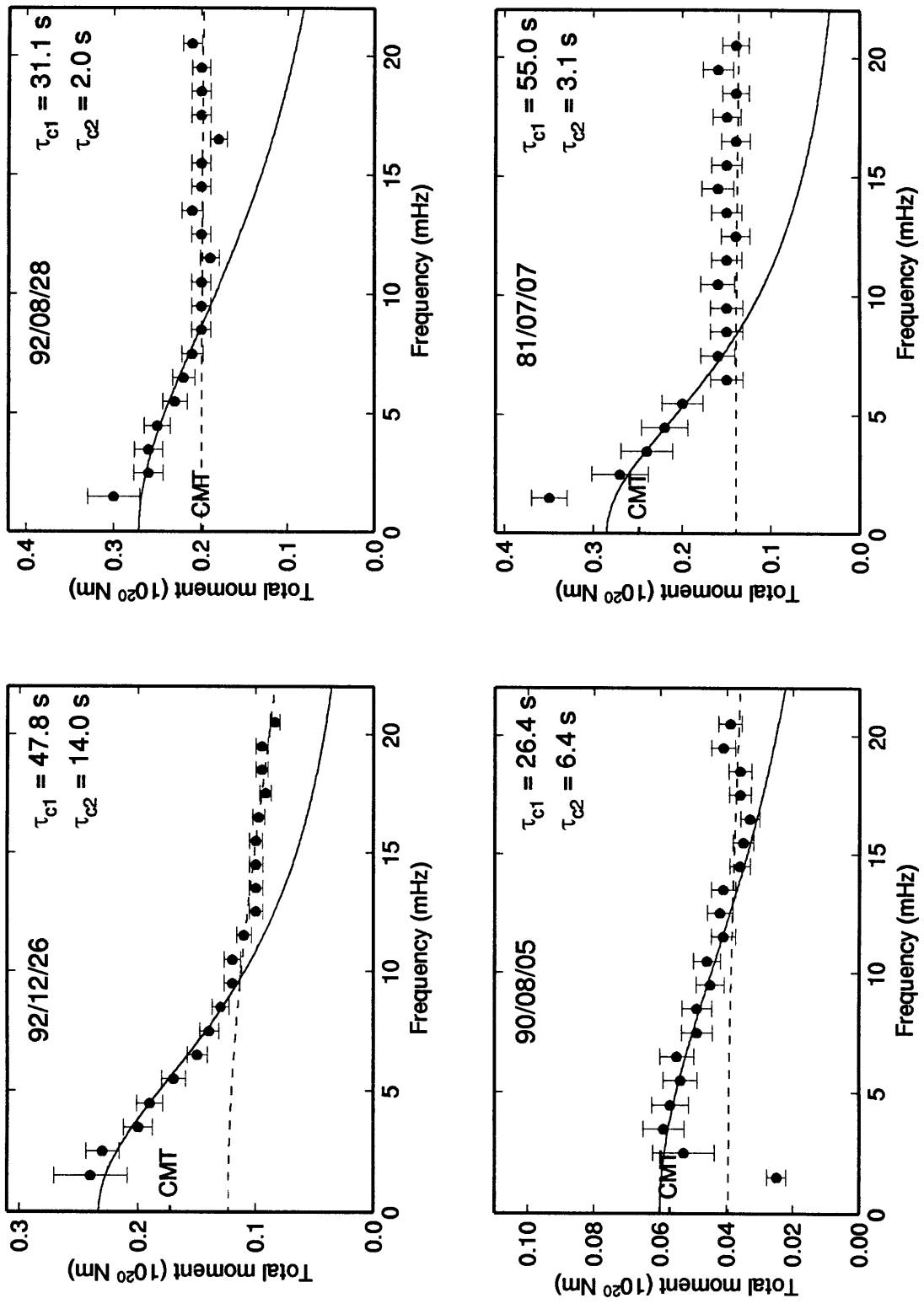
92/08/28
τ_{c1} = 31.1 s
τ_{c2} = 2.0 s
CMT
81/07/07
τ_{c1} = 55.0 s
τ_{c2} = 3.1 s
CMT
92/12/26
τ_{c1} = 47.8 s
τ_{c2} = 14.0 s
CMT
90/08/05
τ_{c1} = 26.4 s
τ_{c2} = 6.4 s
CMT
Total moment (10^{20} Nm)
Frequency (mHz)

Figure 2.6

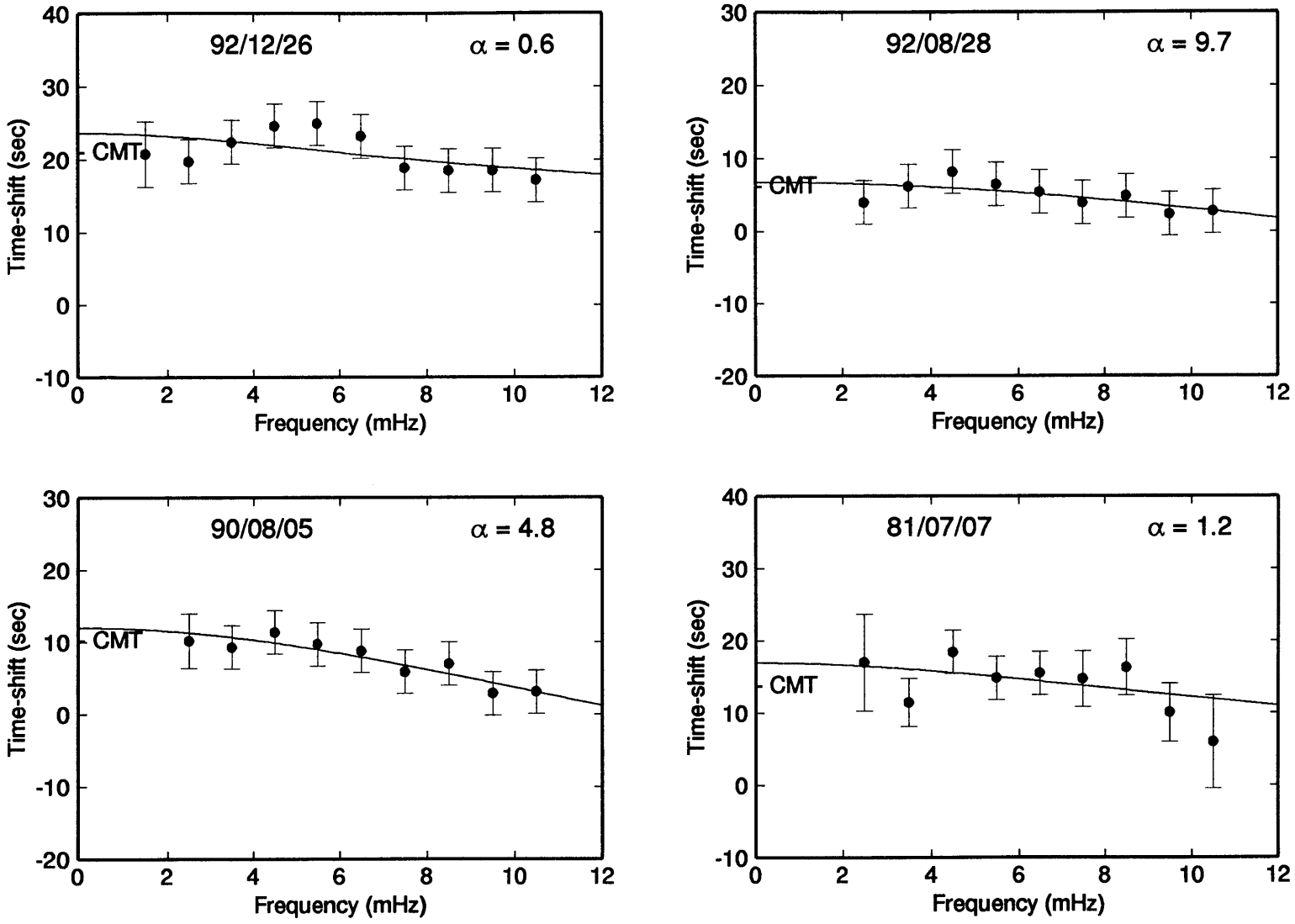
92/12/26
α = 0.6
CMT
Time-shift (sec)
Frequency (mHz)
92/08/28
α = 9.7
CMT
Time-shift (sec)
Frequency (mHz)
90/08/05
α = 4.8
CMT
Time-shift (sec)
Frequency (mHz)
81/07/07
α = 1.2
CMT
Time-shift (sec)
Frequency (mHz)

Figure 2.7

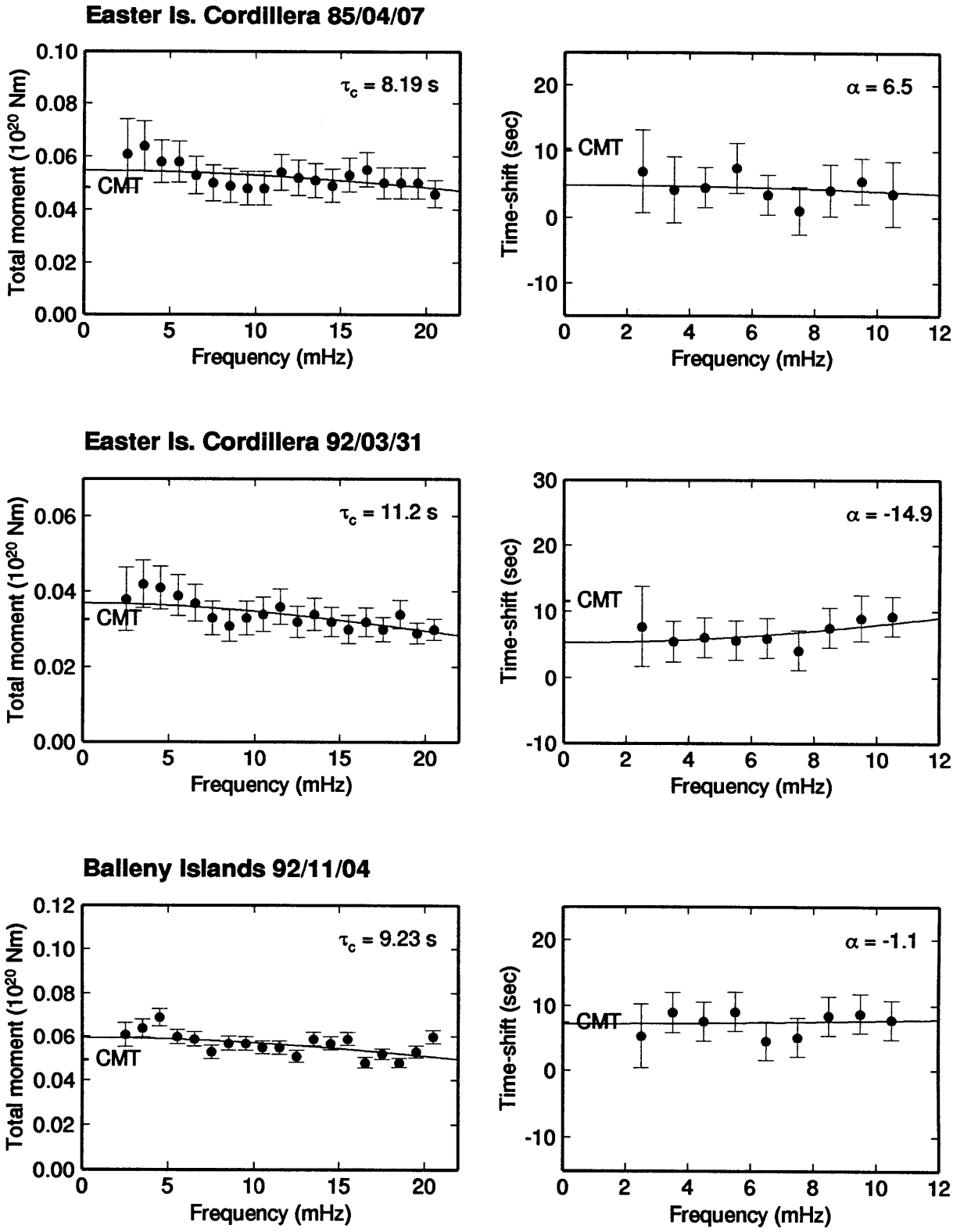
Easter Is. Cordillera 85/04/07
Total moment (10^{20} Nm)
τ_c = 8.19 s
CMT
Frequency (mHz)
Time-shift (sec)
α = 6.5
CMT
Frequency (mHz)
Easter Is. Cordillera 92/03/31
Total moment (10^{20} Nm)
τ_c = 11.2 s
CMT
Frequency (mHz)
Time-shift (sec)
α = -14.9
CMT
Frequency (mHz)
Balleny Islands 92/11/04
Total moment (10^{20} Nm)
τ_c = 9.23 s
CMT
Frequency (mHz)
Time-shift (sec)
α = -1.1
CMT
Frequency (mHz)

Figure 2.8

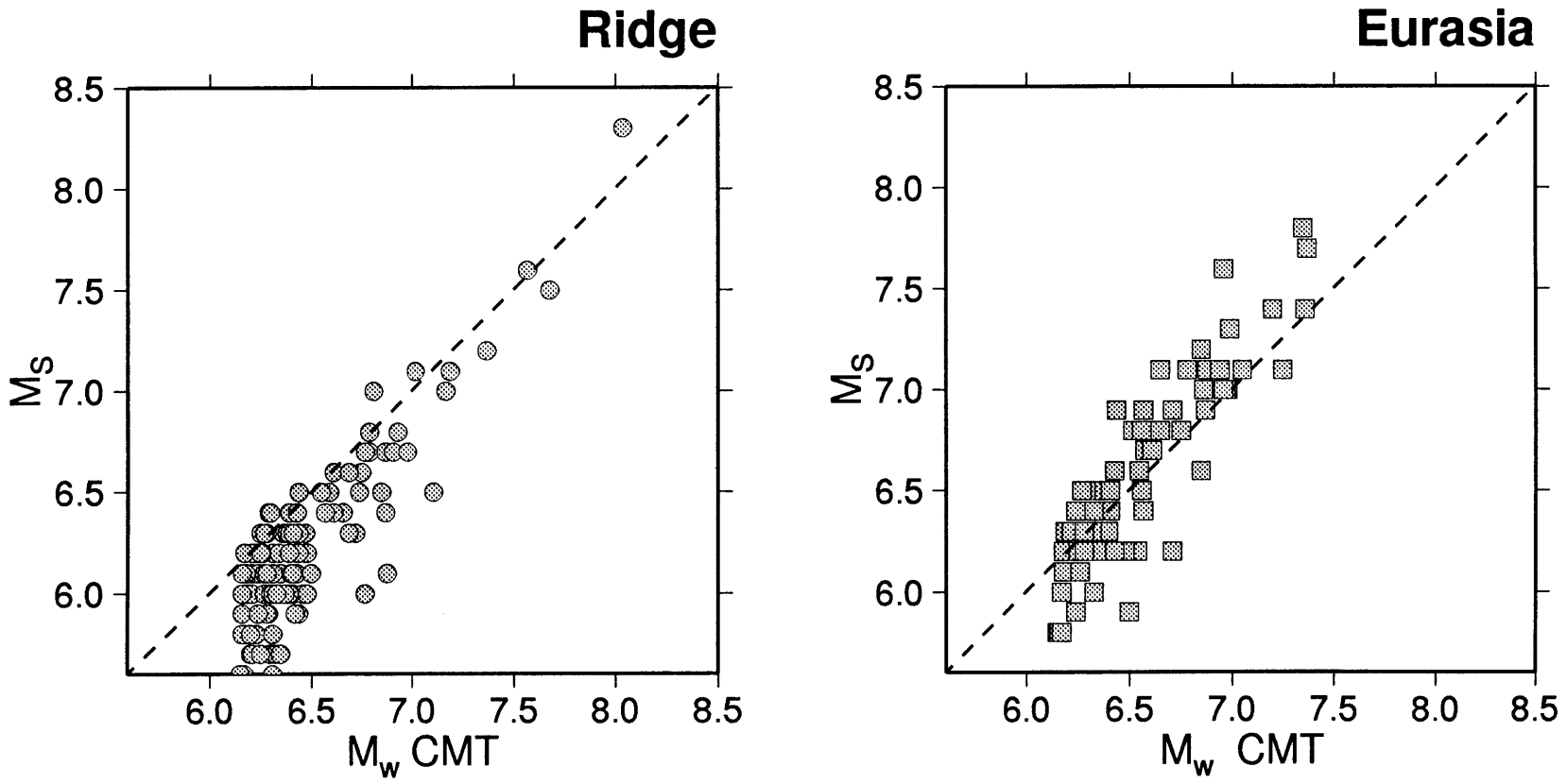

Figure 2.9

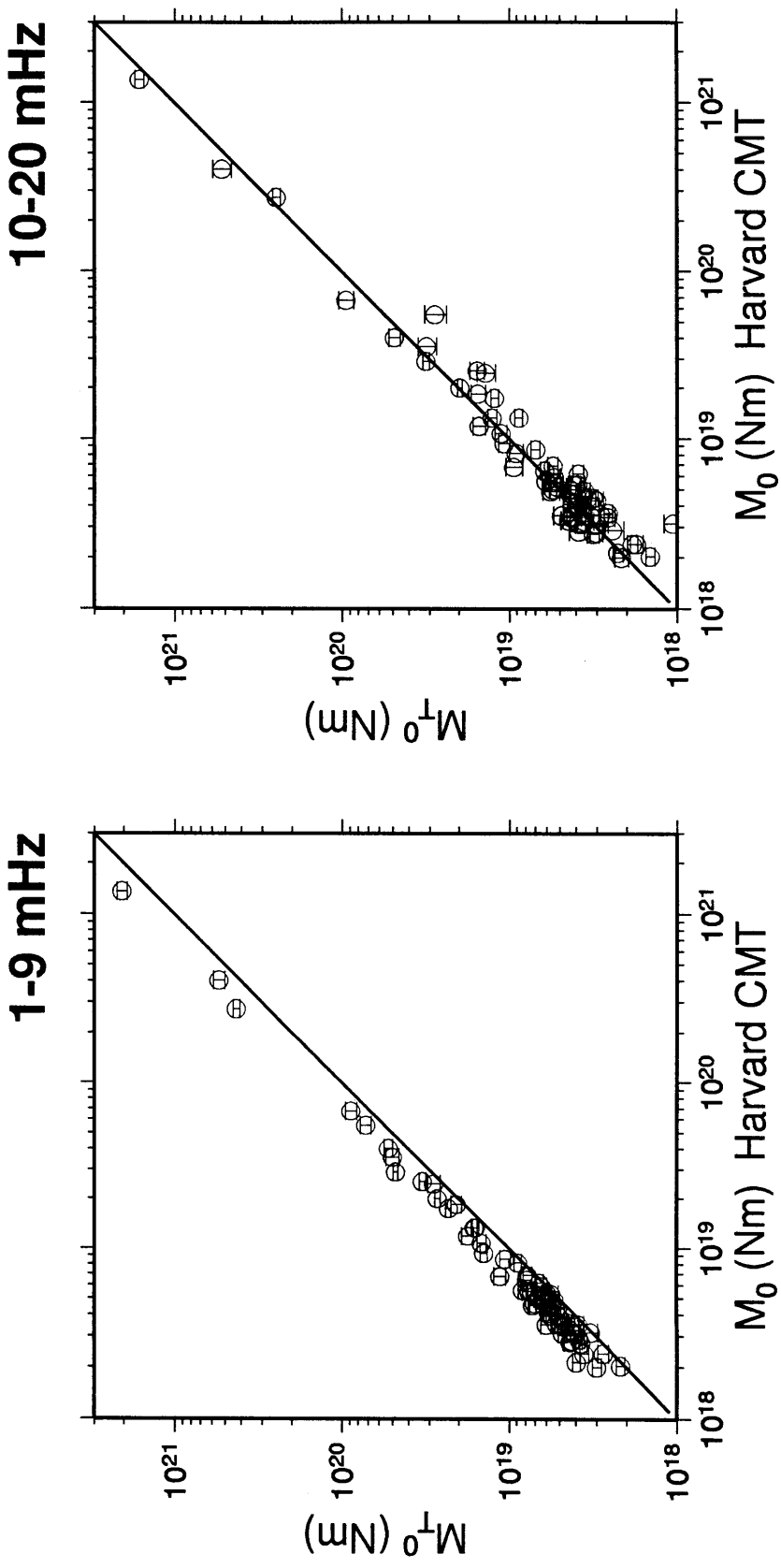

Figure 2.10

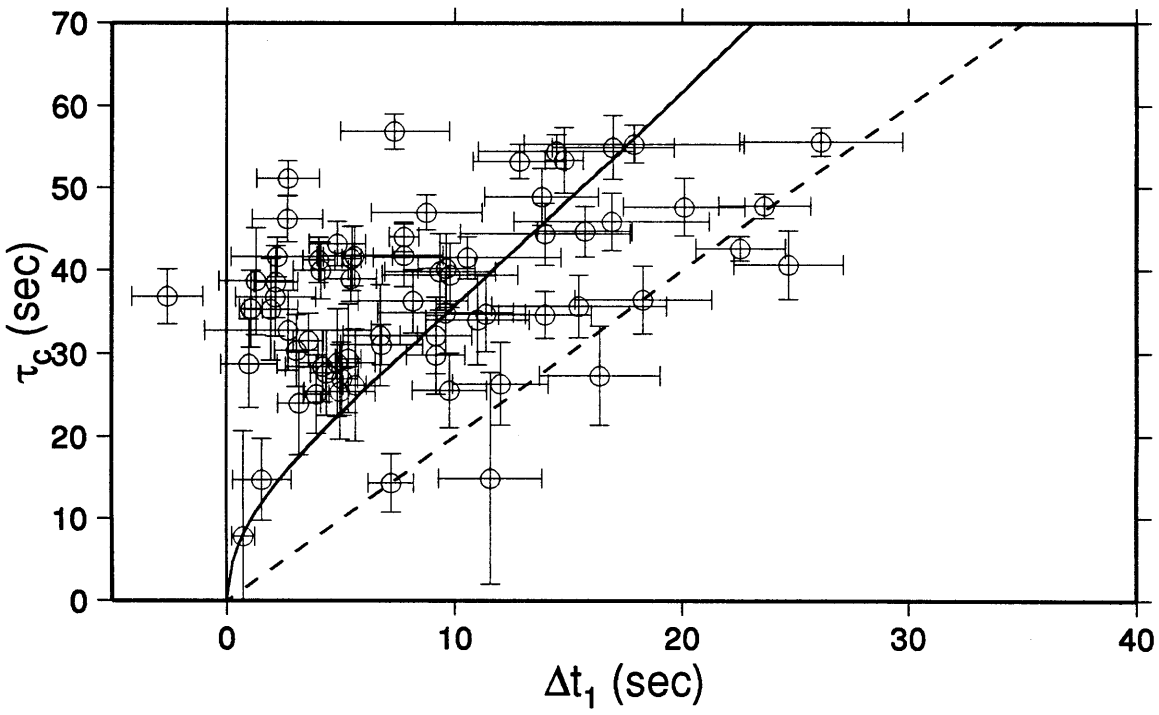

Figure 2.11

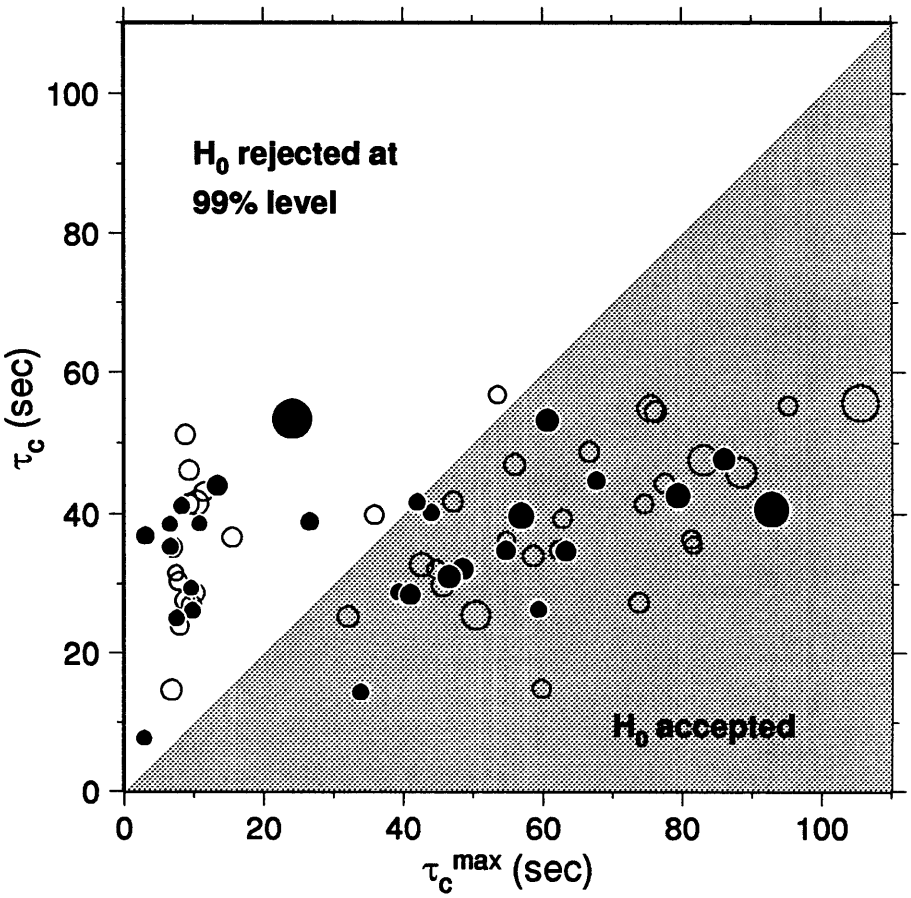
H_0 rejected at
99% level
H_0 accepted
τ_c (sec)
τ_c^{max} (sec)
0
20
40
60
80
100

Figure 2.12

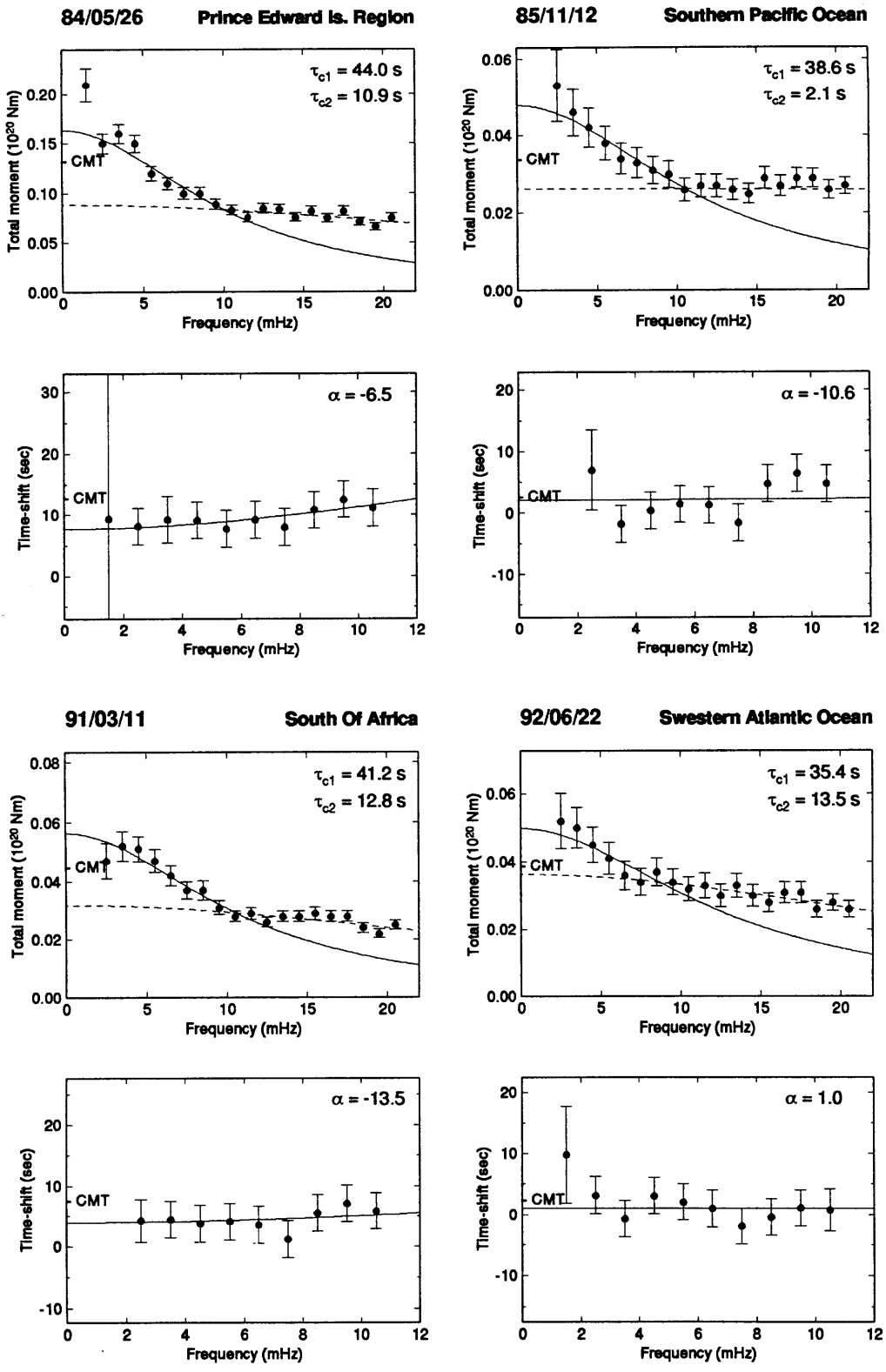
84/05/26
Prince Edward Is. Region
τ_{c1} = 44.0 s
τ_{c2} = 10.9 s
CMT
Total moment (10^{20} Nm)
Frequency (mHz)
α = -6.5
Time-shift (sec)
85/11/12
Southern Pacific Ocean
τ_{c1} = 38.6 s
τ_{c2} = 2.1 s
α = -10.6
91/03/11
South Of Africa
τ_{c1} = 41.2 s
τ_{c2} = 12.8 s
α = -13.5
92/06/22
Swestern Atlantic Ocean
τ_{c1} = 35.4 s
τ_{c2} = 13.5 s
α = 1.0

Figure 2.13

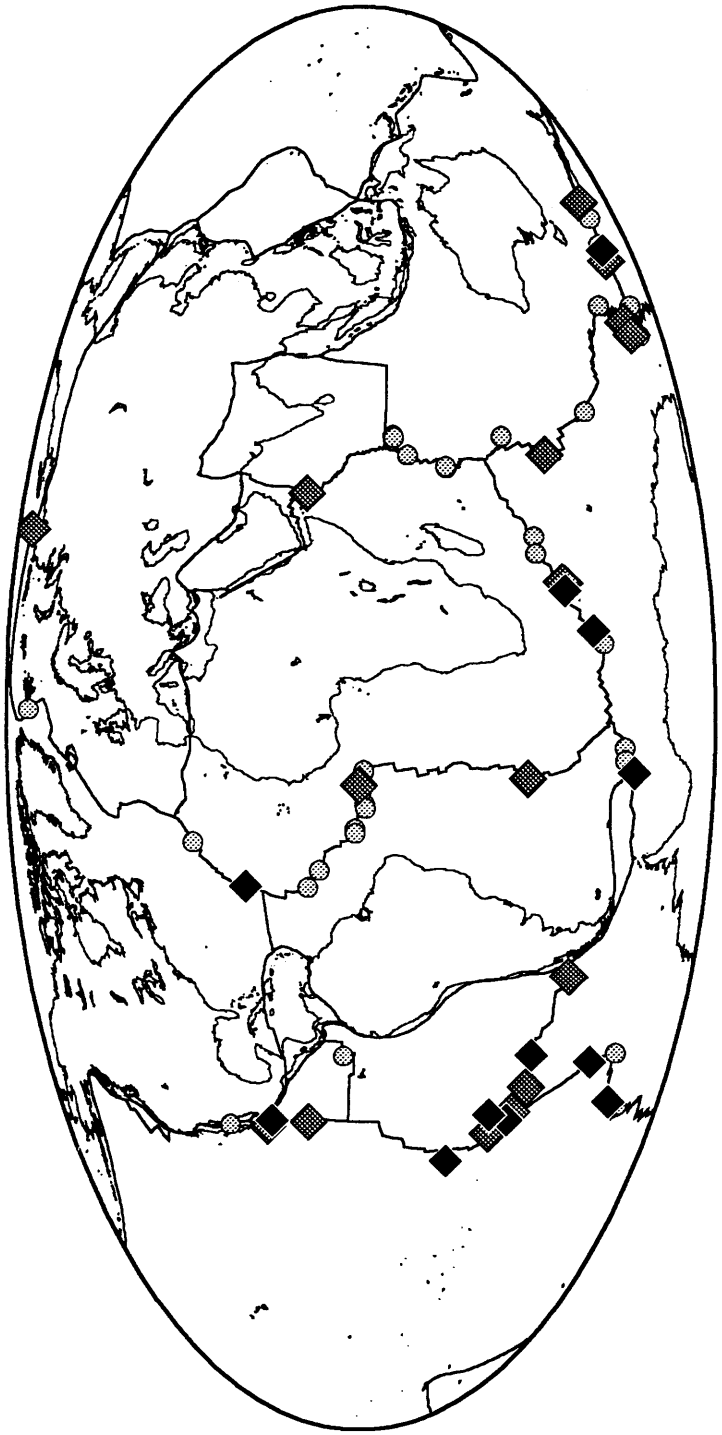

Figure 2.14

CHAPTER 3

Inversion of low-frequency spectra for the source time function

3.1 Introduction

Although the spatio-temporal history of rupture is plausibly fractal, limitations in the bandwidth of seismic data, incomplete azimuthal sampling, and observational errors allow at best to the retrieval of some average properties of the seismic source. One of these is the source time function, which describes the fault averaged rate of moment release during an earthquake. Waveform inversion techniques are routinely employed to infer the time history of rupture of large events (for example: Ekström, 1989; Nabelek , 1984; Ruff, 1989; Kikuchi and Kanamori, 1982, 1986, 1991; Das and Kostrov, 1990), usually from first arrival *P* and *SH* waves for stations at epicentral stations between 30 and 90 degrees. The waveform fitting is typically performed in a narrow window 20 to 100 s long. So-called broad-band inversions lack low-frequency resolution and it is not surprising that the scalar moment obtained by these techniques often underestimates the total scalar moment of an event. This drawback has long been recognized, and low-frequency constraints have been imposed on broad-band inversion for the source time function (Ekström, 1989). However, no account has been made so far of the actual spectral shape of events below 10 mHz, and we will show that frequency resolution in the band 1-10 mHz is indispensable in studying events with long duration, such as slow earthquakes and slow precursors.

Time domain methods also may be biased towards the dominant periods of the time series, which in turn may partly explain why separate inversions of *P* and *SH* waves for the same event sometimes disagree (compare Figure 15 and 16 in Das, 1993). Moreover, in

order to retrieve details of the rupture history and to eliminate epicentral mislocation artifacts, waveforms are aligned relative to onset times at a individual station, with the adverse effect of losing information about absolute time. We present a method to estimate, in a self-consistent manner, the source time function (or moment rate function) of large earthquakes. The technique is based on the inversion of network-averaged source amplitude and phase-delay (equivalently time-shift) spectra from 1 to 50 mHz. These spectra are obtained from the analysis of normal-mode, surface-wave, and body-wave data. Our method incorporates such low-frequency information as the total scalar moment, the centroid time-shift, and the characteristic duration of an earthquake, which are not readily available from classical waveform inversion. We illustrate our procedure with a discussion of two recent large California earthquakes, the 1992 Landers and the 1994 Northridge events, and the 1992 Nicaragua slow earthquake (Chapter 4). Further applications will be shown in Chapter 5, with the detection of slow precursor to the great 1989 Macquarie event, and Chapter 6, where we discuss the time domain observation of a slow precursor to the 14 Mar 1994 Mid-Atlantic Ridge event.

3.2 Normal mode techniques

Spectral quantities in the frequency band 1-20 mHz are obtained from very-long period seismograms using optimized spectral and network averaging procedures that are aimed at reducing bias due to unmodeled source and propagation effects. Differential measurements are made with respect to synthetics and the philosophy adopted here is to always perform the same operation both on the synthetics and on the data. The spectral data in Figures 3.3 and 3.5 are obtained by two types of analysis having different sensitivities to unknown propagation effects. In the next paragraphs, we briefly summarize the spectral retrieval methods presented in Chapter 2.

The solid circles in Figures 3.3 and 3.5 are estimates based on normal-mode techniques. The total-moment spectrum $M_T(\omega)$ is recovered by a variant of the method described by Silver and Jordan (1982, 1983): the squared-amplitude spectrum for each seismogram is integrated over disjunct 1-mHz bands and the integrals for all seismograms are inverted using an algorithm optimized to account for aspherical heterogeneity, errors in the assumed source mechanism, and ambient seismic noise. The result of the inversion is insensitive to incorrect centroid time of the event and to unmodeled elastic structure of the earth. The Harvard CMT mechanism serves as our best point source approximation and is generally suited for this purpose.

Estimates of $\Delta t(\omega)$ are derived by an algorithm formulated by Riedesel et al (1986) and Jordan (1991): the complex Fourier spectrum for each observed and synthetic seismogram is integrated over narrow (~0.1 mHz) intervals centered on the average eigenfrequencies of the fundamental modes, and a phase-delay time relative to the synthetic is calculated from the peak of a cross-correlation function constructed by summing products of the complex-valued spectral integrals over 1-mHz bands. $\Delta t(\omega)$ is then obtained by averaging the phase-delay times over the network. Because the Riedesel-Jordan method integrates over individual modes, it is not applied at frequencies above 11 mHz, where the mode spectrum becomes densely populated and the fundamental-mode resonance peaks begin to overlap considerably. In both procedures, the spectral integrals are derived from 6-hr time series, which include fundamental-mode surface waves with orbits up to R_4 and G_5. Normal modes methods, because they average over multiple orbits show little sensitivity to source finiteness effects, such as directivity (Silver and Jordan, 1983).

3.3 Traveling wave techniques

Surface waves

The filled squares in Figures 3.3 and 3.5 are spectral estimates measured from surface waves by a narrow-band cross-correlogram analysis similar to the generalized seismological data functional approach of Gee and Jordan (1992). Isolation filters are obtained for the Rayleigh-wave or Love-wave groups by windowing these wave-groups from synthetic seismograms. Synthetic seismograms are computed for a step source function. Isolation filters are then cross-correlated in the time domain with both observed and full synthetic seismograms, yielding two broad-band cross-correlograms for each station/receiver pair. These cross-correlograms are windowed to reduce the influence of other phases on the seismograms, as well as edge effects. A Hanning taper centered on the peak of the cross-correlograms is used to minimize signal distortion by the window and its width is set according to the smallest frequency to be resolved (Gee and Jordan, 1992). Both windowed cross-correlograms are filtered at one mHz intervals with a narrow-band Gaussian filter. Synthetic test indicated that filters with one-sigma width of 0.5 mHz are optimal to robustly resolve spectra in the band 2-20 mHz.

Gee and Jordan (1992) approximate the windowed narrow-band filtered broad-band cross-correlograms with a five-parameter Gaussian wavelet . One of these parameters is the bandwidth of the cross-correlogram. The four others are frequency dependent quantities which are functionals of the earth structure, i.e. the differential phase and group delay between observed waveforms and synthetics, and two related amplitude parameters. Gee and Jordan apply corrections to these quantities for the effect of windowing and filtering.

In our procedure, we determine only two of these parameters, the differential phase delay and its related differential amplitude. Instead of using the Gaussian wavelet formalism, $\Delta t(\omega)$ for an individual station, is determined from the lag time difference between of the two narrow-band cross-correlograms peaks. Gee and Jordan show that this approximation is warranted as long as the bandwidth of the filter is small (eq. 54a). In that case, the envelope of the cross-correlogram decays slowly, and the lag-time of the peak is a good estimator of the differential phase delay. In case of a large bandwidth, the envelope rolls off quickly and the lag time of the peak is biased towards the differential group delay. Further, one has to require that the group delay of the source be small. In our experience, we find that phase delay spectra of large earthquake display little frequency dependence and therefore have negligible group delays.

The differential amplitude between observed seismograms and synthetics is obtained from the ratio of the narrow-band cross-correlograms peak amplitudes. The total moment $M_T(\omega)$ for a given station is then the product of the differential amplitude with the scalar moment used to compute the synthetics. This approximation is valid as long as the window is wider than the broad-band cross-correlogram (Gee and Jordan, 1992, eq's. 58 and 59), i.e. when the full frequency dependence of the cross-correlograms is retained. In the limit of a very narrow window, the broad-band cross-correlogram is reduced to a spike with a flat spectrum, and we could not resolve any frequency dependence of the source. In our application, the Hanning taper used to window the cross-correlogram is typically set to the lowest frequency that we want to resolve.

Moreover we will also neglect effects due to the shift of the effective center frequency of the narrow band cross-correlogram. This approximation is going to be best at the center of the effective full bandwidth and worse at its edges and, in fact, we observe large variability in estimates made at the lowest frequency point, typically at 2 mHz for surface waves (which may also be due to the increasing noise level between 1 and 3 mHz).

To avoid cycle skipping, a one-cycle search is performed for a positive peak of the narrow-band cross-correlogram around the time lag obtained from the narrow-band cross-correlogram between isolation filter and synthetics. Phase unwinding starts at the lowest frequency band because cycle-skipping is not likely to occur at very low-frequencies. We keep track of differential phase delays from band to band and center our search in each band at the differential lag time obtained at the next lowest frequency. Improvement in the continuity of time-shift spectra is obtained, especially between 10-20 mHz.

Estimates of $M_T(\omega)$ and $\Delta t(\omega)$ are then constructed by averaging these differential phase and amplitude measurements over the global network. Figure 3.6 shows an example of the scatter of individual stations. In this study, we process only the first-orbit groups — R_1 on vertical components and G_1 on transverse components — using isolation filters with optimal durations of about one hour. In the case of strong source directivity and of poor azimuthal sampling of the source mechanism, residual source directivity effects can bias estimates of $M_T(\omega)$ and $\Delta t(\omega)$. This can however be tested by comparing spectra retrieved from R_1 and R_2 orbits that leave the source at opposite azimuths. Figure 5.8 (Chapter 5) shows the similar time-shift spectra obtained from R_1 and R_2 orbits for the Macquarie 1989 event indicating little or no directivity of the source process, a fact confirmed by other studies (e.g. Ekström and Romanowicz, 1990; Braumiller and Nabelek 1990).

A description of data selection criteria is given in Chapter 2. We proceed in a similar fashion with spectral data obtained with the traveling wave technique. Individual spectra showing amplitude or time-shift problems are eliminated prior to averaging, as well as spectra that show erratic behavior. Sometimes trimming of outliers is necessary to stabilize the average.

Body waves

In the band 12-50 mHz, the cross-correlation procedure is applied at 2 mHz intervals to the body wave part of the seismogram, where time-windows of 200 to 400 s in duration isolate waveforms of interest from long period or broad-band records. Since we compute theoretical transfer functions by normal-mode summation, the choice of phases and seismograms is not restricted to direct arrivals and can typically include multiple surface-reflected phases, diffracted phases and core phases, with the advantage of providing a wider sampling of the focal mechanism. In general, we prefer to use the early part of the body wave train in order to diminish the influence of scattered and converted energy on our body wave estimates of $M_T(\omega)$ and $\Delta t(\omega)$. Amplitude spectra show sometimes large scatter, which may be due to source complexity or to near source structure. This effect is most pronounced for shallow dip-slip events, where surface reflected phase contribute significantly to first arrival waveforms. On the other hand, time-shift measurements are typically stable, and show little scatter around the mean. Consistent overlap of body-wave and surface wave data between 12 and 20 mHz indicates a successful retrieval of a continuous source spectrum over a wide frequency range (see for example Figure 3.3 and Figure 3.5), and higher-order, spatio-temporal properties of the source, such as directivity, are averaged out, provided sufficient azimuthal coverage is available.

3.4 Assessment of propagation bias

Amplitude spectrum

In Chapter 2, we discussed at length biases that can affect amplitude spectra retrieved with the normal mode technique. The sensitivity to the radial attenuation model used to

compute synthetics will be similar for both the normal mode and the traveling wave methods. Directivity, mislocation, and near source effects are also expected to affect both techniques in a similar way, but we found that azimuthal averaging is appropriate to eliminate them. The modal techniques rely on temporal and spectral averaging to reduce scattering effects. Contrary to the powerspectral standing-wave method used to retrieve amplitude spectra, the cross-correlation procedure is phase-sensitive and more likely to be affected by focusing/defocusing and multipathing effects, and may be biased to low values, especially between 8-20 mHz. As a remedy, the traveling-wave method captures information about the source from the first-orbit surface waves, which have not had much time to interact with aspherical heterogeneities. Spectral averaging is also performed in the cross-correlation procedure by the use of narrow band Gaussian filters. The cross-correlation procedure is effective in rejecting signals incoherent with the isolation filters, including any pseudo-Love and pseudo-Rayleigh waves due to Coriolis and anisotropy coupling. Comparison between the two methods gives independent checks on how well the spectra-recovery procedures eliminate propagation effects, and we note on Figure 3.3 and 3.5 that the spectra derived by the standing-wave and traveling-wave algorithms are in excellent agreement, despite the different sensitivities of the two methodologies to various types of scattered signals.

Time-shift spectrum

The time-shift spectra are most sensitive to inaccuracies in the radial elastic structure used to compute synthetics. From a global study of shallow seismicity, we find that PREM+S12_WM13 is slow, on average, for vertically polarized surface waves between 7-20 mHz, leading to large negative time-shifts. Figure 3.1 displays a contour plot of time-shifts referenced to the CMT centroid time from 2 to 20 mHz obtained with the traveling wave technique. All available stations (very-long period channel) of 102 large shallow events (R1

only) contribute to the analysis. The contour plot is in multiples of a uniform distribution and is constructed from over twenty thousand estimates of $\Delta t(\omega)$, centered at $\{\omega_n = 2+n$; n = 0,1,...,19} mHz. It is well known that the band from 4-6 mHz have the smallest variance. Figure 3.1 shows that the spherically averaged structure of PREM is slow by about 0.4% for fundamental mode Rayleigh waves in the frequency band 10-20 mHz. In this band, the large spread of phase-delay measurements diagnoses the inadequacy of S12_WM13 to account for high-wavenumber lateral heterogeneity in the crust and upper mantle. Unless accounted for, PREM's bias for vertically polarized surface waves can cause serious errors in the interpretation of low-frequency spectra. To correct for this bias, we use phase delay maps, expanded in spherical harmonics up to degree and order 36, obtained from surface waves in the range 8 to 25 mHz (Ekström and Tromp, unpublished material, 1994). We recompute all the time-shifts with surface wave isolation filters corrected for the predicted phase delays. Figure 3.1 shows that the propagation bias has been effectively accounted for. There appears to be a residual 1-2 second negative bias from 2-15 mHz that could be due to our choice of events, to an unbalanced coverage of the earth lateral structure, or to the fact that in some cases the CMT centroid time is biased to large values.

Other radial earth models exist, but not all of them are suited for our analysis, such as 1066A (Gilbert and Dziewonski, 1975), an early model satisfying normal mode data. The IASPEI91 model (Kennett, 1991), based on travel-time data, is not appropriate for our low-frequency analysis. CORE11 (Widmer, 1991) has been constructed as a smooth perturbation to PREM that satisfies an augmented data set of modal eigenfrequencies. For our purpose, PREM has the advantage of being constructed from normal mode, surface wave and body-wave data sets. In addition, most 3D tomographic models of the earth that we employ in our synthetic calculations use PREM as a starting model, such as the SH8-series (Woodward et al., 1993), S12_WM13 (Su et al., 1994) and SH10 (Masters et al., 1992). Recently obtained phase delay maps for Rayleigh waves in the period range of 40 to 120 s are based on PREM (Ekström and Tromp; Trampert and Woodhouse, unpublished material).

3.5 Spectral Inversion

The amplitude and time-shift spectra of large earthquakes are retrieved from 1 to 50 mHz through network averaging procedures in narrow frequency bands centered at $\{\omega_m; m = 1,..., M\}$. The phase and amplitude data are combined to form estimates of the complex Fourier spectrum of the moment release function, $f(t)$, yielding a linear relationship between the data and the model. In the point source approximation, we define the moment release function as

$$f(t) = \frac{1}{\sqrt{2}} \int_V \hat{\mathbf{M}} : \dot{\Gamma}(\mathbf{r},t)\, dV(\mathbf{r}), \tag{3.1}$$

where $\hat{\mathbf{M}}$ is the time independent source mechanism with unit Euclidean norm, and $\dot{\Gamma}(\mathbf{r},t)$ is the stress glut rate tensor (Backus and Mulcahy, 1976). The inversion method[1] presented here assumes no-backslip on the fault and a constant source mechanism. Errors in the data are assumed to be uncorrelated. The fact that errors in the data are statistically independent cannot be entirely satisfied for two reasons. First of all, the narrow band Gaussian filters used in the traveling wave method overlap at their trailing edges, leading to serially correlated errors. Secondly, it is likely that lateral heterogeneities correlate errors across adjacent spectral bands, even though network averaging and band-averaging should considerably diminish this effect. The constant-mechanism assumption holds in most cases. We rarely observe variations in mechanisms retrieved with the normal mode technique of Riedesel (1985) in the band 1-11 mHz. For example, Figure 3.3 shows our inversion results for the Landers 1992 event. The earthquake's source process has strong northward directivity, superposed on an westward azimuthal rotation of its strike-slip

---

[1] Details of the inversion algorithm and of its properties can be found in Appendix A

mechanism by over 30°. We find that the event's mechanism is stable in the 1-11 mHz band (Figure 3.7). Our results are in good qualitative and quantitative agreement with other studies (e.g. Wald and Heaton, 1994). On the other hand, some crustal earthquakes, such as the 1980 Irpinia, Italy (Harabaglia, 1993), and the 1988 Spitak, Armenia (Kikuchi et al.,1993) events , show strong frequency dependence of their focal mechanisms in the 1-11 mHz band, indicating multiples source with time varying geometry. In the present stage of our procedure, such events cannot be reliably processed.

The inversion algorithm minimizes a chi-squared measure of misfit to the data and a quadratic form that measures the roughness of $f(t)$, subject to the positivity constraint $f(t) \geq 0$ for $t \in [t_*, t_{max}]$ and vanish outside the specified start t_* and end t_{max} of moment release, $f(t) = 0$ for $t \notin [t_*, t_{max}]$. The smoothing constraint is key to regularizing the inversion (Tikonov and Arsenin, 1977) and damping the non-uniqueness of the problem. In many applications, it is preferable to obtain a smooth solution that satisfies the data, rather than building into it unnecessary details not required by the observations (Constable et al, 1987; Stark and Parker, 1987). Together with a measure of misfit to the data, we choose to minimize the scalar functional

$$R_k = \int_{t_*}^{t_{max}} \left| f^{(k)}(t) \right|^2 dt, \qquad (3.2)$$

where (k=1,2) indicates the order of the time derivative. In the inversion, R_k is given a weight $\mu > 0$ (eq. A.10 of Appendix A) and in general, we find that the final solution is insensitive to a particular choice of k, unless μ is very large. This quadratic programming problem is solved using a computer code written by Stark and Parker, based on Lawson and Hanson's original NNLS algorithm (Lawson and Hanson, 1974). $f(t)$ is typically discretized into steps of 1 to 5 seconds in length over the interval $[t_*, t_{max}]$. We find that the solution is insensitive to the choice of the sampling interval, provided it is small enough.

In order to determine the acceptable start and end time required by the spectral data, a suite of inversions are performed for a range of t_* and t_{max}. The choice of the regularization parameter is constrained in two ways. The solution moves along a trade-off curve between data misfit and smoothness. The rougher solution fits the data best, whereas the cost of increased smoothing is a larger misfit. A range of μ is found that produces an acceptable misfit to the data and for which features of the solution are robust. The choice of the regularization parameter is a subject of active research in optimization theory. For example, cross-validation techniques (Wahba,1990) offer another way to determine an optimal value of μ by requiring internal consistency of the data. We will comment more on the choice of the regularization parameter in the section dealing with the estimation of solution errors. Finally, an external check on the choice of μ is an assessment of the misfit between the waveforms predicted by the solution and the observed time series.

The smoothing parameter that can be made time-dependent $\mu = \mu(t)$, and allows for the study of episodes of smooth moment release. This particularity was used by Ihmlé et al, (1993) to test the hypothesis that a slow precursor was necessary to account for the spectral characteristic of the great 1989 Macquarie earthquake. Station residuals computed relative to the prediction of a particular solution can be used to perform frequency dependent or broad-band relocation. Moreover, station-averaged spectra and individual spectra can be jointly inverted for a directivity vector, either band by band or in a broad-band sense. Future work will also include the recovery of the frequency dependent moment tensor up to 50 mHz. Such data could in principle be inverted to infer the time history of complex ruptures.

In the following sections, we will present an application of the spectral retrieval and inversion procedures to two well-known California earthquakes that have compact source time functions: the 1992 Landers and the 1994 Northridge events. Chapter 4 will be

concerned with the slow 1992 Nicaragua event. Chapter 5 discusses in detail the detection of a slow precursor to the great 1989 Macquarie event, and in Chapter 6, we present a study of an unusual earthquake that occurred on the Romanche transform on 14 Mar 1994.

3.6 The 1992 Landers earthquake

The 28 June 1992, Landers earthquake (M_W= 7.3) appears to belong to a group of events having large stress drop and long recurrence time (Kanamori et al., 1992), typical of inter-plate earthquakes. As the rupture proceeded northward from the epicenter, the earthquake broke several vertical fault strands, leading to a rotation of the focal mechanism by nearly 35°. A total source process time of about 24 s has been obtained from the joint inversion of teleseismic, strong-motion and geodetic data (Wald and Heaton, 1994). The strong directivity produced large impulsive waveforms in a northern azimuth and dynamic stress changes associated with the shear waves are thought to have remotely triggered burst of seismic activity north of the epicenter (Hill, 1993). Total fault length is estimated to be 70 km from the aftershock distribution and from surface breaks, which reached peak values of 6 m of right-lateral strike-slip (Sieh et al., 1993).

The network-averaged spectra retrieved from vertical component seismograms with the normal mode and traveling wave techniques are displayed in Figure 3.3. We note the good agreement of the normal mode and the surface wave data in the band 1-8 mHz. The overlap between surface wave and body wave time-shift data is excellent, but less satisfactory in the amplitude spectrum. The scalar moment of 1.0 10^{20} Nm is in agreement with the CMT moment of 1.0 10^{20} Nm. Kanamori et al. (1992) and Sieh et al. (1993) obtain a scalar moment of 1.1 10^{20} Nm from long period surfaces waves. Inversion of strong motion records give a value of 1.1 10^{20} Nm (Campillo and Archuleta, 1993). The static moment obtained by geodetic methods is lower, for example, 0.8 10^{20} Nm (Murray et al., 1993) and

0.7 10^{20} Nm (Wald and Heaton, 1994). We obtain a centroid time-shift of 14.7 s, which is 3 s earlier than the CMT estimate of 17.7 s. The mechanism spectrum for this event shows no sign of frequency dependence in the band 1-11 mHz (Figure 3.4). The vertical fault plane of these mechanisms has a strike of 340° in agreement with both the CMT solution and Kanamori et al.'s, (1992) long-period surface wave mechanism. It represents an average of the faulting geometry, which is composed of three main fault segments striking at 355° (Johnston Valley and Landers faults), at 334° (Homestead valley fault) and at 320° (Camp Rock faults) (Wald and Heaton, 1994).

In Figure 3.3, the total moment spectrum is flat up to 10 mHz and begins to roll-off primarily in the body wave band. In addition to direct *P* and P_{diff}, *PP* waves are included in the body wave estimates. Except for *PP*, these phases have a diminished sensitivity to directivity effects because they leave the vertical fault plane with steep take-off angles. Nevertheless, we experienced some difficulty in obtaining stable estimates of the amplitude spectrum in the body wave band, reflected in the large standard errors (Figure 3.3), probably because of the combined effect of mechanism rotation and directivity of the event. The time-shift spectrum is slightly curved upward, indicating that the overall source process was asymmetric, with more moment being released near the end of the rupture.

We invert the spectra for the best point source moment release function, under the assumptions that no-backslip occurred during the event and that the focal mechanism remained constant. Our preferred model and the average mechanism employed to recover the spectra are shown in Figure 3.3. Our model tends to slightly underestimate the scalar moment in the band 10-50 mHz, and we do not attempt to fit spectral details in the body wave band, where amplitude spectra show large variations, possibly because of source complexity. The model also predicts time-shifts that are larger than the data by about 1-2 s in the band 1-8 mHz, probably because of inaccuracies in the earth model used to compute synthetics. This fact is also shown in Figure 3.1, where PREM appears to be slow for Rayleigh wave by about 1-2 s in this band.

Our preferred source time function has a duration of about 25 s and has two distinct pulses of moment release located at +5 s and +17 s relative to GMT 11:57:35.3. The actual origin time of the event, listed by the PDE, is at GMT 11:57:34.1, and corresponds to a very small foreshock in the hypocentral region that lasted for about 2.5-3 s (Abercrombie et al, 1992). This time delay is accounted for here by allowing very little moment release in the two initial seconds of rupture.

Our result is in agreement with those obtained by waveform fitting which uses multiple sources to model the complex rupture process (Wald and Heaton, 1994; Campillo and Archuleta, 1993). The moment ratio of the first subevent relative to the second subevent is 1:4, less than the factor of 1:2 found by Campillo and Archuleta (1993) and Kanamori et al. (1992). The distribution of moment release as a function of time is determined by the shape of the time-shift spectrum. In order to allow more moment release in the early part of the source time function, the time-shift spectrum would need to be somewhat flatter in the 20-50 mHz band.

Future work will include directivity effects into the inversion procedure, and we will also attempt to retrieve mechanism spectra up to 50 mHz. Individual seismograms for the 1992 Landers event cannot be satisfactorily modeled with a point source with constant mechanism. As demonstrated here, however, the network averaging methods are successful in retrieving spectral estimates consistent with the assumption needed to carry out the spectral inversion for the source time function.

3.7 The 1994 Northridge earthquake

The 17 Jan 1994 Northridge event (M_W=6.7) occurred south-east of the Ventura basin, an east-west trending sedimentary basin located in the Western Transverse ranges of Southern California. Its thrust mechanism is consistent with the "transpressional" regime

caused by the bend of the San-Andreas faults that impedes right lateral motion between the North-American and Pacific plates. Preliminary seismological investigation indicates that the event nucleated at a depth of about 18 km and propagated upward without reaching the surface. In the Ventura basin earthquakes occur up to a depth of 28 km, nearly twice the maximum depth observed for other parts of Northern and Southern California (Bryant and Jones, 1992). The dip of focal plane, as obtained by long-period surface waves and teleseismic broad-band body waves, is about 45° south-southwest, slightly larger than that obtained from the aftershock distribution which indicates a fault dipping at 35°.

Figure 3.5 displays the network-averaged spectra obtained from vertical component seismograms. We note the agreement between the normal- modes, surfaces-wave and body-wave time-shift spectra in the range where they overlap. Total moment estimates obtained from body waves are larger that those from surfaces waves, but standard errors are large. We obtain a scalar moment of 1.2 10^{19} Nm in agreement with the CMT moment of 1.2 10^{19} Nm and with the identical value obtained at regional distances by Dreger et al. (1994, unpublished abstract). Spectra are flat, an indication that the source duration was short. Indeed, inversion of the spectra yields a source time function composed of a single pulse about 10 s in duration. This is slightly more than 6-8 s duration estimated by waveform inversion of broad-band records (Dreger et al, 1994, unpublished abstract). There is evidence that the shock was composed of two subevents 2 s apart (Wald et al, 1994, unpublished abstract). As discussed in Appendix A, the nominal resolution obtained from spectra with cut-off at 50 mHz is 5 s. Therefore, we do not expect to resolve such features of the source time function. Figure 3.7 shows the fit between data and synthetics convolved with the source time function of Figure 3.5. An excellent agreement, both in phase and amplitude, is found for the first arrival P and P_{diff} waves (at epicentral distances larger than 98°). Later arriving PP waveforms are well modeled as well. It appears that the 1994 Northridge event was a "normal" fast earthquake and that our algorithm correctly recovers the main features of the rupture process.

Figure captions

FIGURE 3.1. Contoured time-shift spectra from a global study of shallow earthquakes. *Panel A*: The traveling wave technique has been used to measure phase-delays between synthetics and first arrival Rayleigh wave packets, which for shallow focus events are dominated by fundamental spheroidal mode energy. All available stations of 102 large shallow focus events are used and time is reference to the CMT centroid time. Contours are in multiples of a uniform distribution. Over twenty thousand estimates of $\Delta t(\omega)$ contribute to the analysis. The solid and dashed lines indicate the average and the median, respectively. Synthetics have been computed via normal mode summation using PREM (Dziewonski and Anderson, 1981) and the low-order tomographic model S12_WM13 (Su et al., 1994), using the asymptotic formalism of Woodhouse and Dziewonski (1984). The bias in the radial earth model is apparent between 6 and 20 mHz. This indicates that the spherically structure of PREM is slow by about 0.4% in this band for fundamental mode Rayleigh waves. *Panel B*: Same plotting convention as *Panel A*. Synthetics include the phase delay maps, expanded in spherical harmonics up to degree and order 36, that Ekström and Tromp (unpublished material, 1994) obtained from surface-wave phase-delay measurements in the range 8 to 25 mHz. PREM's slow bias is accounted for. Both the average and the median closely follow the zero time-shift line. Compared to *Panel A*, the spread in the band 6-20 mHz has been notably reduced.

FIGURE 3.2. Location map for the 1992 Landers and the 1994 Northridge events. Stations employed in the body wave analysis are shown as filled circles; gray-shaded triangles denote stations used for the normal mode and surface wave observations. The major double-couple mechanism is shown in the usual lower hemisphere convention and is located at the epicenter. Current plate boundaries are indicated with the solid line.

FIGURE 3.3. Source time function of the 28 June 1992, Landers event. The solid line in *Panel A* shows the source time function obtained from the inversion of the total-moment and phase-delay spectra in *panels B* and *C*. A value of 10^3 for the regularization parameter has been used. The inset is the mechanism used in the spectral recovery methods. In panels A and C, time is referenced relative to the high-frequency origin time at GMT 11:57:35.3. This 2 s time delay, accounting for a small preshock near the epicenter, is implemented here by allowing very little moment release in the two initial seconds of

moment release. Three solid symbols denote the network-averaged spectra from the analysis of free oscillations (circles), surfaces waves (squares), and body waves (triangles). The spectral bandwidth is 1.5 to 48 mHz. The source time function of this event has a very long duration of about 24 s.

FIGURE 3.4. Mechanism spectrum of the 1992 Landers event. Due to the shallow hypocenter, the $M_{r\theta}$ and $M_{r\varphi}$ components of the moment tensor have been projected out of both data and model space (Riedesel, 1985). The major double-couple is shown with the solid lines. Equal area, lower hemisphere projection. The shaded areas are compressional, white areas dilatational. The cross is the principal compressional axis and the square is the tensional axis. Except for the 1.5 mHz band where noise levels are high, no frequency dependence is visible on these diagrams.

FIGURE 3.5. Source time function of the 17 Jan 1994, Northridge event. Same plotting convention as Figure 3.3. Note the small frequency dependence of the spectra, indicative of a short source duration. The source time function is sampled at 1 s intervals for a total duration of 25 s. The moment release rate function is 11 s long.

FIGURE 3.6. Scatter plot of amplitude and time-shift spectra from individual stations for the Northridge event. The traveling wave method has been used to measure the quantities in *panels A* and *B* from first orbit Rayleigh waves (R1). Symbols and shades of gray differentiate individual stations. *Panel A:* the vertical axis is the ratio of the cross-correlation between data and isolation filter at peak time divided by the autocorrelation of the isolation filter at zero lag. The isolation filter is constructed by windowing R1 from full synthetics. The synthetics are computed for a step function and incorporate the source mechanism. One obtains the total moment of the event in each frequency band by multiplying each estimate by the scalar moment used to compute the synthetic seismograms. *Panel B*: the synthetics are computed for the PREM+S12_WM13 model and use the phase delay maps of Ekström and Tromp (unpublished material, 1994).

FIGURE 3.7. Waveform fit of long-period *P* waves. Top traces of each group are data from vertically polarized seismograms; lower traces are synthetics convolved with the source time function of Figure 3.5. Traces have been low-pass filtered with a 10 pole Butterworth filter with corner at 35 mHz. They are aligned with respect to the predicted *P*-wave arrival time. The filter group delay is about 10-12 s.

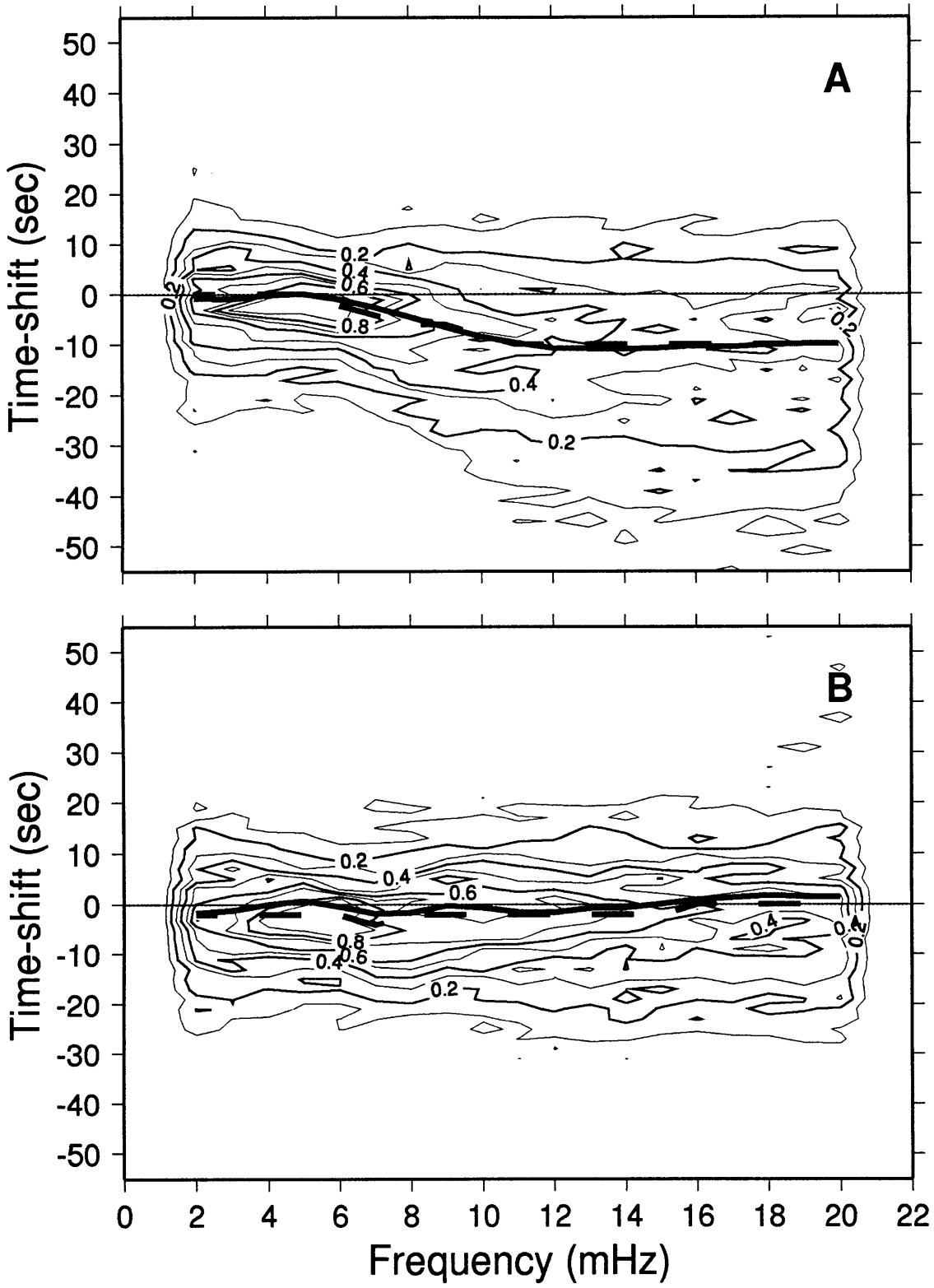
A
B
Time-shift (sec)
Frequency (mHz)
50
40
30
20
10
0
-10
-20
-30
-40
-50
0
2
4
6
8
10
12
14
16
18
20
22
0.2
0.4
0.6
0.8

Figure 3.1

Landers 92/06/28

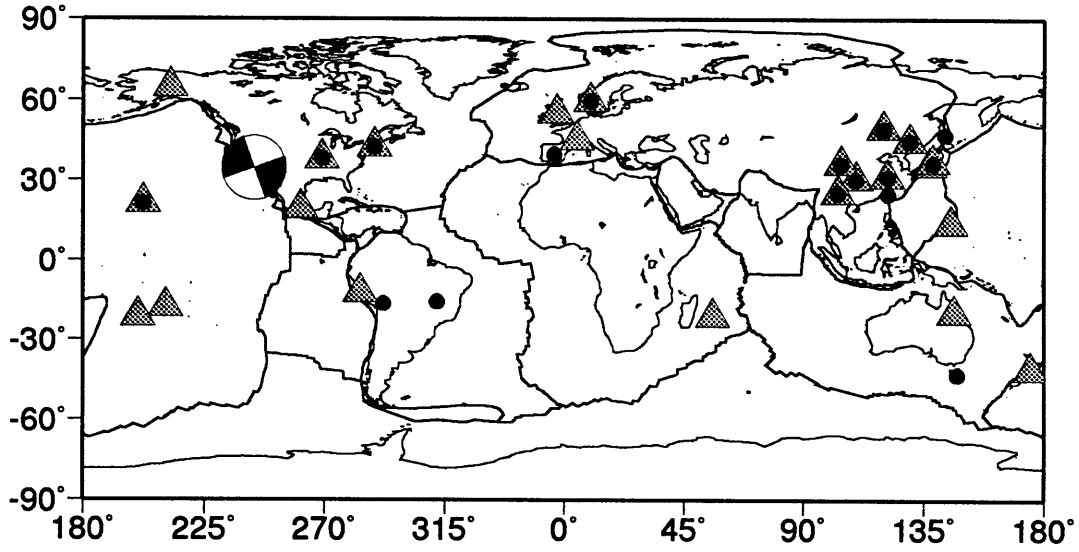

Northridge 94/01/17

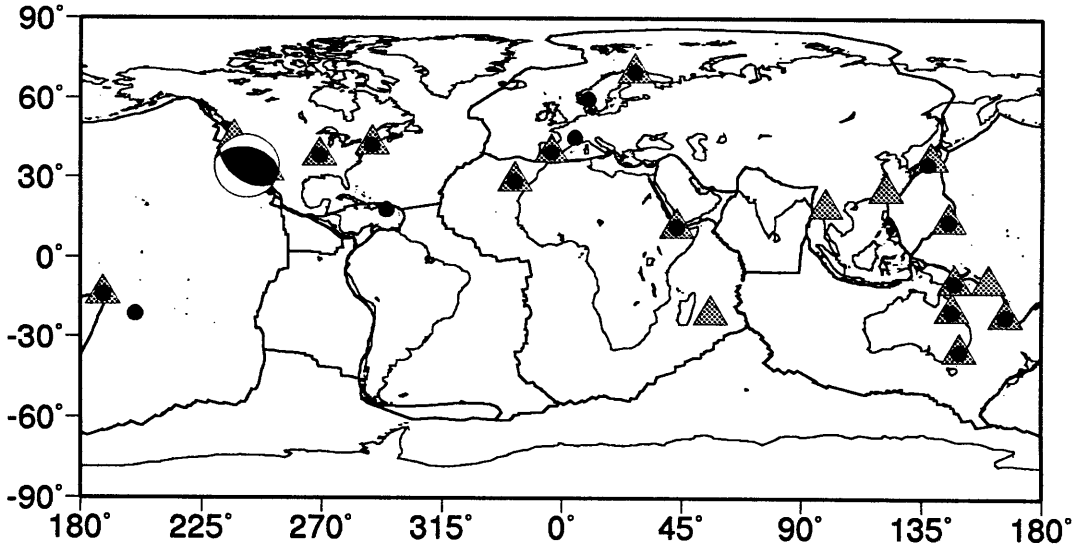

Figure 3.2

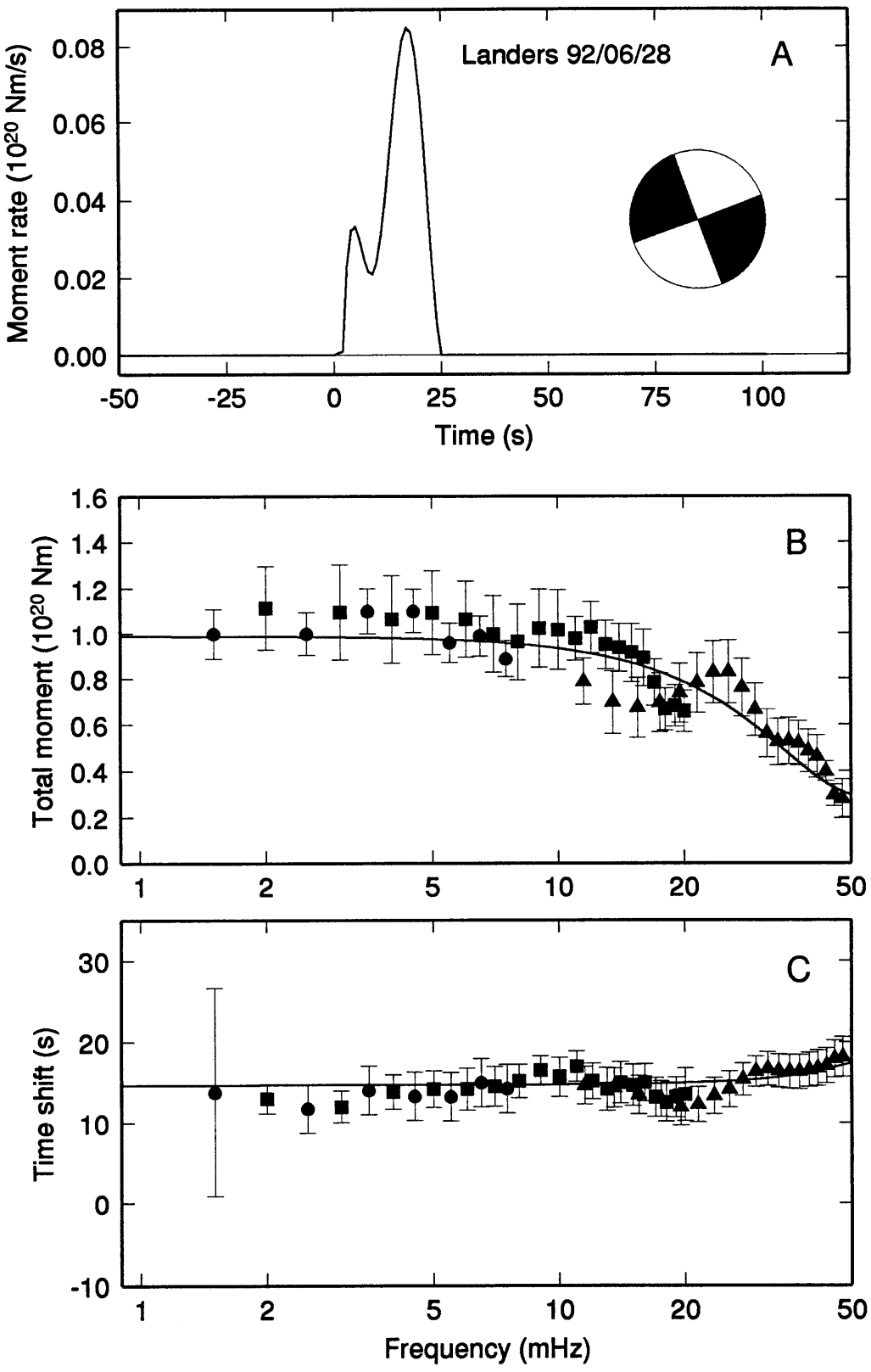
Landers 92/06/28
A
Moment rate (10^{20} Nm/s)
0.08
0.06
0.04
0.02
0.00
-50
-25
0
25
50
75
100
Time (s)
B
Total moment (10^{20} Nm)
1.6
1.4
1.2
1.0
0.8
0.6
0.4
0.2
0.0
1
2
5
10
20
50
C
Time shift (s)
30
20
10
0
-10
1
2
5
10
20
50
Frequency (mHz)

Figure 3.3

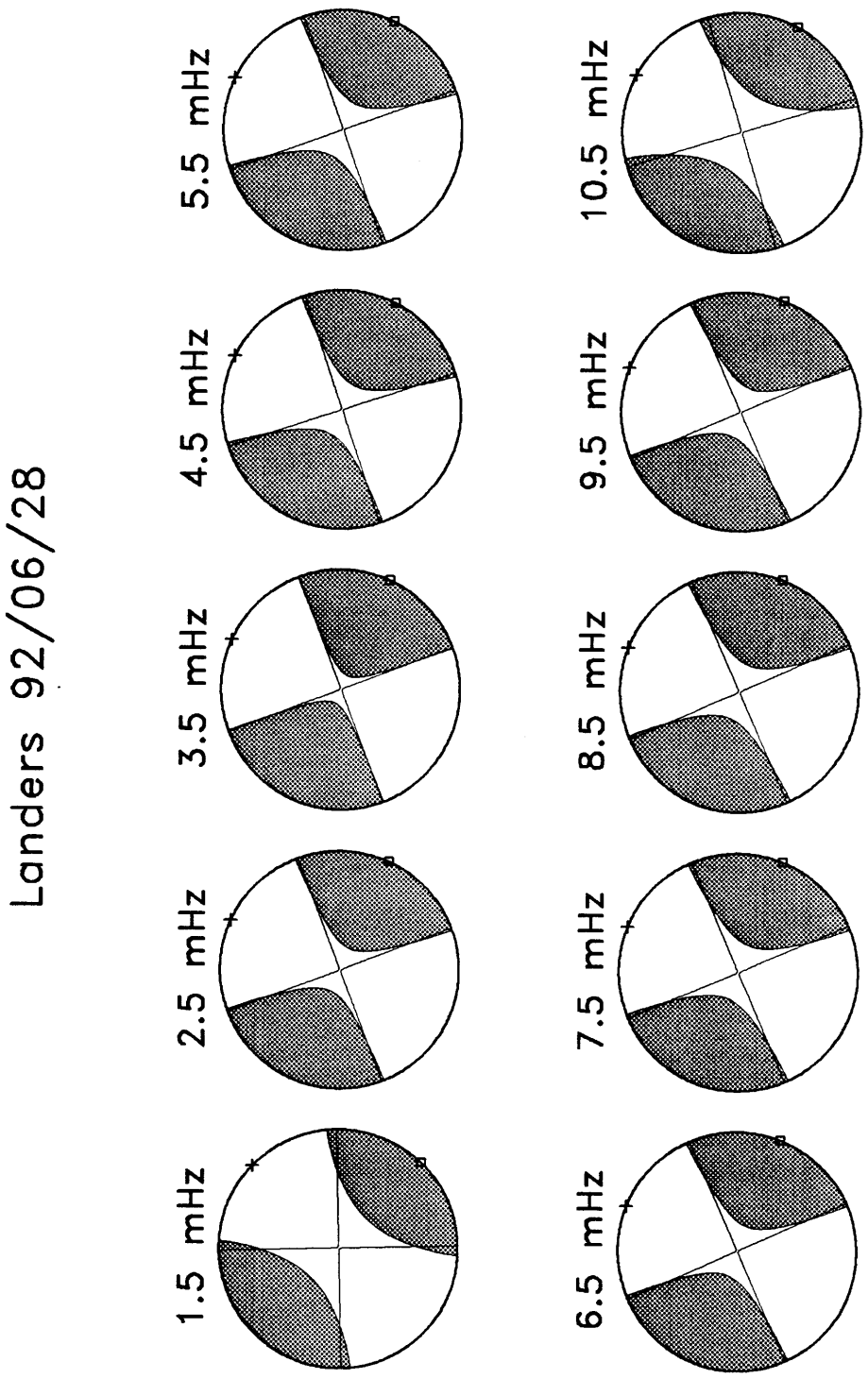
Landers 92/06/28
1.5 mHz
2.5 mHz
3.5 mHz
4.5 mHz
5.5 mHz
6.5 mHz
7.5 mHz
8.5 mHz
9.5 mHz
10.5 mHz

Figure 3.4

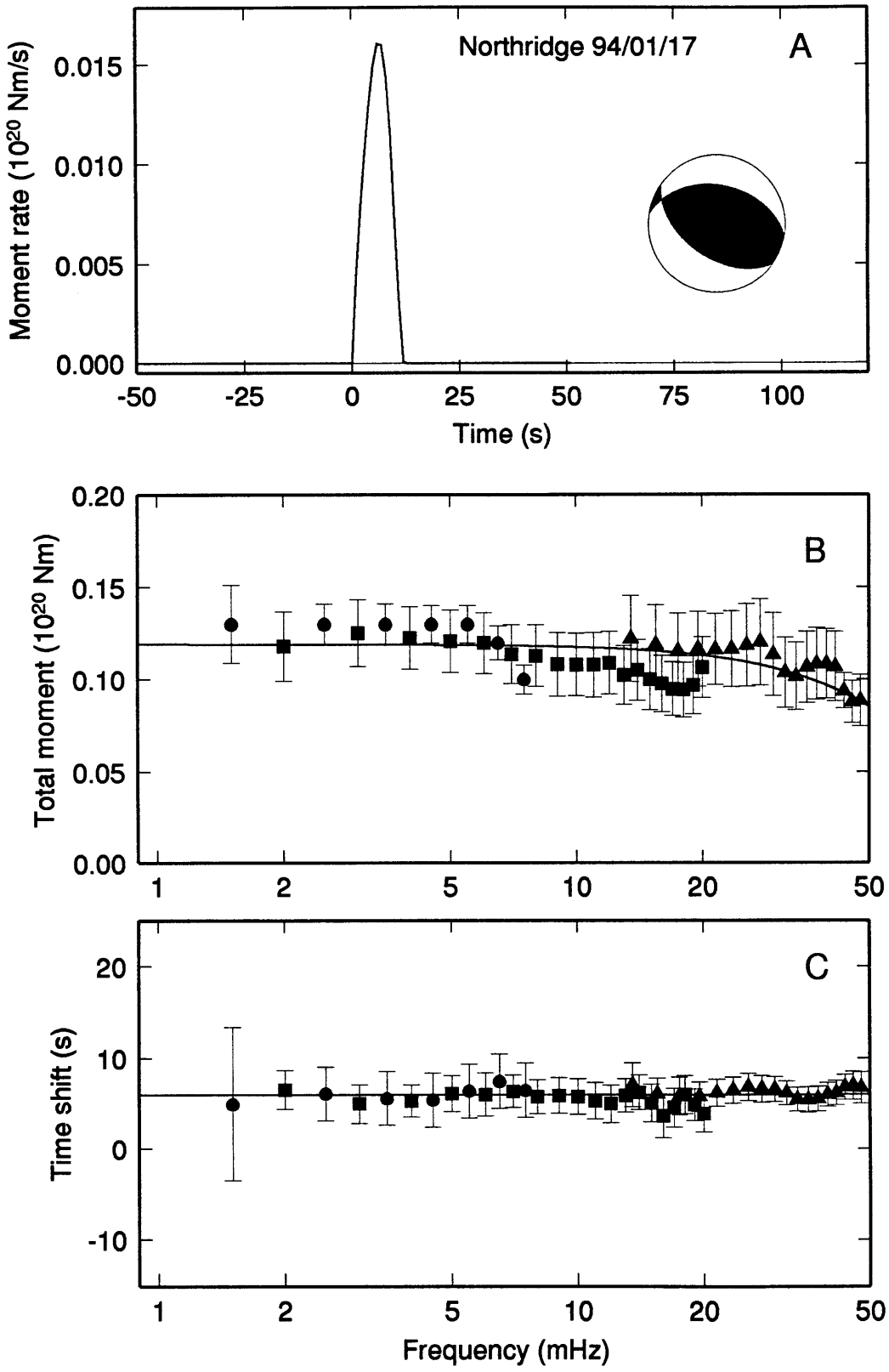
Northridge 94/01/17
A
Moment rate (10^{20} Nm/s)
0.015
0.010
0.005
0.000
-50
-25
0
25
50
75
100
Time (s)
B
Total moment (10^{20} Nm)
0.20
0.15
0.10
0.05
0.00
1
2
5
10
20
50
C
Time shift (s)
20
10
0
-10
1
2
5
10
20
50
Frequency (mHz)

Figure 3.5

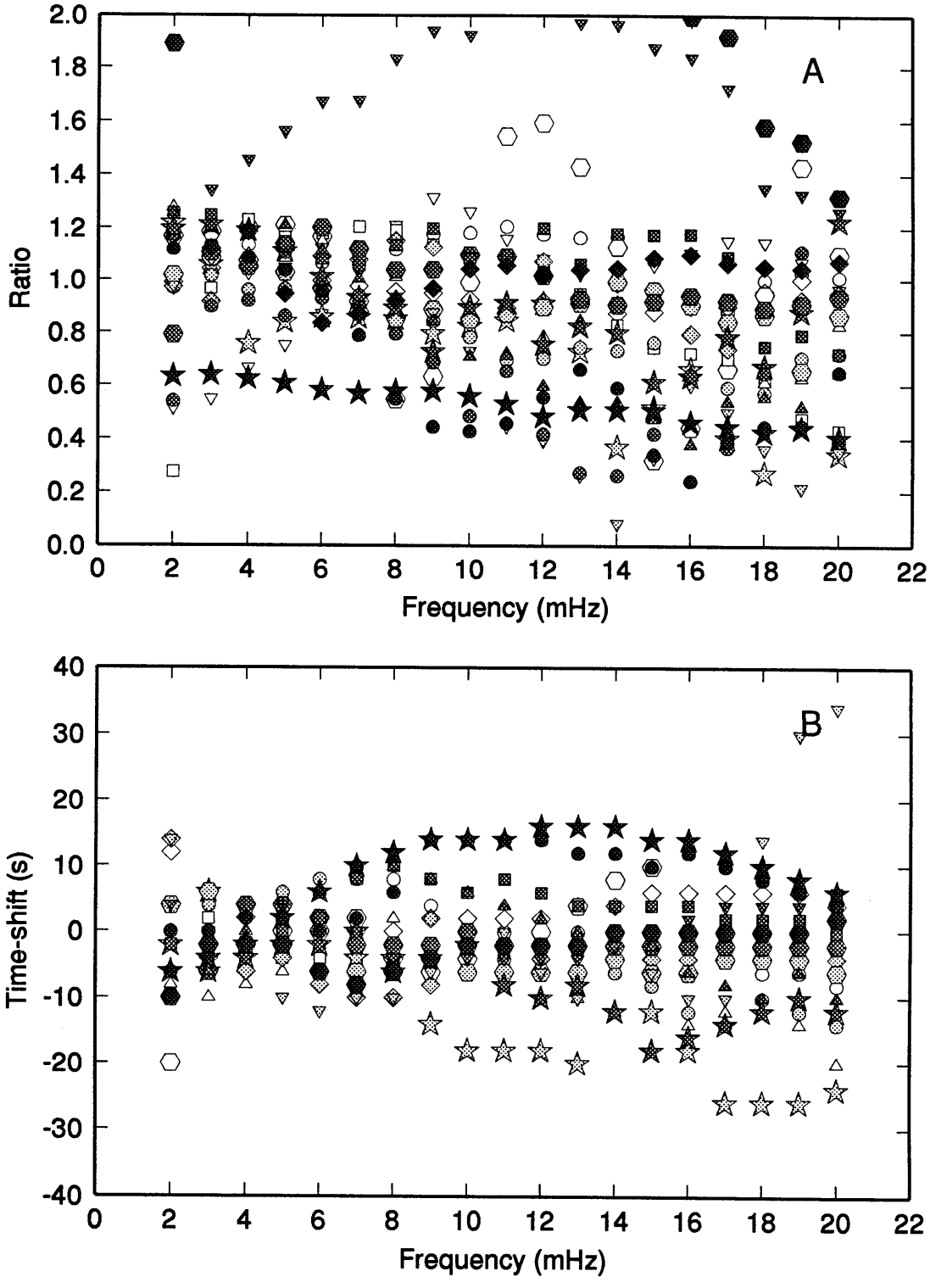
A
Ratio
2.0
1.8
1.6
1.4
1.2
1.0
0.8
0.6
0.4
0.2
0.0
0
2
4
6
8
10
12
14
16
18
20
22
Frequency (mHz)
B
Time-shift (s)
40
30
20
10
0
-10
-20
-30
-40
0
2
4
6
8
10
12
14
16
18
20
22
Frequency (mHz)

Figure 3.6

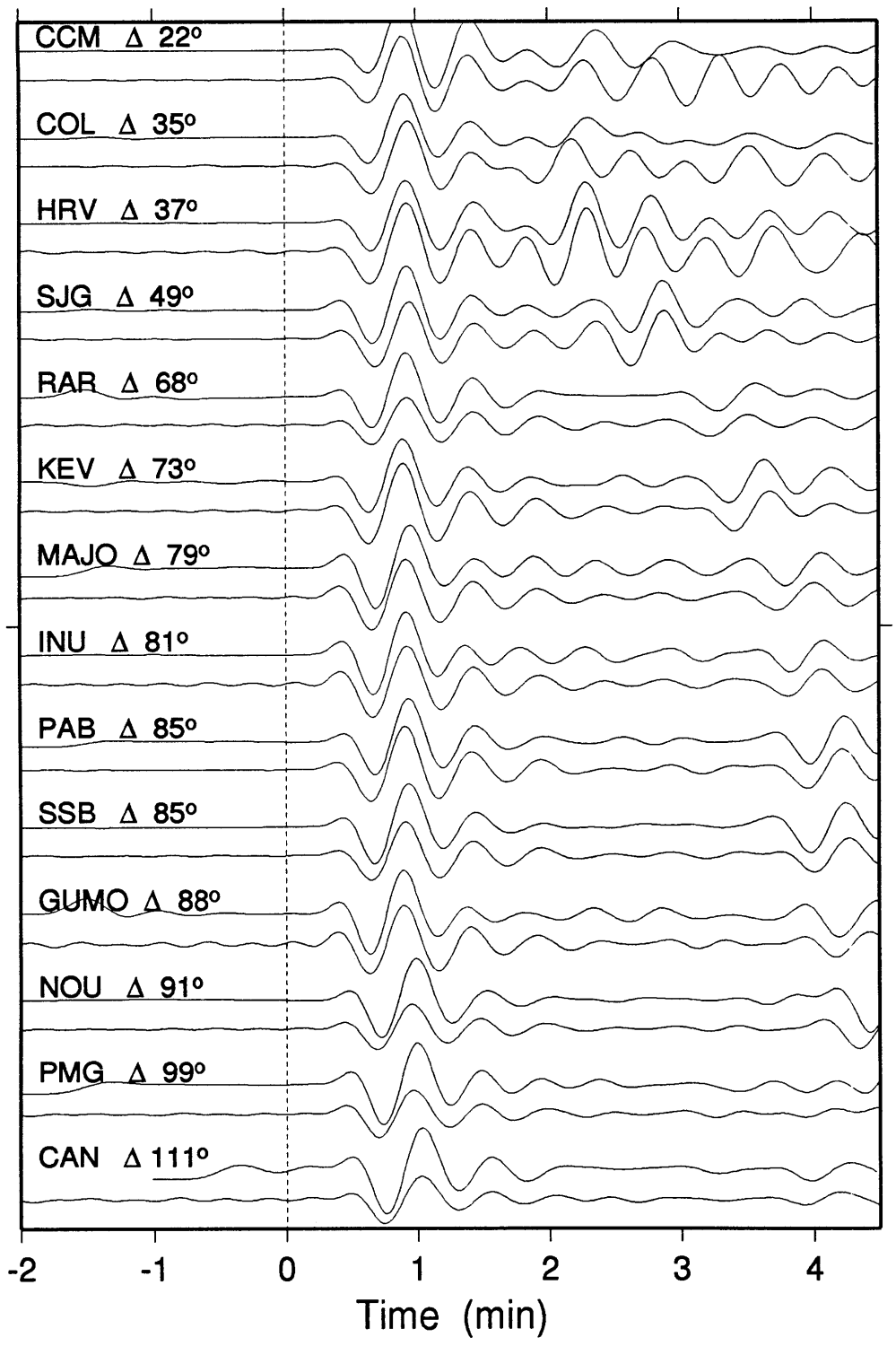
Northridge 94/01/17
CCM Δ 22°
COL Δ 35°
HRV Δ 37°
SJG Δ 49°
RAR Δ 68°
KEV Δ 73°
MAJO Δ 79°
INU Δ 81°
PAB Δ 85°
SSB Δ 85°
GUMO Δ 88°
NOU Δ 91°
PMG Δ 99°
CAN Δ 111°
-2
-1
0
1
2
3
4
Time (min)

Figure 3.7

CHAPTER 4

The 2 September 1992 Nicaragua slow earthquake

4.1 Introduction

The M_W = 7.7 September 2, 1992 Nicaragua earthquake took place at the interface between the subducted Cocos plate and the Caribbean plate. The seismic rupture produced a tsunami that was unusually large compared to the observed M_S = 7.2 (Kanamori and Kikuchi, 1993; Ide et al., 1993; Satake et al., 1993). The slow nature of this event was rapidly diagnosed by the large discrepancy between M_W and M_S. A number of investigators have studied the time history of rupture of the event from the inversion of a set of *P* and *SH* waveforms (Kanamori and Kikuchi, 1993; Ide et al., 1993; Satake et al., 1993). They obtain scalar moments in the range 1.4-2.7 10^{20} Nm that underestimate the actual scalar moment of the earthquake by 40% to 200% [1]. Waveform inversions using body-waves alone are inadequate for studying slow earthquakes, because these methods have no resolution at frequencies lower than about 10 mHz. The source time functions obtained in that way account for only part of the moment released by an earthquake (Figure 4.3). The spectral inversion method introduced in the previous chapter is ideally suited for the study of events with long durations and takes full advantage of the low-frequency information contained in network-averaged spectra of this event.

---

[1] The total moment of the source time function of Kanamori and Kikuchi (1993) is not referenced in their paper (see their figure 1). We ascribe to it the value of 3.7 10^{20} Nm, which is the moment they obtain from long-period surface waves. It is therefore not included in this comparison.

4.2 Data used and inversion results

In order to estimate $M_T(\omega)$ and $\Delta t(\omega)$, we calculate normal-mode synthetic seismograms up to 50 mHz for the transversely anisotropic radial anelastic structure of the PREM earth model (Dziewonski et al, 1981). Aspherical correction to eigenfrequencies and eigenfunctions are computed following the asymptotic formalism of Woodhouse et al., (1984) for the model S12_WM13 (Su et al., 1994). The centroid location used in this computation is taken from the Harvard CMT catalog. Submarine sliding can cause tsunamis and can be modeled as a single force seismic source (Kawakatsu, 1989; Dahlen, 1993). Ide et al., (1993) and Kanamori and Kikuchi (1993) have found no seismological evidence that the tsunami was caused by slumping of sediments, however. The shallow nodal plane of our preferred mechanism has a strike of 303°, a rake of 91° and dip of 15°. It allows for a good overlap of surface and body wave amplitude data (Figure 4.2). In order to avoid azimuthal oversampling towards the north-west, we restricted our analysis to 12 vertical component very long period seismograms (AAK, CAN, COL, ESK, KONO, LZH, NNA, RAR, RER, SSB, TOL, WFM) for the normal-mode and the surface wave analysis and to 12 vertical component long period seismograms (BDF, CCM, COL, COR, HRV, KIP, KONO, PFO, RAR, TOL, SSB, ZOBO) for the body wave analysis.

The origin time of the earthquake is reported by the NEIC at 00:15:57.5 (UT). We relocate the epicenter of the main shock (see below) at 11.75°N, 87.38°W, very near the NEIC epicenter. The origin time of the main shock is 00:16:00.4 (UT), 2.9 s later than that reported by the NEIC. Time is always referenced to t_0, the high-frequency origin time of the relocated epicenter.

Figure 4.2 shows the network-averaged spectra of the 2 Sep 1992, Nicaragua earthquake obtained with the spectral averaging methods described in Chapters 2 and 3. Modal and surface wave spectra are inverted from synthetics computed for the CMT centroid

location, whereas the body-wave spectra are for the 16-44 mHz centroid indicated on Figure 4.6. Essentially similar body-wave spectra are obtained using the CMT centroid. We observe overlap within error bars of the modal and surface wave data, as well as of the surface and body wave data. The large errors attributed to the total-moment estimates from normal-mode data in the range 1-6 mHz are a consequence of the error analysis that incorporates uncertainties in the moment tensor, i.e. for shallow thrusts, a slight change in the dip of the nodal planes leads to large variations in moment. The strong curvature of $M_T(\omega)$ reflects the long duration of the event, whereas that of $\Delta t(\omega)$ is symptomatic of the skewness of the earthquake's moment release, i.e., a rapid acceleration of moment release followed by a long decay. This implies that a source time function symmetric about its centroid, of the type proposed by Kanamori and Kikuchi, (1993), cannot fit the spectral data (Figure 4.3). Our preferred model for the source time function is given in Figure 4.2. It has a moment of M_T^0=4.4 10^{20} Nm, a centroid time-shift Δt_1=44 sec and a characteristic duration of τ_c=54 s and the skewness parameter α = 0.1. Figure 4.4 shows a comparison of the predicted and observed vertical component waveforms in a 6-minute window following the *P*-wave arrival time. Waveform amplitudes and phase are generally good; note the good agreement at stations WMQ and QIZ that were not used in the inversion.

The origin time t_0 reported by the NEIC refers to the onset of a small preshock, clearly visible on broad-band seismograms, that precedes the main rupture by about 8-10 sec. Interestingly our source time function (Figure 4.2) includes this preshock as a small onset of moment release before the main shock. The seismic rupture comprises a series of subevents, with a prominent main shock that starts at t_0+8 s and lasts for about 30 s. It is followed by one subevent, centered around t_0+60 s, which is imbedded in what appears to be a smooth background of moment release that ceases after slightly more than 2 minutes. Our source time function presents similarities with those determined from waveform inversions (Ide et al, 1993; Satake et al., 1993), see Figure 4.3, but has the advantage of

satisfying low-frequency observations. In particular, it allows for correct distribution of that part of the moment release function missing from body wave studies.

4.3 Discussion

The significant discrepancy between the high-frequency epicenter and the low frequency centroid reported for this event suggests that slow motion on the fault is concentrated trenchward of the epicenter, as suggested by Kanamori and Kikuchi (1993). In order to confirm the low-frequency location, we apply the modal phase-equalization technique for centroids located on a 0.2° grid surrounding the CMT location. In order to achieve optimal phase alignments, the synthetics incorporate the source time function of Figure 4.2. A suite of inversions is performed at the grid points and contours of variance reduction are determined (Figure 4.5). Between 1 to 7 mHz, epicentroids in 1 mHz bands scatter by at most 25 km around the weighted average location. At higher frequencies, we observe strong scattering of surface waves, possibly due to near source or path velocity anomalies associated with the subduction zone, leading to unreliable centroid locations. These difficulties are also expressed in the large variance of the surface-wave determined time-shifts (see Figure 4.2). A similar analysis of variance reduction indicates that the centroidal depth cannot exceed 25 km. Although a location bias due to unmodeled aspherical heterogeneity or local source structure cannot be entirely ruled out between 1-7 mHz, it is striking how different methods, using different data sets, all point toward a near trench very low-frequency centroid (Figure 4.6).

We further investigate the frequency dependence of the epicentroid using long-period body-waves. Frequency dependent relocation of the event is possible because our procedure preserves absolute time, and does not require the alignment of the seismograms

on the onset of high-frequency waves, as is the case in classical waveform inversions. From 16 to 44 mHz, *P*-wave station residuals are determined at 2 mHz intervals with respect to the CMT location and the prediction of our preferred source time function. These residuals are considered to pertain to an event in a cluster and a multiple event relocation (Jordan and Sverdrup, 1981) is performed, with depth fixed at 15 km. The relocation technique is based on the premise that path anomalies are correlated among the members of a cluster and leads to unbiased location estimates. Figure 4.6 displays the cluster's hypocentroidal location. It is situated 25 km southward of the NEIC location (PDE).

Using reported station residuals from short period instruments, we also relocate the main shock and the aftershocks that occurred in a three-month period following the main shock, using the Herrin tables (Herrin, 1968), with depth again fixed at 15 km. After relocation, a clear pattern becomes visible: the aftershocks span a 300 km long narrow zone parallel to the trench. The tight clustering is not an effect of the slab's dip since it dives at a small angle under Central America. The scarcity of aftershocks trenchward of the epicenter is consistent with the observation that the seismogenic zone does not reach the surface in subduction zones (Byrne et al., 1988). This shallow aseismic zone can probably be ascribed to the velocity strengthening behavior of unconsolidated and semi-consolidated sediments at near lithostatic pore pressure (e.g., Marone and Scholz, 1988), in which aftershock nucleation is only marginally possible. It appears that the September 2, 1992 Nicaragua earthquake nucleated as a regular event and propagated sideways along the trench. As the upward propagating rupture breached into subducted weak sediments, a very slow earthquake was generated by the decelerating rupture front. Despite small particle and rupture velocities, the slow event released may be as much as 50% of the total moment of the earthquake, and is an outstanding example of rupture termination in a velocity strengthening material.

TABLE 4.1

Low-order polynomial moments of source time functions for the 1992 Nicaragua event obtained by Kanamori and Kikuchi (KK, 1993), Satake et al., (SA, 1993), Ide et al., (ID, 1993) and from this study. M_T^0 is in 10^{20} Nm, Δt_1 and τ_c are both in seconds (see also Figure 4.3).

	M_T^0	Δt_1	τ_c	α
KK	3.7	66	59	0.0
SA	1.5	47	52	0.1
ID	2.7	43	54	0.1
This study	4.4	44	54	0.1

Figure captions

FIGURE 4.1. Location map. Stations employed in the body wave analysis are shown as filled circles; gray-shaded triangles denote stations used for the normal mode and surface wave observations. The major double-couple mechanism is shown in the usual lower hemisphere convention and is located at the epicenter.

FIGURE 4.2. Source time function of the 2 Sep 1992, Nicaragua event. The solid line in *Panel A* shows the source time function obtained from the inversion of the total-moment and phase-delay spectra in *panels B* and *C*. A value of $5x10^3$ for the regularization parameter has been used. The inset is the mechanism used in the spectral recovery methods. In panels A and C, time is referenced relative to the high-frequency origin time of the relocated main shock. Three solid symbols denote the network-averaged spectra from the analysis of free oscillations (circles), surfaces waves (squares), and body waves (triangles). The spectral bandwidth is 1.5 to 48 mHz. The source time function of this event had a very long duration of about 120 s. Note the agreement among the spectra retrieved by different analysis methods.

FIGURE 4.3 Comparison with source time functions obtained by body-wave inversions. Same conventions as Figure 4.2. Solid line: our preferred model. Short dashed line: Ide et al., (1993); Middle dashed line: Satake et al., (1993); Long dashed line: Kanamori and Kikuchi (1993). The prediction of the latter model is outside the bounds of the lower panel, but is essentially a flat time-shift spectrum with intercept at 66 s. Satake et al., (1993) do not report the origin time of their source time function. We assume they did not take into account the 8-10 s preshock of the event, and we shift their source time function 8 s forward in time. Even if some of the source time functions bear similarities to our preferred model, none of them simultaneously fit the amplitude and time-shift spectra of the event.

FIGURE 4.4. Waveform fit of long-period *P* waves. Top traces of each group are data from vertically polarized seismograms; lower traces are synthetics convolved with the source time function of Figure 4.2. Our best centroid location in the band 16-44 mHz has been used to compute the synthetic seismograms (see Figure 4.6 and text). Traces have been low-pass filtered with a 10 pole Butterworth filter with corner at 35 mHz. They are aligned with respect to the predicted *P*-wave arrival time. Positive time shifts of the first arrivals are

primarily due to the group delay of the low-pass filter, as well as to the small preshock (8-10 s) that is visible on broad-band records but does not contribute any appreciable energy in this frequency band. Stations WMQ and QIZ have not been used in the network averaging, but are well predicted by the moment release function of Figure 4.2.

FIGURE 4.5. Very-low frequency relocation of the event. Synthetics have been computed on a 0.2°x0.2° grid and convolved with the source time function of Figure 4.2 in order to achieve optimal phase alignment. Riedesel's (1985) modal inversion technique has been applied at each node. Contours of variance reduction as a function of frequency are shown. The black dot indicates the maximum in each band. The CMT centroid is given for reference (open diamond), as well as the Cocos-Caribbean plate boundary (dashed line). Our optimal centroid (average 3-6 mHz) is indistinguishable from the CMT location, although very different methods are used in each case for similar frequency-bands.

FIGURE 4.6. Map of the epicentral region. Bathymetry is in shades of gray, the trench is in darker shades. The plate boundary is roughly denoted with the solid line and triangles point towards the overriding plate. Aftershocks in a period of three months following the main shock have been jointly relocated in four sections perpendicular to the trench . Only those with 95% confidence ellipses less than 0.3° are shown. The high-frequency epicenter (PDE), the CMT centroid location and Ide et al.'s, (1993) low-frequency location are indicated with black diamonds. We relocated the 1992 Nicaragua event using normal mode techniques in the band 3-7 mHz (white circle). Body-wave phase-delays have been obtained in the band 16-44 mHz relative to the prediction of the source time function in Figure 4.2. They have been used to find the optimal centroid in this band (white ellipse). Very-low frequency centroids (3-7 mHz, CMT, IDE) are significantly trenchward of both the epicenter and the aftershock zone.

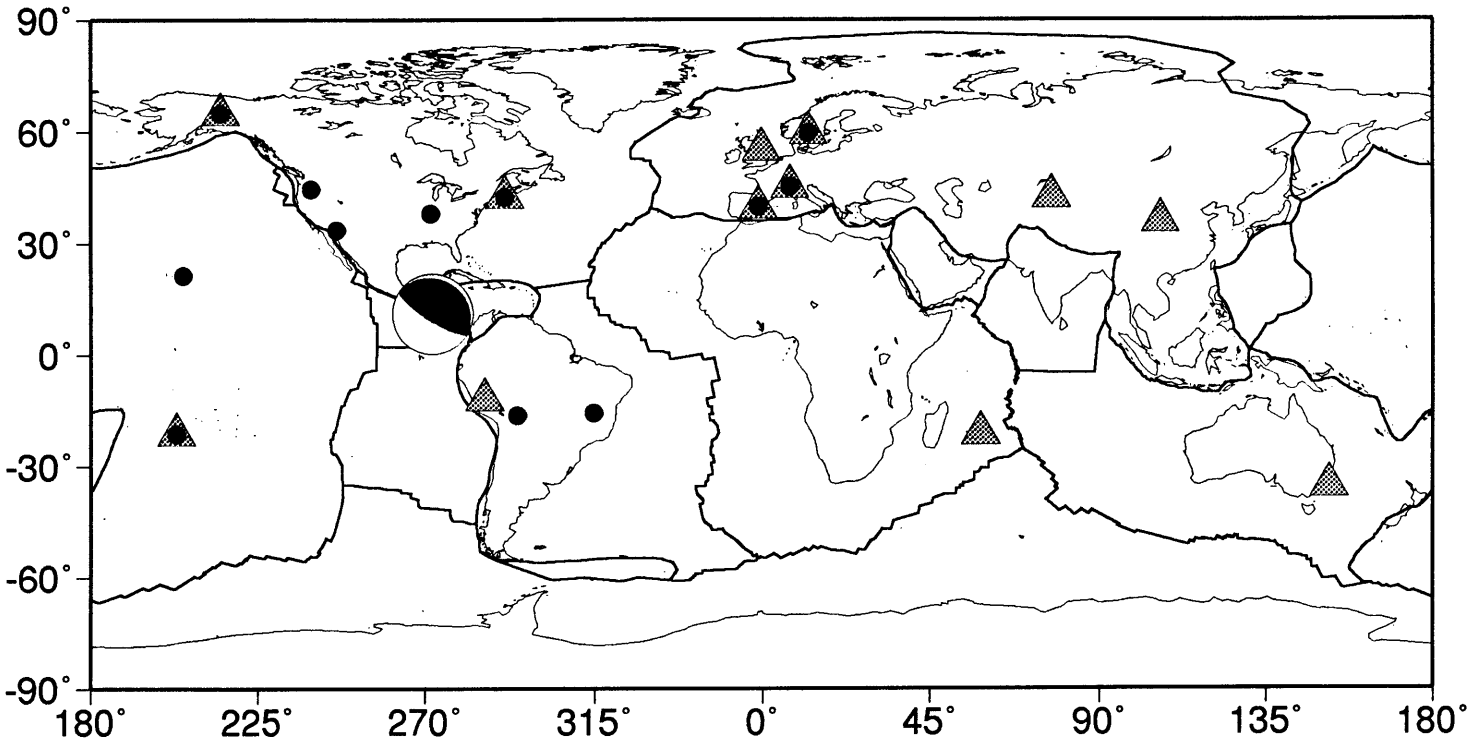

Figure 4.1

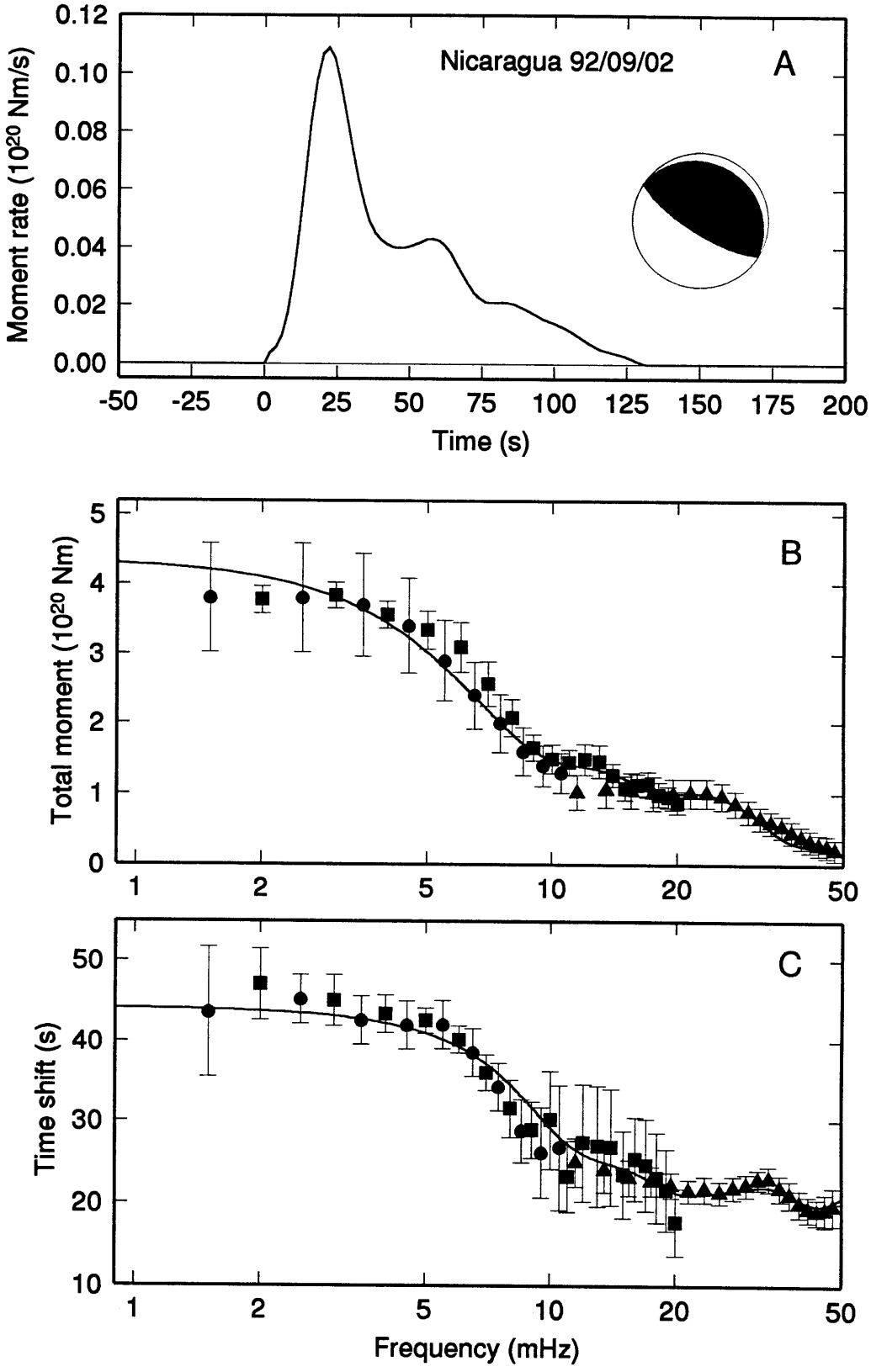
Nicaragua 92/09/02
A
Moment rate (10^{20} Nm/s)
0.12
0.10
0.08
0.06
0.04
0.02
0.00
-50 -25 0 25 50 75 100 125 150 175 200
Time (s)
B
Total moment (10^{20} Nm)
5
4
3
2
1
0
1 2 5 10 20 50
C
Time shift (s)
50
40
30
20
10
1 2 5 10 20 50
Frequency (mHz)

Figure 4.2

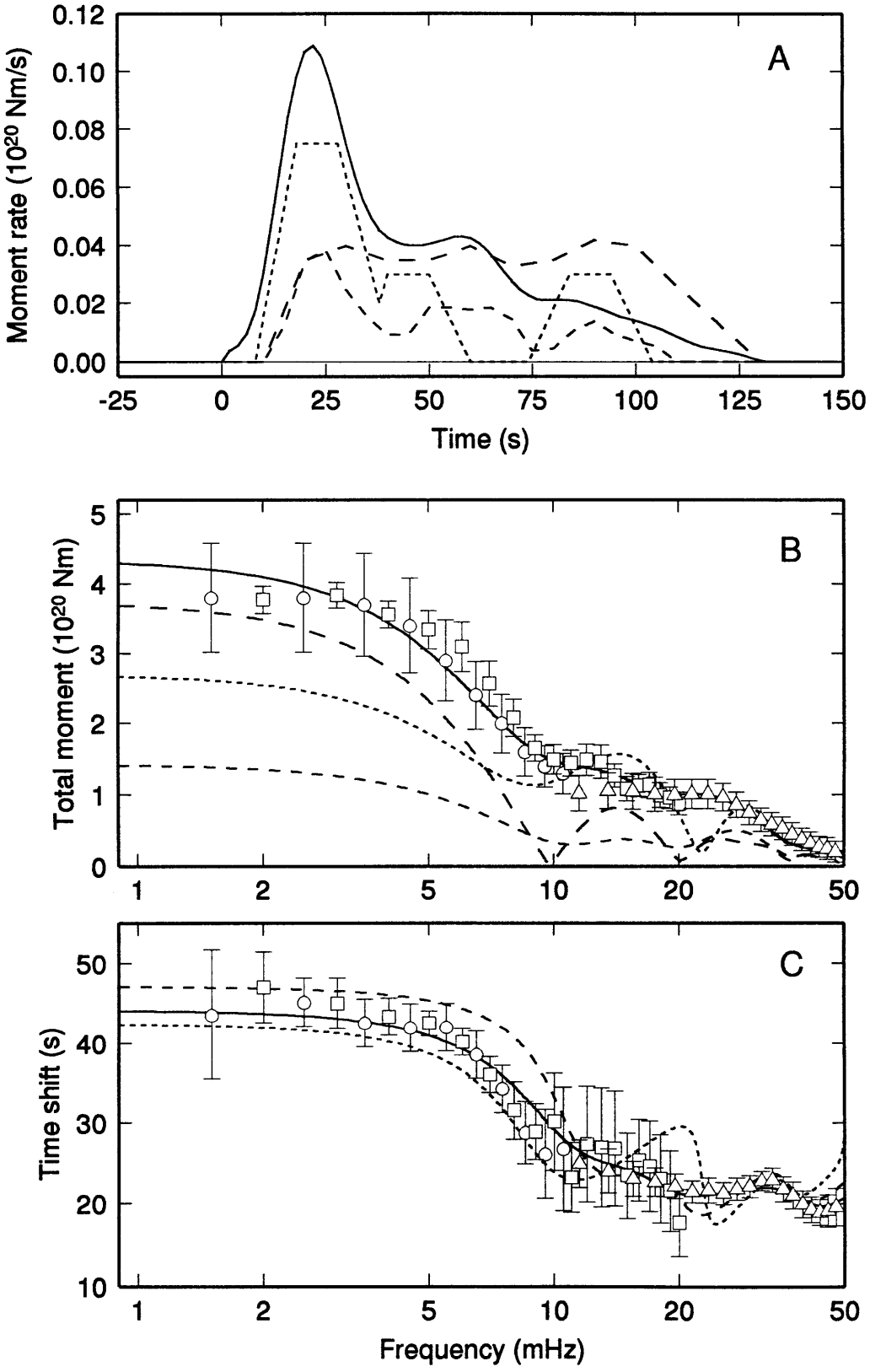
A
Moment rate (10^{20} Nm/s)
0.12
0.10
0.08
0.06
0.04
0.02
0.00
-25
0
25
50
75
100
125
150
Time (s)
B
Total moment (10^{20} Nm)
5
4
3
2
1
0
1
2
5
10
20
50
C
Time shift (s)
50
40
30
20
10
1
2
5
10
20
50
Frequency (mHz)

Figure 4.3

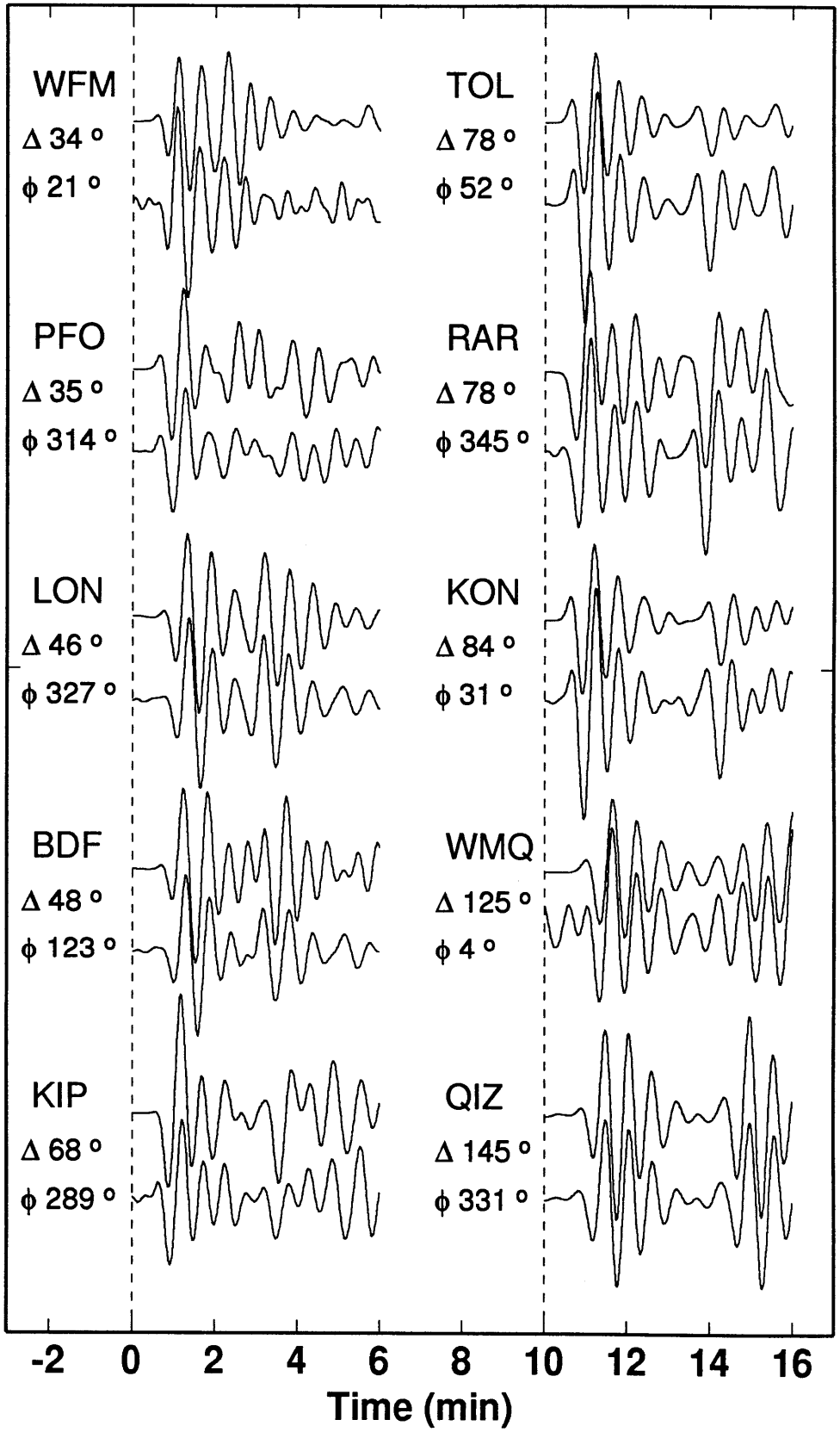
WFM
Δ 34 °
ϕ 21 °
TOL
Δ 78 °
ϕ 52 °
PFO
Δ 35 °
ϕ 314 °
RAR
Δ 78 °
ϕ 345 °
LON
Δ 46 °
ϕ 327 °
KON
Δ 84 °
ϕ 31 °
BDF
Δ 48 °
ϕ 123 °
WMQ
Δ 125 °
ϕ 4 °
KIP
Δ 68 °
ϕ 289 °
QIZ
Δ 145 °
ϕ 331 °
-2
0
2
4
6
8
10
12
14
16
Time (min)

Figure 4.4

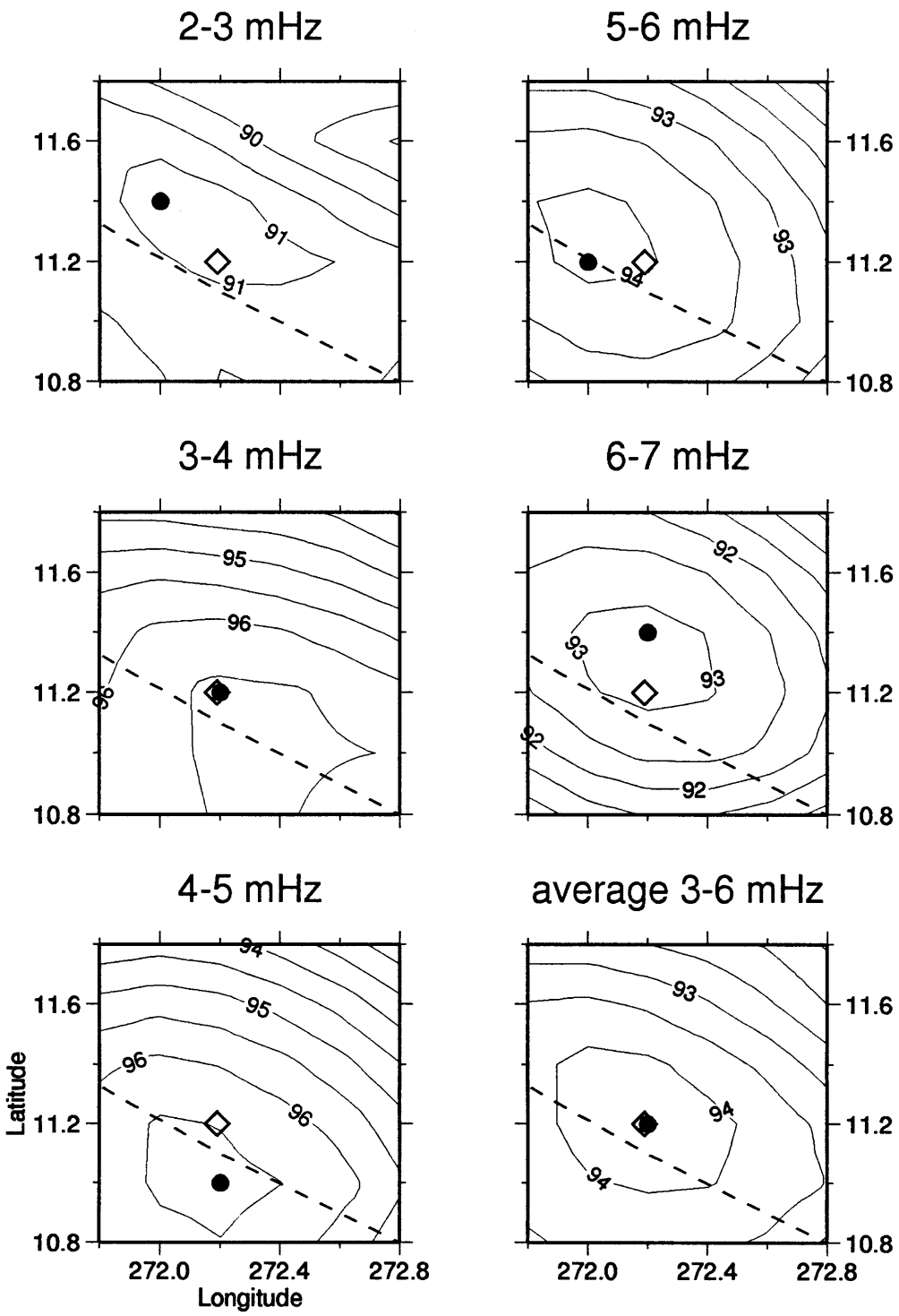
2-3 mHz
5-6 mHz
3-4 mHz
6-7 mHz
4-5 mHz
average 3-6 mHz
11.6
11.2
10.8
272.0
272.4
272.8
Latitude
Longitude

Figure 4.5

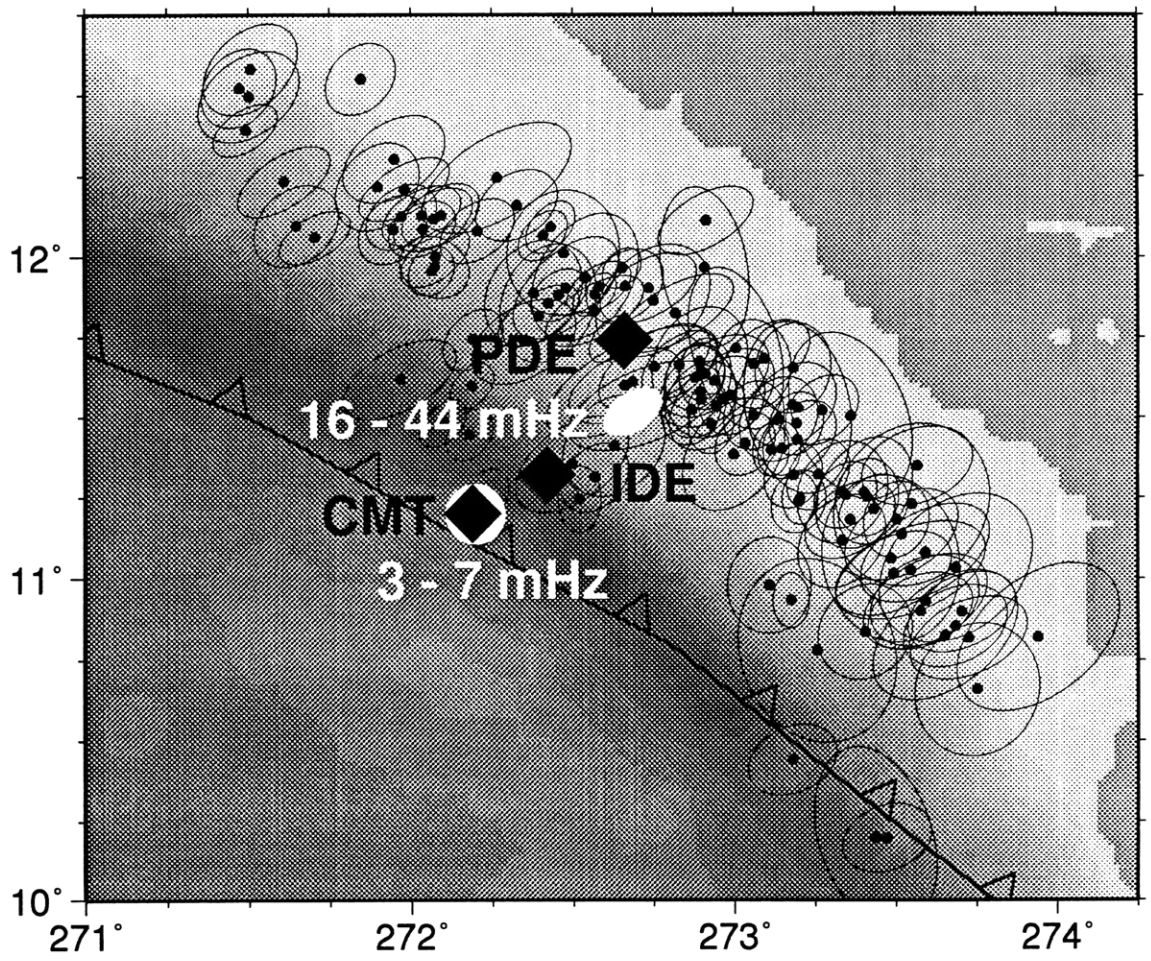
Nicaragua 92/09/02
PDE
16 - 44 mHz
IDE
CMT
3 - 7 mHz
12°
11°
10°
271°
272°
273°
274°

Figure 4.6

CHAPTER 5

Teleseismic Detection of a Slow Precursor to the Great 1989 Macquarie Ridge Earthquake[1]

5.1 Introduction

Slow precursors associated with the nucleation of large earthquakes are interesting to seismologists, because their behavior may provide valuable insights regarding the mechanics of the rupture process; in particular, detecting them on strainmeters close to active faults is one strategy for short-term earthquake prediction (Dieterich, 1978; Rice, 1979; Tullis, 1988). Near-field data with adequate resolution to see such precursors are available in only a few areas, however, so there is considerable motivation to observe them at large (teleseismic) distances. In the far-field, the primary signature of a slow precursor is contained in the low-frequency waves that are preferentially excited by sources with long time constants. Slow precursors have been teleseismically detected in the low-frequency radiation from several major earthquakes, including the great 1960 Chilean earthquake (Kanamori and Cipar, 1974; Cifuentes and Silver, 1989), the 1970 Colombian and 1963 Peru-Bolivia deep-focus earthquakes (Dziewonski and Gilbert, 1974), and the 1983 intermediate-focus event on the Peru-Ecuador border (Jordan, 1991). These events occurred in subduction zones, and all but the Chilean event had foci with depths greater than 100 km. Here we employ data collected from the newly installed, high-performance seismic networks to establish the existence of a large, short-term, slow

---

[1] This Chapter is for its major part based on the paper: P. F. Ihmlé, P. Harabaglia, and T. H. Jordan, Teleseismic detection of a slow precursor to the Great 1989 Macquarie Ridge Earthquake, *Science*, **261**, 177-183, 1993.

precursor to a shallow-focus earthquake in a very different tectonic regime: the great 1989 Macquarie Ridge earthquake of 23 May 1989, which was located on an transform fault in oceanic lithosphere south of New Zealand (Figure 5.1).

The Macquarie Ridge earthquake had a static moment M_T^0 of about 20×10^{20} Newton-meters (Nm) and moment-magnitude M_W of 8.2, making it the largest seismic event since 1979. A detailed description of the earthquake and its tectonic setting is given in Anderson and Zhang (1991) and Das (1993). It was one of the first great earthquakes to be registered by a large network of broadband, high-dynamic-range, triaxial, digital seismographs (Figure 5.1). The main shock can be approximated by a simple double-couple mechanism (Dziewonski et al., 1990) dominated by right-lateral movement on a 200-km segment of the Australian-Pacific plate boundary. Several groups of investigators (Braumiller and Nabelek, 1990; Ekström and Romanowicz, 1990; Anderson and Zhang, 1991; Das, 1993, 1994) have inverted the broadband waveforms to obtain information about the time dependence of the faulting, which can be specified in terms of a source time (or moment-rate) function $\dot{M}_T(t)$[2] (Figure 5.2). The models differ substantially, especially in terms of the low-order polynomial moments of $\dot{M}_T(t)$ that describe the source behavior at low frequencies (see Chapter 2 for a description of notation and convention). Braunmiller and Nabelek (1990) reported the smallest total static moment M_T^0 and the most compact time function, as measured by the centroid time shift Δt_1 and characteristic duration τ_c. They inverted only the body waves, whereas Ekström and Romanowicz (1990) and Anderson and Zhang (1991) constrained their solutions to satisfy the moment determined from low-frequency (3-6 millihertz (mHz)) surface waves. The moment discrepancy led Anderson and Zhang to conclude that the main rupture was accompanied by an episode of slow moment release, perhaps in the

---

[2] The source time function is usually denoted by $f(t)$ in this thesis.

mantle below the seismogenic zone. Interestingly, the value of M_T^0 derived from Harvard centroid moment tensor (CMT), which also used surface-wave data, agrees best with the Braunmiller-Nabelek source time function.

Additional discrepancies are revealed by a comparison of the published source time functions with the low-frequency spectra recovered by the methods outlined below (Figure 5.2). We express the Fourier spectrum of the moment-rate function as $\int_{-\infty}^{\infty} \dot{M}_T(t) e^{-i\omega(t-t_0)} dt = M_T(\omega) e^{-i\omega\Delta t(\omega)}$, where ω is the angular frequency, $M_T(\omega) \geq 0$ is the amplitude spectrum, and $\Delta t(\omega)$ is the phase-delay spectrum, defined relative to the high-frequency origin time t_0[3] . The Anderson-Zhang model provides a rough fit to our estimates of $M_T(\omega)$, but none of the three models even qualitatively matches the observed shape of $\Delta t(\omega)$. In particular, the phase delays from all three models decrease monotonically, corresponding to a positive skewness in $\dot{M}_T(t)$, whereas the actual data show a distinct phase-delay increase from 1 to 6 mHz.

This increase is diagnostic of an episode of slow, smooth moment release that began before, and initiated, the main rupture of the Macquarie Ridge earthquake. A compound source, comprising a main rupture with a static moment of 16×10^{20} Nm superposed on an episode of slow deformation with a static moment of 6×10^{20} Nm, satisfies the low-frequency spectra (Figure 5.3). According to this simple model, over half of the slow deformation occurred in a 130-second interval before the beginning of the main rupture. Hence, if the model's main features are valid, the slow precursor to the Macquarie Ridge earthquake was itself an event of $M_W \approx 7.6$.

---

[3] We adopt the National Earthquake Information Center value of t_0 = 10:54:46.3 s. Both the amplitude and phase-delay spectra are even functions of frequency (Jordan, 1991)

5.2 Low-frequency observations

We obtained the spectral data in Figure 5.3 by two methodologies having different sensitivities to unmodeled propagation effects. The first was an analysis of normal modes based on spectral integrals computed from 6-hr time series, which include up to fourth-orbit Rayleigh waves (R_4) and fifth-orbit Love waves (G_5). The total-moment spectrum $M_T(\omega)$ was recovered from a variant of the method described by Silver and Jordan (1982, 1983), and the phase-delay spectrum $\Delta t(\omega)$ was derived using an algorithm formulated by Riedesel et al. (1986) and Jordan (1991). Because the latter integrates over individual modes, it was not applied at frequencies above 11 mHz, where the spectrum becomes densely populated and the fundamental-mode resonance peaks begin to overlap considerably.

The second technique was a traveling-wave method based on broad-band cross-correlograms of fundamental-mode mantle waves (Gee and Jordan, 1992). To minimize the effects of aspherical heterogeneities, we processed only the first-orbit groups, R_1 on vertical components and G_1 on transverse components. Spectra similar to Figure 5.2 were obtained from the second-orbit mantle waves, however, an observation that precludes strong directivity effects (Figure 5.8).

Both the normal-mode and traveling-wave techniques rely on synthetic seismograms to model the source geometry and propagation effects. All synthetics were calculated by normal-mode summation using the spherically symmetric, nonrotating, anisotropic, anelastic structure of PREM (Dziewonski and Anderson, 1981) and the aspherical, elastic structure of SH8/WM13. The latter is a tomographic model derived by Woodward et al. (1993) from the inversion of waveform and travel-time data out to spherical-harmonic degree and order eight. Aspherical corrections to the eigenfrequencies and eigenfunctions were based on the asymptotic theory of Woodhouse and Dziewonski (1984).

We culled and edited the available long-period seismograms from the IDA, GEOSCOPE, CDSN, and IRIS stations and rotated the horizontals, if available, to obtain the transversely polarized components, obtaining 18 vertical and 18 transverse components from 27 stations with good global distribution (Figure 5.1). These were inverted for the moment-tensor spectrum and centroid depth. The maximum reduction of variance was obtained for a centroid depth of 23 km, eight kilometers deeper than the CMT value; shallower centroids yielded a poorer fit in the lower frequency bands (1-3 mHz), while deeper centroids degraded the fit at high frequencies (> 7 mHz). We also varied the geographical location of the centroid, but found the spectra to be insensitive to these parameters. The spectrum of mechanism tensors, $\hat{\mathbf{M}}(\omega)$, is displayed in Figure 5.4. The higher-frequency values are consistent with the Harvard CMT, but below 6 mHz, the mechanism shows a rotation of up to ~35° about the principal compressional (P) axis. This rotation may indicate that the slow component had a different mechanism than the main rupture. However, the rotation is almost entirely a result of variations in the $M_{r\theta}$ and $M_{r\varphi}$ components, which tend to be poorly constrained at low frequencies for shallow-focus events (Dziewonski et al., 1981; Kanamori and Given, 1981; Dziewonski and Woodhouse, 1983). Because of this uncertainty, the spectral estimation in Figure 5.3 was done with synthetic seismograms calculated for a point source with the frequency-independent CMT mechanism. Inversions with the frequency-dependent mechanisms of Figure 5.4 gave essentially identical results.

5.3 Assessment of propagation bias

There are several independent checks on the efficacy of the spectra-recovery procedures in eliminating propagation effects. First, the spectra derived by the standing-wave and traveling-wave algorithms are in excellent agreement, despite the differing

sensitivities of the two methodologies to various types of scattered signals. The modal techniques rely on temporal and spectral averaging to reduce scattering effects, whereas the traveling-wave method captures information about the source from the first-orbit surface waves, which have not had much time to interact with aspherical heterogeneities.

We performed separate inversions of the vertically and transversely polarized data sets, obtaining the four spectra in Figure 5.7. The toroidal-mode (T) and Love-wave (L) spectra derived from the transverse components are systematically lower than the vertical-component spheroidal-mode (S) and Rayleigh-wave (R) spectra at frequencies above 10 mHz, perhaps because the spherically symmetric PREM attenuation model inadequately represents the anelastic structure of the upper mantle along the paths sampled in this experiment[4]. The standing-wave ($S + T$) and traveling-wave ($R + L$) averages at these frequencies are in good agreement with the source models derived from broadband waveform analysis, however (Figure 5.2). All four spectra show a decrease in the phase delay below 6 mHz, which is the primary signature of the slow precursor, although this feature is more strongly expressed in the vertical-component estimates. This difference would be expected if the slow precursor had a mechanism with more of a dip-slip component than the main rupture, a hypothesis consistent with the frequency-dependence in Figure 5.4. In any case, the general agreement shown among the four types of spectra makes it unlikely that unmodeled propagation effects can explain the basic features of the spectra in Figure 5.3.

As a further check, we generated synthetic seismograms for the data set using a non-asymptotic code that incorporates along-branch aspherical coupling among the fundamental modes and Coriolis coupling between fundamental spheroidal and toroidal

---

[4] In an analysis of a global distribution of earthquakes, we found that the PREM attenuation structure is superior to the recently published model of R. Widmer, et al., (1991) which predicts quality factors for the 10-mHz fundamental spheroidal modes that are higher by about 10%.

modes [5]. Experiments with these synthetics demonstrate that these types of mode coupling have a negligible effect on the spectra recovered by the normal-mode analysis. Evidently, the spectral averaging employed in the modal techniques, combined with the criteria used to select the data, are effective in eliminating any coupling bias.

Because the 12 to 16-km-thick oceanic crust in the focal zone (Anderson and Zhang, 1991) is different from the PREM structure, we investigated the excitation anomalies due to near-source structure by computing synthetic seismograms based on an adiabatic mode approximation. Again, the effects were found to be inconsequential.

The teleseismic techniques have also been validated by applying them to a variety of earthquakes studied by other methods. For example, the spectra recovered for the 1992 Landers earthquake (M_W = 7.3), the 1989 Loma Prieta earthquake (M_W = 6.9), and other large strike-slip California events are consistent with the source mechanisms and moment-rate functions determined from near-field data, which preclude these events from having slow precursors observable at teleseismic distances (Johnston et al., 1990; Takemoto, 1991). Moreover, the amplitude and phase-delay spectra derived by these same techniques for high-stress-drop, deep-focus events are observed to be flat, as expected for sources with compact time functions, and to have static moments and centroid time shifts in good agreement with the Harvard CMT values.

5.4 Evidence for a slow precursor

The source time function in Figure 5.3 is not unique in providing a good fit to the low-frequency spectra, but theoretical arguments and numerical experiments confirm that

---

[5] The code for computing the coupled-mode synthetics was written by J. Park and modified by P. Puster, based on the first-order subspace projection approximation of Park (1987) and Dahlen (1987).

all models which fit these data do have a slow precursor. Assuming the source time function is nonnegative (no-backslip) and the mechanism is constant, Jordan (1991) derived a set of inequalities among low-order polynomial moments of $\dot{M}_T(t)$ and used them to detect a slow precursor for the 26 April 1983 Peru-Ecuador intermediate-focus earthquake. We can apply one of Jordan's inequalities to show that the upward curvature of the phase-delay spectrum at very low frequencies requires a slow precursor — that is, the start time t_* must have been less than the high-frequency origin time t_0 — without appealing to a specific source time function. Jordan's inequality (1a) states that any nonnegative function $\dot{M}_T(t)$ constrained to be zero before t = 0 satisfies $\alpha \equiv \hat{\mu}_3 / 2\mu_1 \geq -1/8$, where μ_1 is the first moment and $\hat{\mu}_3$ is the third central moment of $\dot{M}_T(t)$. This inequality places an upper bound on the magnitude of the upward curvature of the phase-delay spectrum at zero frequency: $[d^2\Delta t(\omega)/d\omega^2]_{\omega=0} \leq \Delta t_1^3/12$. A curvature exceeding this bound is indicative of a moment-release starting time t_* that is less than the high-frequency origin time t_0, which is Jordan's definition of a slow precursor. Because $\Delta t(\omega)$ is an even function of frequency, its slope at the frequency origin is zero, and its behavior for small frequencies can be approximated by the theoretical phase-delay spectrum (4), $\Delta t(\omega) = (1-\alpha)\Delta t_1 + (\alpha/\omega)\arctan\omega\Delta t_1$. To test the null hypothesis that $t_* = t_0$ (no precursor), we computed the misfit of this spectrum to the data in the frequency interval 1 to 6 mHz as a function of Δt_1 and α. Using Jordan's inequality, the null hypothesis could be rejected in favor of the alternative (the Macquarie Ridge earthquake had a slow precursor) at the 95% confidence level (Figure 5.5).

The requirement of a slow precursor has also been tested by the direct inversion of the spectral data under the no-backslip, constant-mechanism assumption. The phase and amplitude data were combined to form estimates of the complex Fourier spectrum, which yields a set of linear constraints on $\dot{M}_T(t)$. We discretized $\dot{M}_T(t)$ at a 1-s sampling rate and inverted the spectral estimates using a quadratic programming

algorithm (Parker and Stark, computer code; Lawson and Hanson, 1974). Smoothness constraints were imposed on $\dot{M}_T(t)$ before t_0, and the start times t_* were varied from t_0 to $t_0 - 400$s. For all values of t_* within 100 s of t_0, solutions could not be found that provided acceptable fits to the data, even when the smoothness constraints were relaxed, which is consistent with the hypothesis test based on Jordan's inequality. Figure 5.6 gives some representative examples. Inversions with $t_* = t_0$–130 s and heavy smoothing for $t < t_0$ yielded solutions similar to the analytical model in Figure 5.3.

5.5 Constraints from *P* waves

The broadband seismograms were examined for a precursor arriving in front of the *P* waves from the main shock, but no signal was observed, even at relatively close, high-gain stations like Nouméa, New Caledonia (NOU) and Charters Towers, Australia (CTAO), where the *P*-wave amplitudes are 800 and 300 times greater than the noise level, respectively (Figure 5.9). The absence of such signals places a strong observational constraint on smoothness of the source time function before t_0. Synthetic seismograms computed for the source model in Figure 5.3, for example, display a *P*-wave precursor large enough to be easily detected on the time series.

The *P* waves also constrain the source spectrum at higher frequencies. We analyzed *P* wavegroups from 21 stations (Figure 5.10) using the cross-correlation method to obtain amplitude and phase-delay spectra at 2-mHz intervals over a band from 17 to 45 mHz. The phase-delay measurements of the *P* waves are consistent with the surface-wave data to within the standard errors of the two techniques (Figure 5.10). The *P*-wave amplitudes are somewhat higher, in better agreement with the free-oscillation estimates (Figure 5.10).

We inverted the complete data set subject to the requirement that the signal amplitude before the high-frequency P-wave arrival time is smaller than the noise levels at NOU and CTAO, which are the stations in our data set with the highest sensitivity to signals from the Macquarie Ridge area. Taking $t_* = t_0$–400 s, we obtain the $\dot{M}_T(t)$ plotted in Figure 5.10. The integrated moment of the precursor is 4.7×10^{20} Nm, larger than the one in Figure 5.3; it extends to earlier times and is much smoother. The net effect is to double the perturbation to the phase-delay spectrum at low frequencies (Δt_1 decreases from 20 s to 8 s) and increase τ_c from 64 s to 116 s. This inversion does not match the phase delays at frequencies less than 5 mHz as well as the previous model, although the overall fit to the spectral data is quite satisfactory. Moreover, because the time function is very smooth for $t < t_0$, it generates a P-wave precursory signal that is below the detection threshold at CTAO (Figure 5.9), as well as the other stations for which we have seismograms.

The main earthquake is characterized by a large, 20-s episode of moment release beginning 10 s after the high-frequency origin time, followed by a sequence of several smaller subevents ending abruptly at +75 s. The structure for $t > +30$ s is similar to Ekström and Romanowicz's (1990) source time function, although the ability of our data (and theirs) to resolve such details is questionable. As can be seen from Figure 5.10, however, the spectral data require that a larger peak amplitude and a significant delay of the main episode relative to their model. (Examination of the short-period seismograms suggests that the 10-s gap between t_0 and the main episode is due to high-frequency radiation from small subevents.) Our model provides a better fit to both the amplitudes and arrival times of the long-period P waves (Figure 5.11). Comparisons of transversely polarized S waves (Figure 5.12) which were not used in the spectral estimation, yield similar results.

In summary, the source time function in Figure 5.10 satisfies the spectral data from 1-45 mHz and is consistent with the time-domain records of the principal body

waves, including the lack of any *P*-wave precursor on seismograms from regional high-gain stations. Despite the disappointing absence of any direct observation of a precursor on the time series, we have been unable to erect a viable alternative explanation for the low-frequency data.

5.6 Interpretation

The Macquarie Ridge earthquake occurred on an oceanic transform fault. Slow earthquakes—events with anomalously large characteristic durations relative to their static moment—are common on such strike-slip faults (Kanamori and Stewart, 1976; Okal and Stewart, 1982; Beroza and Jordan, 1990). Our analysis of low-frequency spectra indicates that some slow earthquakes may be initiated by slow precursors (see Chapter 2). In continental regions like California and Japan, on the other hand, slow earthquakes are infrequent (a few small, slow events have been detected by strainmeters in Japan, (Sacks et al., 1978), and California (Kanamori, 1989, 1992)), and any preseismic nucleation events are constrained by sensitive near-field and regional sensors to be very small (Johnston et al., 1990; Takemoto, 1991). We suspect, therefore, that the existence of slow precursors reflects a stratification in the mechanical properties of the oceanic lithosphere.

The teleseismic data can be satisfied by modeling the Macquarie Ridge earthquake as a compound source comprising two distinct types of faulting. The initial episode was an infraseismic source or "quiet earthquake" [6], radiating significant energy

---

6 The term infraseismic was used by Sacks et al. (1978) in their seminal paper on slow and silent earthquakes detected by strainmeters. Infraseismic sources were postulated by Beroza and Jordan (1990) to explain anomalous episodes of low-frequency normal-mode excitation detected by the IDA network during periods when no ordinary earthquakes were observed. We have adopted the term "quiet earthquake" to

only at the very low end of the seismic spectrum ($\lesssim$ 6 mHz). In the inversion model of Figure 5.10, this precursor has a moment-release time function that grows smoothly—approximately exponentially with a time constant of ~100 s—and integrates to a total moment of about 5×10^{20} Nm. The lack of a detectable signal before the main *P*-wave arrivals constrains the high-frequency roll off of its spectrum to decay as ω^{-n} where $n >$ 3. We infer that during this transient deformation the rupture velocity v_r and particle velocity $\Delta\dot{u}$ were anomalously low, although the stress drop $\Delta\sigma$ was not; these conditions imply that the rise time for the motion was long [7].

Although the location of the slow precursor relative to the Macquarie Ridge main shock is not directly constrained by our data, the variance reduction at frequencies below 3 mHz increases for centroid depths greater than our reference value of 23 km, consistent with other long-period studies (Ekström and Romanowicz, 1990; Anderson and Zhang, 1991), whereas the variance reduction at higher frequencies decreases. This observation supports the notion that the quiet earthquake was generated in a region of the oceanic upper mantle below the main episode of faulting.

One plausible explanation for the low values of v_r and $\Delta\dot{u}$ inferred for the quiet earthquake is that the material in this layer undergoes a rapid transition from velocity weakening to velocity strengthening when slip velocities exceed a relatively low

---

describe an infraseismic event that excites free oscillations, but does not produce detectable wave groups on seismograms at teleseismic distances (Jordan, 1991).

[7] The characteristic velocity of the source process is $v_c = L_c / \tau_c$, where L_c is a characteristic dimension. For the main event, $\tau_c \approx$ 33 s. If L_c for the precursor is the same or smaller than for the main event, then $\tau_c >$100 s for the former implies that v_c was at least three times less (the precursor was slow). Since the static moment of the slow component was a significant fraction of the entire event, the average fault displacement Δu and stress drop $\Delta\sigma$ of the precursor were comparable to those of the main event. The conclusion that v_r and $\Delta\dot{u}$ are anomalously small follows from the scaling relations, $v_c \sim (v_r^2 \Delta\dot{u})^{1/3}$ and $\Delta\sigma \approx \mu \Delta\dot{u} / v_r$, valid for an ω^{-3} model (F. A. Dahlen, 1974; K. Aki and P. G. Richards, 1980, vol. 2, chap. 14). A small value of $\Delta\dot{u}$ implies that the rise time of the slow precursor must be anomalously long.

threshold value. This behavior is qualitatively consistent with some laboratory experiments on halite (Shimamoto and Logan, 1986) and granite (Blanpied et al., 1987), at least at low normal stress (Kilgore et al., 1993), although the available data indicate that serpentinized peridotites, which are presumably major constituents of the uppermost mantle in this region, behave in the opposite sense; that is, they are velocity strengthening at low velocities and velocity weakening at higher velocities (Reinen et al., 1991, 1992). Slow events would not be expected to nucleate in such a material. The temperature, pressure and compositional dependence of the transitions from velocity weakening to velocity strengthening are not well understood, however, and more laboratory data are needed.

The moment-tensor inversions displayed in Figure 5.4 suggest that the mechanism of the slow precursor may have had a significant dip-slip component. Accounting for such a component increases the estimated size of the precursor. Such a mechanism could help to explain the anomalous excitation of radial free oscillations observed by Park (1990) and other low-frequency modes observed by Kedar et al. (in review)[8].

---

[8] The results obtained in the present chapter do not incorporate the phase-delay maps of Ekström and Tromp (unpublished material, 1994), that were shown in Chapter 3 (Figure 3.1) to effectively correct PREM's bias for Rayleigh wave in the band 8-20 mHz. However, Figure 5.8 shows that the conclusions reached in this chapter will not be altered by the use of synthetic seismograms that incorporate these new phase-delay maps.

TABLE 5.1

Low-order polynomial moments of source time functions for the 1989 Macquarie event obtained by Braumiller and Nabelek (BN, 1990), Ekström and Romanowicz (ER, 1990), Anderson and Zhang (AZ, 1990) and from this study. M_T^0 is in 10^{20} Nm, Δt_1 and τ_c are both in seconds.

	M_T^0	Δt_1	τ_c	α
BN	13	18	23	0.1
ER	18	29	36	0.1
AZ	21	28	44	0.2
This study	23	8	116	0.0

Figure Captions

FIGURE 5.1. Map showing location of the 1989 Macquarie Ridge earthquake (white cross) and seismic stations, which include elements of the CDSN, GEOSCOPE, GDSN, IDA, AND IRIS networks. Large shaded symbols are stations used in the low-frequency analysis: vertical only (triangles), transverse only (squares), both (circles). Small black dots are stations used in the high-frequency P wave analysis.

FIGURE 5.2. *Panel A*: Three source time functions $\dot{M}_T(t)$ for the Macquarie Ridge earthquake obtained from broadband waveform inversions by Braunmiller and Nabelek (1990) (short dashed line), Ekström and Romanowicz (1990) (solid line), and Anderson and Zhang (1991) (long dashed line). Table 5.1 gives M_T^0 , Δt_1 and τ_c for the three source time functions. *Panel B and C*: Amplitude and phase-delay spectra for this earthquake, defined according to the conventions of Jordan (1991). The phase-delay spectrum is referenced to the NEIC origin time (t_0 = 10:54:46.3 s). Harvard CMT values of M_T^0 and Δt_1 (Dziewonski et al., 1990) are indicated as zero-frequency intercepts. The three lines are the spectra computed by Fourier transforming the source time functions in *panel A*. Points with standard deviations are the low-frequency data obtained in this study. Results from two separate methods are shown: standing-wave analysis using 6-hr records (solid circles), and traveling-wave analysis using only the R_1 and G_1 wave groups (open circles). Because of mode overlap, phase-delays were not measured by the normal-mode method above 11 mHz. The two methods have different sensitivities to unmodeled propagation effects; therefore, the good agreement indicates that the propagation bias is likely to be small.

FIGURE 5.3. *Panel A*: A simple, compound-source model of $\dot{M}_T(t)$ for 1989 Macquarie Ridge earthquake that fits the low-frequency observations. The earthquake began with a slow event, here represented by a symmetric Hanning function (cosine-square bell) with a moment of 6×10^{20} Nm and a total duration of 240 s, starting 130 s before the high-frequency origin time ($t = 0$). The main (fast) event is represented by a function of the form $Ae^{-a/t-t/b}H(t)$, where a = 55 s, b = 10 s, H is the Heaviside step function, and the constant A is chosen to give a static moment of 16×10^{20} Nm. The dashed line indicates the contribution of the slow component for $t > 0$. *Panel B* and *C*:

Amplitude and phase-delay spectra, comparing this model (solid lines) to the data from Figure 5.2 (circles). The dashed lines are the spectra of the main event alone, which show that the signature of the slow component is confined to frequencies less than 6 mHz.

FIGURE 5.4. Lower focal hemisphere projections of the source mechanism for the 1989 Macquarie Ridge earthquake. The first five diagrams are estimates obtained from spheroidal and toroidal mode data in 2-mHz bands using the inversion algorithm of Riedesel and Jordan (1986); the sixth is the Harvard CMT solution. The compressional (P) and tensional (T) axes are indicated with a cross and an open square, respectively. The shaded region is the compressional field of *P*-wave radiation and the thin solid lines indicate the nodal planes of the best-fitting double couple. A systematic rotation of the mechanism about the P axis is observed at the lower frequencies, indicating that the slow precursor may have had a significant dip-slip component.

FIGURE 5.5. Test of the null hypothesis H_0 = {the Macquarie Ridge earthquake was ordinary} against the alternative H_1 = {it had a slow precursor} using eq. 2.12 (Chapter 2). Triangle is the centroid time shift Δt_1 and skewness parameter α that provide the best fit of eq. 2.6 (Chapter 2) to the phase-delay data below 6 mHz; the dark shaded region is the corresponding 95% confidence interval. 99% confidence region is indicated with the thin solid line. Since the 99% confidence interval includes no points with $\alpha \geq -1/8$, we reject H_0 in favor of H_1.

FIGURE 5.6. *Left Panels* : Source time functions obtained from the inversion of the spectral data up to 15 mHz in the *right panels* and for different values of the start of moment release t_*. χ^2 , the misfit to the spectral data is indicated as well as the value of t_*. Strong smoothing is applied at times prior to the high-frequency origin time $t_0 = 0$. *Right Panels*: Amplitude and phase-delay spectra up to 15 mHz. Solid symbols are estimates obtained with the normal mode methods, whereas the open symbols are from the traveling wave technique. Line patterns corresponds to that of the source time function in the left panels. The solutions with t_*=-75 s and $t_* = t_0 = 0$ do not satisfy the spectral data.

FIGURE 5.7. *Panel A* and *B*: Amplitude and phase-delay spectra derived from four different wave types: spheroidal modes (closed triangles) and first-orbit Rayleigh waves (open triangles) from vertical-component seismograms, and toroidal modes (closed squares) and first-orbit Love waves (open squares) from transverse-component seismograms. For plotting clarity, the transverse-component data have been shifted downward by 9 units in *panel A* and 30 units in *panel B*. The lines are the same reference spectra, calculated from the model in Figure 5.3. All four data types show similar deviations from the main-shock spectrum (dashed lines) below 6 mHz.

FIGURE 5.8. Time-shift spectra obtained for the minor arc Rayleigh waves (R1, solid circle) and the major arc (R2, open circle). Because R1 and R2 leave the source at opposite azimuths, the agreement between both spectra indicates that any directivity of the source process must be small. The synthetics employed for this experiment include the contribution from the global phase delay maps of Ekström and Tromp (unpublished material, 1994). Their maps are expanded up to degree and order 36 in spherical harmonics and cover the frequency range from 8 to 25 mHz (for more details, see also Chapter 3, Figure 3.1). The results obtained in the present chapter do not incorporate the phase-delay maps. However, this figure shows that the conclusions reached in this chapter will not be altered much by the use of these improved synthetics. At the time of writing, phase delay maps for Love waves were not available.

FIGURE 5.9. Comparisons of data and synthetics in 10-min intervals before the *P* waves at GEOSCOPE station NOU (Nouméa, New Caledonia) and GSDN station CTAO (Charters Tower, Australia). Horizontal scale is in minutes, referenced to the high-frequency *P*-wave arrival time (vertical dashed line). First trace in each set is the unfiltered observed seismogram from the long-period vertical channel, arbitrarily normalized to the peak-to-peak amplitude of the *P* wave. Positive time shifts of the first arrivals are primarily due to the group delay of the instrument. The other three traces are amplified by factors of 70 for NOU and 40 for CTAO. The second in each group is again the unfiltered data, showing that no precursor is observed above the noise levels. The third (syn 1) is the ray-theoretical synthetic computed for the analytical source model in Figure 5.3, and the fourth (syn 2) is for the inversion model in Figure 5.10; arrows give the ray-theoretical arrival times for the precursor onsets at $t_0 - 130$ s and $t_0 - 400$ s, respectively. The precursor amplitude for syn 1 is significant above the noise levels, but the amplitude for syn 2 is not.

FIGURE 5.10. *Panel A*: Source time function (solid line) obtained from the inversion of the amplitude and phase-delay spectra in *panel B* and *C*, compared to the Ekström-Romanowicz (1990) estimate (dashed line) derived from broadband body waves. The minimization to obtain the former included a smoothing constraint designed to minimize the precursor amplitude on the *P* wave seismograms in Figure 5.9. Data in *panel B* and *C* are from the analysis of normal modes (solid circles), surface waves (open circles), and *P*-waves (open triangles). Solid lines are the spectra predicted by this model; dashed lines are the predictions of the Ekström-Romanowicz model. Time scales are linear with zero at high-frequency origin time. Frequency scales are logarithmic.

FIGURE 5.11. *Left Panel*: Comparisons of observed and synthetic *P* waves for vertical-component instruments at Nouméa, New Caledonia (NOU), Port aux Français, Kerguélen Is. (PAF), and Taipei, China (TATO). Top trace of each station group is the observed seismogram; middle trace was calculated from the inversion model of Figure 5.10 by complete summation of spheroidal modes to 50 mHz; lower trace was calculated from the Ekström-Romanowicz model (1990) by the same procedure. The synthetics were based on a PREM structure, the Harvard CMT centroid and mechanism, and instrument responses assigned by the network operators. Horizontal scale is in minutes, referenced to the high-frequency *P*-wave arrival time (vertical dashed line). Vertical scale is arbitrary digital units, but the amplitudes of the synthetics relative to the data have been maintained for each station. All seismograms have been low-passed by a 10-pole Butterworth filter with corner at 35 mHz. The shift of the *P*-wave first motion to positive times is a signal delay resulting primarily from the instrument and filter responses. The small ripple in advance of the *P*-wave on the synthetics is an artifact of the synthesis procedure. The synthetics for our model provide a better match to the *P*-wave amplitudes and group arrival times on these and most other stations.

Right Panel: Comparisons of observed and synthetic *SH* waves. Horizontal components have been rotated to obtain the transverse component. Same conventions as the *left panel*. Seismograms are aligned on the predicted S arrival time (vertical dashed line). Note the excellent match both in amplitude and phase. The *SH* data has not been used in the retrieval of the body wave spectra of Figure 5.10.

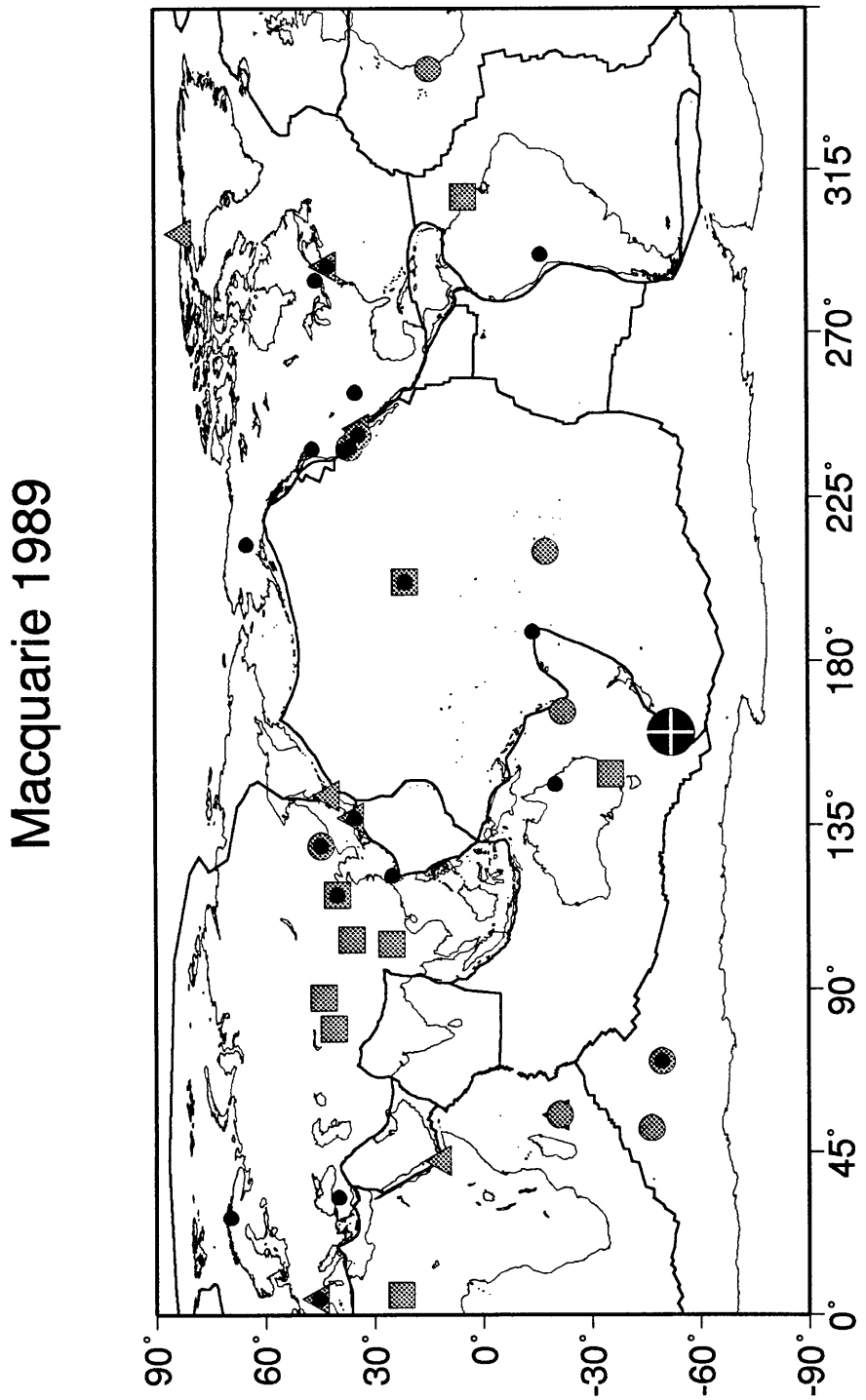

Figure 5.1

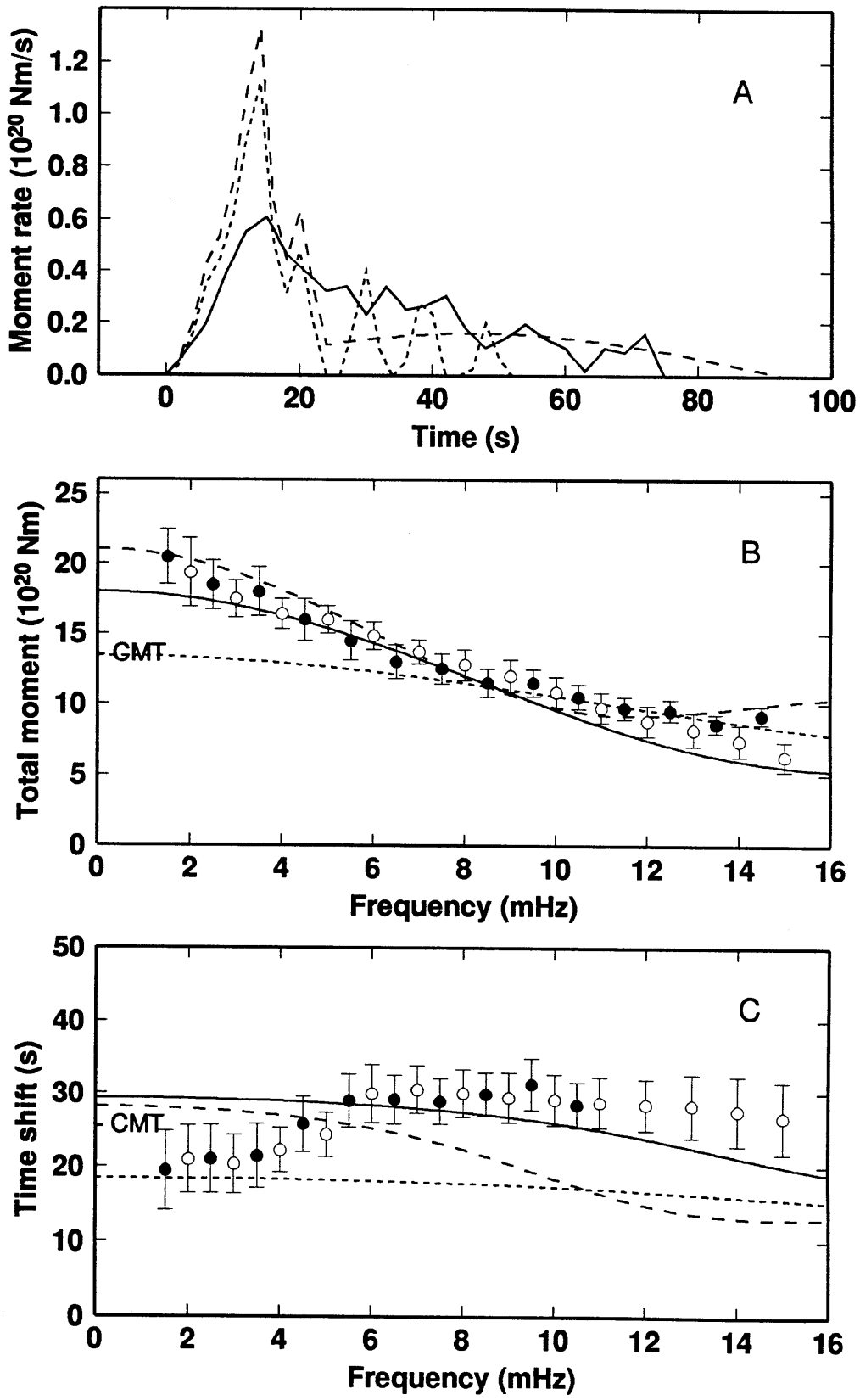
A
Moment rate (10^{20} Nm/s)
1.2
1.0
0.8
0.6
0.4
0.2
0.0
0
20
40
60
80
100
Time (s)
B
Total moment (10^{20} Nm)
25
20
15
10
5
0
GMT
0
2
4
6
8
10
12
14
16
Frequency (mHz)
C
Time shift (s)
50
40
30
20
10
0
CMT
0
2
4
6
8
10
12
14
16
Frequency (mHz)

Figure 5.2

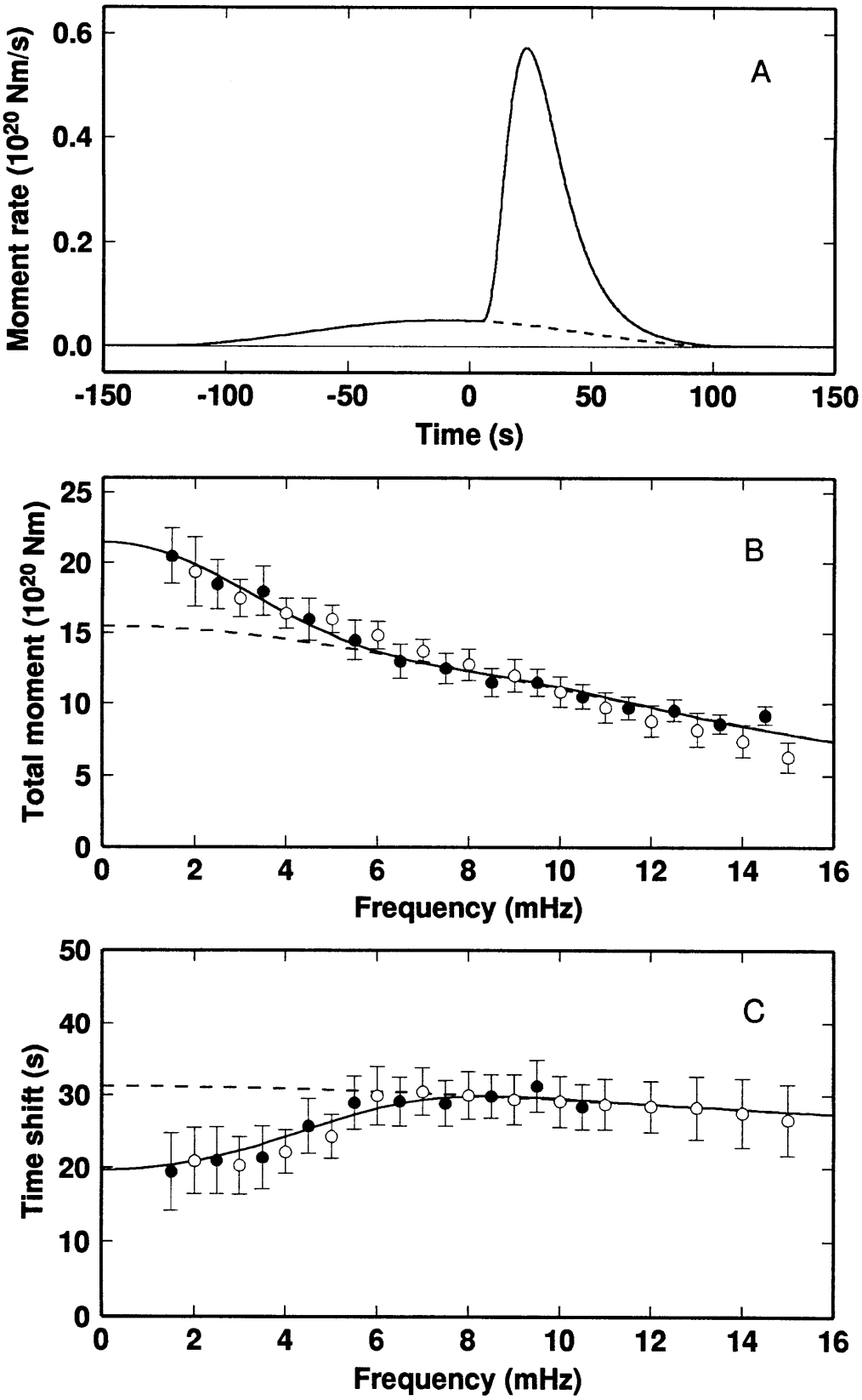
A
Moment rate (10^{20} Nm/s)
0.6
0.4
0.2
0.0
-150
-100
-50
0
50
100
150
Time (s)
B
Total moment (10^{20} Nm)
25
20
15
10
5
0
0
2
4
6
8
10
12
14
16
Frequency (mHz)
C
Time shift (s)
50
40
30
20
10
0
0
2
4
6
8
10
12
14
16
Frequency (mHz)

Figure 5.3

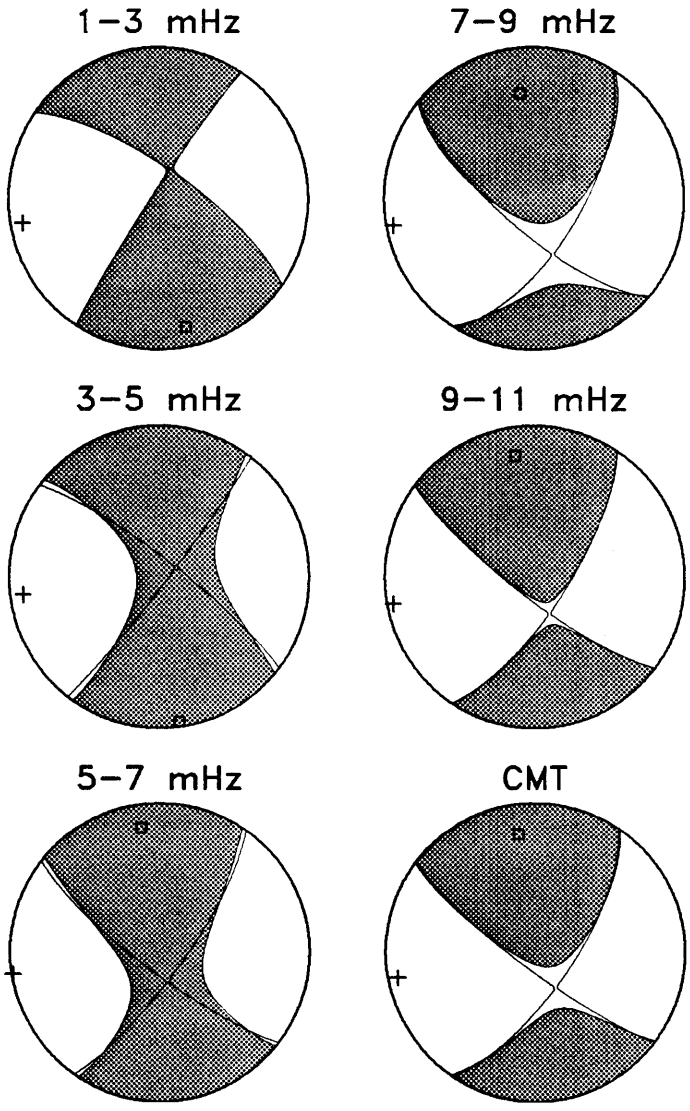

Figure 5.4

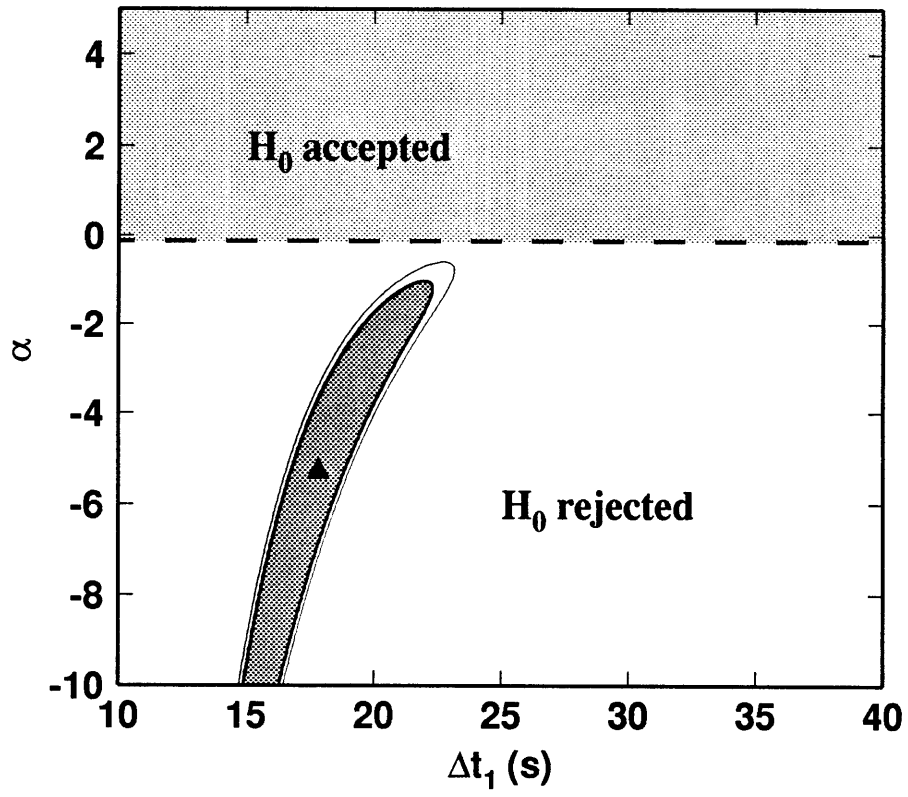

Figure 5.5

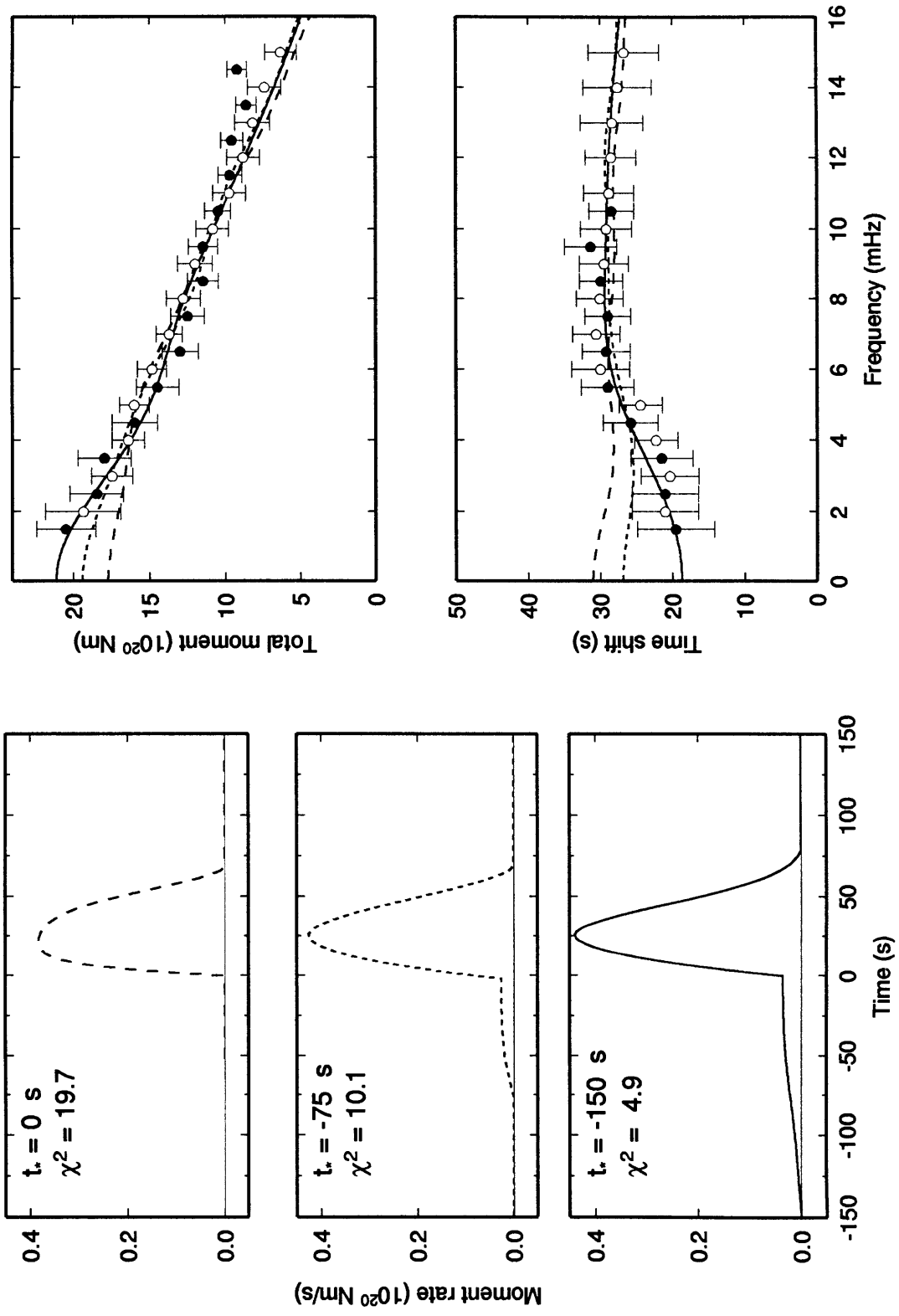
Total moment (10^{20} Nm)
Time shift (s)
Frequency (mHz)
Moment rate (10^{20} Nm/s)
Time (s)
$t_* = 0$ s
$\chi^2 = 19.7$
$t_* = -75$ s
$\chi^2 = 10.1$
$t_* = -150$ s
$\chi^2 = 4.9$

Figure 5.6

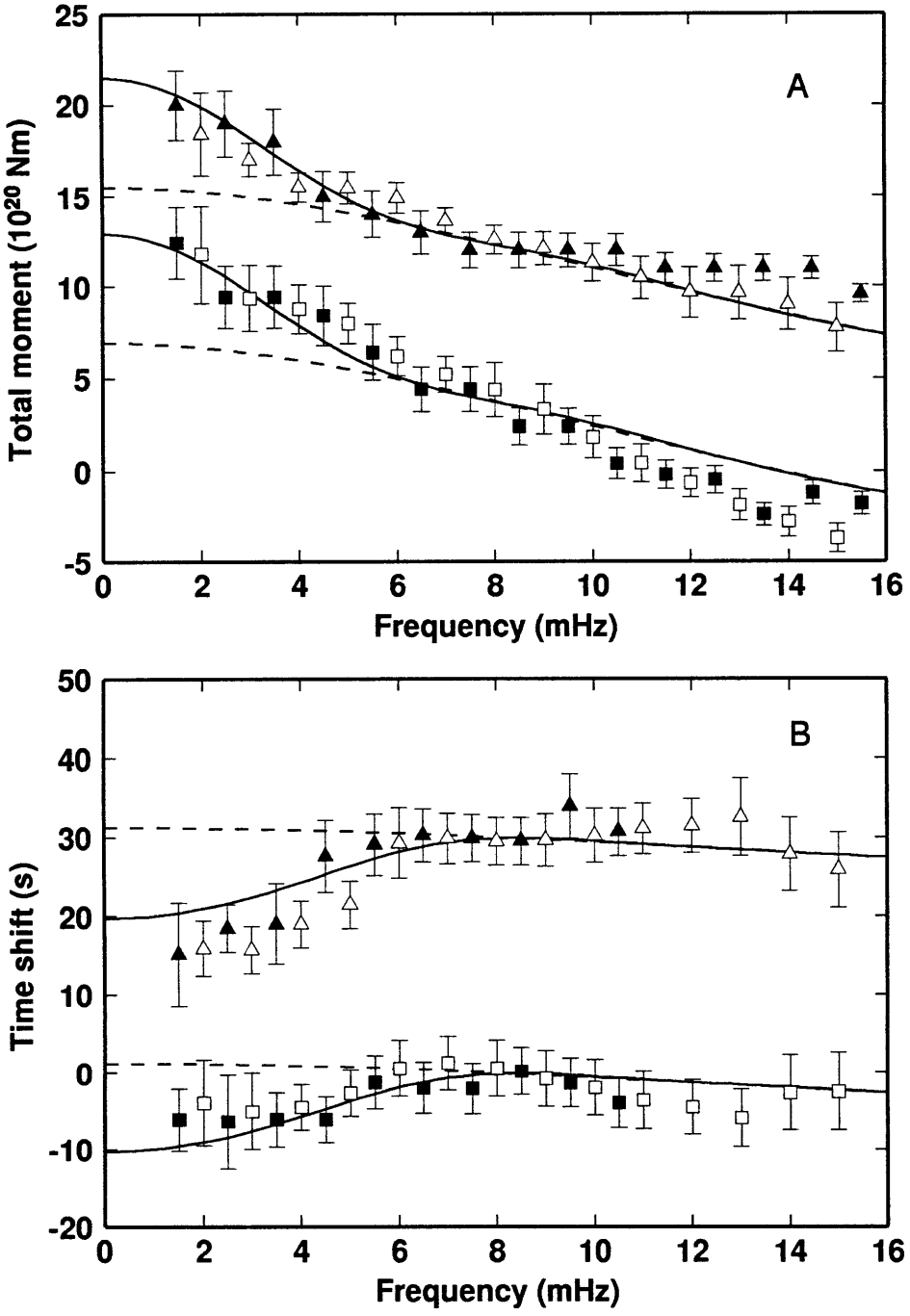
A
Total moment (10^{20} Nm)
25
20
15
10
5
0
-5
0
2
4
6
8
10
12
14
16
Frequency (mHz)
B
Time shift (s)
50
40
30
20
10
0
-10
-20
0
2
4
6
8
10
12
14
16
Frequency (mHz)

Figure 5.7

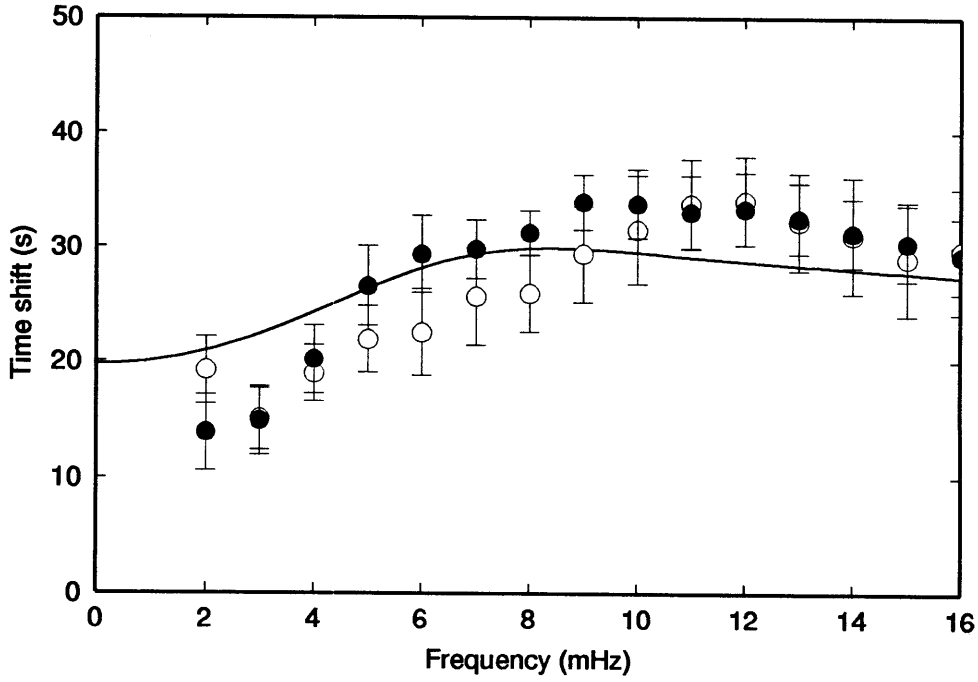

Figure 5.8

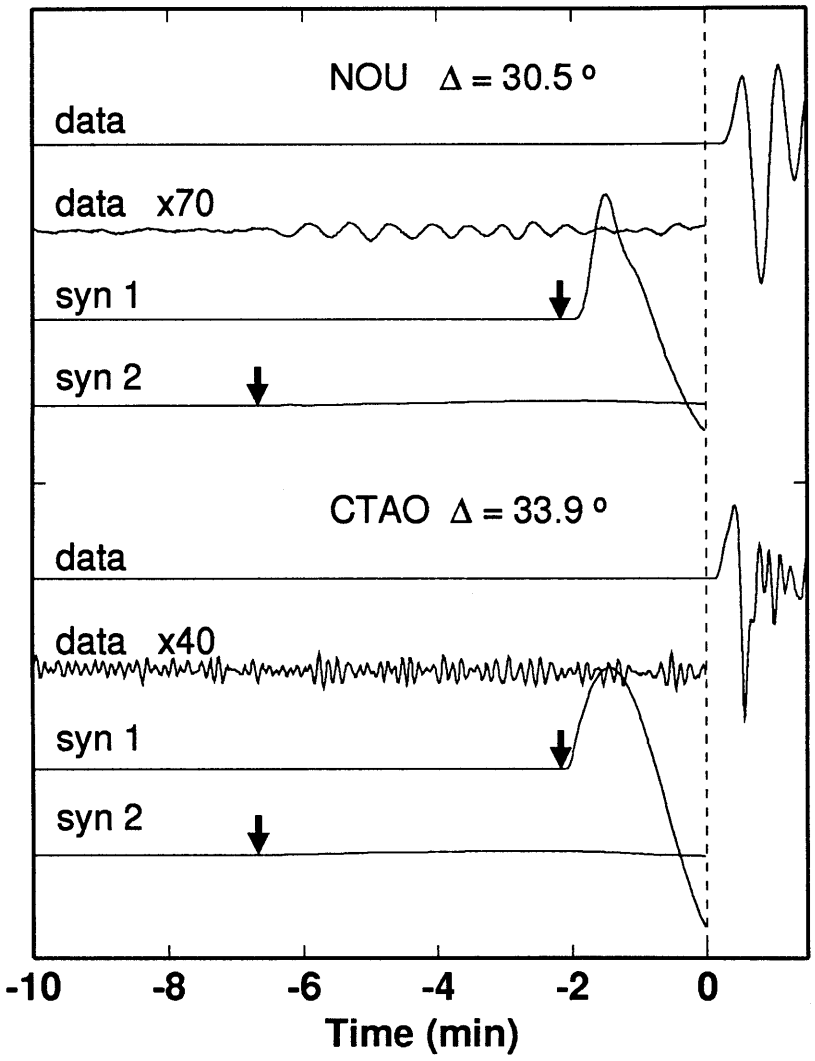
NOU Δ = 30.5 °
data
data x70
syn 1
syn 2
CTAO Δ = 33.9 °
data
data x40
syn 1
syn 2
-10
-8
-6
-4
-2
0
Time (min)

Figure 5.9

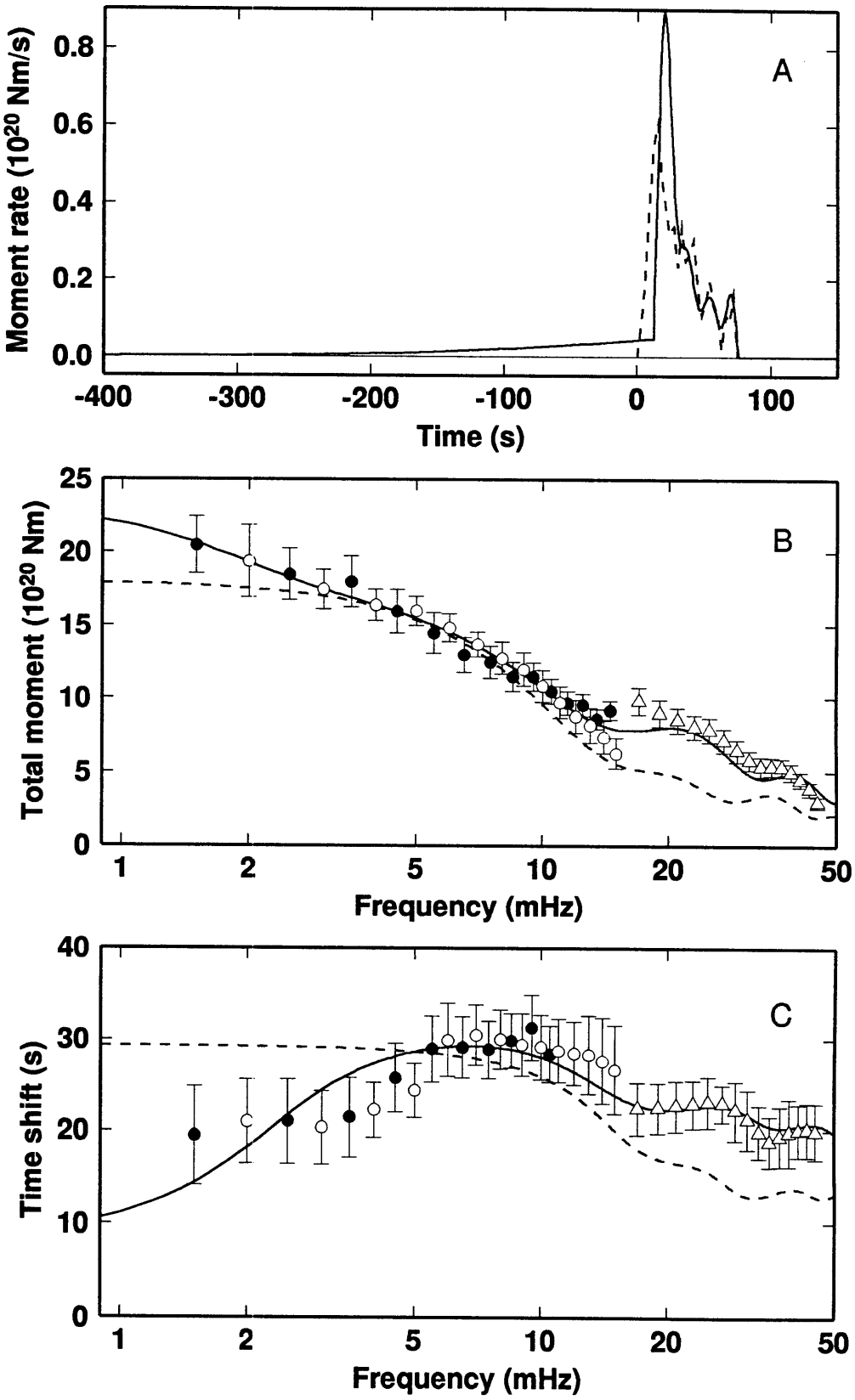
A
Moment rate (10^{20} Nm/s)
0.8
0.6
0.4
0.2
0.0
-400
-300
-200
-100
0
100
Time (s)
B
Total moment (10^{20} Nm)
25
20
15
10
5
0
1
2
5
10
20
50
Frequency (mHz)
C
Time shift (s)
40
30
20
10
0
1
2
5
10
20
50
Frequency (mHz)

Figure 5.10

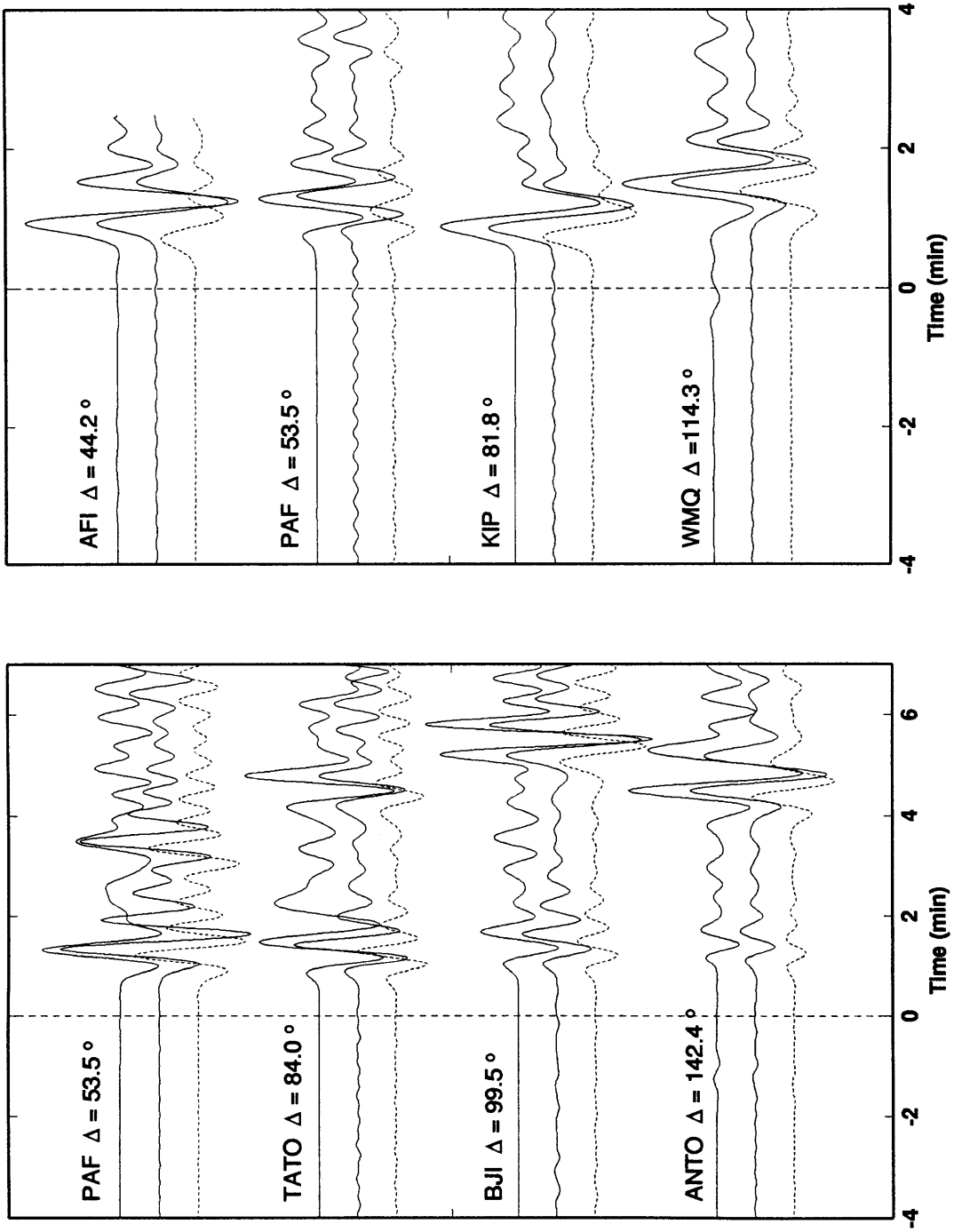
AFI Δ = 44.2°
PAF Δ = 53.5°
KIP Δ = 81.8°
WMQ Δ =114.3°
PAF Δ = 53.5°
TATO Δ = 84.0°
BJI Δ = 99.5°
ANTO Δ = 142.4°
Time (min)
Time (min)

Figure 5.11

CHAPTER 6

The rupture initiation of the 14 March 1994 Mid-Atlantic Ridge event: slow precursor and preshocks.

6.1 Introduction

The 14 Mar 1994 Mid-Atlantic Ridge event (M_W=7.1) provides us with a unique opportunity to study the rupture initiation of a large earthquake. This event occurred at the western end of the Romanche transform fault, which offsets the Mid-Atlantic ridge by 940 km and accommodates the relative plate motion between South-America and Africa at a present rate of 32 mm/y (DeMets et al., 1990). Figure 6.8 shows the distribution of seismicity in the focal region from 1964 to 1993 (ISC and PDE catalogs), as well as source mechanisms from the CMT catalog covering the period 1977 to 1992. Seismicity is concentrated at the ridge and along discontinuous segments of the transform. The 14 Mar 1994 is the second largest event to rupture this portion of the transform since 1977. The largest event (M_W=7.2) occurred on 3 Jan 1982. The amplitude and phase-delay spectra of this slow event are given in Appendix B. In Chapter 2, Figure 2.6, we show spectra of events that took place on the Romanche and the Chain transforms such as the 26 Dec 1992, the 28 Aug 1992, and the 7 Jul 1981 events. These events were shown to be slow earthquakes, i.e., events with characteristic rupture velocities of 1 km/s or less. The null hypothesis H_0 , i.e., the high-frequency origin time corresponds to the start of moment release, was not rejected at the 99% confidence level for any of them. In other words, these events appeared to be regular earthquakes. However, they show a kink in the amplitude spectrum between 6-12 mHz, an indication that their source time functions

are dominated by both a short and a long time constant of rupture, i.e. they are compound events. The relative time location of both types of rupture is a key question that cannot be fully addressed in the hypothesis testing procedures of Chapter 2. In Chapter 3, we develop an inversion algorithm for the source time function to resolve rupture processes with long duration by taking full advantage of the spectral shape of an event. Normal modes, surface waves and body waves are used to obtain network-averaged source spectra from 1.5 to 50 mHz.

6.2 Source time functions

Figure 6.2 and 6.3 display source time functions for the 14 Mar 1994 Mid-Atlantic Ridge event, obtained from separate inversions of vertically and transversely polarized seismograms. The station coverage is adequate, but predominantly samples northerly azimuths of the focal sphere (Figure 6.1). Comparison between Figure 6.2 and 6.3 indicates the agreement between the different data sets and the different methods used to recover the spectra, especially between normal mode and surface wave measurements. In general, spectral continuity is satisfactorily achieved over the entire bandwidth. However, there appears to be a systematic time-shift difference of about 2 s between the transverse and vertical components, which may point out inaccuracies of the earth model used to compute the synthetics.

Overlap between surface-wave and body-wave estimates is good for the transverse component (Figure 6.3). For the vertical component (Figure 6.2), there is however a 6 s discrepancy in time-shifts in the band 10 to 20 mHz. Comparison between the surface-wave time-shift spectra retrieved from both the vertical and transverse components show a discrepancy of 4-5 s. It appears that time-shift estimates obtained from vertically polarized Rayleigh waves have a negative bias in this band. Synthetics used to recover

the surface-wave estimates from vertically polarized seismograms incorporate the phase-delay maps of Ekström and Tromp (unpublished material, 1994), which are expanded up to degree and order 36 in spherical harmonics. These maps account for PREM's slow bias in this band (see Chapter 3, Figure 3.1), but it is nevertheless plausible that some regional variations are not fully resolved by the phase-delay maps.

The spectra for both components are inverted with identical sets of parameters. The source time functions in Figure 6.2 and 6.3 show similar characteristics. In particular, both have a slow precursor starting at -180 s. A large amount of smoothing is applied prior to t_0 = 0 s and after +40 s. Time delays are relative to the high-frequency origin time of the rupture, which we take to be at GMT 4:30:10.6, corresponding to subevent A in Table 6.1. From 0 to 15 s, moderate smoothing is applied, and from 15 to 40 s, comparatively little smoothing is used. This segmentation is justified by the presence of a number of preshocks before the onset of the main shock that starts with subevent C. Inspection of vertically polarized broad-band and short period seismograms reveals two subevents, denoted by A and B, that can unequivocally be picked on a number of stations, such as SJG (Figure 6.4). The body-wave magnitude of the main shock reported by the NEIC is m_b=6.0. The body-wave magnitude is obtained from short-period records, and is proportional to $\log(A/T)$, where A is the maximum amplitude of direct P waves measured at the period T, usually 1 s (e.g., Fowler, 1990). From a comparison of the amplitudes of subevents A and B relative to the main shock, we obtain $m_b \approx 4.7$ for subevent A, and $m_b \approx 5.7$ for subevent B.

At the same time, superimposed on this high-frequency activity, a ramp emerges from the noise at about the same time as event A, i.e., 15-20 s before event C. Low-pass filtering of the seismograms enhances this low-frequency contribution (Figure 6.4), and Figure 6.5 shows that the polarity of the ramp is consistent with a strike-slip mechanism similar to that of the main shock. This low-frequency behavior, both in duration and

amplitude, is also observed in front of a number of *S* waves on the transverse component, such as station HRV.

However, the moment released during the interval A-C is not sufficient to satisfy the spectra of Figures 6.2 and 6.3. Inversions that do not allow for any moment release prior to time A cannot satisfy the spectral data, and any satisfactory source time function requires a slow precursor (Figure 6.6).

Figure 6.6 shows a comparison of source time functions obtained for different values of t_*, the start time of moment release. At $t_* = t_0 = 0$ s, the souce time function displays a small event reminiscent of the behavior observed in the seismograms (subevent A). This small event, however, has a moment magnitude of M_W=6.2, significantly larger than the value of m_b=4.7 estimated from short-period records. The source time function obtained with t_*=11 s, which corresponds to the onset of subevent B, underestimates the total moment of the event by 30%. In both case, the time-shift spectrum is satisfied within error bars, even though the source time functions overestimate the time-shift spectrum by 2-3 s between 1-10 mHz, and underestimate the time-shift spectrum in the body-wave band by the same amount. Because the time-shift spectrum is flat at very-low frequencies, the slow precursor is required by the increase in the amplitude spectrum between 1-5 mHz. The source time function starting at t_*=-180 s satisfies the spectral data. The ramp between 0-15 s contributes to increasing the scalar moment, while allowing for a better fit of the time-shift spectrum in the body-wave band. The source time functions of Figure 6.2 and 6.3 are somewhat sketchy and, in particular, do not adequately represent the complex *P* waveforms observed at teleseismic distances. This indicates that the main shock was composed of multiple subevents. Even if the source time functions in Figure 6.2 and 6.3 are valid azimuthal averages of the source process, they do not account for the lateral extent of rupture.

6.3 Relocation procedures

In order to gain insight into the location of moment release during the 14 Mar 1994 Mid-Atlantic event, we determine the location of the subevents A, B and C, as well as the long-period body-wave and surface-wave centroids. We pick onset times of the subevents A, B, and C from broad-band and short period records. The delay times between A and B, as well as those between B and C, are larger at stations to the west, indicating that event A lies west of B, which itself lies west of the main shock (that starts with subevent C). We use the station residuals to locate the preshocks with the procedure of Jordan and Sverdrup (1981). The location of subevent A is the least well constrained, because its onset could not always be seen above the noise level. Subevent B is well determined, and subevent C marks the onset of the main shock. Their relative locations are given in Table 6.1 and shown on Figure 6.8. Most of the stations are at northerly azimuths with respect to the source, a fact accounted for in the error analysis that produces 95% confidence error ellipses with their long-axes oriented north-northwest (Figure 6.8). Subevent A, located only 25 km away from the ridge (Figure 6.8), is the smallest of the preshocks. Subevents B and C locate further away from the ridge, at a distance of 115 km and 135 km, respectively.

In order to obtain the centroid location of the sequence of events, we apply the modal phase-equalization technique (Riedesel et al., 1986) for epicenters located on a 0.2° grid surrounding the CMT location. A suite of inversions is performed at the grid points and contours of variance reduction are determined separately for the vertical and transverse components. Synthetics are corrected for the low-order lateral heterogeneity of the earth (see Chapter 2 and 3). Figure 6.7 shows the weighted-average contours of both components. Epicentroids in 1 mHz bands from 3 to 9 mHz scatter by at most 30 km around the weighted average location and display no frequency dependence. They stay close to the CMT location (Figure 6.7).

In the body-wave band, *P*-wave station residuals are determined from 20 to 40 mHz at 2 mHz intervals with respect to the CMT location and the prediction of our preferred source time function. These residuals are considered to pertain to an event in a cluster, and a multiple event relocation (Jordan and Sverdrup, 1981) is performed, with depth fixed at 15 km. The optimal epicentroid in this band is slightly eastward of the very-low-frequency centroid (Figure 6.8).

6.4 Broad-band faulting models

Table 5.1 gives the location and origin time of the high-frequency subevents and of the centroids. Inspection of broad-band records reveals that the subevents A and B release very little moment. The integrated moment of the low-frequency ramp that becomes visible about 15-20 s prior to the onset of the main shock is also small. From a high-frequency point of view, the rupture process started with subevent A at or near the ridge-transform intersection (Figure 6.8), and proceeded eastward along the Romanche transform. There is no evidence for any bilateral motion in that time interval. The distance along the transform between A and B is about 115 km, and implies an apparent rupture velocity of 8 km/s. Between B and C, one obtains a rupture velocity of 5 km/s. There is however, an uncertainty of about 20 km in the location of those subevents, so that lower rupture velocities in the order of 4 km/s cannot be ruled out. The total extent of rupture from event A to the body-wave centroid is about 180 km, four times the length expected from an L^2 scaling for an event of this size (Scholz, 1994).

Inversions for the source time function for the 14 Mar 1994 event indicate that the network-averaged spectra require the presence of moment release prior to the onset of event A. The slow precursor in these inversions starts at -180 s relative to event C, but its location is not constrained by our data. For example, the slow precursor could nucleate

east of event C, propagate unilaterally westward towards event A, loading segments of the transform faults. After some delay time, the sequence of subevents, from A to C, is initiated leading to an apparent unilateral propagation direction opposite to that of the slow precursor. In another model, the slow precursor could initiate near the ridge, nucleating high-frequency preshocks as the slow rupture is proceeding eastward toward the event's centroid. In both scenarios, a delay time of several tens of second is necessary between the passage of the precursor and the onset of brittle rupture.

In Figure 6.9, we present schematically a spatio-temporal model that attempts to satisfy both low-frequency and high-frequency observations, without requiring any, or very little, delay time between the precursor's loading and the onset of a subsequent normal rupture. On the horizontal axis, we report time delays of subevents relative to subevent A. On the vertical axis, the distance from the ridge is taken as positive westward along the transform. The centroid location (VLF) represents the center of mass of both the temporal and spatial dimensions. Given the uncertainties in the data, any model of the rupture should at least be consistent in the centroid time and location of the event. The intensity of the gray shaded areas is proportional to the density of moment release; for example, subevents A and B release little moment, but with great intensity.

In this model, the 14 Mar 1994 event would start as a slow, smooth rupture at t = -180 s between A and B (Figure 6.9)[1]. The depth of the precursor is not directly constrained by our data, but is likely to be deeper than the normal rupture (Ihmlé et al., 1993).

The large apparent rupture velocity between A and B suggests that the slow precursor developed bilaterally, reaching point A about 15 second earlier that point B. In that case, the slow precursor would have a rupture velocity of about 200 m/s, for a nucleation at t =- 180 s relative to the onset of A, midway between A and B. From a study of normal-

[1] For plotting convenience, we truncated the precursor at times prior to -50 s relative to the onset of A.

mode excitation anomalies, Beroza and Jordan (1990) postulated the existence of quiet earthquakes, events with rupture velocities of about 10-100 m/s, and the rupture velocity of 200 m/s is consistent with their hypothesis. This value, however, is not well constrained, mainly because of uncertainties in the spatial locations of subevents. The ramp that is visible on broad-band seismograms starts about 15-20 s prior to event C (Figure 6.4 and 6.5), and has a strike-slip mechanism consistent with that of the main shock . The ramp appears to be more compact for stations to the east, suggesting an eastward directivity. The ramp could tentatively be interpreted as an intensification of moment release of the slow precursor, possibly related to the rupturing of the transform fault between locations A and B. The main shock starting at C is shown with a rupture velocity of 3 km/s; but we do not attempt here to resolve any details of the complex broad-band *P* waveforms for this event. In Figure 6.9, the body wave centroid (LP) lies outside the main shock's area, but it is located east of the very-low frequency centroid (VLF) and is not well resolved. In the source time functions of Figure 6.2 and 6.3, it appears that the period of slow motion outlasted the arrest of regular rupture. The areal extent of the slow and smooth motion on the fault, especially its depth centroid, is not well constrained by the data, and many different models of spatio-temporal moment release could satisfy the data.

6.5 Discussion

As in the case of the 1989 Great Macquarie Ridge earthquake (Ihmlé et al., 1993), the teleseismic data for the 14 Mar 1994 Mid-Atlantic event can be satisfied if the event is a compound event, i.e. an event composed of two different physical mechanisms. The first has a rupture velocity of about 3 km/s and radiates energy over a broad band of frequencies. This is typical of ordinary events. The second mechanism has much lower

rupture velocity in the range 10-500 m/s, releases moment in a smooth way, and radiates energy only at very low frequencies. This second mechanism is referred to as an infraseismic event (Ihmlé et al., 1993), or to a quiet earthquake (Beroza and Jordan, 1990). Ihmlé et al., (1993) hypothesize that the existence of this type of event is related to the rheological stratification of oceanic lithosphere.

The seismic budget of the Romanche transform fault, as well as that of other transforms on the Mid-Atlantic ridge, is nearly complete, i.e., the seismic slip rates match predictions of current plate motion (Chapter 2; Kanamori and Stewart, 1976; Burr and Solomon, 1978; Kawasaki et al., 1985). The lack of seismic deficit on the Romanche transform precludes that an appreciable amount of slip be accumulated by infraseismic events alone. Several large events on the Central Mid-Atlantic transforms are slow earthquakes which present a kink in their amplitude spectra, an indication of the compound nature of faulting (Chapter 2). It appears that infraseismic events accompany regular events, sometimes preceding them, and that this type of moment release significantly contributes to the seismic budget of Central Mid-Atlantic Ridge transform faults.

Large earthquakes occurring on Mid-Atlantic transforms appear to commonly have preshocks of the sort observed for the 14 Mar 1994 Romanche transform event. Kanamori and Stewart (1976) inferred from a comparison between the scalar moment, surface-wave and body-wave magnitude that two large events that occurred on the Gibbs transform fault, the 13 Feb 1967 and the 16 Oct 1974 events, were slow earthquakes. Interestingly, both events had a small preshock that preceded the main shock by about 5-6 s. Bergman and Solomon (1988) located the preshock of the 13 Feb 1967 earthquake 15-20 km to the west of the event's centroid, implying a sense of directivity compatible with that of the main shock. They located the preshock of the 16 Oct 1974 event 30 km to the east of the event's centroid. In that case, Bergman and Solomon pointed out that the sense of directivity of the main shock is toward the preshock's epicenter. In both cases,

the preshock nucleates near the ridge-transform intersection, whereas the event centroids are toward the center of the transform.

Bergman and Solomon also reported a small preshock to the 25 Aug 1979 Vema transform event that preceded the main shock by about 5 s. In that case, the preshock epicenter was in the vicinity of the main shock, but somewhat deeper, and had a well-resolved dip-slip mechanism. The 11 Oct 1973 St. Paul's transform event also presented a 10 s preshock (Wolfe et al., 1993). Another examples involves the 12 Dec 1992 Romanche transform event, which occurred 470 km east of the 14 Mar 1994 event. The NEIC location, that presumably locates the preshock, is 60 km to the west of the CMT location (taken along the transform), and 21 s earlier than the CMT centroid time. The low-frequency amplitude and phase-delay spectra for this slow earthquake are given in Appendix B. Unfortunately, we could not analyze the long-period waveform for this event with great confidence, because of a small earthquake (M_W=5.7) that occurred 38 minutes earlier in the Kermadec region and contaminates body-waves estimates.

Transform faults are characterized by complex thermal, mechanical, and hydrological processes, involving heterogeneous mafic and ultramafic rock assemblages, serpentinized peridotites and serpentine diapirs (Fox and Gallo, 1986). The preshocks to the Gibbs transform events described earlier, as well as subevent A of the 14 Mar 1994 earthquake, nucleate near the ridge-transform intersection. Plate cooling models (e.g. Parsons and Sclater, 1977) predict that isotherms become shallower in the vicinity of the ridge. The small size of the preshocks appears to be related to the shallower depth extent of brittle rupture near the ridge. This is consistent with a microearthquake study on the Kane transform, in which focal depths of 3-6 km near the ridge-transform intersection, and 5-9 km away from the ridge, are reported (Wilcock et al., 1990). In one of the faulting models presented here, the slow precursor initiates between subevents A and B, presumably at depth, about 50 km away from the ridge-transform intersection. This behavior may be related to either the thermal condition near the ridge, or the state of

stress of depth in that part of the transform. The rupture process of the 14 Mar 1994 Mid-Atlantic earthquake is characterized by complex processes both at low-frequencies, where spectra require a slow precursor, and at high-frequencies, where the main shock is preceded by a number of preshocks. The location of the slow precursor is not directly constrained by our data, which can be satisfied by several models of spatial moment release. In one such model, the 20 s long ramp, emerging from the noise in front of broad-band *P* and *S* waveforms, is interpreted as the time domain signature of the final stage of precursory motion in the focal region. Although attractive, we have no evidence so far of a systematic connection between slow precursors and the common occurrence of preshocks to large Mid-Atlantic ridge transform events.

TABLE 6.1

Location of subevents, very-low frequency, and long-period centroids for the 14 Mar 1994 Mid-Atlantic Ridge earthquake. A, B, C have been obtained from picks of onset times on vertically polarized broad-band and short-period records. VLF is the very-low frequency centroid obtained in the band 3-7 mHz from vertical and transverse components. LP designates the centroid of long-period *P* waves in the band 20-40 mHz. The origin time (or centroid time) is given in hh:mm:ss. The distance from the ridge is in km measured eastward from the ridge-transform intersection. The delay time is relative to subevent A. In the text, the high-frequency origin time of the event is taken to be the onset of the C subevent. Standard errors in timing are of the order of 1-1.5 s, and errors in distance from the ridge are of the order of 10-20 km. See Figure 6.8.

	Origin time	Latitude	Longitude	Distance from ridge	Delay w.r.t. event A
A	4:30:10.6	-1.51	-24.24	25	0.0
B	4:30:21.3	-0.90	-23.53	115	10.7
C	4:30:25.6	-0.87	-23.35	135	15.0
VLF	4:30:31.6	-0.90	-23.00	170	21.0
LP	4:30:33.0	-0.79	-22.71	200	22.4

Figure captions

FIGURE 6.1. Map showing location of the 14 Mar 1994 Mid-Atlantic Ridge earthquake and seismic stations, which include elements of the GEOSCOPE, GDSN, IDA, and IRIS networks. Large shaded symbols are stations used in the low-frequency analysis: vertical only (triangles), transverse only (squares), both (circles). The same convention is used for stations used in the high-frequency *P* wave analysis (small solid symbols). The source mechanism is shown at the epicenter.

FIGURE 6.2. Source time function of the 14 Mar 1994 event obtained from vertical component seismograms. The solid line in *Panel A* shows the source time function obtained from the inversion of the total-moment and phase-delay spectra in *panels B* and *C*. The inset is the mechanism used in the spectral recovery methods. In panels A and C, time is referenced relative to the high-frequency origin time, which we take to be that of event A (see text). Three solid symbols denote the network-averaged spectra from the analysis of free oscillations (circles), surfaces waves (squares), and body waves (triangles). Parameters calculated from the time function are $M_T^0 = 5.2\ 10^{19}$ Nm, $\Delta t_1 =$ 2.5 s, $\tau_c = 68.1$ s and $\alpha = 0.0$.

FIGURE 6.3. Source time function of the 14 Mar 1994 event obtained from transversely polarized seismograms. Same plotting convention as Figure 6.2. Parameters calculated from the time function are $M_T^0 = 5.5\ 10^{19}$ Nm, $\Delta t_1 = 4.7$ s, $\tau_c = 93.4$ s and $\alpha =$ 0.0.

FIGURE 6.4. *P*-wave seismogram at the station SJG ($\Delta = 47°$, $\phi = 296°$) of the 14 Mar 94 Mid-Atlantic Ridge earthquake. The top trace is the broad-band record for this station, the middle and lower traces are a high-pass and low-pass filtered version, respectively. The maximum amplitude is given next to each trace in digitization units. The latter has been shifted forward by 4 s to account for the group delay of the filter, which is a six-pole Butterworth with a corner frequency at 100 mHz. The arrival time of the main shock corresponds to event C, indicated by the vertical dashed line. Events A and B represent small preshocks that locate to the west of event C. A low-frequency ramp is visible on the low-pass traces that emerges from the noise at about -5 s.

FIGURE 6.5. Low-pass filtered P-wave records. The filter is a causal six-pole Butterworth with a corner frequency at 100 mHz. Stations are arrayed according to azimuth ϕ from the source. The first four ($296° \leq \phi \leq 325°$) correspond to dilatational arrivals. These records have been inverted, so that the first motion is the same on all records. Seismograms have been aligned on the first upward pulse. The dashed line for A and B do not take into account the moveout of these subevents relative to event C (see Figure 6.8). The ramp has the same polarity as the main shock (event C), indicating that it has a similar strike-slip mechanism.

FIGURE 6.6. *Left Panels* : Source time functions obtained from the inversion of the spectral data in the *right panels* and for different values of the start of moment release t_*. *Right Panels*: Amplitude and phase-delay spectra up to 50 mHz obtained from transverse component seismograms. Same plotting convention as Figure 6.2. Line patterns corresponds to that of the source time functions in the left panels. The solutions with t_*=-180 s is that of Figure 6.3. The solutions with t_*=0 s (onset of subevent A) and t_*=+11 s (onset of subevent B) do not satisfy the spectral data.

FIGURE 6.7. Very-low frequency relocation of the event. Synthetics for the vertical and transverse component have been computed on a 0.2° grid. Riedesel's modal inversion technique has been applied at each node (Riedesel, 1985; Riedesel et al., 1986; Jordan, 1991). Contours of variance reduction as a function of frequency are shown. The black dot indicates the maximum in each band. The CMT centroid is given for reference (open diamond), as well as the trace of the Romanche transform (dashed line). Our optimal centroid (average 3-7 mHz) is slightly north of the CMT location.

FIGURE 6.8. *Top panel*: Seismicity at the western end of the Romanche transform. Bathymetric contours, interpolated from the dbdb5 database, are given at intervals of 1000 m. The plate boundary between the African (north) and South-American plates (south) is indicated with the solid line. All events larger than magnitude 4.0 in the ISC (from 1964-1989) and the NEIC (from 1990-1993) catalogs are shown (gray circles). Source mechanisms of events in the CMT catalog are plotted at the centroid location, with size proportional to the moment magnitude. The 14 Mar 1994 event is marked. Seismicity is highest near the ridge intersection and around longitude 338°. A small M_W=5.9 CMT event is located next to the 14 Mar 1994 earthquake (M_W=7.1). *Lower Panel.* Location of subevents of the 14 Mar 1994 earthquake. The plate boundary is given for reference. Arrival times of subevents A, B, and of the onset of the main shock

have been used to located A, B, and C with the multiple-event relocation procedure of Jordan and Sverdrup (1981). 95% confidence ellipses are shown, and the solution for A is the least well constrained. VLF indicates the very-low frequency centroid of the event (solid star). The long-period body wave (LP) centroid is also indicated (square). The open diamond near A is the epicenter of the event as reported by the NEIC and the other open diamond is the CMT centroid.

FIGURE 6.9. Spatio-temporal model of the rupture. The abscissa is time in seconds relative to event A. The vertical axis is the distance away from the ridge. A, B and C are high-frequency events, VLF is the very-low frequency centroid and LP is the long-period body-wave centroid of the event. Error bars are the 95% confidence intervals. Periods of moment release are indicated with shades of gray, the intensity of which reflects moment-rate density. The slow precursor is indicated by a light shade of gray and, in this model, has a rupture velocity of 100 m/s. In the source time function of Figures 6.2 and 6.3, the slow precursor starts at -180 s relative to event A. For plotting convenience, the time axis starts at -50 s.

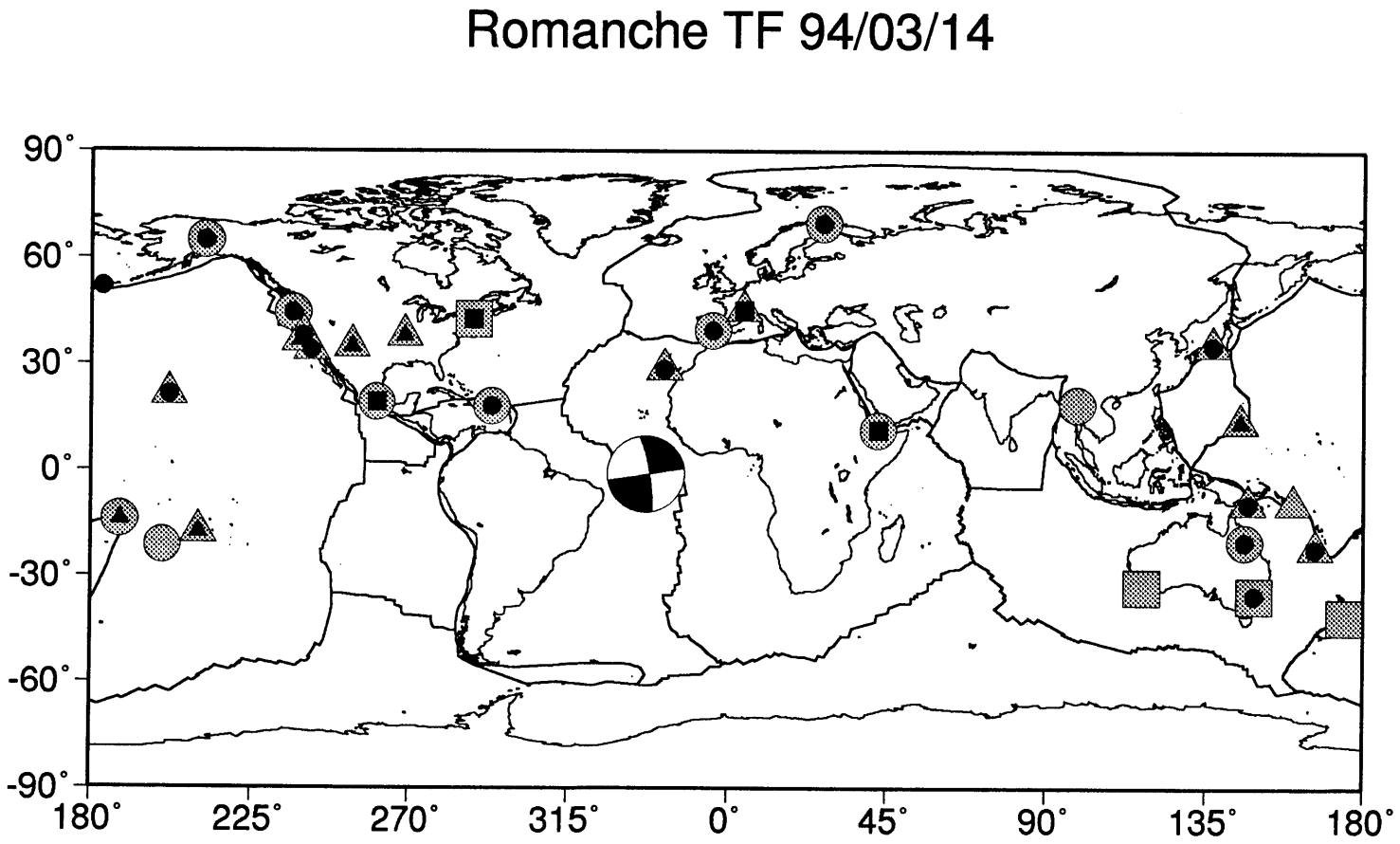
Romanche TF 94/03/14
90°
60°
30°
0°
-30°
-60°
-90°
180°
225°
270°
315°
0°
45°
90°
135°
180°

Figure 6.1

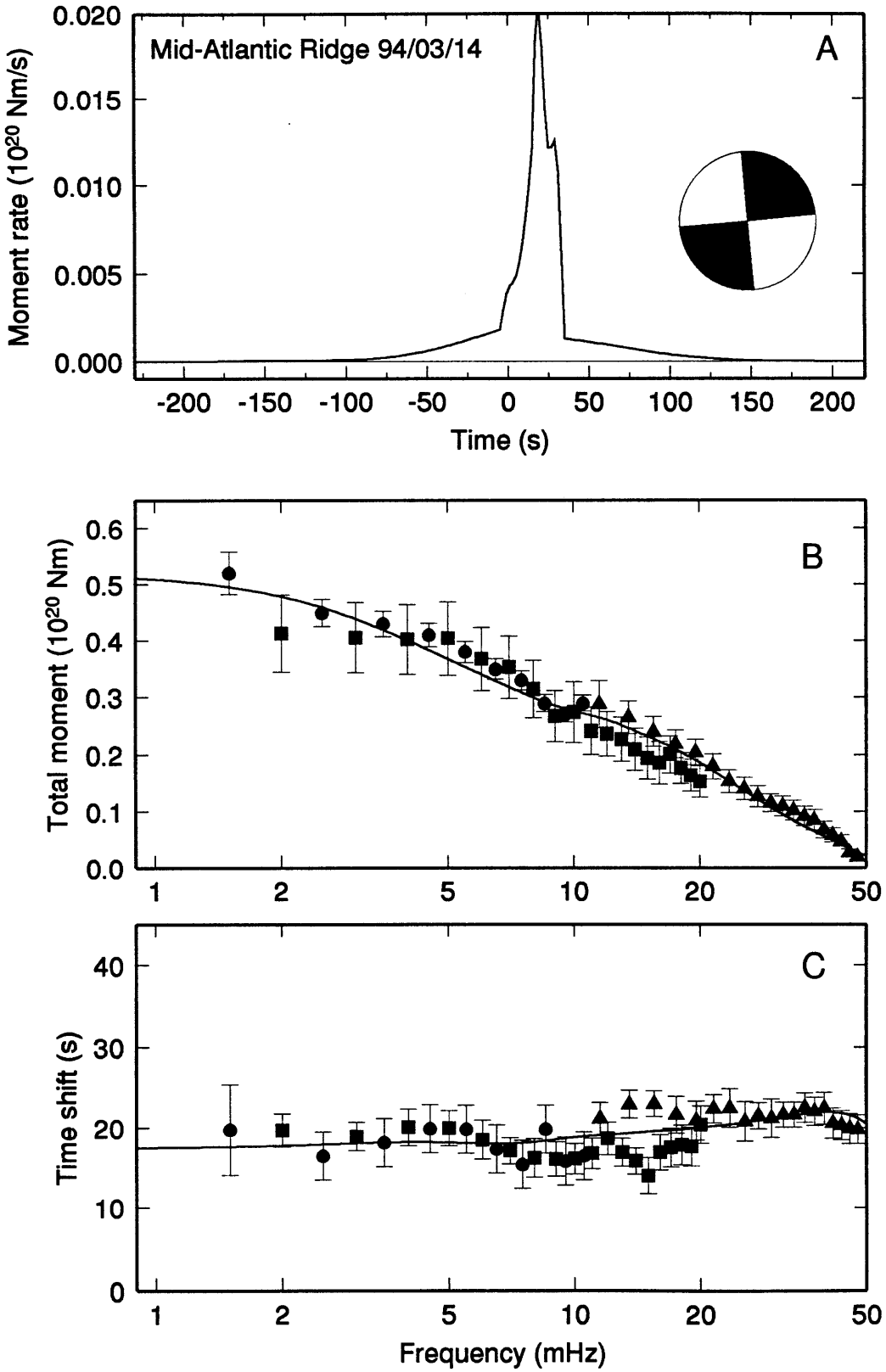
Mid-Atlantic Ridge 94/03/14
A
Moment rate (10^{20} Nm/s)
0.020
0.015
0.010
0.005
0.000
-200 -150 -100 -50 0 50 100 150 200
Time (s)
B
Total moment (10^{20} Nm)
0.6
0.5
0.4
0.3
0.2
0.1
0.0
1 2 5 10 20 50
C
Time shift (s)
40
30
20
10
0
1 2 5 10 20 50
Frequency (mHz)

Figure 6.2

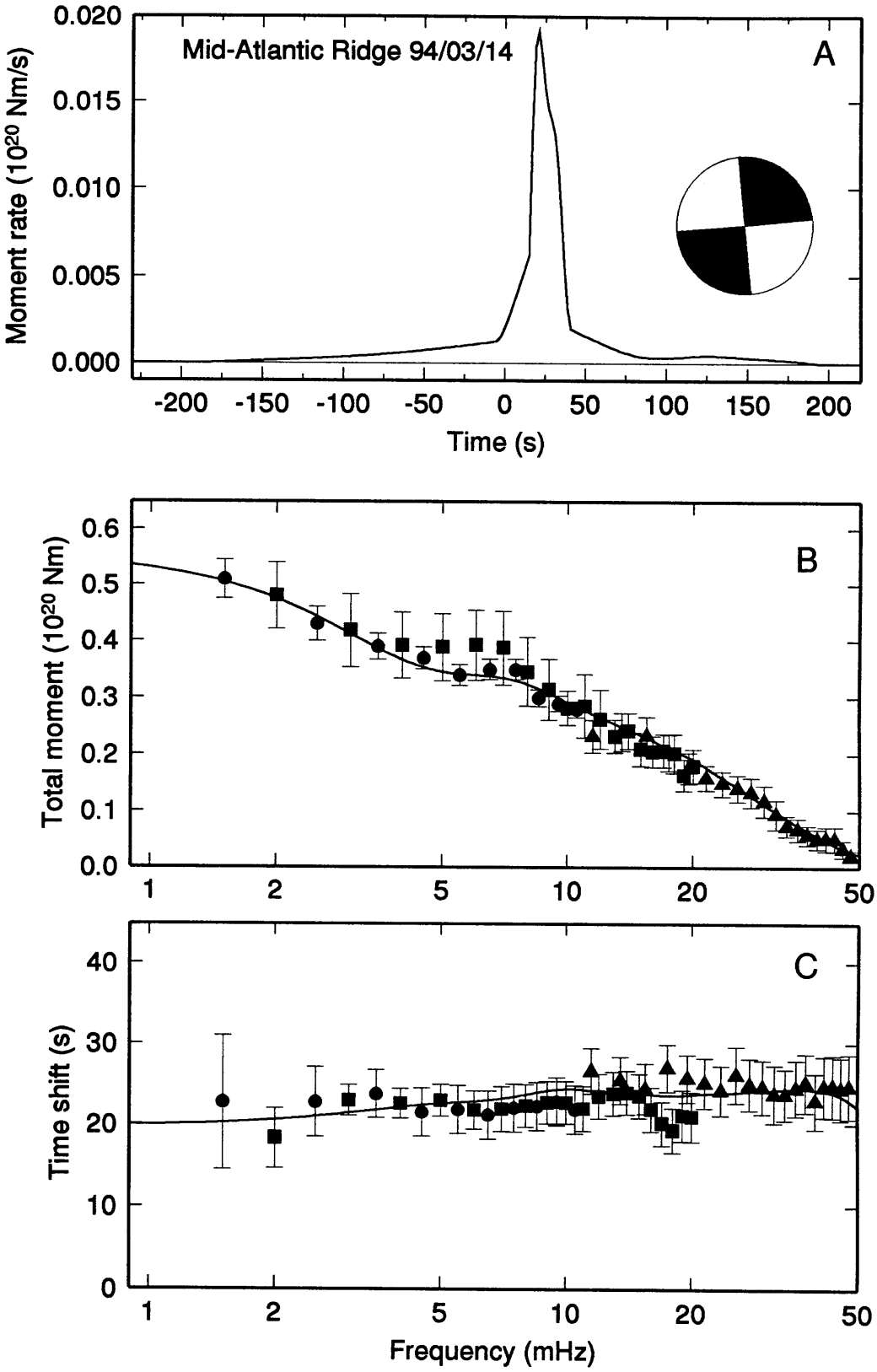
Mid-Atlantic Ridge 94/03/14
A
Moment rate (10^{20} Nm/s)
0.020
0.015
0.010
0.005
0.000
-200 -150 -100 -50 0 50 100 150 200
Time (s)
B
Total moment (10^{20} Nm)
0.6
0.5
0.4
0.3
0.2
0.1
0.0
1 2 5 10 20 50
C
Time shift (s)
40
30
20
10
0
1 2 5 10 20 50
Frequency (mHz)

Figure 6.3

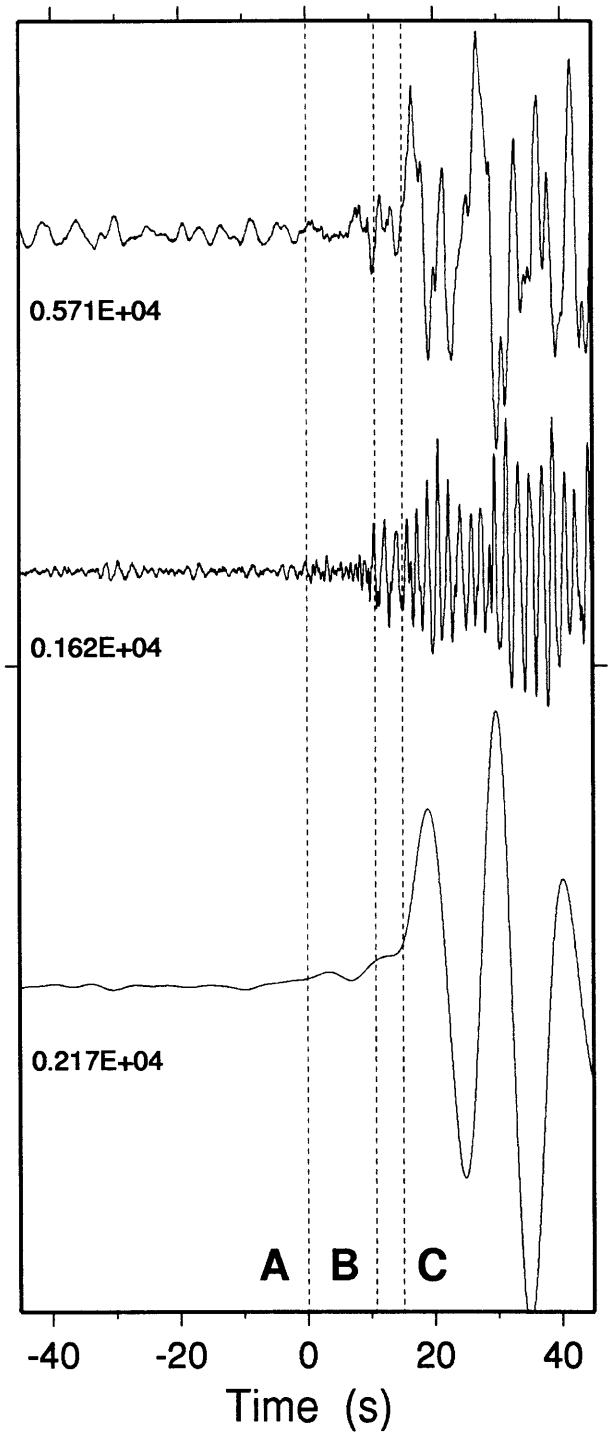

Figure 6.4

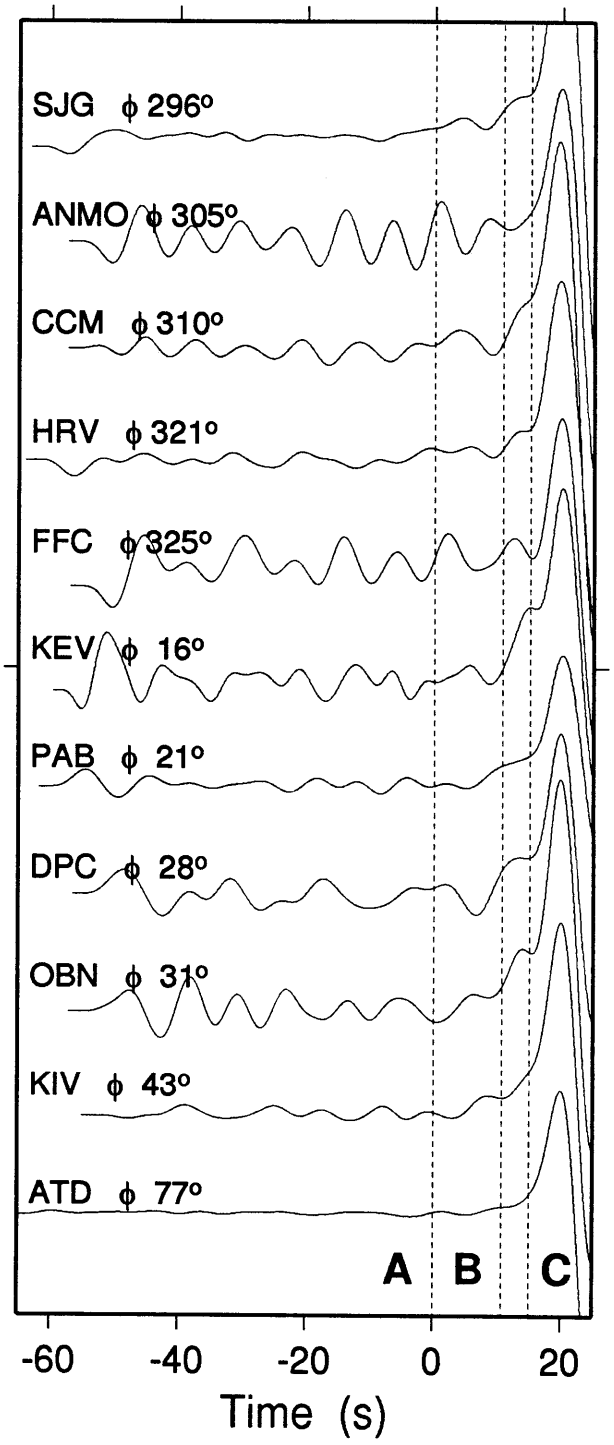
SJG ϕ 296°
ANMO ϕ 305°
CCM ϕ 310°
HRV ϕ 321°
FFC ϕ 325°
KEV ϕ 16°
PAB ϕ 21°
DPC ϕ 28°
OBN ϕ 31°
KIV ϕ 43°
ATD ϕ 77°
A
B
C
-60
-40
-20
0
20
Time (s)

Figure 6.5

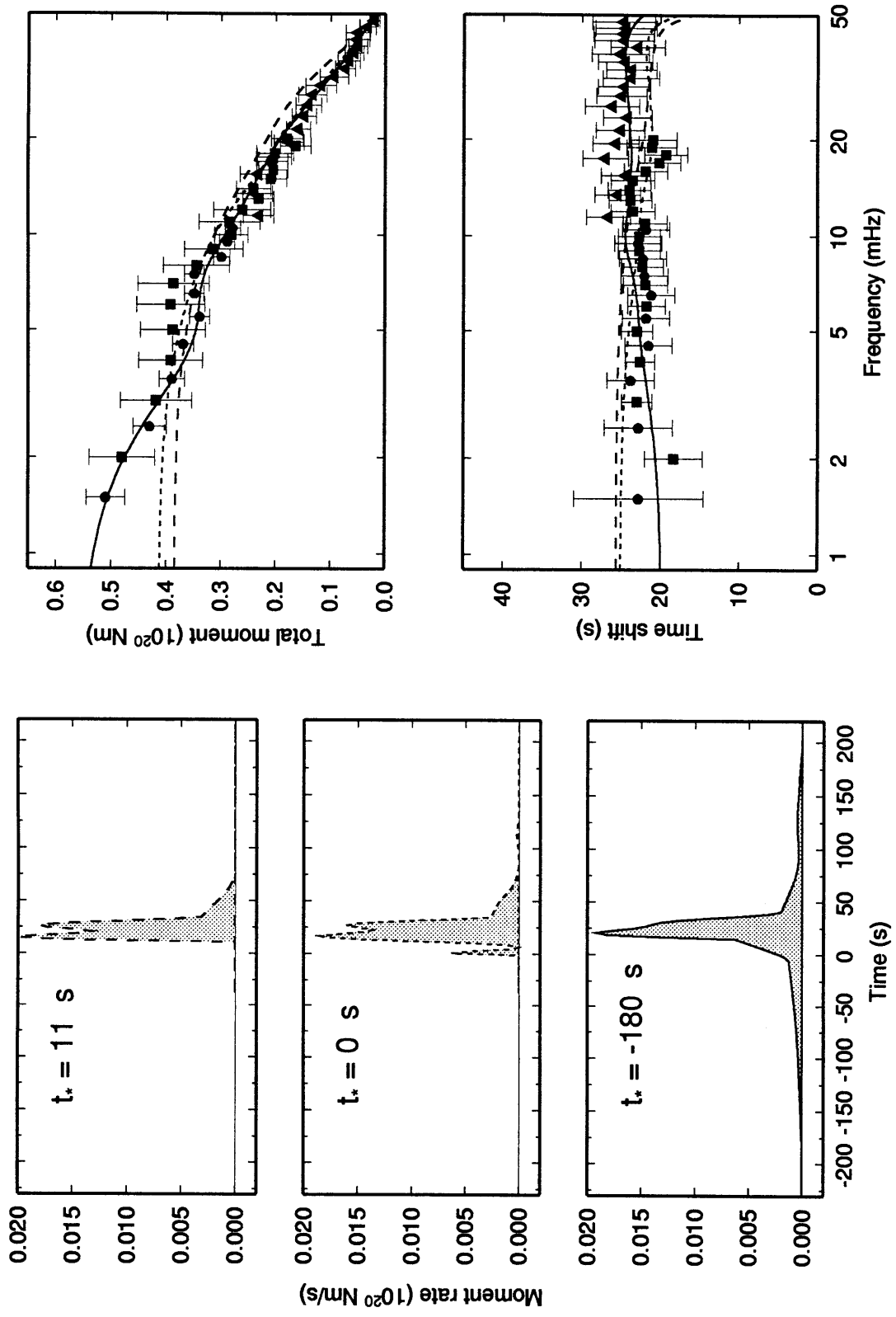
Total moment (10^{20} Nm)
0.6
0.5
0.4
0.3
0.2
0.1
0.0
Time shift (s)
40
30
20
10
0
1
2
5
10
20
50
Frequency (mHz)
Moment rate (10^{20} Nm/s)
$t_* = 11$ s
$t_* = 0$ s
$t_* = -180$ s
0.020
0.015
0.010
0.005
0.000
-200 -150 -100 -50 0 50 100 150 200
Time (s)

Figure 6.6

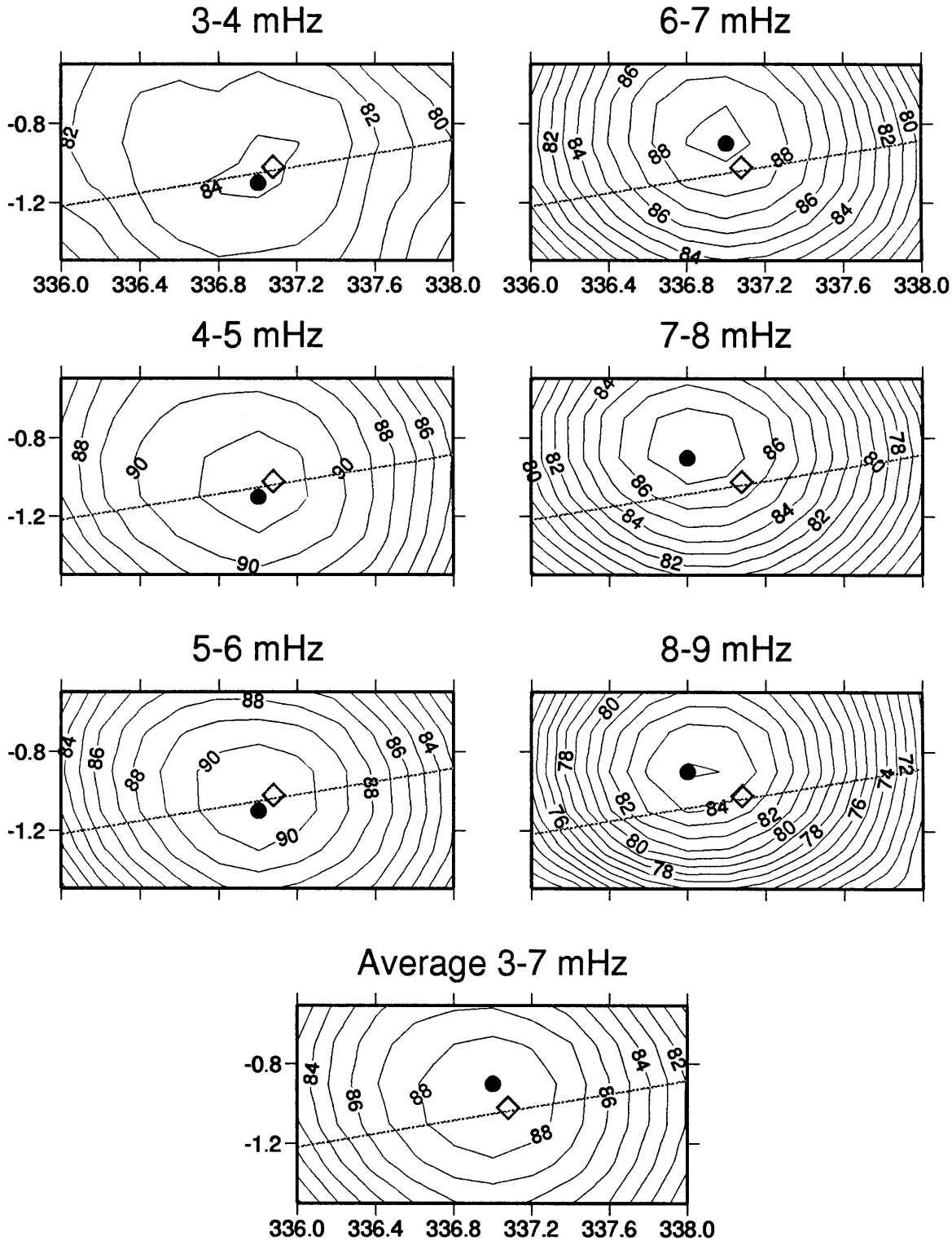
3-4 mHz
6-7 mHz
4-5 mHz
7-8 mHz
5-6 mHz
8-9 mHz
Average 3-7 mHz
-0.8
-1.2
336.0
336.4
336.8
337.2
337.6
338.0

Figure 6.7

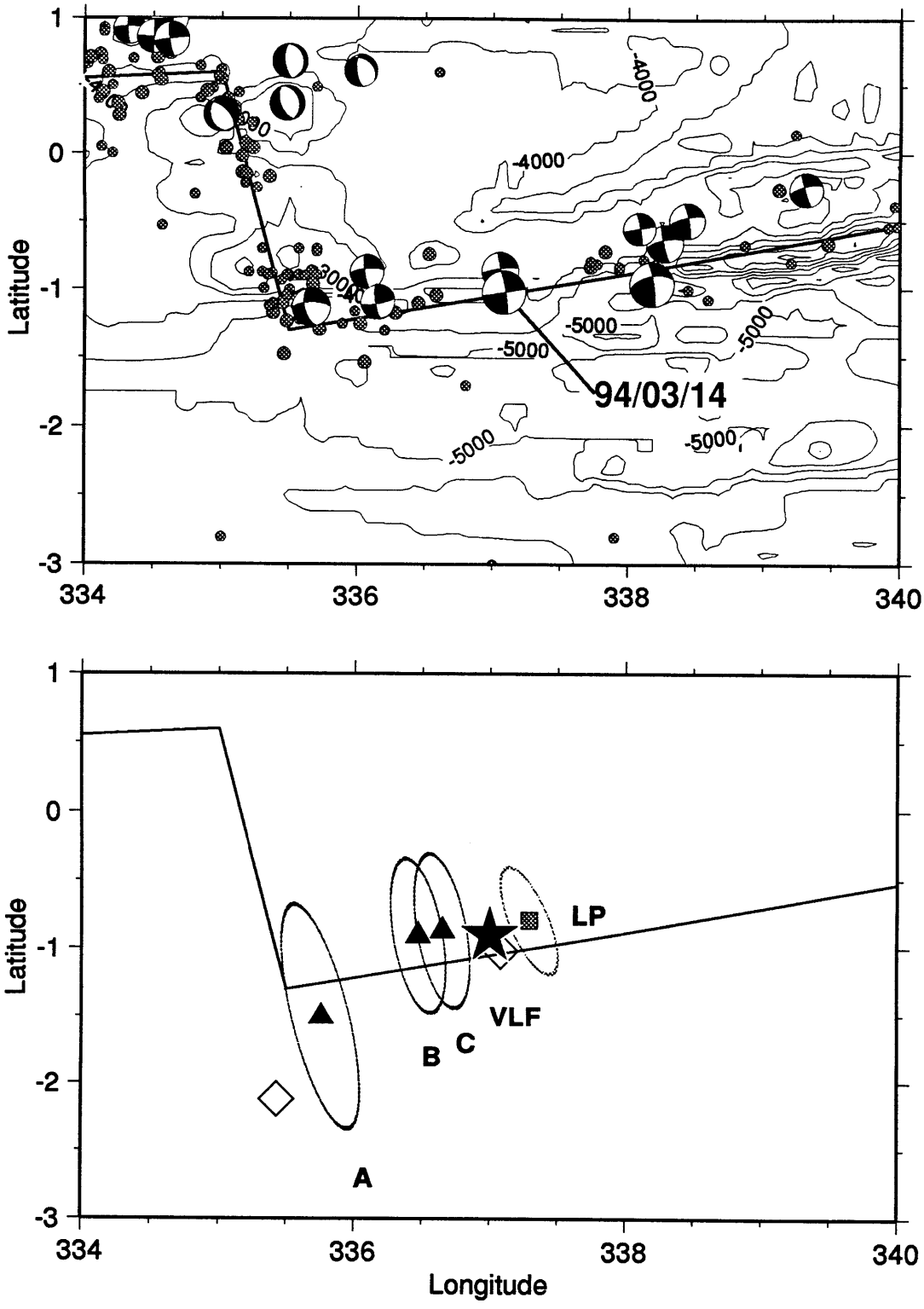

Figure 6.8

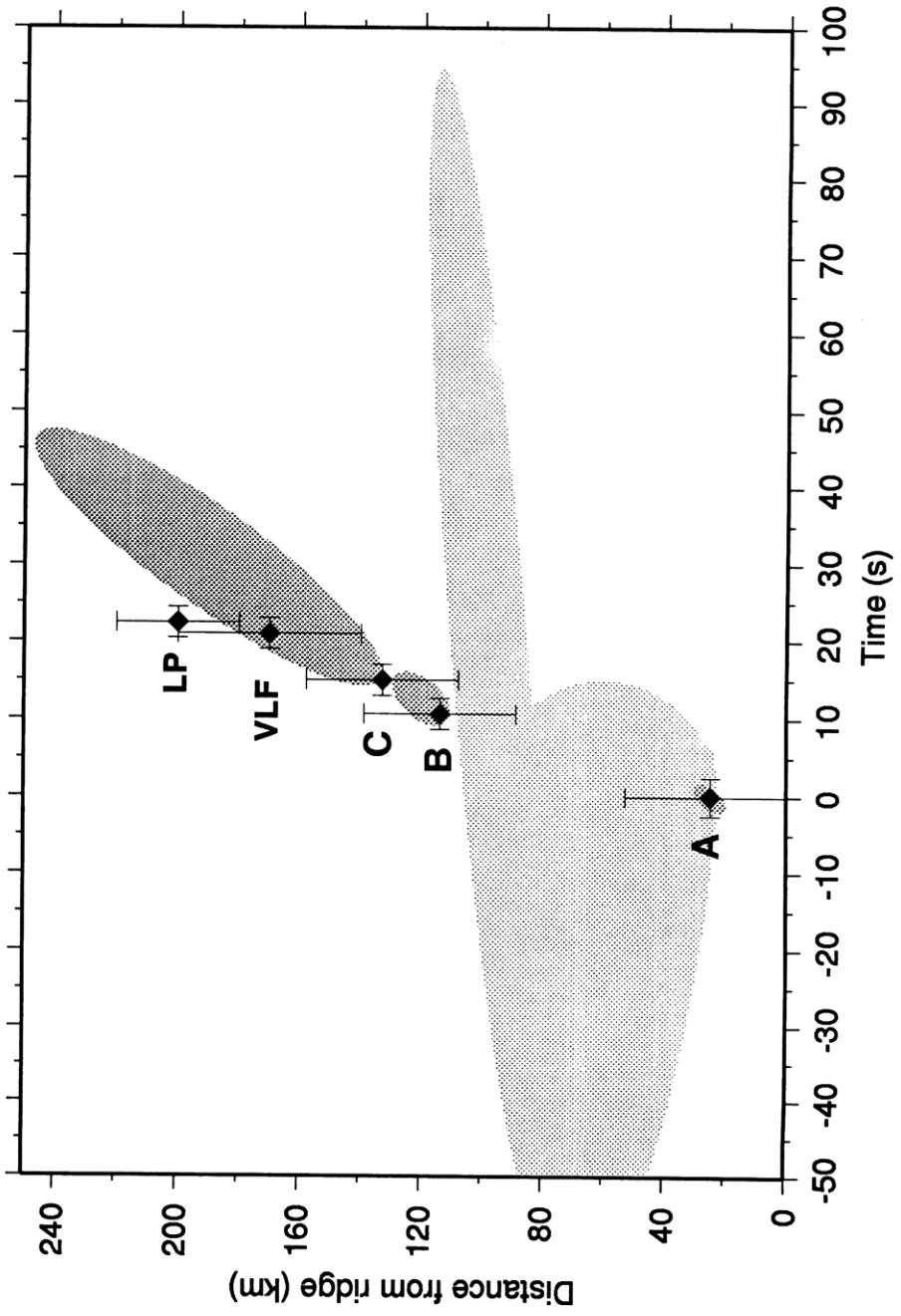
LP
VLF
C
B
A
Distance from ridge (km)
240
200
160
120
80
40
0
-50
-40
-30
-20
-10
0
10
20
30
40
50
60
70
80
90
100
Time (s)

Figure 6.9

CHAPTER 7

Summary, conclusions, and open questions

Slow earthquakes, events with anomalously long durations relative to their static moment, have been known to occur for about two decades (Kanamori and Stewart, 1976), and except for the work of Beroza and Jordan (1990), and Kanamori and co-workers, have received relatively little attention. The existence of slow precursors, events with smooth moment release that do not radiate energy at high-frequencies, has been first postulated by Jordan (1991) for the 1983 Peru-Ecuador intermediate-focus earthquake. Spectra of events with long duration are enriched in low-frequencies, and we improve and develop methods (Silver and Jordan, 1982, 1983; Riedesel et al., 1989; Jordan, 1991; Gee and Jordan, 1992; Ihmlé et al., 1993) to reliably recover network-averaged source spectra at very-low frequencies.

In Chapter 2 , we present the first systematic teleseismic study of slow earthquakes, and discuss evidence that some large earthquakes may have slow precursors. We show that most events occurring on the mid-oceanic ridge-system appear to be slow events. In many cases, the amplitude spectra of ridge systems events show a strong roll-off up to 6-12 mHz, leading to large characteristic durations. From about 10 to 20 mHz, their spectra are much flatter, indicating a regular type of relatively fast rupture. In Chapter 2, we discuss in detail the sources of bias on the retrieved total scalar moment and time-shift spectra, and we conclude that the kink in the amplitude spectra is presumably related to a source, rather than to a propagation effect. It appears that the source time function of these events is dominated by both a long and short time constant, leading to the hypothesis that these events are compound events, i.e., events with both a slow and a fast type of rupture (Jordan, 1991; Ihmlé et al., 1993). In many cases, we observe that these

events have small centroid time-shifts compared to their long duration. We use Jordan's (1991) formalism to detect short-term slow precursors, without recourse to any specific model of earthquake rupture. For almost half of the events (44%), the hypothesis that these events do not require a slow precursor is rejected at the 99% confidence level.

Low-frequency spectra that require a slow precursor are of two different types, depending on whether the spectral anomaly is more developed in the amplitude or in the time-shift spectrum. First, the amplitude spectrum displays a strong roll-off that diagnoses an event's long duration, whereas the time-shift spectrum is structureless and has a small zero frequency centroid. In other words, one is faced with the difficulty of accommodating a source time function with a long time constant around a small centroid time-shift. This type of behavior is observed for many ridge-system events, most notably on the East Pacific Rise and the Chile Rise transform, but also for the 1983 Peru-Ecuador intermediate-depth focus earthquake (Jordan, 1991). The second diagnostic is a significant upward curvature of the time-shift spectrum at very-low frequencies, suggesting that the time centroid of the long duration component is earlier that the main shock centroid. Examples of this type include the spectra for the great 1989 Macquarie earthquakes. Any conclusion on that type of behavior requires the reliable recovery of very low-frequency spectra.

In Chapter 2, we study the low-frequency properties of events of the mid-oceanic ridge systems. It is desirable to systematically study other populations of shallow earthquakes in continental regions and subduction zones. Using methods similar to those employed in Chapter 2, Harabaglia (1993) found that deep and intermediate events appear to be fast, regular, events that do not require any precursors. His findings are consistent with numerous studies of deep and intermediates earthquakes (e.g., Vidale and Houston, 1993). This type of comparison is important to further assess possible sources of propagation related biases, as well as differences in source characteristics.

In order to further understand the mode of strain release during events with long duration, we focus, in Chapter 3, on expanding the spectral recovery method to higher frequencies. We present a narrow-band cross-correlation technique, similar to Gee and Jordan's (1992) approach, that allows us to recover network-averaged source spectra up to 50 mHz. The spectral recovery procedures employ synthetic seismograms corrected for low-degree aspherical structure using recent tomographic models. We find an excellent agreement between the normal modes and the traveling wave methodologies in the band 1-11 mHz, indicating that the averaging procedures efficiently reduce various types of scattered signals.

We develop an algorithm to invert network-averaged spectra (1-50 mHz) for the source time function of an event. Applications to events with known source time functions, such as the 1992 Landers and the 1994 Northridge events, indicate that our results compare well with time-domain waveform inversions (Kanamori et al., 1992; Wald and Heaton, 1994; Wald et al., unpublished abstract). In contrast to time domain methods, our spectral inversion algorithm is well suited to study events with long duration, and satisfies the low-frequency characteristics of events. This is demonstrated in Chapter 4, where we analyze in detail the rupture process of the 1992 Nicaragua slow earthquake. Our data suggest that a significant part of the total scalar moment of the event is released by a slow rupture, in a velocity strengthening regime, involving shallow subducted sediments.

In contrast to the 1992 Nicaragua event, very low-frequency spectra of the great 1989 Macquarie earthquake require a slow precursor (Chapter 5). Although sources of bias cannot be entirely ruled out, we are unable to find reasonable alternatives that could satisfactorily explain the spectral anomaly observed on both the vertical and the horizontal components. The low-frequency radiation of both the vertical and the transverse components require that the earthquake's main shock was initiated by a slow, smooth precursor with significant moment release more than 100 s prior to the event's

high-frequency origin time. The source time function satisfies observations from normal modes, surface waves and long period body waves. In particular, it satisfies the lack of an observable precursor in front of *P* waves at nearby high-gain stations. In Chapter 6, we study the rupture initiation of the 14 Mar 1994 Romanche transform earthquake. The spectra of this event cannot be satisfied if all the moment is released after the onset of brittle rupture. Inspection of broad-band seismograms reveals that a 20 s long ramp precedes the onset of the main shock, which suggests that we may be observing the time domain signature of a slow precursor. Unfortunately, the location of the precursor relative to the main shock is difficult to assess, and methods are needed to better characterize the low-order spatial moments of earthquake ruptures. Also, special effort should be devoted to discovering time domain signatures of slow precursors or quiet earthquakes.

Some speculations are presented in Chapter 2 and 5 concerning the physical mechanism of slow motion on faults that could account for the inferred low rupture velocities of slow earthquakes and slow precursors. The location of the slow precursor relative to the main ruptures is not directly constrained by our data, but may involve a region of transitional frictional behavior at the base of the seismogenic layer in the oceanic lithosphere. In addition to the two cases presented here, known examples of slow precursors involving the oceanic lithosphere include the great 1960 Chilean earthquake (Kanamori and Cipar, 1974; Cifuentes and Silver, 1989), the 1970 Colombian and 1963 Peru-Bolivia deep-focus earthquakes (Dziewonski and Gilbert, 1974), and the 1983 intermediate-focus event on the Peru-Ecuador border (Jordan, 1991). Although slow earthquakes have been known to occur for almost two decades (Kanamori and Stewart, 1976), little is known about the physics of infraseismic rupture processes, and its implication for earthquake prediction must be assessed. More laboratory data is needed on the frictional properties of geological materials at high temperature, and high

confinement pressure, together with a better understanding of the rheology of olivine and serpentine.

Numerical experiments with state and rate variable friction laws (Dieterich, 1978, 1986; Tse and Rice, 1986; Marone et al., 1991) could be carried out in order to explore what range and combination of parameters could yield slow ruptures. A particularly relevant question is to know if infraseismic events can exist *per se*, without being accompanied by any regular type of rupture, as suggested by Beroza and Jordan (1990). In other words, do quiet earthquakes exist ? Does smooth and slow moment release happen over a sufficiently short interval to be seismologicaly significant ?

Other questions come to mind, such as: Does the moment release during a slow precursor scale with the total moment of an event ? How does the slow precursor's slip scale with its lateral dimensions ? And a key problem is to locate a slow precursor relative to the main shock and to try to assess its areal dimensions. Our work so far suggests that the study of the frequency dependence of the event's very-low frequency centroid may help resolve part of the question. To our knowledge, this type of work has never been attempted before and could yield promising insights into the rupture initiation process.

Improvements both in the inversion algorithm and in the theoretical transfer functions are necessary to reliably address this point. Refinements of our methodologies will aim at including higher spatio-temporal moments of the rupture process, such as directivity. The mechanism spectrum of an event could be obtained over a wide range of frequencies, and, in principle, could be inverted for the history of rupture of complex events. In Appendix A, we show how waveforms can, in principle, be incorporated into the spectral inversion. This may be one of many possible ways to extend the bandwidth of spectral data. The techniques presented in Chapter 3 are not limited to synthetics computed via

normal mode summation. Extension of the spectra to higher frequencies can be achieved using body wave transfer functions calculated with ray theoretical methods, such as the WKBJ (Chapman, 1978), or reflectivity (Fuchs and Müller, 1971) methods. At very-low frequencies, non-asymptotic normal-mode theories can be employed to compute seismograms that incorporate mode-coupling effects (Lognonné, 1991; Park, 1986; Dahlen, 1987). At low-frequencies, methods exist (Tromp & Dahlen, 1992; Woodhouse and Wong, 1986) that account for the scattering of surface waves by lateral heterogeneity. Any improvement in our knowledge of the 3D lateral heterogeneity of the earth, as well as theoretical advances in the computation of theoretical seismograms, can easily be built into our spectral recovery procedures.

A main goal of earthquake seismology is to understand the initiation and nucleation of large earthquakes. With the increased availability of high-quality digital data (e.g., GSN, IDA, GEOSCOPE, MEDNET, CDSN, GEOFON, POSEIDON, regional and global networks), we feel that fundamental aspects of the earthquake process still await discovery. The primary question remains understanding if earthquakes are short-term predictable. Our work so far suggests that this may be the case for some events involving the rupture of oceanic lithosphere, and we hope that the methodologies presented here will open new avenues of research in the field of rock mechanics and earthquake seismology.

APPENDIX A

Details of the spectral inversion for the source time function

A.1 Spectral inversion

The amplitude and time-shift spectra of large earthquakes are retrieved from 1 to 50 mHz through network averaging procedures in narrow frequency bands centered at $\{\omega_m; m = 1,..., M\}$. The azimuthal averaging involved in retrieving these data allow us to approximate the excitation of low-frequency waves by a point source with time varying moment release function $f(t)$and time independent source mechanism $\hat{\mathbf{M}}$ with unit Euclidean norm. $f(t)$ is defined as:

$$f(t) = \frac{1}{\sqrt{2}} \int_V \hat{\mathbf{M}} : \dot{\Gamma}(\mathbf{r},t)\, dV(\mathbf{r}), \tag{A.1}$$

where $\dot{\Gamma}(\mathbf{r},t)$ is the stress glut rate tensor (Backus and Mulcahy, 1976). We write its Fourier transform:

$$\int_{t_*}^{\infty} f(t) e^{-i\omega(t-t_0)} dt = M_T(\omega) e^{-i\omega\Delta t(\omega)}, \tag{A.2}$$

where ω is the angular frequency, $M_T(\omega) \geq 0$ is the amplitude spectrum, and $\Delta t(\omega)$ is the phase-delay spectrum, which is defined relative to the high-frequency origin time t_0. The source time function is zero prior to the origin time of moment release t_*, which may differ from t_0 (Jordan, 1991). We assume a constant source mechanism across the frequency band and no backslip on the fault, i.e. $f(t) \geq 0$.

We would like to take advantage of the linear relationship between a function and its Fourier transform and rewrite the amplitude and time-shift spectra in terms of real and imaginary parts, that we denote respectively by $A(\omega)$ and $B(\omega)$. Defining the phase factor as $\phi(\omega) = -\omega\, \Delta t(\omega)$, we have

$$A(\omega) = \pm\sqrt{M_T^2 \cos^2 \phi(\omega)}$$
$$B(\omega) = \pm\sqrt{M_T^2 \sin^2 \phi(\omega)}, \qquad \text{(A.3)}$$

where the choice of sign is imposed by $\phi(\omega)$.

Let us denote by $\{A_m, B_m, m = 1,...,M\}$ the data observed at discrete frequencies ω_m, which need not be equally spaced, and by $\{f_n, n = 1,...,N)$ the discretized source time function, sampled at intervals Δt. It is then easy to obtain

$$A_m = \sum_{n=1}^{N} f_n \cos(\omega_m[\Delta t\,(n-1) - t_*])\,\Delta t$$
$$B_m = \sum_{n=1}^{N} f_n \sin(\omega_m[\Delta t\,(n-1) - t_*])\,\Delta t \qquad \text{(A.4)}$$

where we have referenced time to the high-frequency origin time t_0 and have allowed for an arbitrary start of moment release t_*. Since we do not allow for slip reversals, we have the following inverse problem:

$$\mathbf{d} = \mathbf{G}\,\mathbf{f} \quad \text{with } \mathbf{f} \geq \mathbf{0}. \qquad \text{(A.5)}$$

Were it not for the positivity constraint on the model space, the solution, in a least-squares sense, would be related to the discrete inverse Fourier transform of the spectral data.

Although the above inverse problem can be solved using a L_1-norm formalism (linear programming, see Press et al, 1992), we prefer to use a quadratic programming technique. An L_2 approach allows us to minimize a measure of data misfit, together with a measure of solution roughness. The data consist of low-frequency spectra with finite bandwidth (up to 50 mHz) and it is intuitively appealing to impose smoothness constraints on the model. In other words, we do not expect to resolve fine features of the source time function. We will elaborate more on this later in this Appendix, and we will see that the smoothing operation is not only appealing but essential in order to obtain meaningful results.

We define roughness as (e.g. Constable et al., 1987; Rodi and Berryman, 1991):

$$R_1 = \int (\frac{df}{dt})^2 dt$$
$$R_2 = \int (\frac{d^2 f}{dt^2})^2 dt \qquad \text{(A.6)}$$

For practical purposes, an equivalent discrete representation is based upon the difference rather than the differential operator. We write:

$$R_1 = \sum_{n=2}^{N} (f_n - f_{n-1})^2$$
$$R_2 = \sum_{n=2}^{N-1} (f_{n+1} - 2f_n - f_{n-1})^2 \qquad \text{(A.7)}$$

In matrix notation:

$$R_k = \mathbf{f}^T \mathbf{W}_m \mathbf{f}, \qquad \text{(A.8)}$$

with k = (1,2) standing for the order of derivative and $\mathbf{W}_m = \mathbf{R}^T\mathbf{R}$. We assess the goodness of fit of model prediction versus data with the usual least-squares criterion:

$$X^2 = \sum_{i=1}^{M} (\frac{d_i - G_{ij} f_j}{\sigma_i})^2 \qquad j = 1,\ldots,N \qquad \text{(A.9)}$$

where σ_i is the uncertainty of the i[th] datum . If the uncertainties are due to a zero-mean Gaussian process, and provided the errors are statistically independent, then X^2 will be χ^2 distributed. Finally, the functional that is minimized is a weighted combination of prediction error and solution roughness:

$$U = [\mathbf{d} - \mathbf{G}\mathbf{f}]^T \mathbf{W}_d [\mathbf{d} - \mathbf{G}\mathbf{f}] + \mu \, \mathbf{f}^T \mathbf{W}_m \mathbf{f}, \tag{A.10}$$

where $\mathbf{W}_d = \text{diag}\{\sigma_j^{-2}, j = 1,...,M\}$ is the data covariance matrix that is obtained from the observed spectra, and where we assume that errors in the data are not correlated. We will call the trade-off parameter $\mu > 0$ the regularization parameter in the spirit of Tikonov and Arsenin (1977) who introduced the notion of regularization as a way to handle ill-conditioned inverse problems. Small values of μ (rough solutions) lead to small values of X^2. Smooth solutions (μ large) are obtained at the cost of a larger misfit.

In order to present the inverse problem in a concise way, let us introduce the augmented data kernel matrix $\mathbf{G}'$ and the augmented data vector $\mathbf{d}'$ such as:

$$\mathbf{G}' = \begin{bmatrix} \tilde{\mathbf{W}}_d \mathbf{G} \\ \mu^{1/2} \mathbf{R} \end{bmatrix} \quad \text{and} \quad \mathbf{d}' = \begin{bmatrix} \tilde{\mathbf{W}}_d \mathbf{d} \\ \mathbf{0} \end{bmatrix}, \tag{A.11}$$

with $\mathbf{W}_d = \tilde{\mathbf{W}}_d^T \tilde{\mathbf{W}}$. We finally write:

$$\min \|\mathbf{d}' - \mathbf{G}'\mathbf{f}\|^2 \quad \text{subject to } \mathbf{f} \geq \mathbf{0}. \tag{A.12}$$

The non-linear minimization is solved iteratively using a computer code written by Parker and Stark, which is based on Lawson and Hanson's (1974) original non-negative least-squares algorithm. If necessary, the regularization parameter μ can be made time dependent; it is then replaced by a regularization vector μ.

A.2 Waveform constraints

The algorithm presented here inverts spectral data, but can be generalized to also include waveform constraints on the solution. In this section, we briefly show how this can be implemented. A far-field seismogram can be written as the convolution (Aki and Richards, 1980):

$$s(t) = \int_{-\infty}^{+\infty} f(t')g(t-t')dt' \tag{A.13}$$

where $f(t)$ is the source time function and g(t) an appropriate transfer function. In the discrete case, one has:

$$s_k = \sum_{n=1}^{K} f_n \, g_{k-n} \, \Delta t \tag{A.14}$$

where $(K-1)\Delta t = t_0 - t_*$ and s_k is the discretized waveform. The waveform constraint is linear and can be implemented by adding additional rows to the augmented data vector, and to the augmented data kernel (A.11). The questions that need to be addressed are that of the weighting of waveform constraints relative to the spectral misfit and roughness criteria and that of the appropriate scaling of waveform data.

The inversion algorithm in its present form allows only for the special case that no time-domain precursor can be observed in front of the first arrival *P* wave (see Ihmlé et al., 1993). The waveform in this case is the null vector and the waveform constraint is given a large weight and minimized together with data misfit and roughness. Each row of the integral constraint equations is normalized to its peak value prior to weighting. The waveform

constraint is designed to account for the lack of observable time-domain precursor and offers superior smoothing relative to classical first or second derivative regularizations. The latters have ramps with inappropriate spectral characteristics and lead to observable signals above the noise level in front of *P* waves.

A.3 Properties of the inversion algorithm

The sampling theorem of the Fourier transform states that the maximum achievable time resolution is given by $\Delta t = 1/(2*f_{Nyquist})$, where $f_{Nyquist}$ stands for the high-frequency cut-off of the spectrum. However, the positivity of $f(t)$ in fact halves the time resolution so that $\Delta t = 1/(4*f_{Nyquist})$. This can be understood if we consider that one doubles the period of a monochromatic sinusoidal wave by taking its absolute value. For example, spectra with a cut-off at 50 mHz, possess a nominal time resolution of 5 seconds with positivity constraint, and 10 seconds without it. This fact is displayed in Figure A.1, where spectra are generated up to 50 mHz by Fourier transforming unit Dirac impulses separated by 10, 5 and 3.3333 seconds. At spacing greater or equal to 5 seconds, the magnitude and phase of the impulses are correctly recovered by the inversion algorithm (no regularization applied). At spacing less than 5 seconds, the input $f(t)$ is no longer recoverable and the total moment and phase of $f(t)$ is partitioned into spikes 5 seconds apart. In the absence of smoothing, the sampling interval of $f(t)$ can therefore be chosen arbitrarily, provided it is smaller that the nominal time resolution imposed by the spectral data. The second intrinsic time constant of the problem is that times larger than the inverse of the frequency spacing cannot be resolved.

This points out a property of the unregularized (rough) model: in the limit of infinitesimal sampling intervals, basis functions of the solution are Dirac functions. Similar

characteristics appears in problems occurring in MT (Parker, 1980) and resistivity sounding (Parker, 1984). Thus, in the infinitesimal sampling limit, a Dirac function can be recovered despite the band-limited nature of the spectral data. It is instructive to keep in mind that the Fourier transform of the theoretical spectral data used in the inversions of Figure A.2 is a sinc function with nodes 20 seconds apart. In other words, the positivity constraint produces compact functions and eliminates leakage of energy in the time-domain. At finite sampling rates, the natural basis function of the model is the isosceles triangle, the Fourier transform of which is the sinc^2 function. The sinc^2 function has an asymptotic ω^{-2} decay rate.

In the case of a large earthquake, source process times are on the order of a few seconds to hundred of seconds for truly large events. Minimum X^2 solutions obtained from spectra of such events would be rough to the point of being physically unreasonable. It is therefore not only necessary to regularize the problem because it is ill-conditioned, but also as a means of obtaining meaningful results. The regularization plays the role of an optimal filter (see a discussion in Press et al., 1992, p. 801, of the conceptual relationship between Wiener filtering and the solution of a regularized linear inverse problem).

However, one is entitled to ask the following question: what is the rationale that allows us to decide that a rough solution, composed of distinct narrow (Dirac) impulses, is less reasonable that a smooth model ?

In the case of no-backslip, the moment release function of an earthquake is a non-decreasing function of time. During a large earthquake, the rupture front propagates over the fault plane and the moment release rate function is likely to be a continuous function of time, however rough. Periods of very low moment release can occur between pulses like subevents (e.g., among many others, the 1987 Gulf of Alaska intraplate event, Hwang and

Kanamori (1992); the 1992 Landers earthquake (Wald and Heaton, 1994). From an observational point of view, teleseismic data, such as first arrival body waves, contain, at frequencies above about 1 Hz, only limited information about the source process, mainly as a consequence of intrinsic attenuation and high-wavenumber scattering. Therefore, in practice, one can at best resolve narrow impulses separated at 1 second interval. See for example Ekström (1987), who has documented source time functions that he obtained from the inversion of broad-band first arrivals. Although source time functions recovered by these types of time domain inversion methods show features at the 1 second level, it is uncertain whether such details are resolvable by the data. Experience shows that subevents of large earthquakes (i.e., with $M_w > 6.2$) always have a resolvable finite width of at least a few seconds. The smallest earthquake for which the spectral recovery methods can be reliably applied is around $M_w > 6.5$. Scaling relationship between size and duration predict that such an event should have a source process time of about 10 seconds (Kanamori and Given, 1981).

Hence, in many cases, rough solutions are not likely to be reasonable models and it appears that regularization is justified by our spectral data. A high-frequency cut-off at 50 mHz seems to be adequate for source studies of large earthquakes, except maybe for some large deep events that are composed of multiple short pulses of moment release. In the view of inverse theory, regularization is justified by the ill-posedness of the problem (Tikonov and Arsenin, 1977; Rodi and Berryman, 1991). The choice of the regularization parameter is non-unique and can be further addressed by inspection of seismic data.

A.4 Error estimation of the model

A jackknife experiment

The non-linear nature of the inverse problem precludes a rigorous analysis of the solution errors. In contrast to the linear case, a formal mapping of data variance to estimates of model variance cannot be carried out (Menke, 1984). Resampling techniques, such as the jackknife or the bootstrap, are useful in this respect, because they rely on the notion that an experiment can be repeated by constructing multiple data sets based on the measured data set. In addition, resampling methods do not make assumptions about the probability distribution of the data (Efron and Gong, 1983; Tichelaar and Ruff, 1989; Thomson and Chave, 1991). Because of its simplicity, we use the "delete-one" jackknife in order to estimate, at each time sample, the variance of our model:

$$\mathrm{var}\{\hat{f}_{all}\} = \frac{N-1}{N}\sum_{i=1}^{N}\left[\hat{f}_{(i)} - f_{(\bullet)}\right]^2, \tag{A.15}$$

with

$$f_{(\bullet)} = \frac{1}{N}\sum_{i=1}^{N}\hat{f}_{(i)}. \tag{A.16}$$

We are free to choose the strategy to obtain the delete-one estimates that we denote by $\hat{f}_{(i)}$. Two obvious possibilities are either to remove the i^{th} spectral point, or to remove the i^{th} station and recompute spectral averages, and in both cases reinvert the spectral data set to obtain the delete-one estimate. It is clear from the spectra for the Nicaragua 1992 event (Chapter 4, Figure 4.2) and other events that deleting a spectral point would not appreciably affect the outcome of the inversion and that, in choosing such a strategy, we would

underestimate the variance of our model $\mathrm{var}\{\hat{f}_{all}\}$. We choose therefore to remove the i^{th} station to obtain N estimates of the source time function of the event for a given value of the regularization parameter,

$$\hat{f}_{(i)} = \{\text{with ith station removed}\}.$$

Its has been shown that the jackknife is a conservative and robust estimate of variance, even if the data are not identically distributed, provided errors are uncorrelated (see for example Thomson and Chave, 1991). We would, however, expect jackknife variances to be biased low in the case of correlated errors.

Figure A.3 displays results of the jackknife experiment for different values of the regularization parameter for the 1992 Nicaragua event. The spectra for this event are shown in Chapter 4. Because of the limited number of stations (N=12), one cannot readily interpret details of the jackknife error estimates. One sigma errors are on the order of 2% or less at any given time point. As expected, errors decrease as smoothing increases: in the limit of infinite smoothing, errors become independent of the data and tend to zero. On the basis of this experiment, one cannot argue that some features are better resolved that others. Subevents of the rough solution appear to be significant, although some of them vanish as smoothing increases.

Monte Carlo Simulation

As a means of understanding further properties of the solution and its error distribution, we carry out a Monte Carlo simulation of the error process. The strategy adopted is to perturb each element of the data vector, by an amount specified by a zero mean Gaussian noise process $\delta d_i \sim N(0, \sigma_i)$, and to reinvert the new data $\mathbf{d}' = \mathbf{d} + \delta\mathbf{d}$. For a given value

of the regularization parameter, the Monte Carlo calculation for N simulations yields an average model and a model covariance matrix, defined in the usual way:

$$\bar{f} = \frac{1}{N}\sum_{i=1}^{N} f_i \,, \tag{A.17}$$

$$C_{ij} = \frac{1}{N-1}\sum_{i}\sum_{j}(f_i - \bar{f})(f_j - \bar{f}) \,. \tag{A.18}$$

Some representative examples are given in Figure A.4 and A.5. Again, one sigma errors are 2% or less and decrease with increased smoothing. There is a good correspondence between the delete-one jackknife and the Monte Carlo variances. In fact, the jackknife strategy adopted here amounts to perturbing the data vector prior to inversion. If we had used a larger number of stations in the jackknife experiment, we would have expected both methods to give identical results.

At low values of the regularization parameter, model covariance matrices display large side-lobe oscillations with a constant period of 20 seconds (Figure A.4). This is an effect of the frequency cut-off of the spectral data at 50 mHz, and is related to the classical Gibbs phenomenon of Fourier analysis. Relevant source time functions show distinct pulses at 20 seconds intervals which, according to their computed standard deviations, are well resolved. However, analysis of the covariance matrix allows us to reject solutions with significant side-lobes, an indication that individual peaks and throughs of the solution are correlated. Additional smoothing is then necessary at the cost of spreading out the median ridge of the covariance matrix. In the case of excessive smoothing, information is spread out over too many model points and becomes independent of the data. Figure A.3 and A.4 illustrate the classical trade-off between variance and resolution. The structure of the covariance matrix can be used as a diagnostic tool to decide of an optimal amount of smoothing.

These experiments point out a number of issues. First of all, it appears that variance estimates are poor indicators of the resolvability of features of the solution. This is probably due to statistically correlated errors in the data leading to biased model errors. Secondly, the non-uniqueness of the choice of the regularization parameter can be satisfactorily resolved by considering stable features of the solution. Smoothing is increased until elements of the model not constrained by the data are eliminated. This procedure (Occam's razor) has been advocated by Constable et al (1987) in the context of smoothest inversion of electromagnetic sounding data .

Figure captions

FIGURE A.1. Synthetic test of the inversion's time resolution. The abscissa is in seconds, the ordinate is in arbitrary units. In this numerical test, spectral data are produced at 2 mHz intervals from 1.5 to 50 mHz. 20% error bars are ascribed to the total moment spectra, and time-shift spectra are attributed 4 s error bars. The source time function is sampled at 0.5 s from 0 to 30 s, and the regularization is not applied ($\mu = 0$). In *panel A*, the inversion correctly recovers the input spike, both in amplitude, given by the horizontal broken line, and location, indicated by the black arrow. In *panel B* and *C*, impulses separated by 10 and 5 s, respectively, are well recovered. In *panel D* , however, the four input impulses at 3.333 s interval are not recovered, but are distributed over 3 unequal spikes, separated by 5 s, which is the nominal time resolution obtained from spectra with a high-frequency cut-off at 50 mHz. In all cases, χ^2 , the misfit to the spectral data, is vanishingly small.

FIGURE A.2. Synthetic test with a boxcar. The input boxcar function starts at t = 10 s, and has a length of 50 s. It is indicated by the dashed line. In this numerical test, spectral data are produced at 2 mHz intervals from 1.5 to 50 mHz. 20% error bars are ascribed to the total moment spectra and time-shift spectra are attributed 2 s error bars. The source time function is sampled at 1 s. χ^2 is computed from the misfits to the spectral data. When no regularization is applied, the recovered source time function is composed of spikes. First derivative regularization is applied in the other cases. At $\mu = 10$, the boxcar's shape is well recovered. The small oscillations with 10 s period are related to the Gibbs phenomenon of Fourier analysis. At $\mu = 10^6$, large oscillations with 20 s period are visible. At $\mu = 10^7$, too much smoothing is applied and the data misfit rises. In the latter case, the solution becomes independent of the data and the total scalar moment of the source time function diminishes.

FIGURE A.3. Delete-one jackknife error analysis. We used the amplitude and time-shift spectra of the 1992 Nicaragua earthquake in this experiment (see Chapter 4, Figure 4.2). In each panel, the top part is the average source time function and the lower part is the 1-σ error bars obtained from the jackknife variance analysis, which are on the order of 2% or less. Note the different vertical scales. The regularization parameter used in the inversion is indicated on top of each panel (first derivative regularization). As μ increases, the solution becomes smoother, the 1-σ error bars diminish and the total area under the

moment release rate function decreases. In the limit of infinite smoothing, errors become independent of the data and tend to zero. At low values of the regularization parameter, the least well resolved feature of the source time function appears to be the small preshock in the first 8-10 seconds of moment release.

FIGURE A.4. Monte Carlo error analysis. Same plotting convention as Figure 3.2. For each value of the regularization parameter, a suite of 200 inversions has been computed. In the simulations, the data vector is perturbed according to a zero-mean Gaussian model of the error process. Results from this experiment are very similar to the jackknife results (Figure 3.3). Differences arise from the fact that the Monte Carlo numerical simulation allows to us produce an large number of models, whereas the delete-one jackknife yields only 12 different models for each value of μ.

FIGURE A.5. Contoured covariance matrices from the Monte Carlo experiment. For display purposes, each covariance matrix is normalized by its maximum value. The square root of the diagonal elements (before normalization) are the standard deviations given in Figure 3.3. At low values of the regularization parameter, large side lobes with a period of 20 s are visible and are related to the Gibbs phenomenon of Fourier analysis. At a large value of $\mu=10^5$, the covariance matrix is band-diagonal, but information is spread over many neighboring model points.

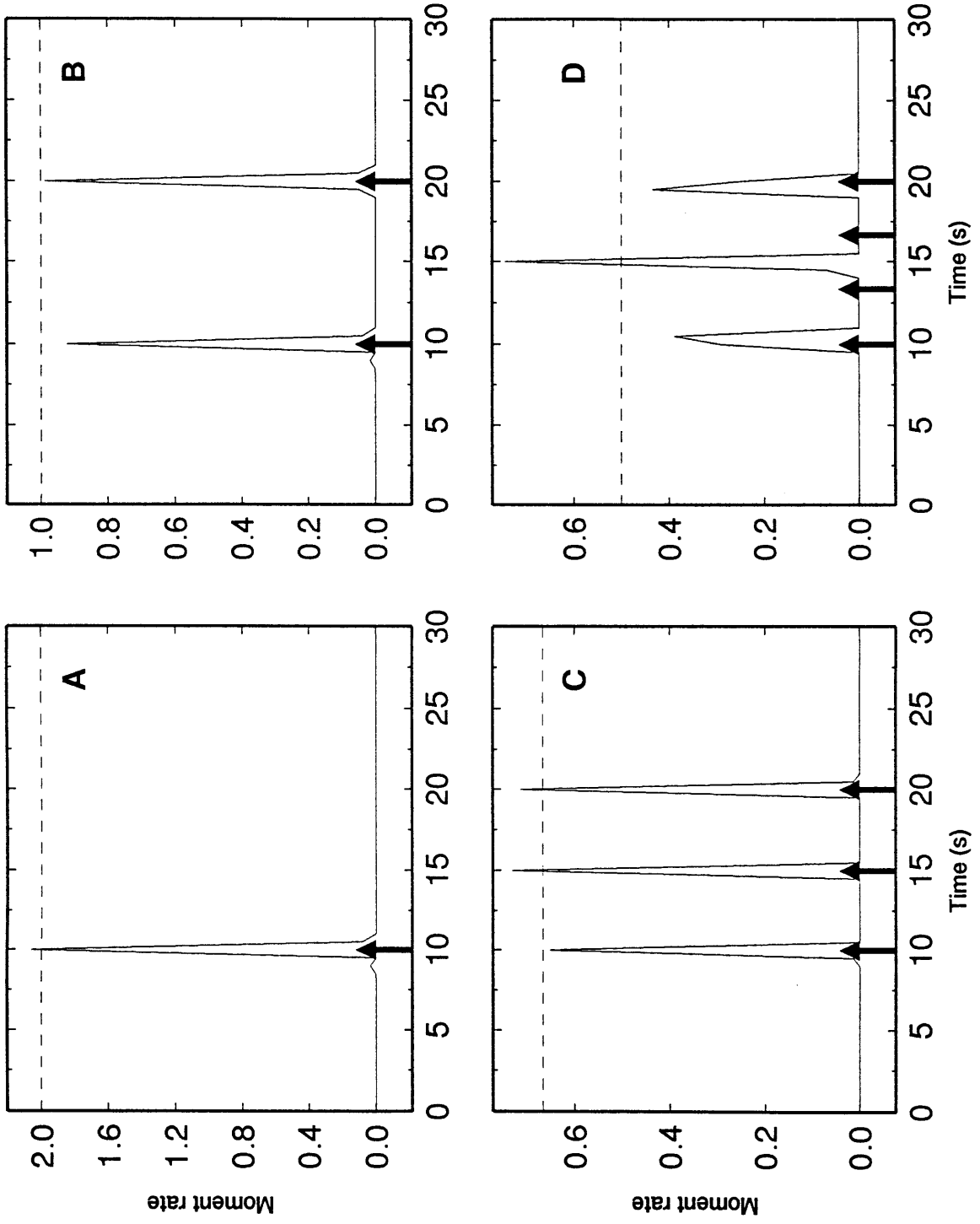

Figure A.1

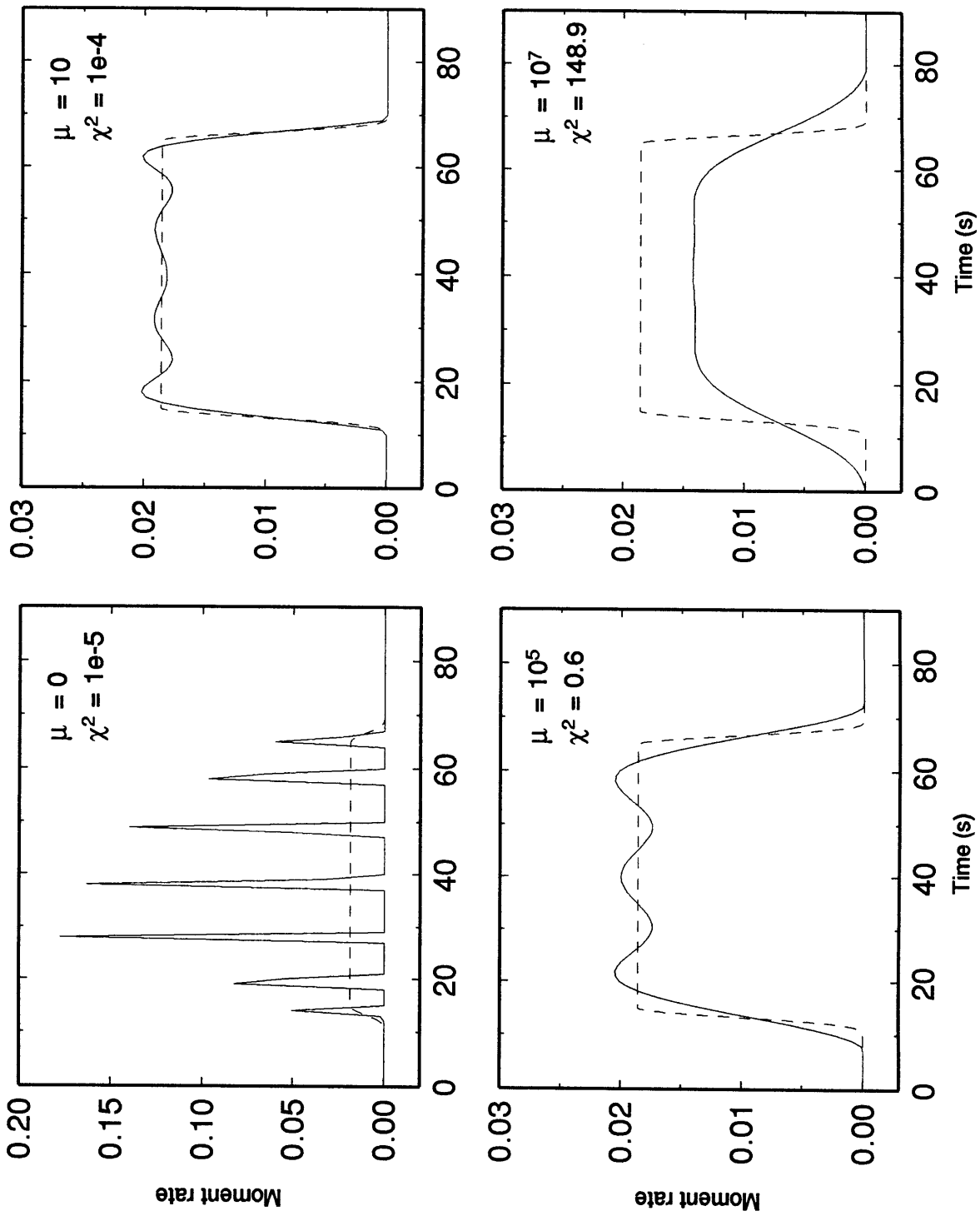
μ = 0
χ² = 1e-5
μ = 10
χ² = 1e-4
μ = 10⁵
χ² = 0.6
μ = 10⁷
χ² = 148.9
Moment rate
Time (s)
0.00
0.05
0.10
0.15
0.20
0.01
0.02
0.03
0
20
40
60
80

Figure A.2

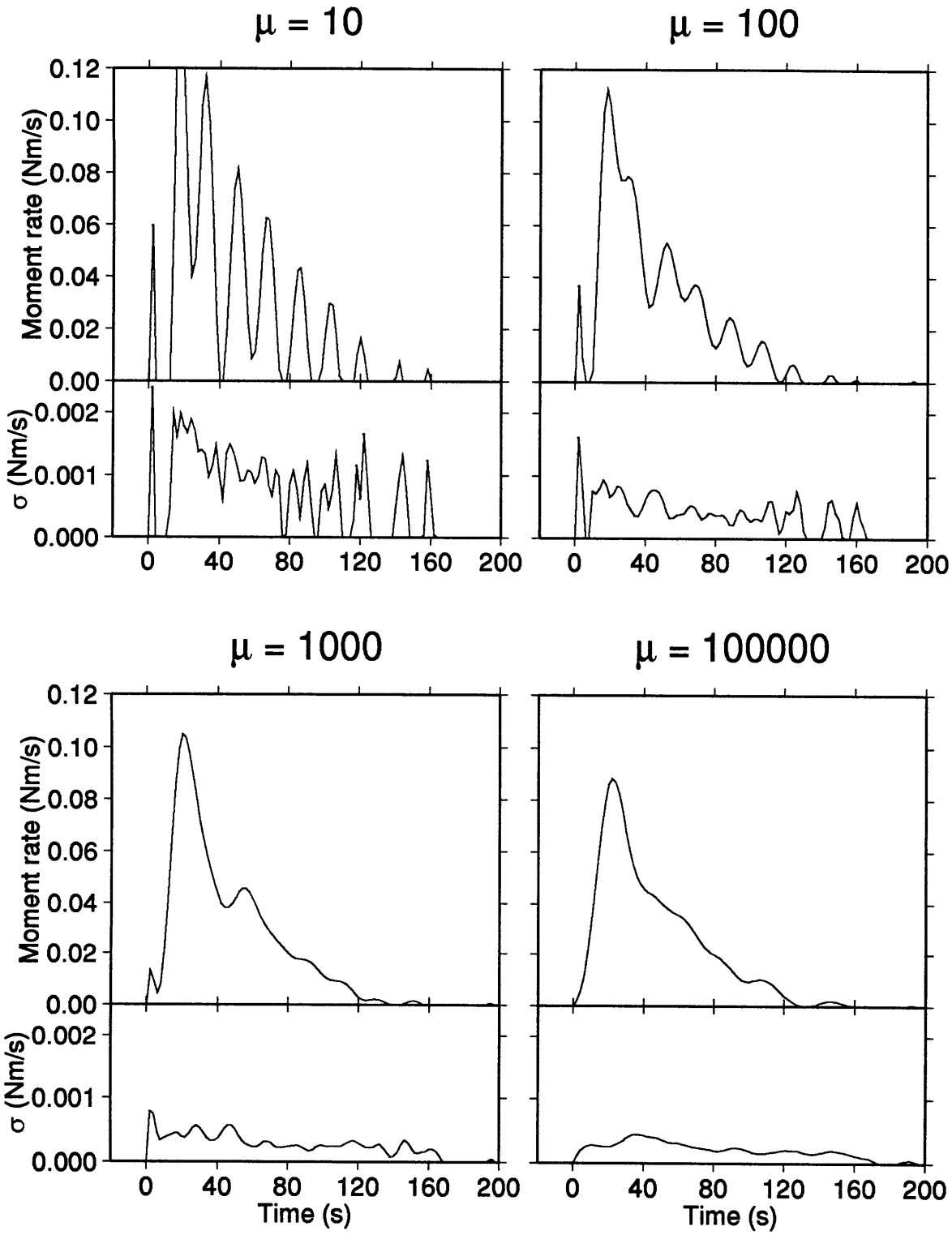
μ = 10
μ = 100
μ = 1000
μ = 100000
Moment rate (Nm/s)
σ (Nm/s)
0.12
0.10
0.08
0.06
0.04
0.02
0.00
0.002
0.001
0.000
0
40
80
120
160
200
Time (s)

Figure A.3

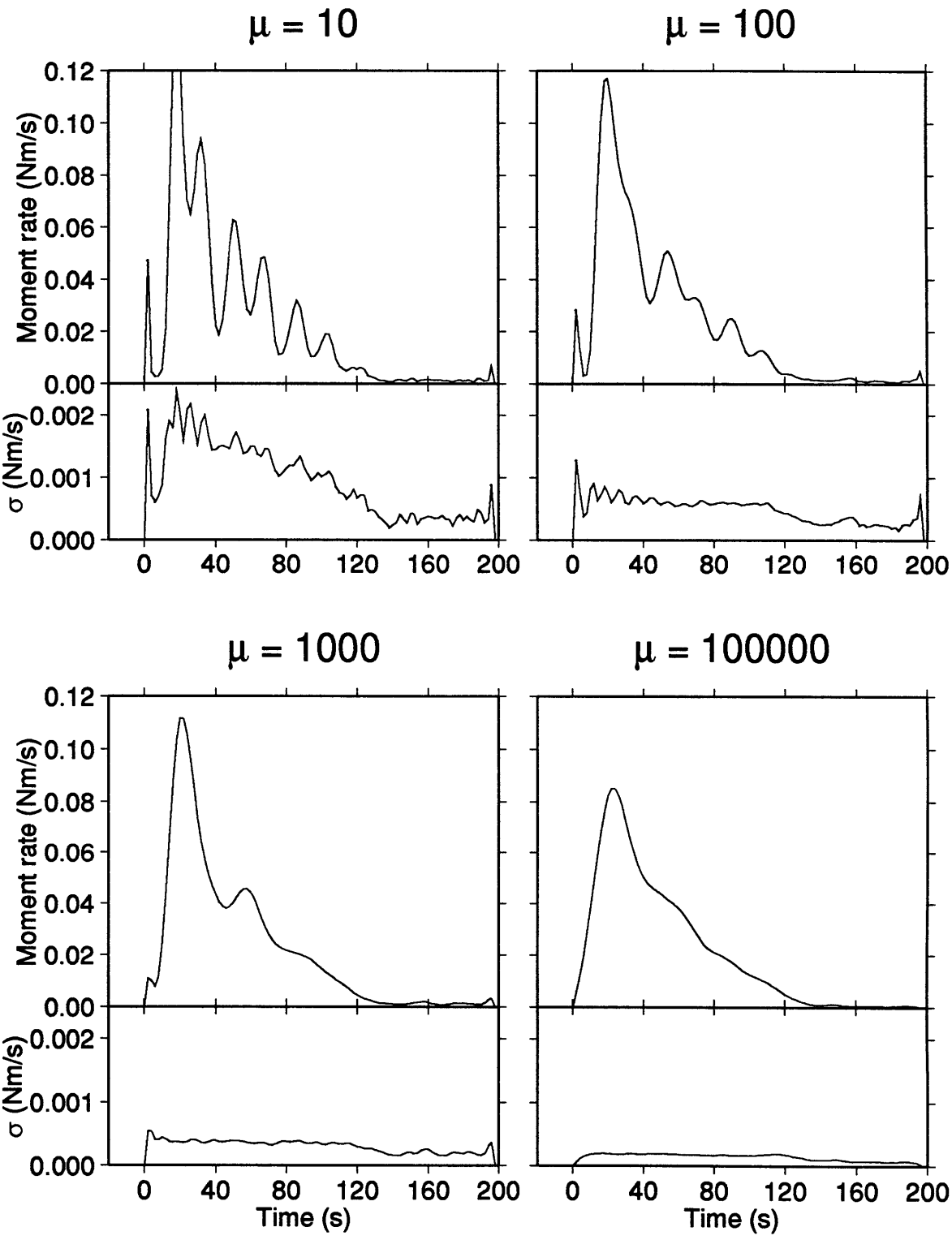
μ = 10
μ = 100
μ = 1000
μ = 100000
Moment rate (Nm/s)
σ (Nm/s)
0.12
0.10
0.08
0.06
0.04
0.02
0.00
0.002
0.001
0.000
0
40
80
120
160
200
Time (s)

Figure A.4

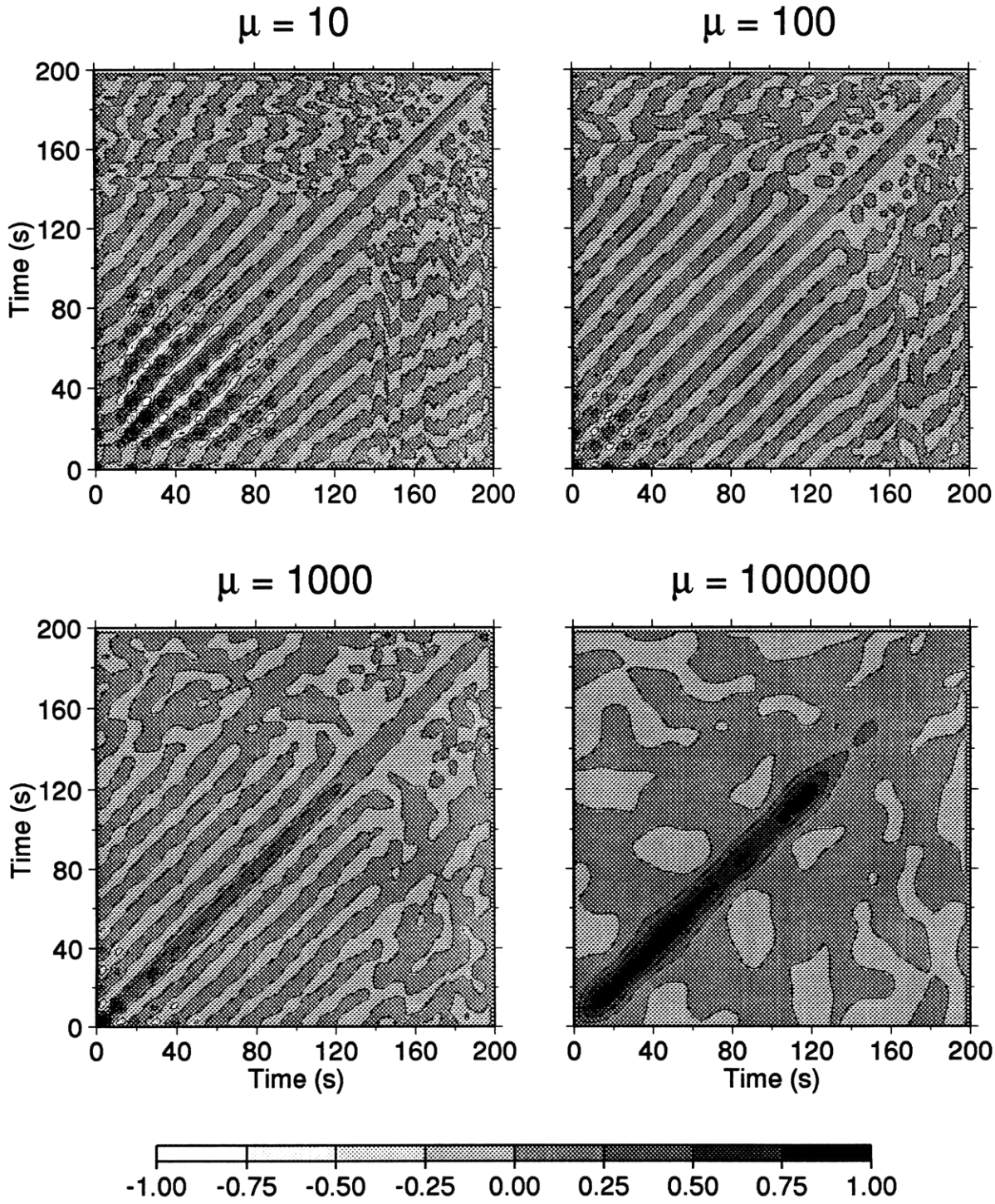
μ = 10
μ = 100
μ = 1000
μ = 100000
Time (s)
Time (s)
0
40
80
120
160
200
-1.00
-0.75
-0.50
-0.25
0.00
0.25
0.50
0.75
1.00

Figure A.5

APPENDIX B

Low-frequency parameters of events of the mid-ocean ridge systems

This Appendix is a compilation of the 68 events of the mid-ocean ridge system, which have been retained in Chapter 2. The data set covers the years 1978 to 1992[1] and comprises 57 strike-slip transform events, 8 dip-slip and 3 compensated linear vector dipole events. All earthquakes have good SNR and are not corrupted by energy from other events. The procedure for station selection is described in Chapter 2, and we keep only events for which 6 seismograms or more could be used in the normal mode techniques. This Appendix includes a table with relevant information about the set of events. Amplitude and phase-delay spectra of the events are shown in chronological order.

Total moment and time-shift spectra are displayed in the usual format. The solid line on the amplitude spectra is a fit between 1-9 mHz, yielding τ_{c1}. The dashed line is a fit from 10-20 mHz, yielding τ_{c2}. The total moment in both cases can be extracted as the zero-frequency intercepts. The scalar moment from the Harvard CMT catalog is given on the abscissa. $M_T{}^0$ obtained from 1-9 mHz spectra and the CMT moment are also listed in Table B1.

Because the Riedesel-Jordan method integrates over individual modes, it is not applied at frequencies above 11 mHz, where the mode spectrum becomes densely populated and the fundamental-mode resonance peaks begin to overlap considerably. The solid line indicates a fit to the time-shift spectra. α, the non-dimensional skewness

[1] The 14 Mar 1994 central Mid-Atlantic event is also include here. This unusual earthquake is the subject of a separate, more detailed analysis (Chapter 6).

parameter is given on the diagrams. The centroid time-shift Δt_1 is the zero-frequency intercept of the curve and the CMT value is indicated on the abscissa. Both quantities are listed in Table B1.

TABLE B1: 68 RIDGE SYSTEM EVENTS

Origin time and location are from the Harvard CMT catalog. dep is the centroid depth in km. Scalar moments are in units of 10^{18} Nm. M_0 is from the CMT catalog, $M_T{}^0$ is from this study, as well the 1σ standard error. Centroid time-shifts, Δt_1, are in seconds relative to the NEIC high-frequency origin time. Both CMT and results from this study are listed. # is the number of stations used in the normal mode techniques. M is the mechanism of the event, where S stands for strike-slip, N for normal faulting, T for thrust and C for events with a large non-double component, i.e., $\varepsilon > 0.25$, where ε is the ratio of smallest to largest eigenvalue of the CMT moment tensor (in absolute value).

Origin time						Region	lat	lon	dep	M_0 CMT	$M_T{}^0$			Δt_1 CMT	Δt_1			#	M
78	5	29	17	20	41.2	Off Coast Southern Chile	-45.20	-81.00	15	5.9	6.5	±	0.5	12.6	4.3	±	0.7	6	S
78	8	10	16	53	46.7	South Atlantic Ridge	-35.44	-17.24	15	3.6	4.6	±	0.3	9.6	4.1	±	1.2	8	S
78	12	25	23	58	1.9	Off Coast Of Mexico	10.41	-103.80	15	9.3	14.3	±	0.7	6.9	2.2	±	2.0	6	S
79	2	18	5	23	59.2	Prince Edward Is. Region	-43.43	41.85	15	4.9	5.4	±	0.3	10.2	5.0	±	0.7	6	S
79	5	16	2	27	9.9	South Atlantic Ridge	-35.26	-16.03	15	6.5	8.0	±	0.6	9.1	4.9	±	1.6	8	S
80	6	8	20	28	42.8	Macquarie Islands Region	-59.13	158.52	15	2.4	2.8	±	0.2	16.8	15.4	±	3.9	8	S
80	6	21	20	19	35.2	S'western Atlantic Ocean	-58.52	-10.90	15	5.2	6.6	±	0.5	8.8	14.0	±	3.7	6	S
80	11	1	22	52	24.1	Off Coast Jalisco Mexico	18.85	-107.57	15	4.0	5.7	±	0.4	4.5	2.6	±	1.5	7	S
81	3	6	19	43	6.3	Off Coast Centrl. Amer.	3.29	-85.99	24	11.8	17.9	±	1.5	6.8	2.7	±	3.7	6	S
81	4	27	18	17	40.0	West Of Macquarie Isl.	-57.58	147.86	10	8.2	9.0	±	0.4	6.3	1.5	±	1.3	6	S
81	5	25	5	25	38.1	"W. Coast, S. Isl.,n. Z."	-48.94	164.39	33	274.0	431.0	±	18.3	23.7	26.1	±	3.6	7	S
81	7	7	21	11	11.6	Cntr Mid-atlantic Ridge	-0.07	-18.59	10	24.6	28.5	±	2.4	13.9	17.0	±	2.7	9	S
81	8	19	22	50	57.5	Mid-indian Rise	-9.32	67.18	10	2.1	4.0	±	0.2	7.9	10.5	±	4.1	7	S
81	10	28	4	34	27.8	Easter Island Region	-32.18	-110.83	10	4.1	5.7	±	0.5	9.5	2.1	±	1.7	7	S
82	1	3	14	10	4.2	Centr Mid-atlantic Ridge	-0.96	-21.83	10	55.6	72.9	±	5.5	13.8	20.1	±	2.7	7	C
82	5	7	5	38	42.7	Sw Atlantic Ocean	-60.96	-20.62	10	35.5	50.4	±	4.4	8.2	9.3	±	2.4	11	S
82	6	6	10	20	36.2	North Atlantic Ridge	35.27	-35.84	10	3.5	6.0	±	0.5	4.7	13.8	±	2.5	8	S
82	7	7	10	43	15.3	North Of Macquarie Is.	-51.18	160.41	10	67.6	89.4	±	6.9	11.9	16.9	±	4.3	6	S
83	4	8	2	28	28.3	Arabian Sea	11.28	57.49	10	6.2	6.7	±	0.4	2.8	2.7	±	1.4	8	S
83	9	1	17	59	44.4	South Of Africa	-52.92	26.26	14	2.8	4.3	±	0.4	15.6	18.3	±	3.0	6	S
83	11	30	17	46	28.9	Chagos Archipelago	-6.35	71.75	10	405.0	549.0	±	43.0	28.5	24.7	±	2.4	10	N
83	12	3	17	43	23.7	Chagos Archipelago Reg.	-6.45	71.27	12	3.1	4.1	±	0.4	9.3	6.7	±	1.6	8	N
84	1	2	22	10	7.7	South Pacific Cordillera	-56.58	-142.42	19	5.0	6.6	±	0.6	9.8	9.6	±	1.2	11	S

TABLE B1: CONT.

Origin time						Region	lat	lon	dep	M_0 CMT	M_T^0			Δt_1 CMT	Δt_1			#	M
84	1	16	12	27	18.6	Easter Island Region	-30.94	-112.15	10	2.8	4.2	±	0.6	4.8	1.3	±	1.6	11	C
84	5	17	16	54	4.8	South Indian Ocean	-36.44	52.85	10	25.4	33.3	±	1.5	13.6	12.8	±	2.0	10	S
84	5	25	23	54	5.2	South Pacific Cordillera	-54.56	-136.54	10	5.3	5.7	±	0.5	13.1	5.6	±	0.5	10	S
84	5	26	3	59	8.4	Prince Edward Is. Region	-43.70	39.50	10	13.3	16.3	±	0.6	12.9	7.8	±	0.7	10	S
84	6	22	15	55	33.3	Southwestern Atlantic O.	-58.65	-16.00	10	3.5	4.9	±	0.4	5.4	9.6	±	3.0	8	S
84	9	17	6	41	52.9	Mascarene Islands Region	-17.49	65.50	10	2.4	3.6	±	0.2	9.4	17.9	±	4.8	6	S
84	11	1	4	48	59.2	Cent. Mid-atlantic Ridge	8.36	-38.82	10	40.3	53.3	±	3.0	9.3	9.8	±	1.6	9	S
85	1	31	4	33	4.0	"Off W Cst South Is.,n.z."	-46.49	164.64	10	3.2	3.3	±	0.3	6.4	7.3	±	2.4	7	C
85	4	7	0	19	44.4	Easter Island Cordillera	-56.25	-122.39	10	4.9	6.4	±	0.6	10.6	4.8	±	1.7	11	S
85	5	16	14	20	34.4	Mid-indian Rise	-29.13	77.81	10	3.6	5.3	±	0.4	9.3	5.6	±	1.7	10	N
85	6	6	2	40	21.1	Cent. Mid-atlantic Ridge	1.00	-28.08	10	5.6	8.4	±	0.4	8.3	8.7	±	2.4	9	S
85	7	8	19	37	44.1	West Of Macquarie Island	-59.65	148.96	10	3.1	4.8	±	0.3	8.0	4.8	±	1.3	9	S
85	10	12	22	20	57.3	Cent. Mid-atlantic Ridge	0.99	-29.15	10	4.6	7.3	±	0.4	19.7	14.5	±	3.5	8	S
85	11	12	3	34	22.6	Southern Pacific Ocean	-36.50	-97.93	14	3.4	4.8	±	0.4	2.8	2.1	±	1.0	10	S
85	11	16	4	12	31.9	Mid-indian Rise	-38.35	78.05	10	5.5	7.6	±	0.7	13.1	11.0	±	2.3	9	S
86	7	7	16	27	7.7	Carlsberg Ridge	11.29	57.33	15	4.0	5.1	±	0.4	10.9	16.4	±	2.7	8	T
86	10	14	13	7	28.2	Prince Edward Is. Region	-42.96	41.96	15	2.0	2.2	±	0.1	9.0	3.5	±	0.7	9	S
86	12	25	17	17	42.4	Off Southern Chile Coast	-44.77	-80.42	15	4.1	5.9	±	0.6	2.7	1.9	±	1.2	9	S
86	12	28	20	4	44.2	Mid-indian Rise	-38.85	78.31	15	2.8	3.8	±	0.3	7.0	0.9	±	1.2	7	S
87	7	8	11	50	22.1	Easter Island Region	-27.32	-108.27	18	5.5	7.4	±	0.4	7.5	5.4	±	1.1	13	N
88	2	26	6	17	41.2	Atlantic-indian Rise	-36.88	48.03	15	18.4	20.9	±	1.5	9.8	9.2	±	1.6	27	T
88	3	21	23	31	24.7	Laptev Sea	77.64	125.78	15	4.3	5.4	±	0.4	3.1	7.8	±	1.7	8	N
88	3	23	15	50	29.1	North Atlantic Ridge	10.86	-43.39	15	2.0	3.0	±	0.2	11.2	8.1	±	2.4	7	S
88	5	5	10	4	22.0	Easter Island Cordillera	-27.01	-113.45	15	3.5	3.9	±	0.3	8.5	3.1	±	0.9	8	S
88	6	18	22	49	48.4	Gulf Of California	26.75	-111.02	15	10.7	14.8	±	0.9	5.7	4.2	±	1.6	16	S
88	10	1	9	43	33.6	Easter Island Cordillera	-35.38	-106.21	15	3.5	4.1	±	0.3	9.0	3.0	±	1.0	8	S
88	11	25	8	35	53.1	Southeast Indian Rise	-47.89	99.80	15	2.9	3.9	±	0.3	11.5	9.8	±	3.0	7	S
89	5	23	10	55	12.2	Macquarie Islands Region	-52.15	160.41	15	1360.0	2070.0	±	137.0	25.7	14.8	±	0.8	18	S
89	8	29	4	16	25.7	"Off Jalisco, Mexico Cst"	17.88	-105.65	15	6.9	7.9	±	0.5	0.8	-2.6	±	1.5	21	S
89	9	13	11	40	59.4	South Atlantic Ridge	-35.28	-16.62	15	4.7	7.1	±	0.5	15.0	15.7	±	2.1	19	S

TABLE B1: CONT.

Origin time						Region	lat	lon	dep	M_0 CMT	$M_T{}^0$			Δt_1 CMT	Δt_1			#	M
90	7	14	5	54	33.2	N Of Ascension Island	0.27	-17.26	23	8.6	10.7	±	0.8	7.9	9.1	±	1.3	8	S
90	8	5	17	42	42.6	N Of Ascension Island	-0.71	-13.81	15	5.3	6.0	±	0.4	10.4	12.0	±	2.1	10	S
90	9	17	13	47	35.4	Macquarie Islands Region	-53.22	159.16	19	4.5	5.9	±	0.5	9.1	5.4	±	0.4	8	S
91	1	18	10	45	25.5	South Of Australia	-51.18	139.65	15	3.4	4.3	±	0.4	8.2	11.6	±	2.3	8	S
91	3	11	21	16	4.1	South Of Africa	-50.49	29.37	15	4.5	5.6	±	0.3	7.7	4.0	±	0.7	10	S
91	6	10	17	35	58.3	North Atlantic Ridge	23.80	-45.29	15	3.3	4.4	±	0.3	8.9	0.7	±	0.5	12	S
91	11	5	21	16	27.1	Mascarene Islands Region	-17.34	65.70	15	6.8	11.5	±	0.9	12.8	11.3	±	1.7	14	S
91	12	11	17	3	18.9	Easter Island Cordillera	-18.10	-116.28	15	4.8	6.0	±	0.4	9.6	3.9	±	0.6	22	N
92	3	31	3	32	14.8	Easter Island Cordillera	-50.04	-114.75	15	3.2	4.3	±	0.4	11.9	5.3	±	0.6	17	S
92	6	22	4	0	46.7	Swestern Atlantic Ocean	-61.11	-21.42	15	3.9	5.0	±	0.4	2.5	1.0	±	0.5	20	S
92	7	20	7	46	59.9	Svalbard Region	78.79	3.80	15	13.3	16.0	±	0.8	13.3	14.0	±	2.1	23	S
92	8	28	18	18	51.7	N Of Ascension Island	-0.71	-13.54	15	20.0	27.1	±	1.0	6.4	6.8	±	1.8	28	S
92	11	4	1	59	34.3	Balleny Islands Region	-61.62	154.41	15	5.0	6.1	±	0.2	7.6	7.2	±	1.0	21	S
92	12	26	19	52	45.9	Cntrl Mid-atlantic Ridge	-0.09	-18.76	15	17.4	23.3	±	0.8	21.2	23.6	±	2.0	26	S
94	3	14	4	30	32.6	Cntrl Mid-atlantic Ridge	0.00	0.00	0	0.0	48.3	±	1.5	0.0	22.6	±	2.0	26	S

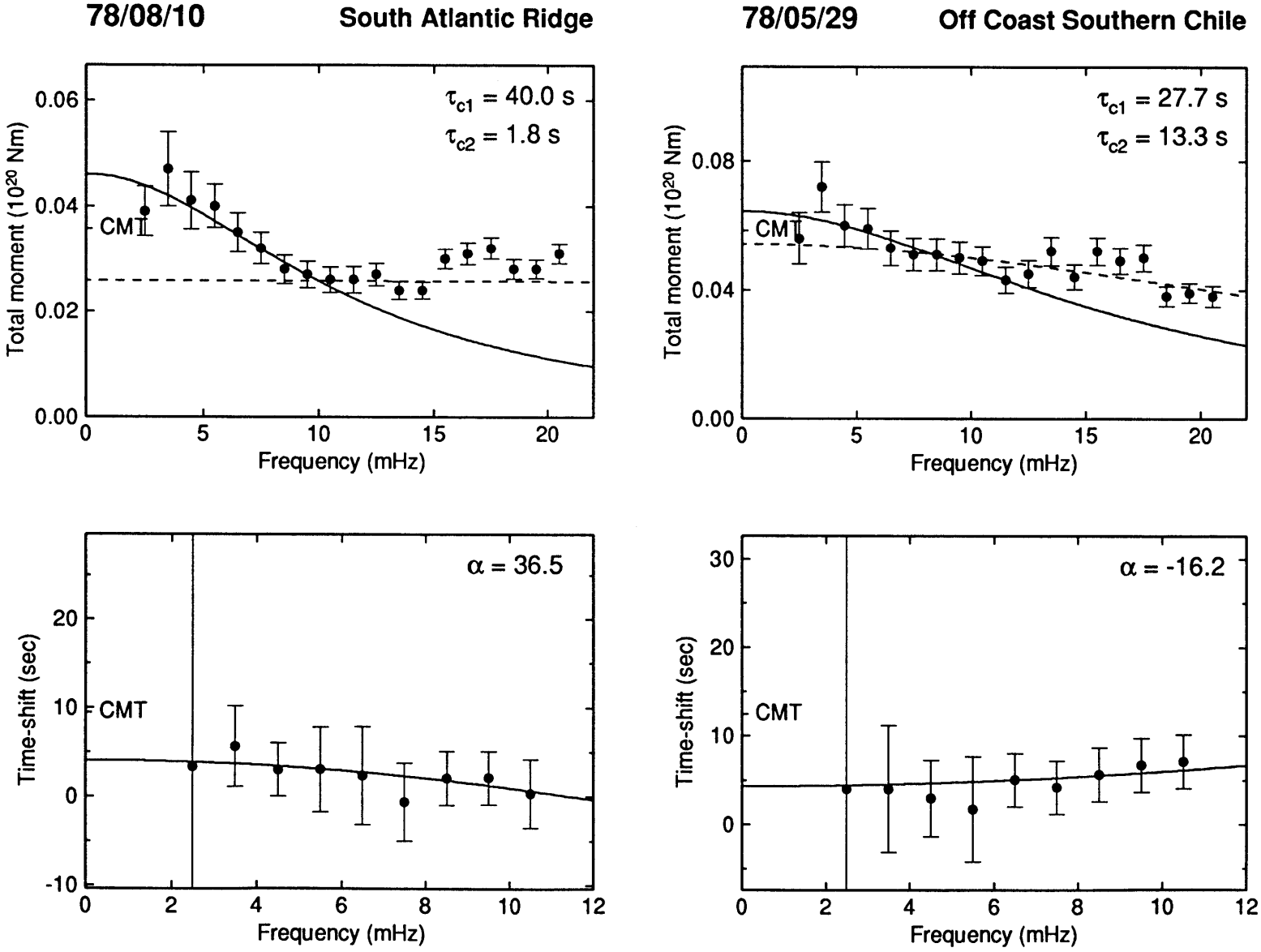
78/08/10
South Atlantic Ridge
78/05/29
Off Coast Southern Chile
τ_{c1} = 40.0 s
τ_{c2} = 1.8 s
τ_{c1} = 27.7 s
τ_{c2} = 13.3 s
CMT
Total moment (10^{20} Nm)
Frequency (mHz)
α = 36.5
α = -16.2
Time-shift (sec)

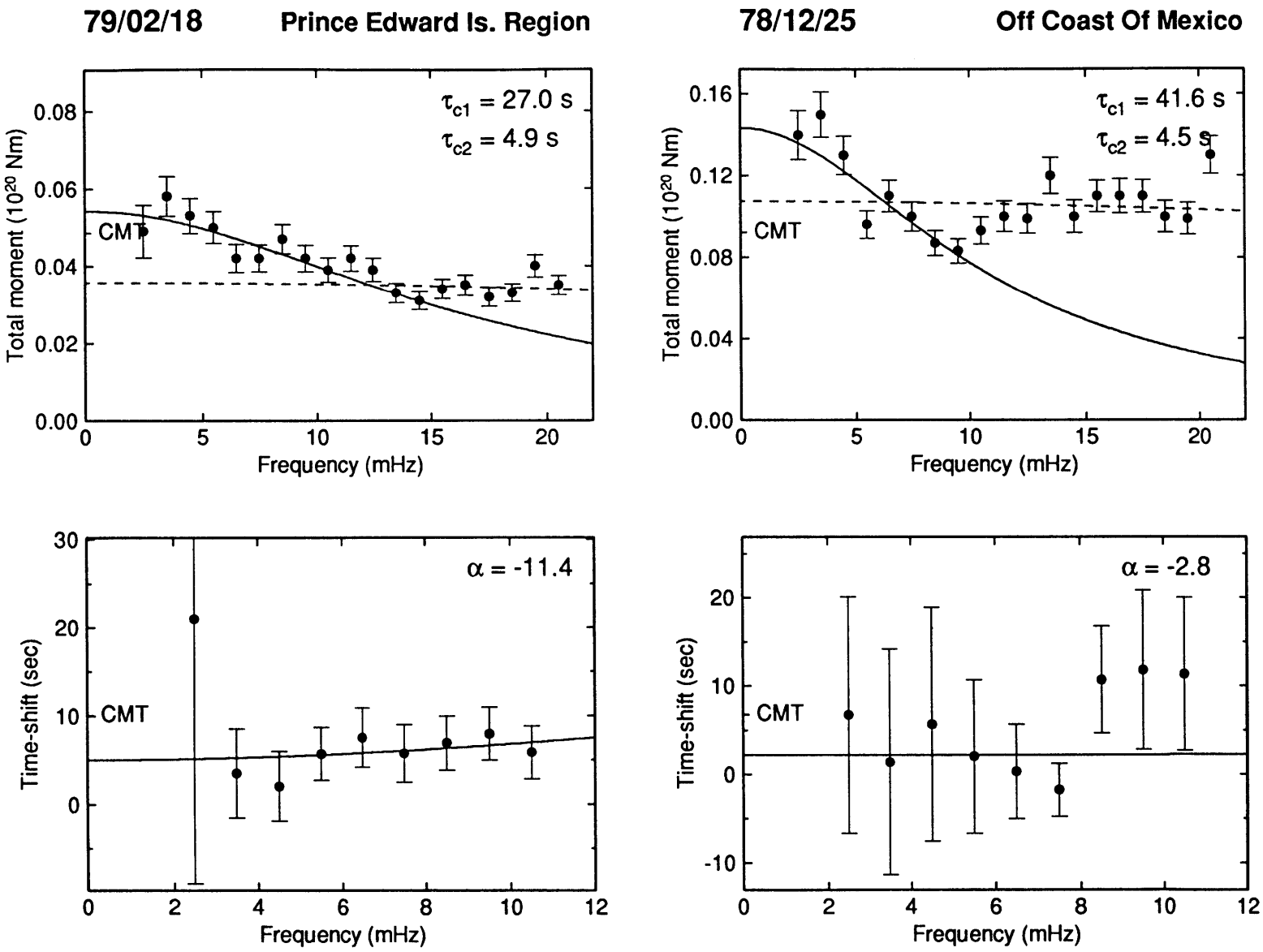
79/02/18
Prince Edward Is. Region
78/12/25
Off Coast Of Mexico
τc1 = 27.0 s
τc2 = 4.9 s
τc1 = 41.6 s
τc2 = 4.5 s
CMT
Total moment (10²⁰ Nm)
Frequency (mHz)
α = -11.4
α = -2.8
Time-shift (sec)

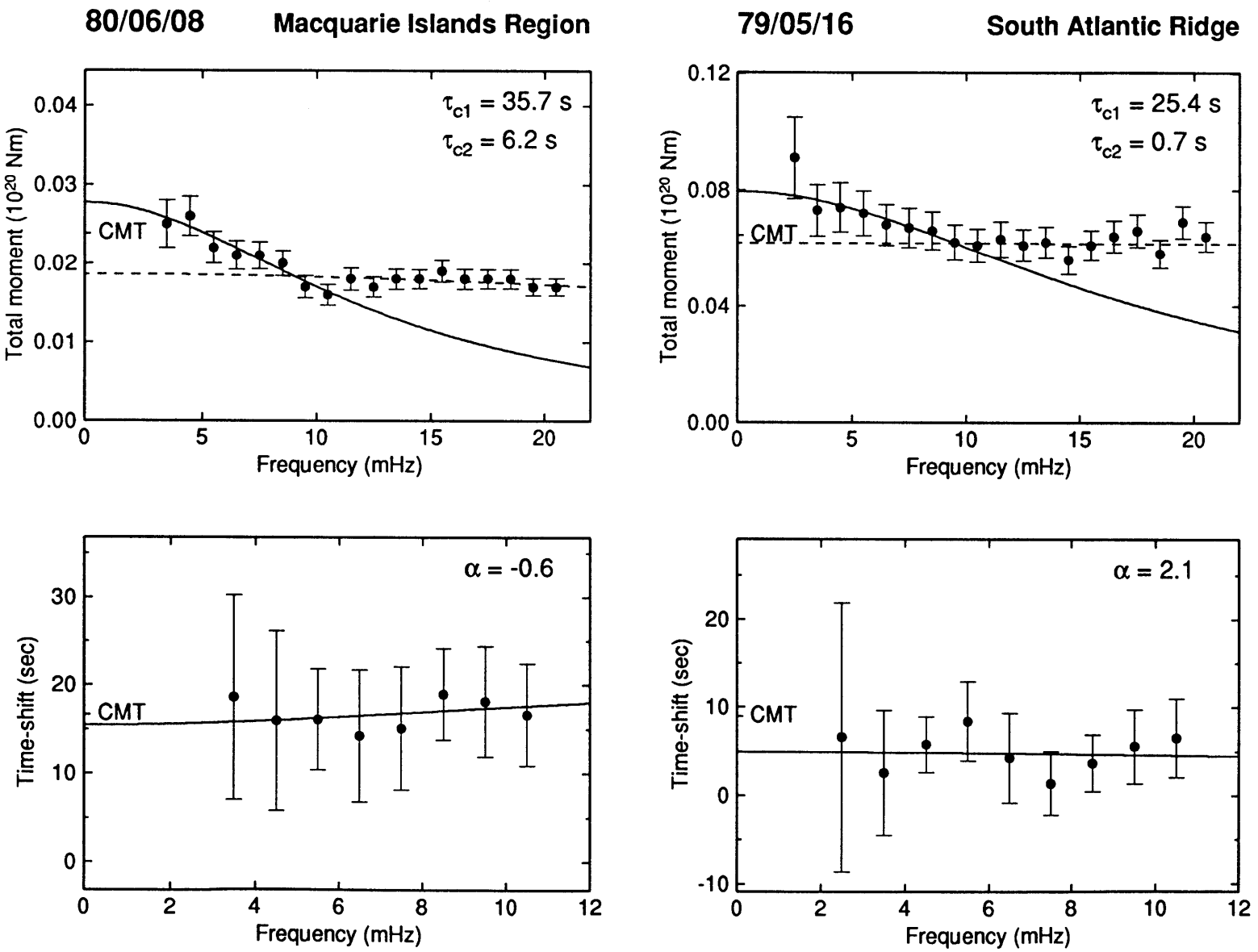
80/06/08
Macquarie Islands Region
79/05/16
South Atlantic Ridge
τc1 = 35.7 s
τc2 = 6.2 s
τc1 = 25.4 s
τc2 = 0.7 s
CMT
Total moment (10²⁰ Nm)
Frequency (mHz)
α = -0.6
α = 2.1
Time-shift (sec)

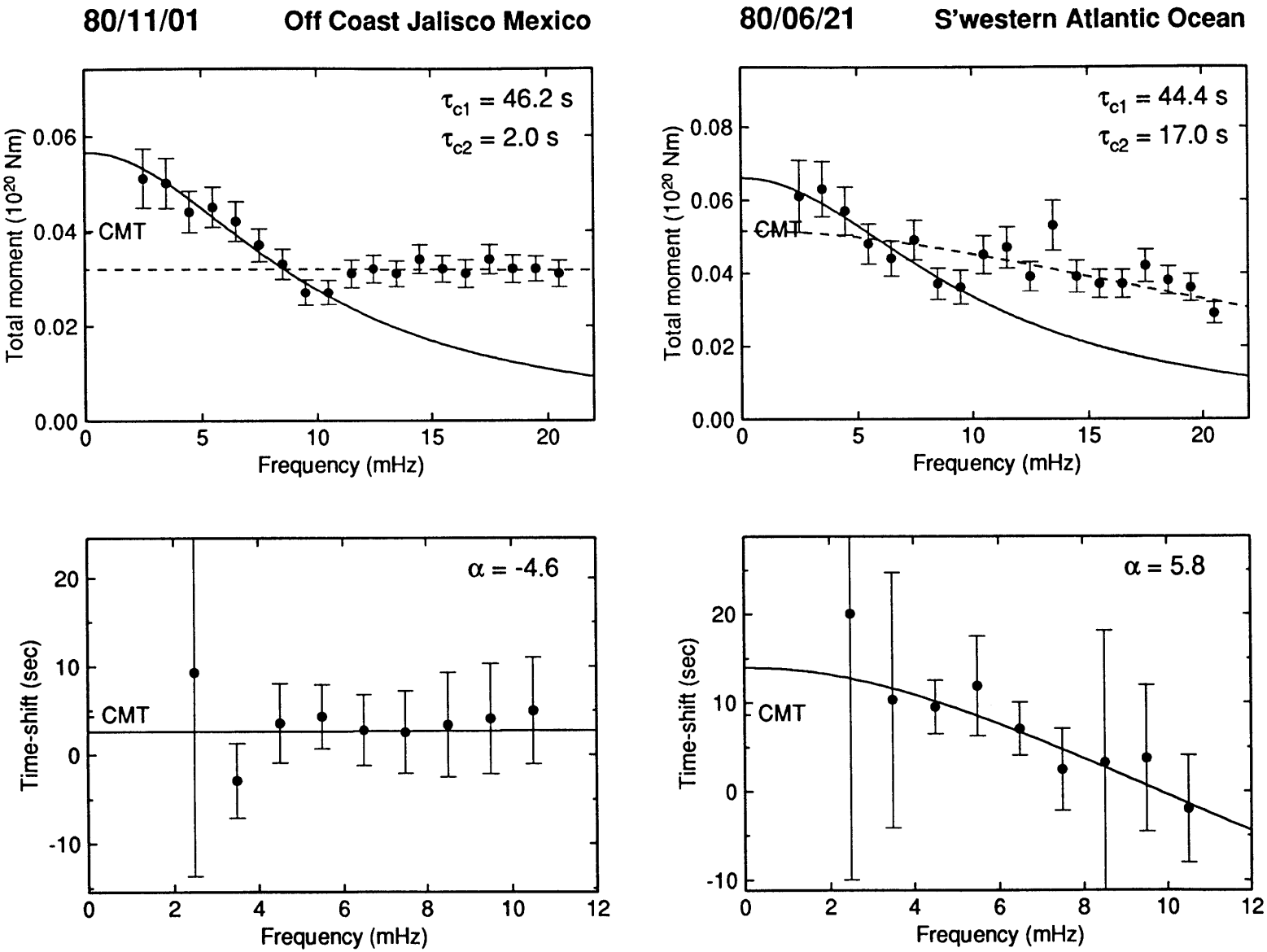
80/11/01
Off Coast Jalisco Mexico
τ_{c1} = 46.2 s
τ_{c2} = 2.0 s
CMT
Total moment (10^{20} Nm)
Frequency (mHz)
80/06/21
S'western Atlantic Ocean
τ_{c1} = 44.4 s
τ_{c2} = 17.0 s
CMT
Total moment (10^{20} Nm)
Frequency (mHz)
α = -4.6
CMT
Time-shift (sec)
Frequency (mHz)
α = 5.8
CMT
Time-shift (sec)
Frequency (mHz)

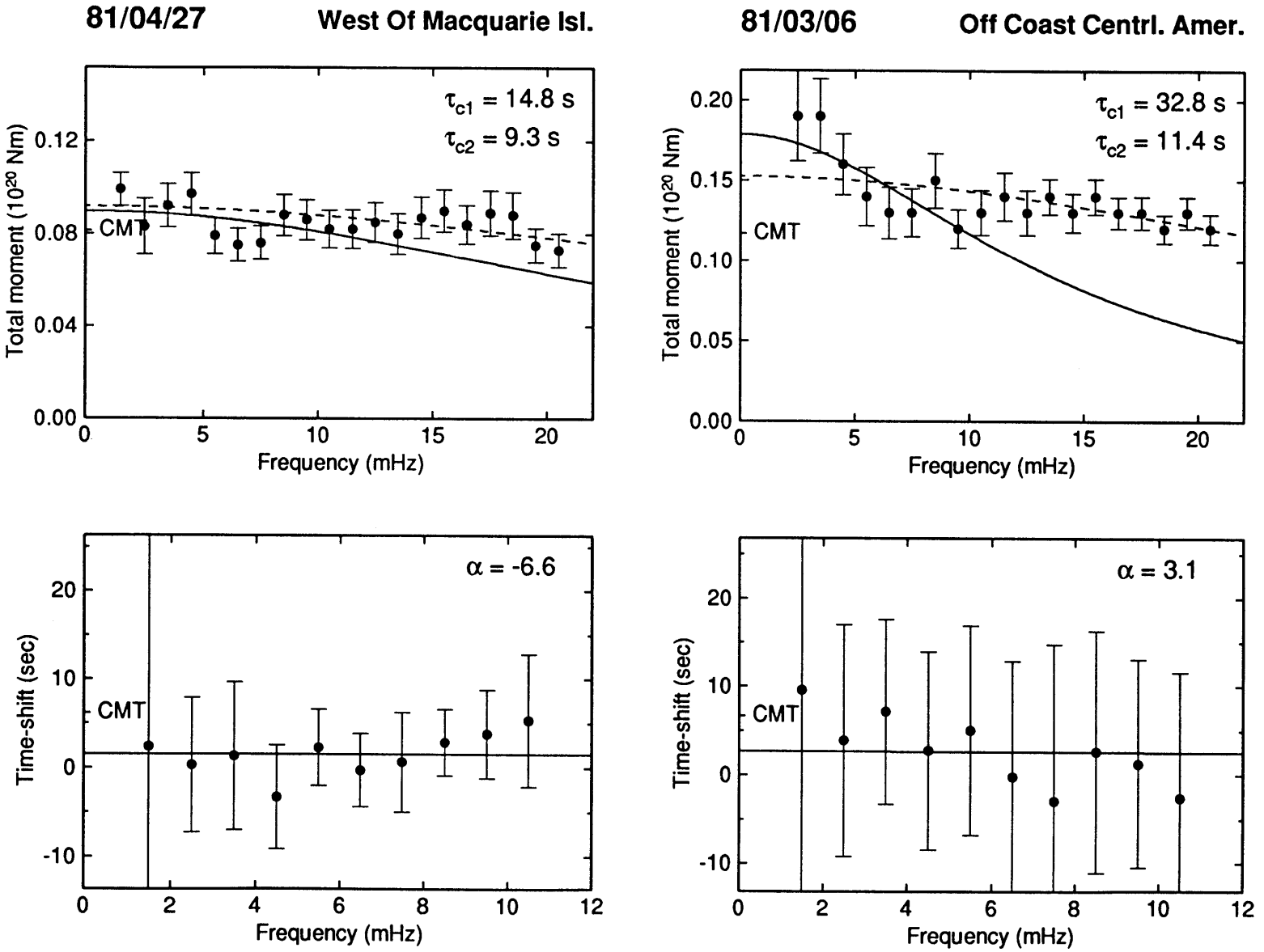
81/04/27
West Of Macquarie Isl.
81/03/06
Off Coast Centrl. Amer.
τ_{c1} = 14.8 s
τ_{c2} = 9.3 s
τ_{c1} = 32.8 s
τ_{c2} = 11.4 s
CMT
Total moment (10^{20} Nm)
Frequency (mHz)
α = -6.6
α = 3.1
Time-shift (sec)

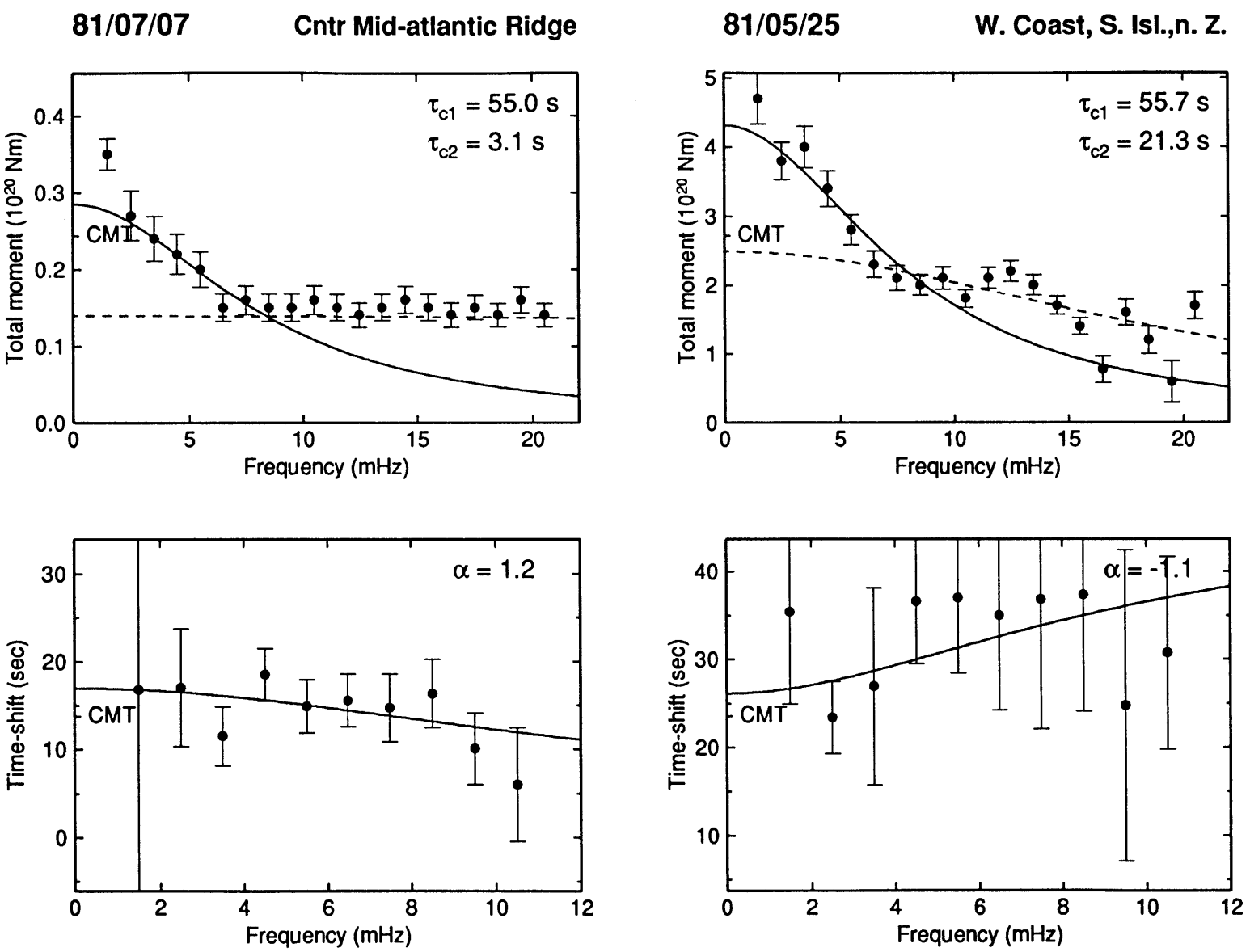
81/07/07
Cntr Mid-atlantic Ridge
81/05/25
W. Coast, S. Isl.,n. Z.
τc1 = 55.0 s
τc2 = 3.1 s
τc1 = 55.7 s
τc2 = 21.3 s
CMT
Total moment (10²⁰ Nm)
Frequency (mHz)
α = 1.2
α = -1.1
Time-shift (sec)

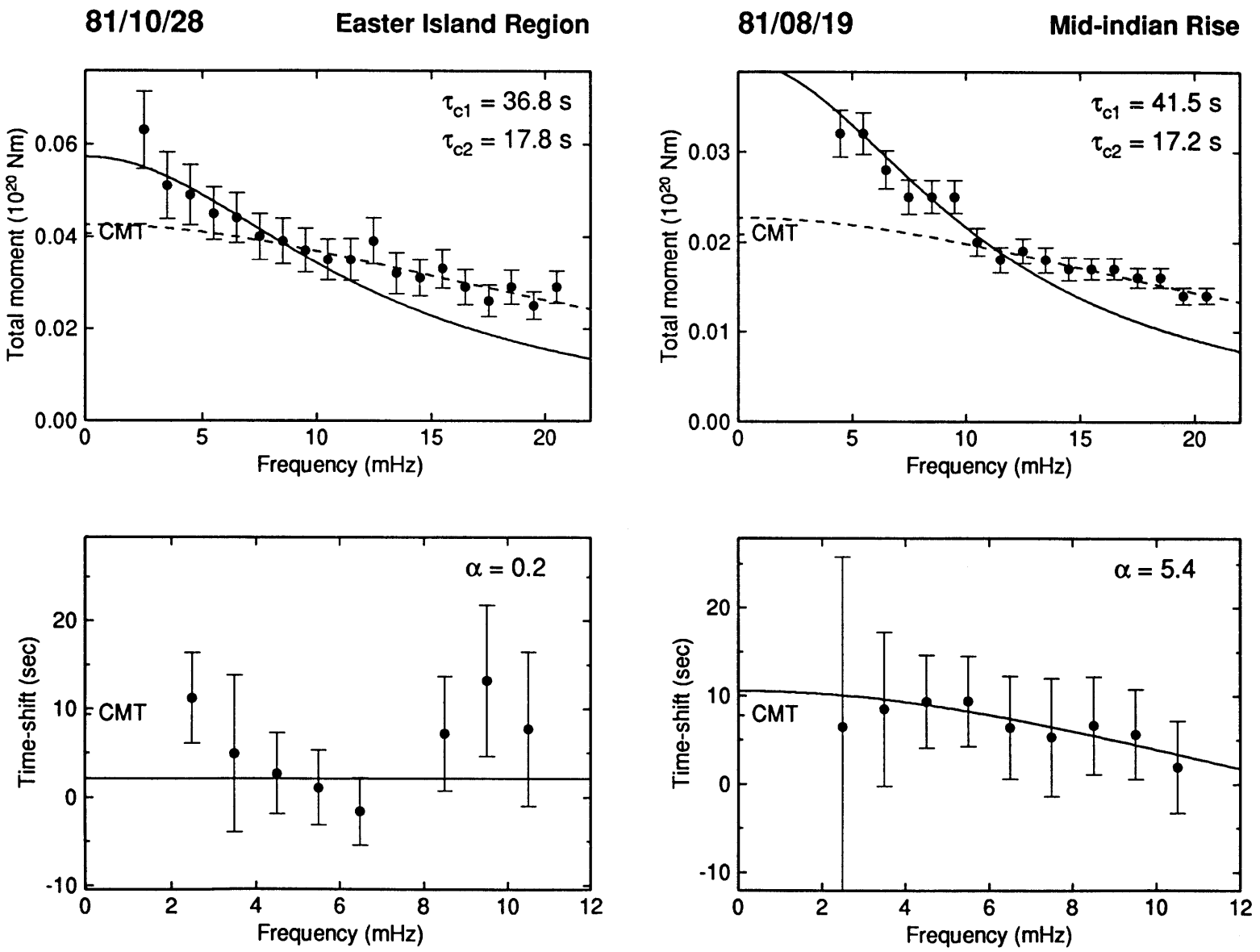
81/10/28
Easter Island Region
81/08/19
Mid-indian Rise
τ_{c1} = 36.8 s
τ_{c2} = 17.8 s
τ_{c1} = 41.5 s
τ_{c2} = 17.2 s
CMT
Total moment (10^{20} Nm)
Frequency (mHz)
α = 0.2
α = 5.4
Time-shift (sec)

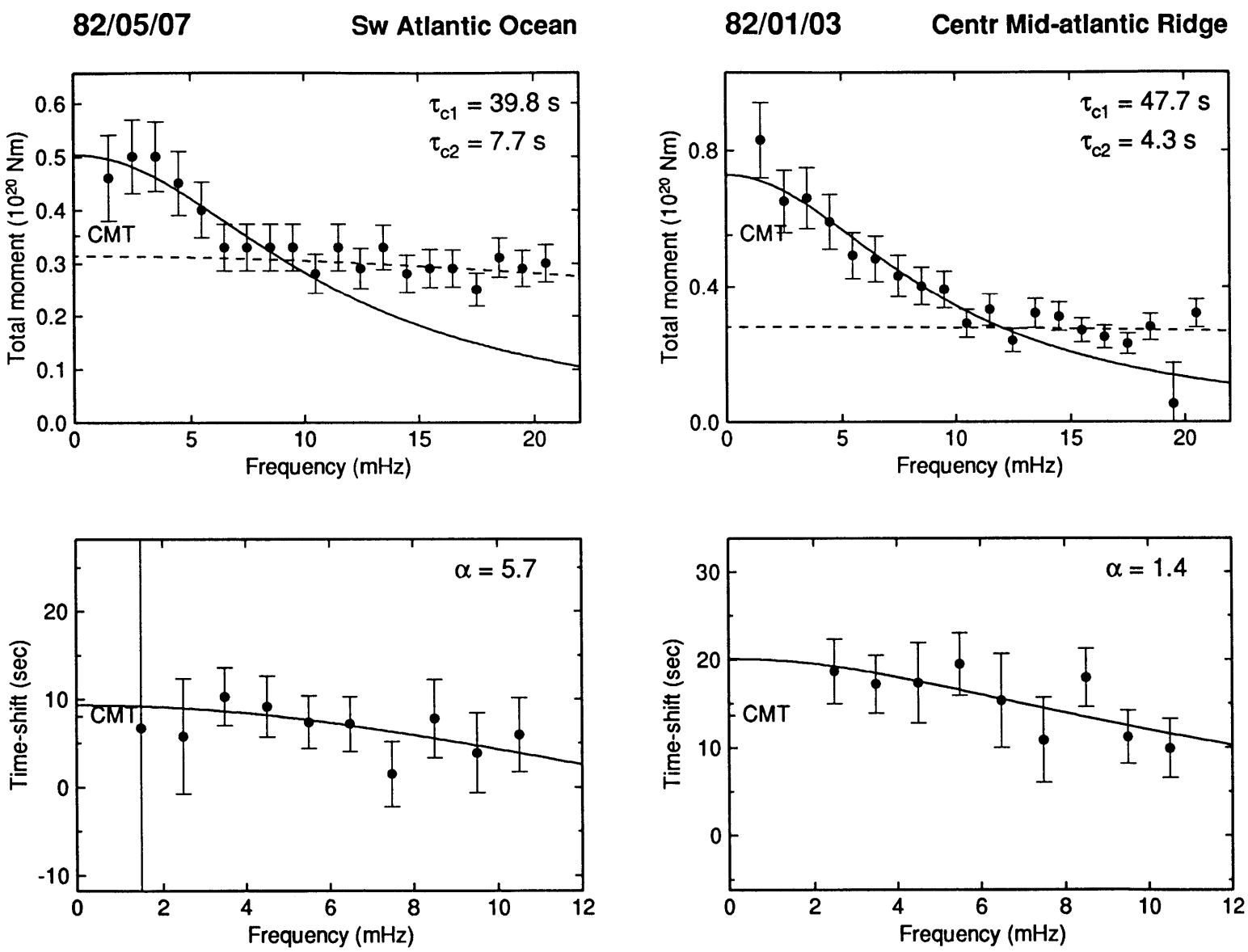
82/05/07
Sw Atlantic Ocean
82/01/03
Centr Mid-atlantic Ridge
τ_{c1} = 39.8 s
τ_{c2} = 7.7 s
τ_{c1} = 47.7 s
τ_{c2} = 4.3 s
CMT
Total moment (10^{20} Nm)
Frequency (mHz)
α = 5.7
α = 1.4
Time-shift (sec)

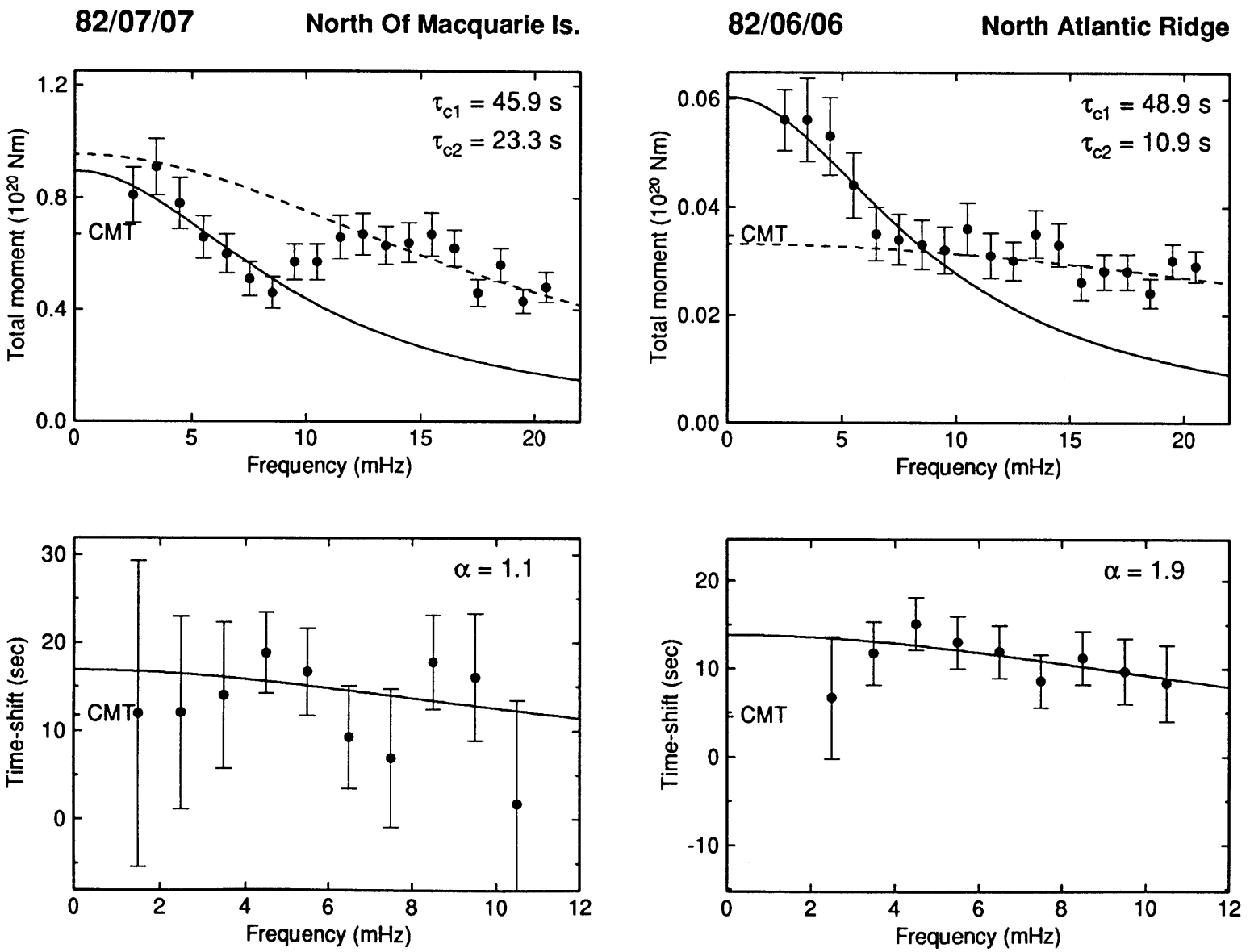
82/07/07
North Of Macquarie Is.
82/06/06
North Atlantic Ridge
Total moment (10^20 Nm)
τc1 = 45.9 s
τc2 = 23.3 s
CMT
Frequency (mHz)
τc1 = 48.9 s
τc2 = 10.9 s
Time-shift (sec)
α = 1.1
α = 1.9

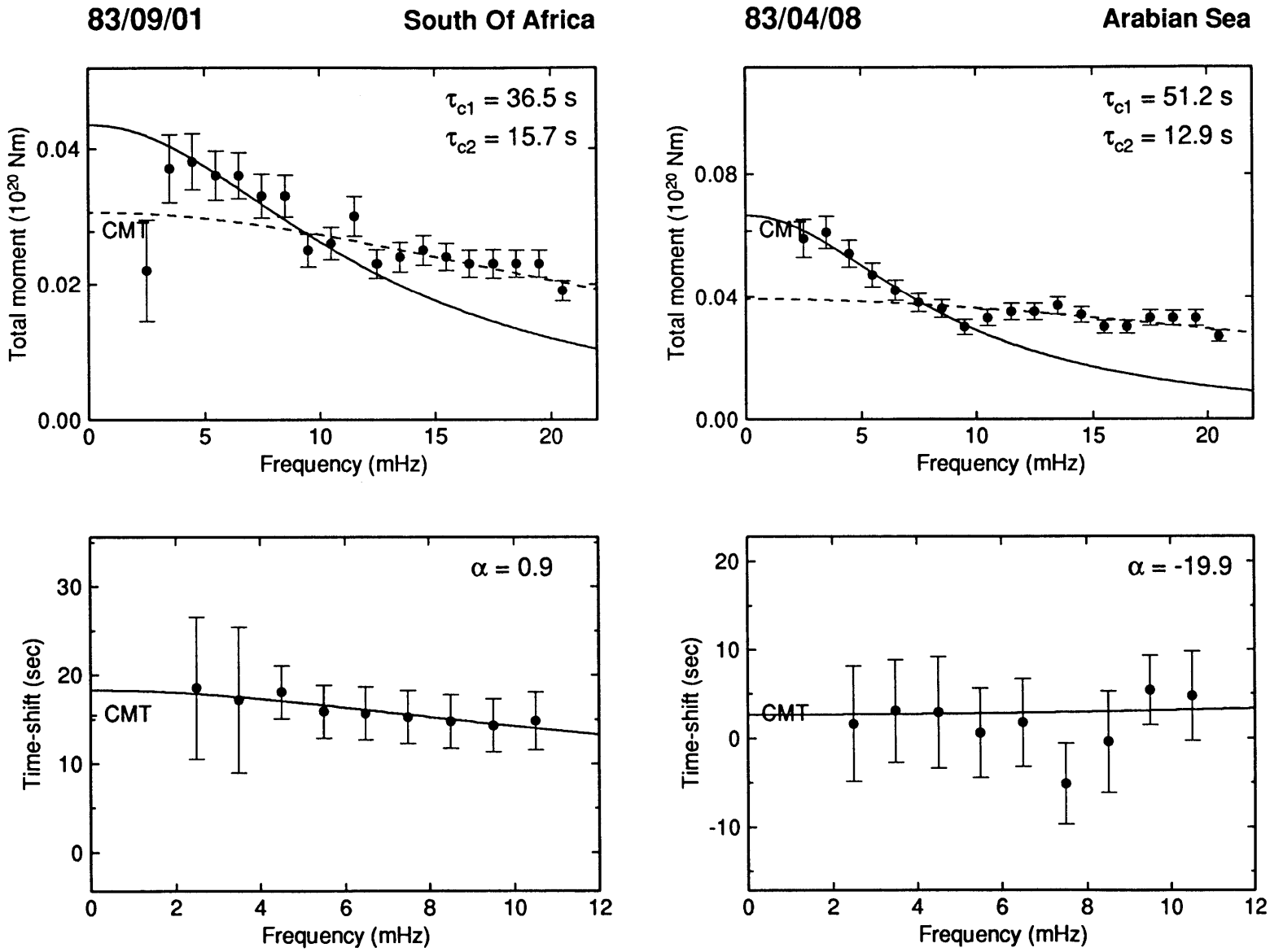
83/09/01
South Of Africa
τ_{c1} = 36.5 s
τ_{c2} = 15.7 s
CMT
Total moment (10^{20} Nm)
0.00
0.02
0.04
0
5
10
15
20
Frequency (mHz)
83/04/08
Arabian Sea
τ_{c1} = 51.2 s
τ_{c2} = 12.9 s
CMT
Total moment (10^{20} Nm)
0.00
0.04
0.08
0
5
10
15
20
Frequency (mHz)
α = 0.9
CMT
Time-shift (sec)
0
10
20
30
0
2
4
6
8
10
12
Frequency (mHz)
α = -19.9
CMT
Time-shift (sec)
-10
0
10
20
0
2
4
6
8
10
12
Frequency (mHz)

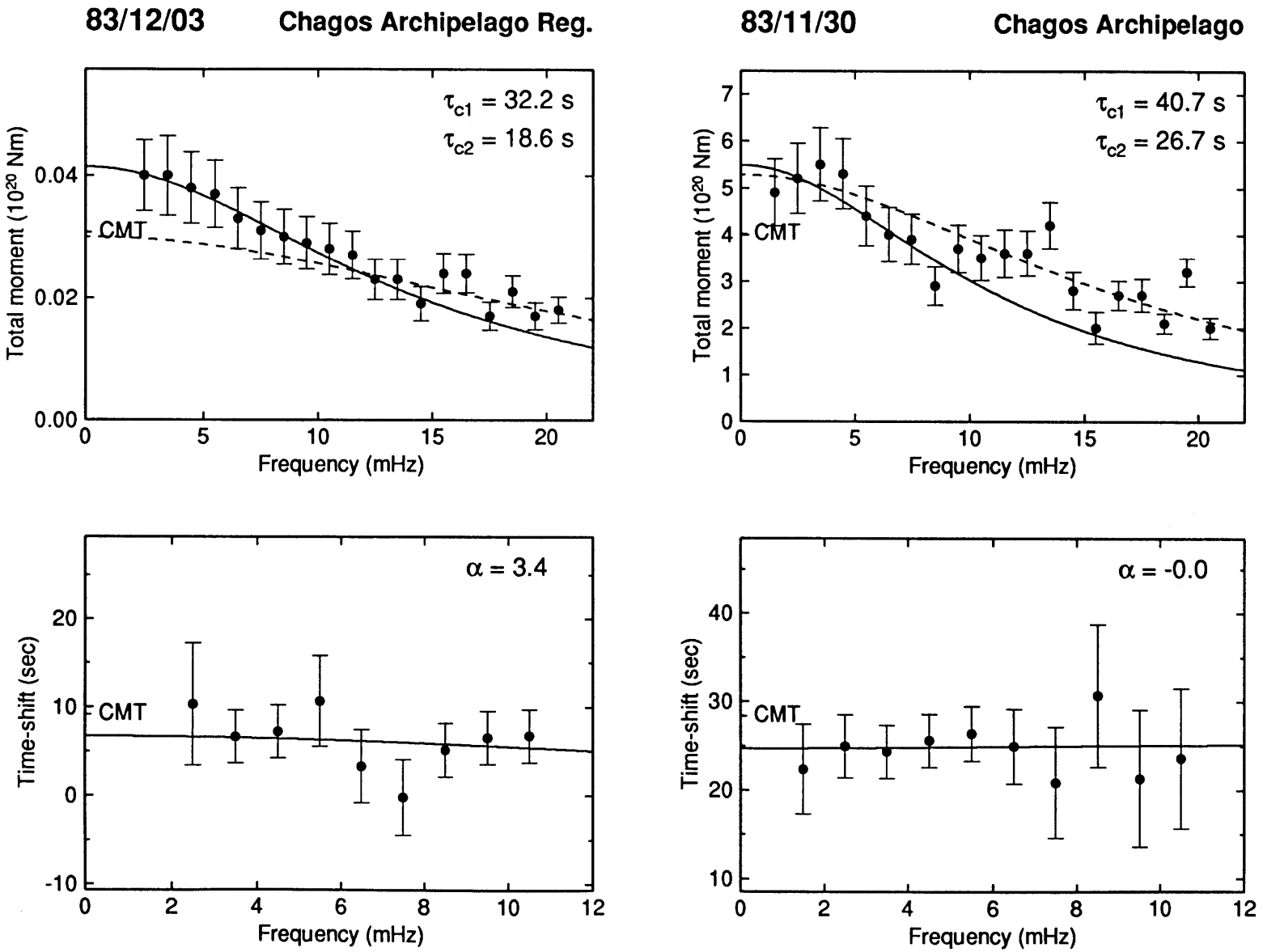
83/12/03
Chagos Archipelago Reg.
τ_{c1} = 32.2 s
τ_{c2} = 18.6 s
CMT
Total moment (10^{20} Nm)
Frequency (mHz)
83/11/30
Chagos Archipelago
τ_{c1} = 40.7 s
τ_{c2} = 26.7 s
CMT
Total moment (10^{20} Nm)
Frequency (mHz)
α = 3.4
CMT
Time-shift (sec)
Frequency (mHz)
α = -0.0
CMT
Time-shift (sec)
Frequency (mHz)

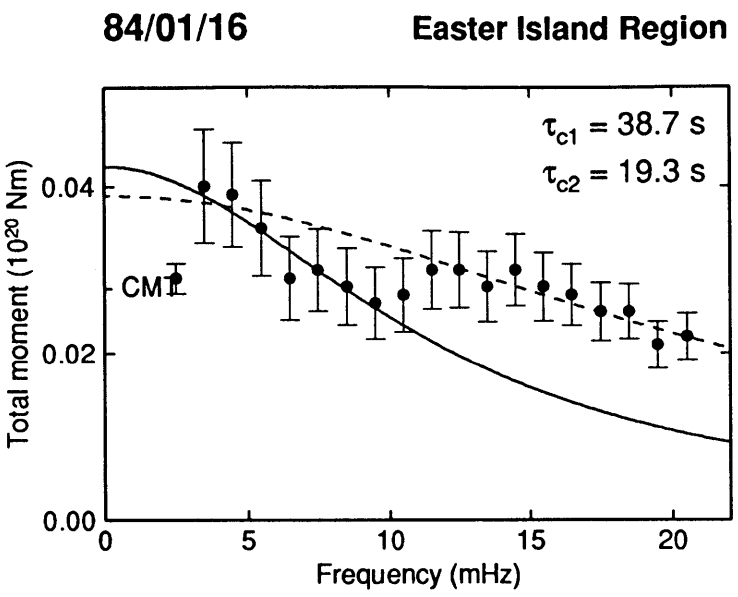
84/01/16
Easter Island Region
τ_{c1} = 38.7 s
τ_{c2} = 19.3 s
CMT
Total moment (10^{20} Nm)
0.00
0.02
0.04
0 5 10 15 20
Frequency (mHz)

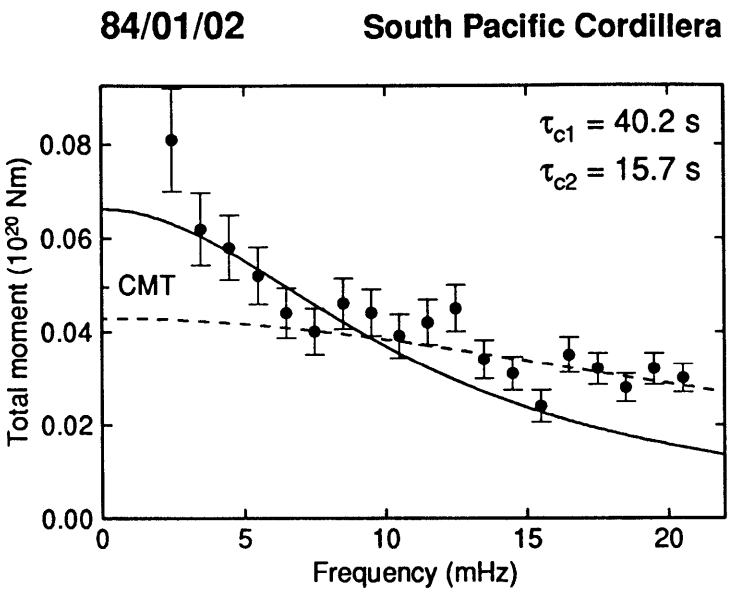
84/01/02
South Pacific Cordillera
τ_{c1} = 40.2 s
τ_{c2} = 15.7 s
CMT
Total moment (10^{20} Nm)
0.00
0.02
0.04
0.06
0.08
0 5 10 15 20
Frequency (mHz)

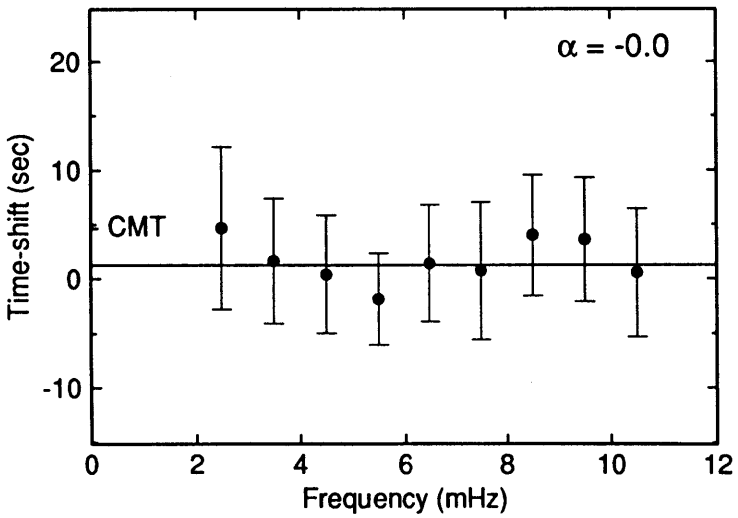
α = -0.0
CMT
Time-shift (sec)
-10
0
10
20
0 2 4 6 8 10 12
Frequency (mHz)

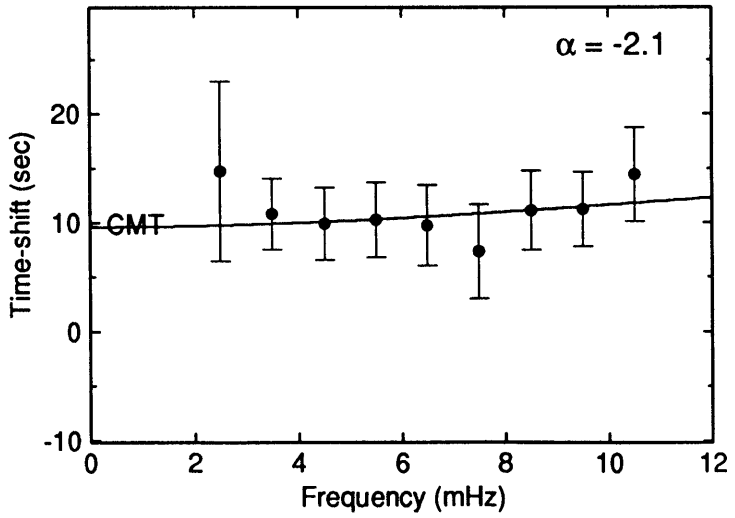
α = -2.1
CMT
Time-shift (sec)
-10
0
10
20
0 2 4 6 8 10 12
Frequency (mHz)

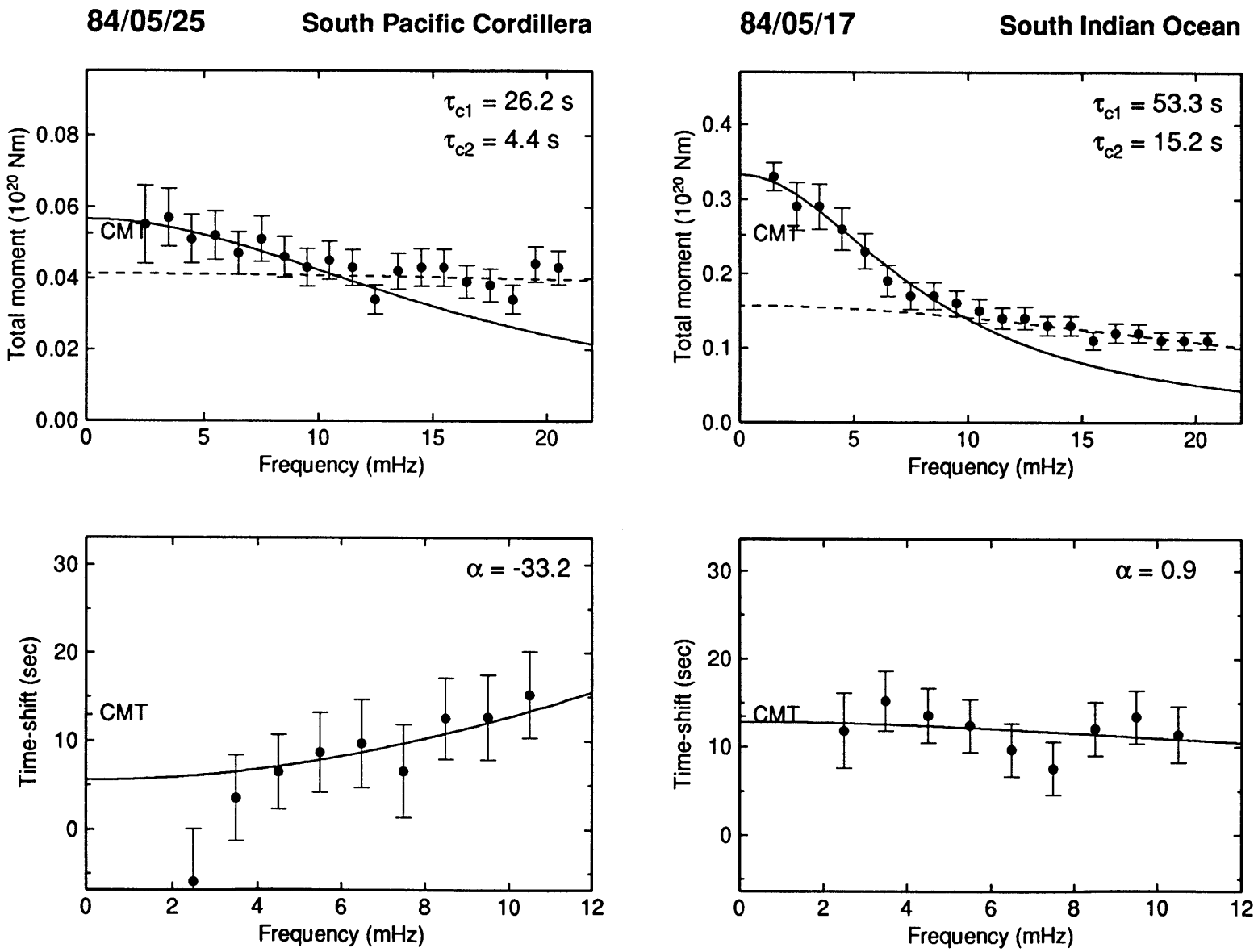
84/05/25
South Pacific Cordillera
84/05/17
South Indian Ocean
τ_{c1} = 26.2 s
τ_{c2} = 4.4 s
τ_{c1} = 53.3 s
τ_{c2} = 15.2 s
CMT
Total moment (10^{20} Nm)
Frequency (mHz)
α = -33.2
α = 0.9
Time-shift (sec)

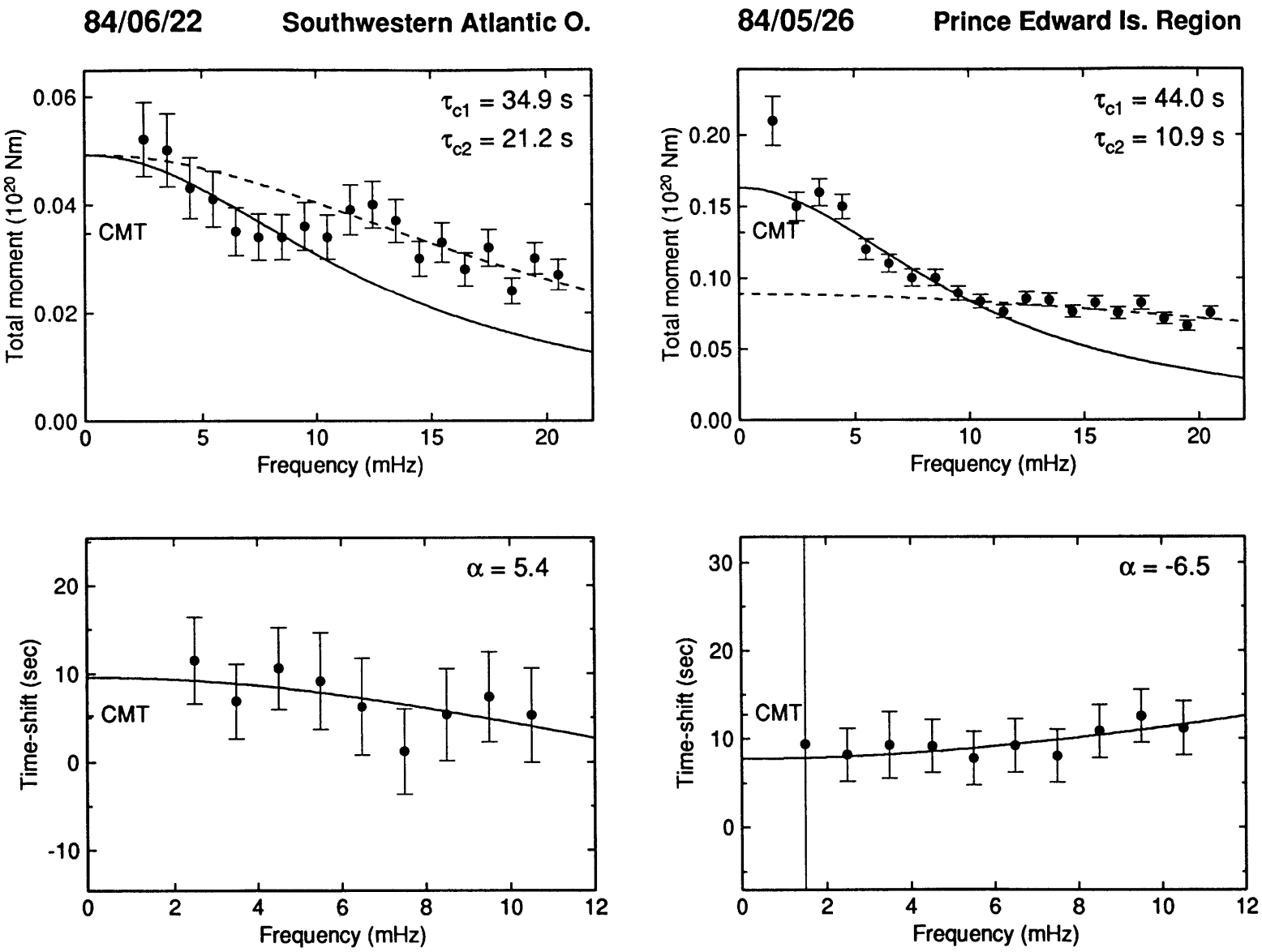
84/06/22
Southwestern Atlantic O.
84/05/26
Prince Edward Is. Region
Total moment (10^20 Nm)
τc1 = 34.9 s
τc2 = 21.2 s
CMT
Frequency (mHz)
τc1 = 44.0 s
τc2 = 10.9 s
Time-shift (sec)
α = 5.4
α = -6.5

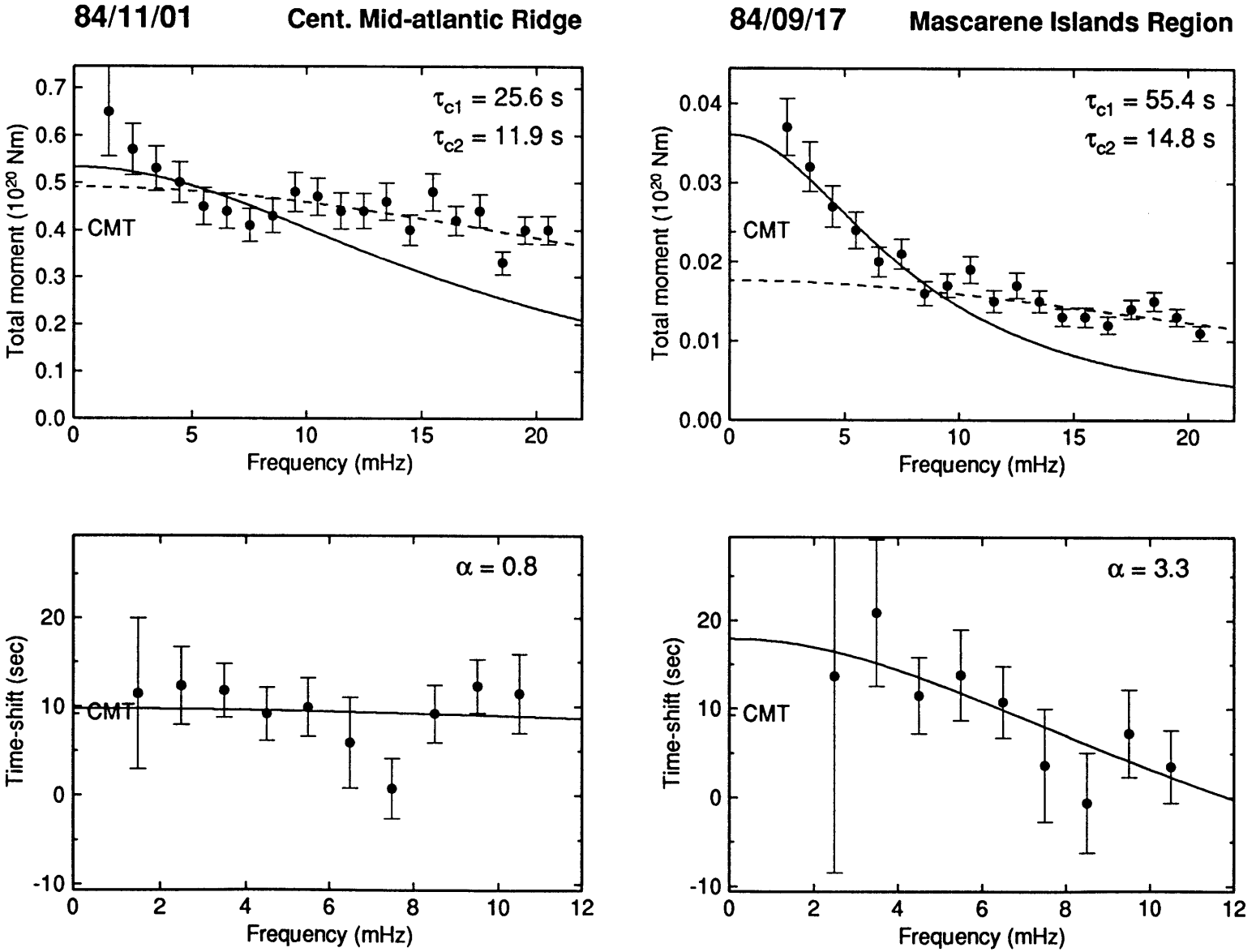
84/11/01
Cent. Mid-atlantic Ridge
84/09/17
Mascarene Islands Region
τ_{c1} = 25.6 s
τ_{c2} = 11.9 s
τ_{c1} = 55.4 s
τ_{c2} = 14.8 s
CMT
Total moment (10^{20} Nm)
Frequency (mHz)
α = 0.8
α = 3.3
Time-shift (sec)

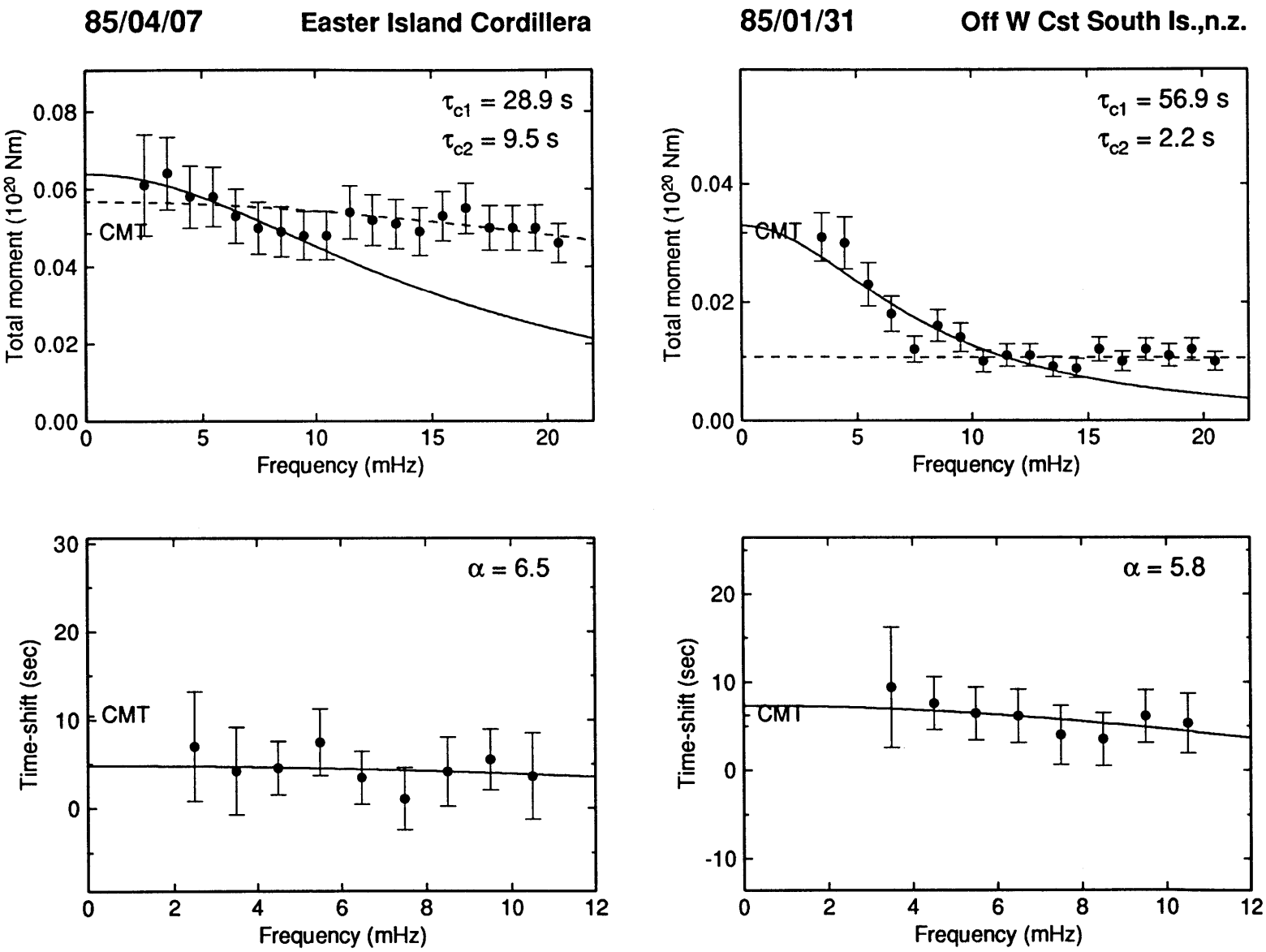
85/04/07
Easter Island Cordillera
85/01/31
Off W Cst South Is.,n.z.
τ_{c1} = 28.9 s
τ_{c2} = 9.5 s
τ_{c1} = 56.9 s
τ_{c2} = 2.2 s
CMT
Total moment (10^{20} Nm)
Frequency (mHz)
α = 6.5
α = 5.8
Time-shift (sec)

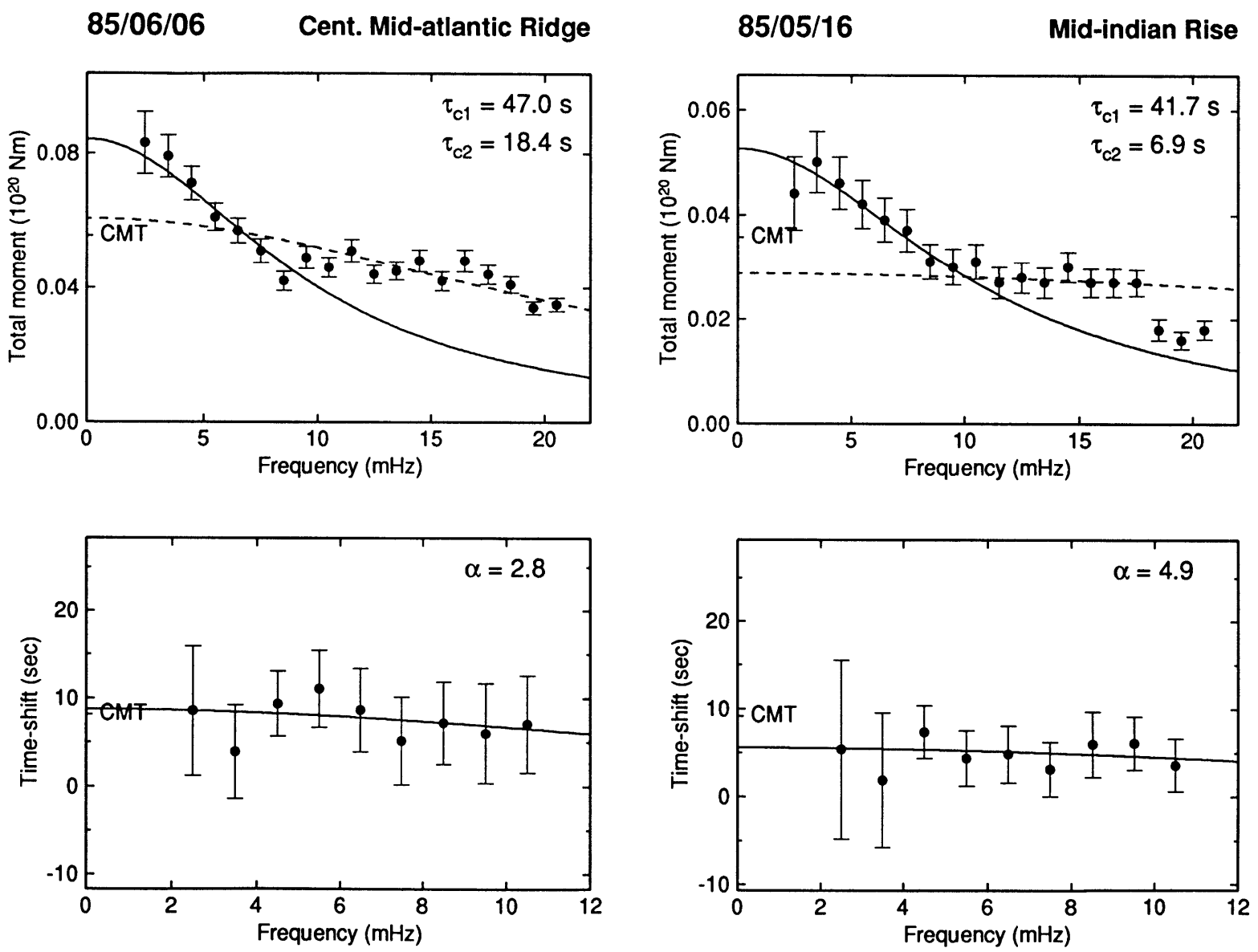
85/06/06
Cent. Mid-atlantic Ridge
τ_{c1} = 47.0 s
τ_{c2} = 18.4 s
CMT
Total moment (10^{20} Nm)
0.00
0.04
0.08
0
5
10
15
20
Frequency (mHz)
85/05/16
Mid-indian Rise
τ_{c1} = 41.7 s
τ_{c2} = 6.9 s
CMT
Total moment (10^{20} Nm)
0.00
0.02
0.04
0.06
0
5
10
15
20
Frequency (mHz)
α = 2.8
CMT
Time-shift (sec)
-10
0
10
20
0
2
4
6
8
10
12
Frequency (mHz)
α = 4.9
CMT
Time-shift (sec)
-10
0
10
20
0
2
4
6
8
10
12
Frequency (mHz)

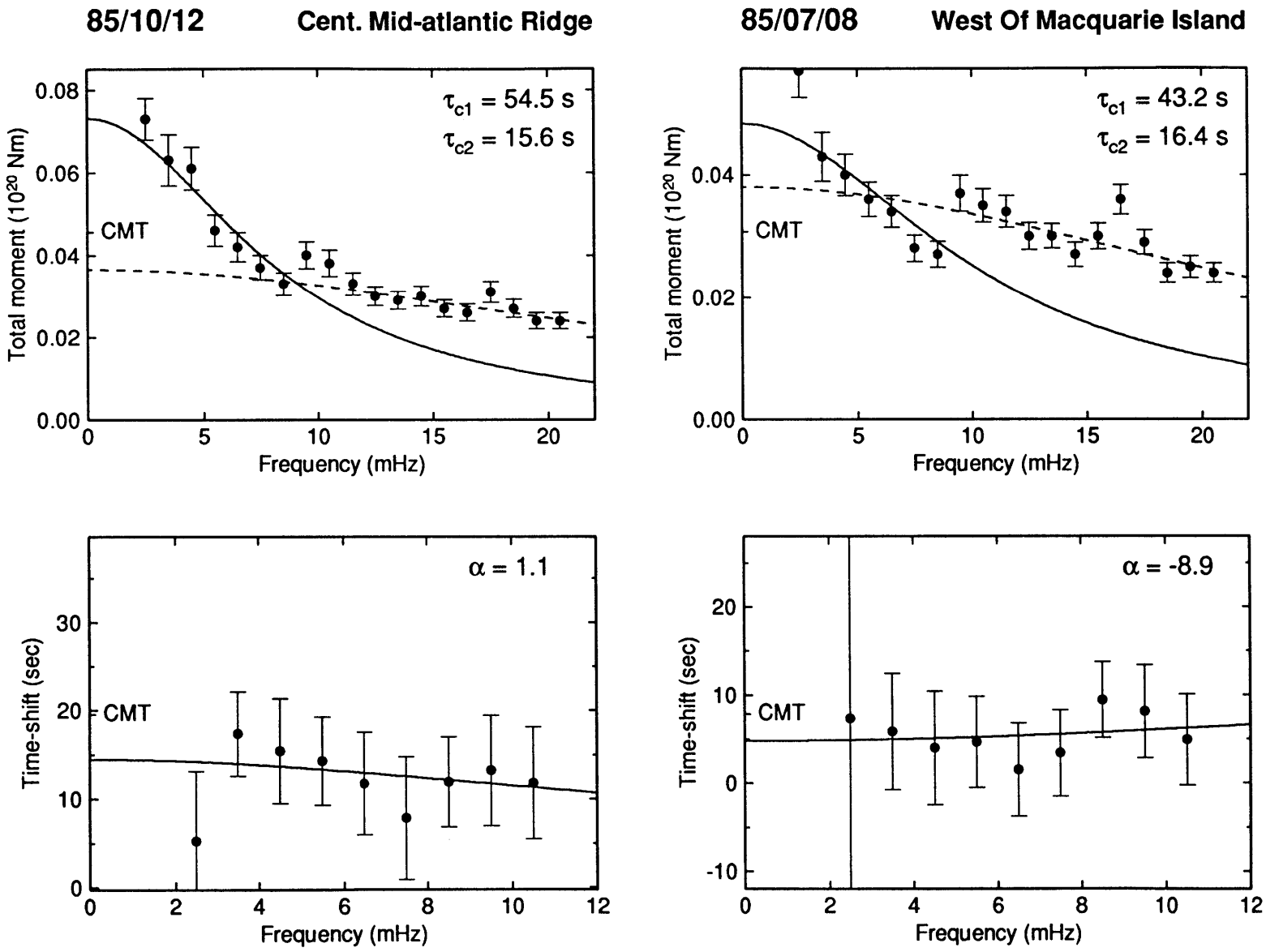
85/10/12
Cent. Mid-atlantic Ridge
85/07/08
West Of Macquarie Island
τ_{c1} = 54.5 s
τ_{c2} = 15.6 s
τ_{c1} = 43.2 s
τ_{c2} = 16.4 s
CMT
CMT
Total moment (10^{20} Nm)
Total moment (10^{20} Nm)
Frequency (mHz)
Frequency (mHz)
α = 1.1
α = -8.9
CMT
CMT
Time-shift (sec)
Time-shift (sec)
Frequency (mHz)
Frequency (mHz)

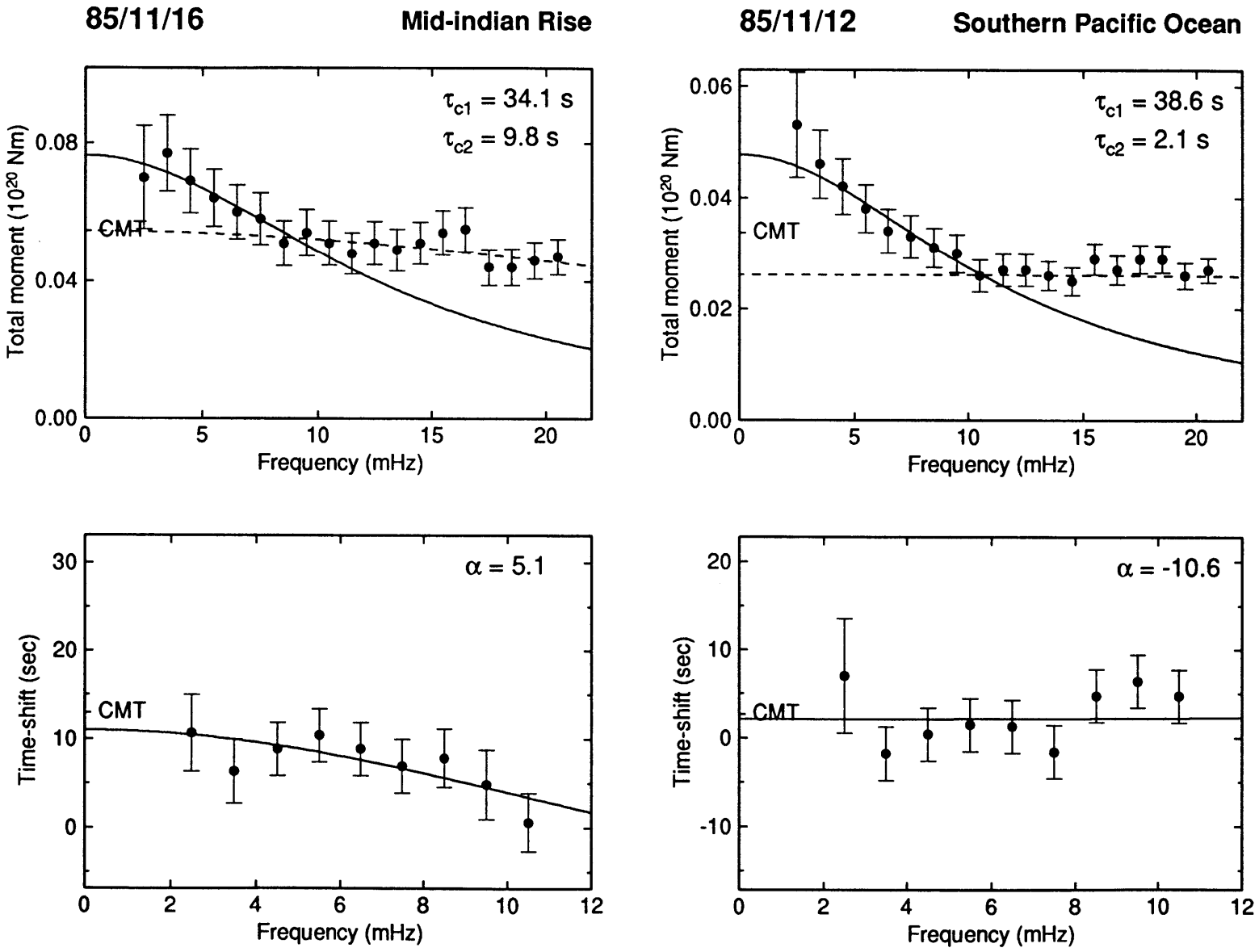
85/11/16
Mid-indian Rise
85/11/12
Southern Pacific Ocean
τ_{c1} = 34.1 s
τ_{c2} = 9.8 s
τ_{c1} = 38.6 s
τ_{c2} = 2.1 s
CMT
CMT
Total moment (10^{20} Nm)
Total moment (10^{20} Nm)
0.00
0.04
0.08
0.00
0.02
0.04
0.06
0
5
10
15
20
Frequency (mHz)
Frequency (mHz)
α = 5.1
α = -10.6
CMT
CMT
Time-shift (sec)
Time-shift (sec)
0
10
20
30
-10
0
10
20
0
2
4
6
8
10
12
Frequency (mHz)
Frequency (mHz)

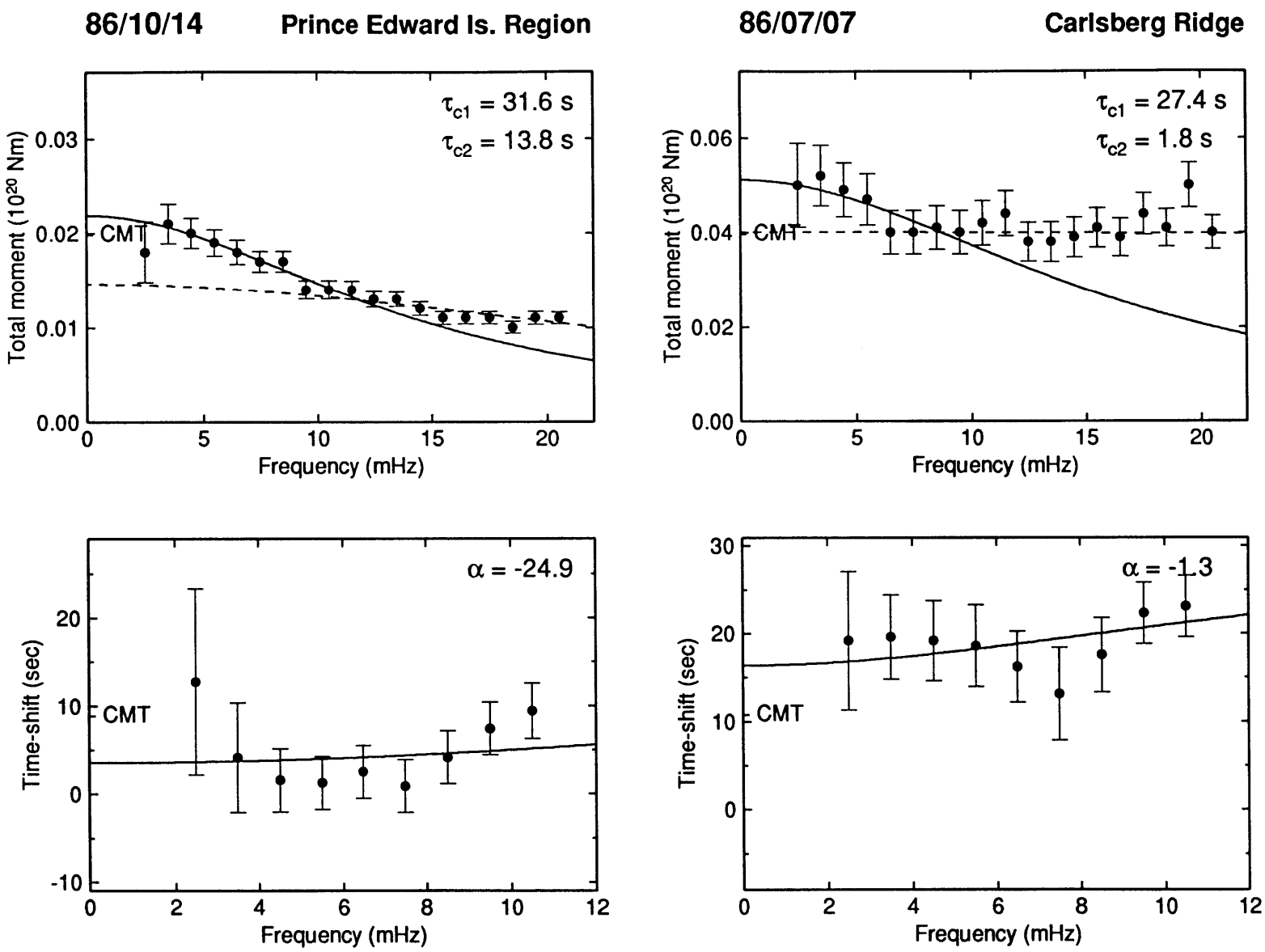
86/10/14
Prince Edward Is. Region
86/07/07
Carlsberg Ridge
τc1 = 31.6 s
τc2 = 13.8 s
τc1 = 27.4 s
τc2 = 1.8 s
CMT
Total moment (10^20 Nm)
Frequency (mHz)
α = -24.9
α = -1.3
Time-shift (sec)

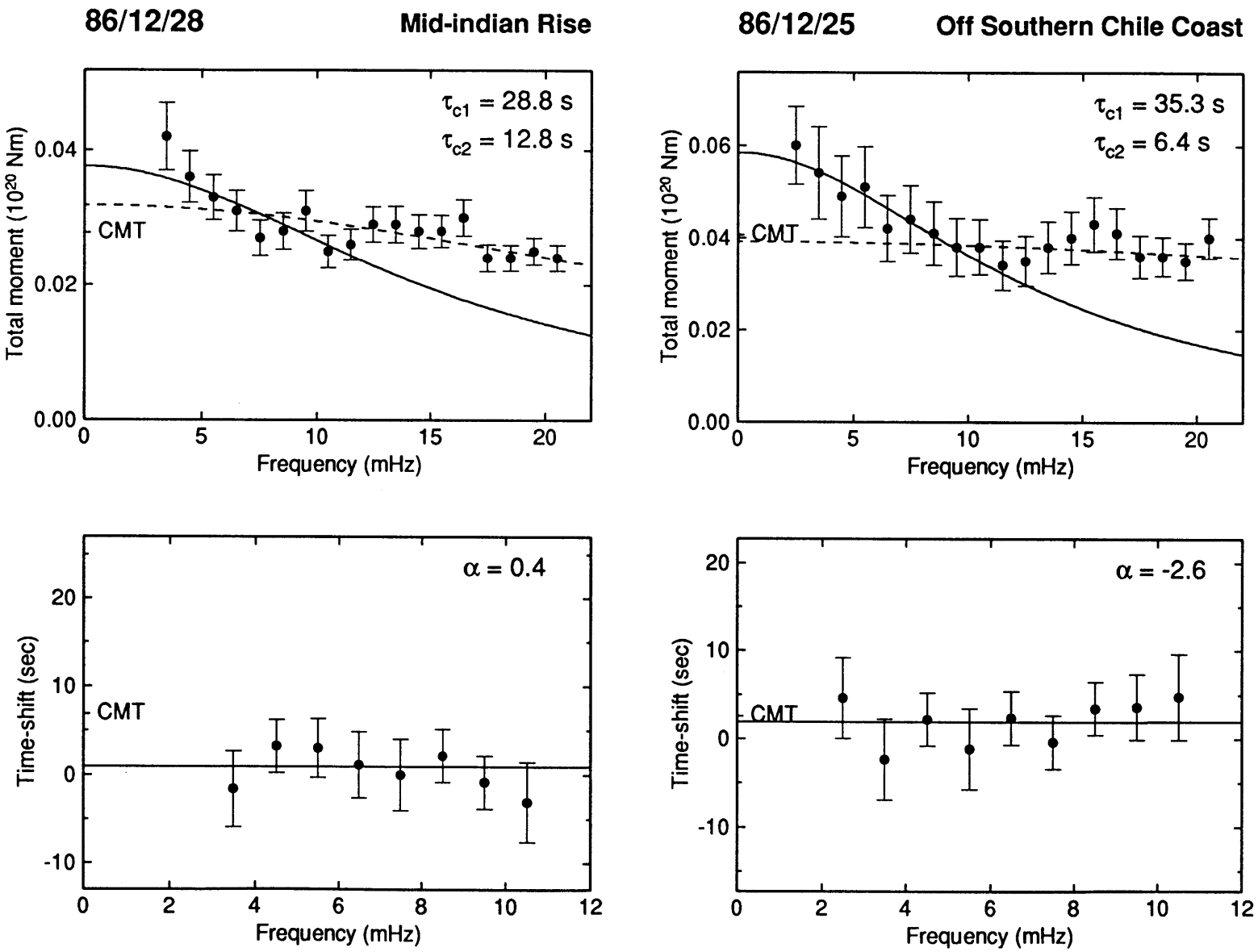
86/12/28
Mid-indian Rise
τ_{c1} = 28.8 s
τ_{c2} = 12.8 s
CMT
Total moment (10^{20} Nm)
0.00
0.02
0.04
0
5
10
15
20
Frequency (mHz)
86/12/25
Off Southern Chile Coast
τ_{c1} = 35.3 s
τ_{c2} = 6.4 s
CMT
Total moment (10^{20} Nm)
0.00
0.02
0.04
0.06
0
5
10
15
20
Frequency (mHz)
α = 0.4
CMT
Time-shift (sec)
-10
0
10
20
0
2
4
6
8
10
12
Frequency (mHz)
α = -2.6
CMT
Time-shift (sec)
-10
0
10
20
0
2
4
6
8
10
12
Frequency (mHz)

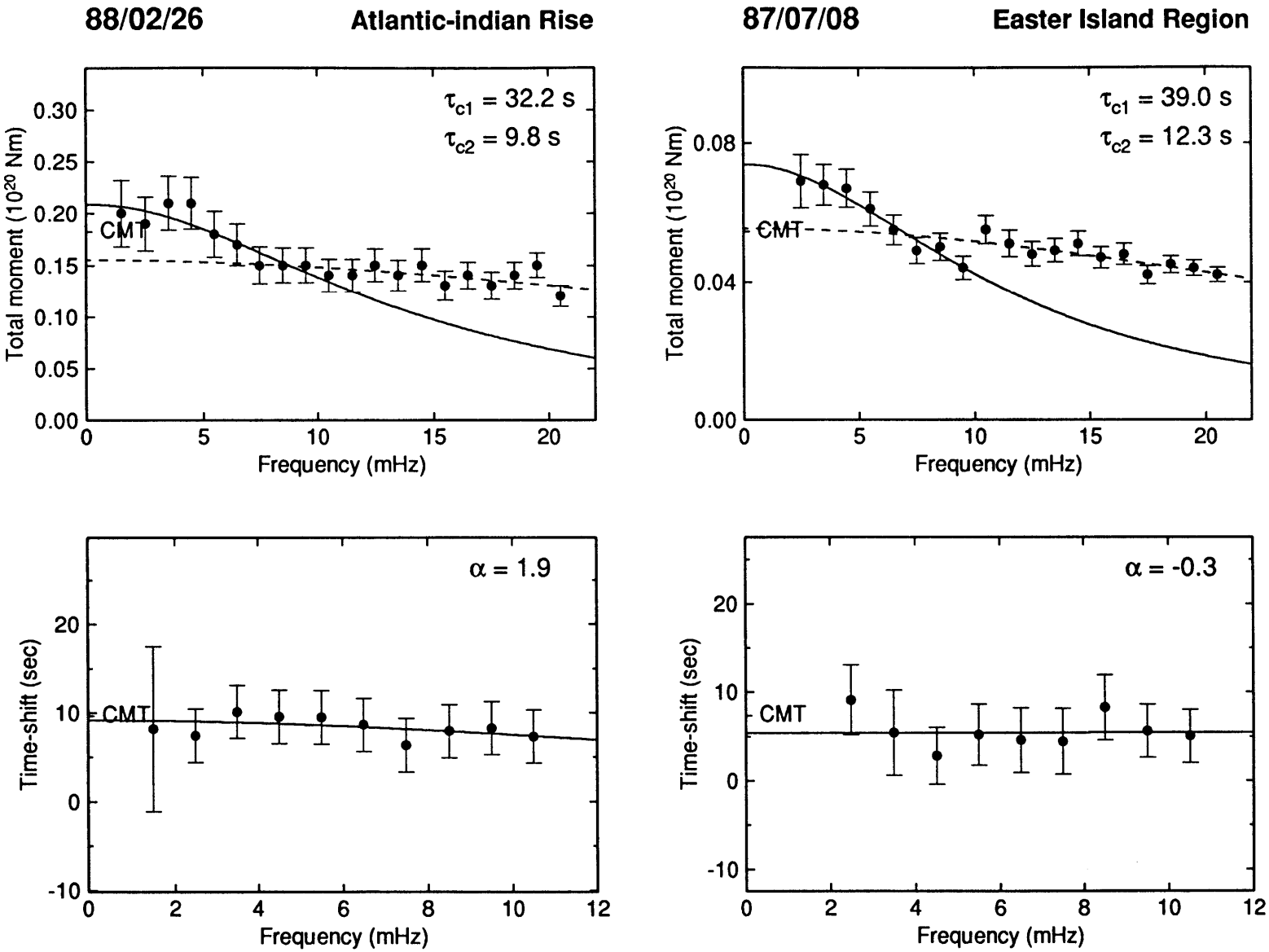
88/02/26
Atlantic-indian Rise
87/07/08
Easter Island Region
τ_{c1} = 32.2 s
τ_{c2} = 9.8 s
τ_{c1} = 39.0 s
τ_{c2} = 12.3 s
CMT
Total moment (10^{20} Nm)
Frequency (mHz)
α = 1.9
α = -0.3
Time-shift (sec)

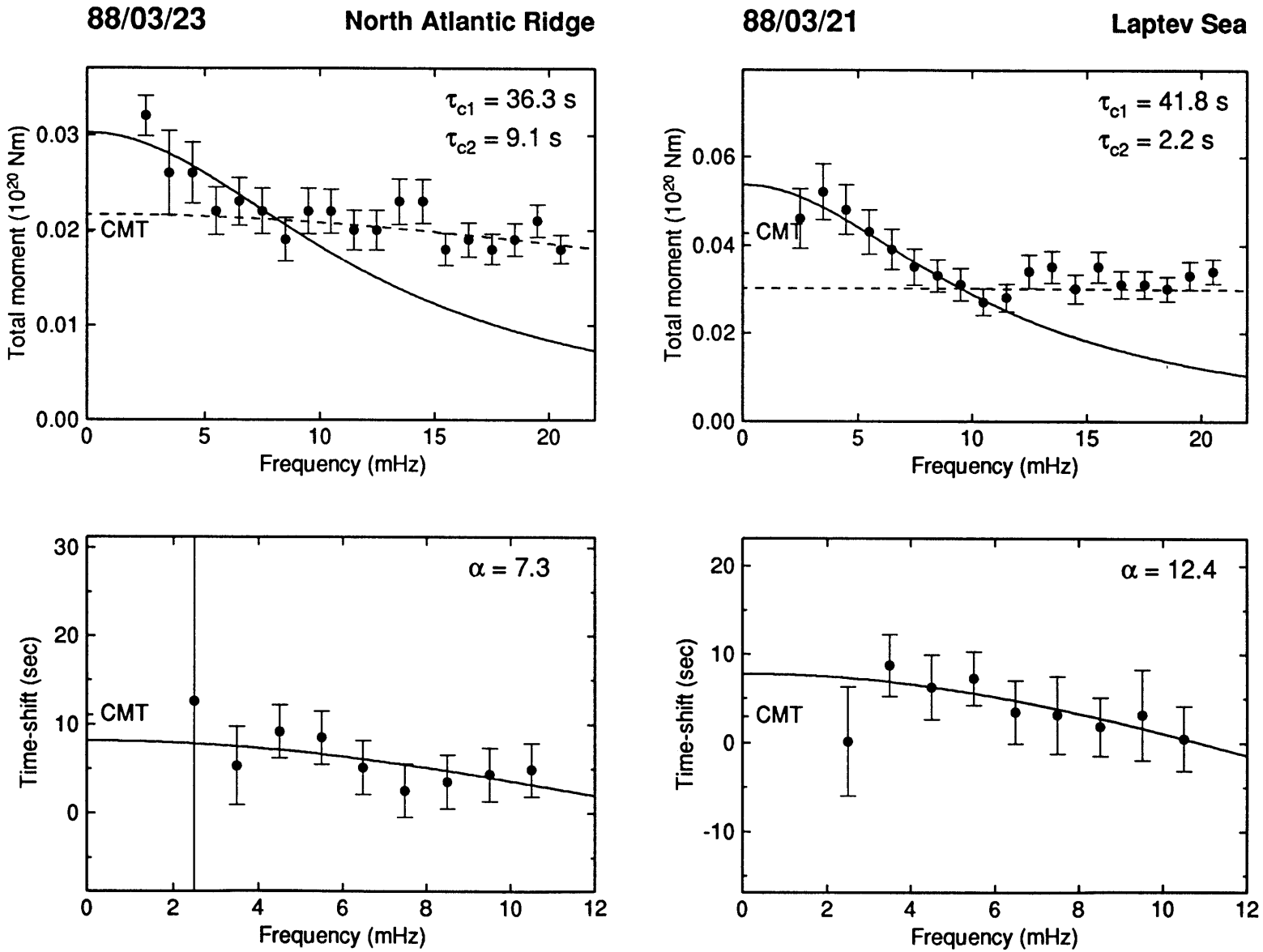
88/03/23
North Atlantic Ridge
88/03/21
Laptev Sea
τ_{c1} = 36.3 s
τ_{c2} = 9.1 s
τ_{c1} = 41.8 s
τ_{c2} = 2.2 s
CMT
CMT
Total moment (10^{20} Nm)
Total moment (10^{20} Nm)
Frequency (mHz)
Frequency (mHz)
α = 7.3
α = 12.4
CMT
CMT
Time-shift (sec)
Time-shift (sec)
Frequency (mHz)
Frequency (mHz)

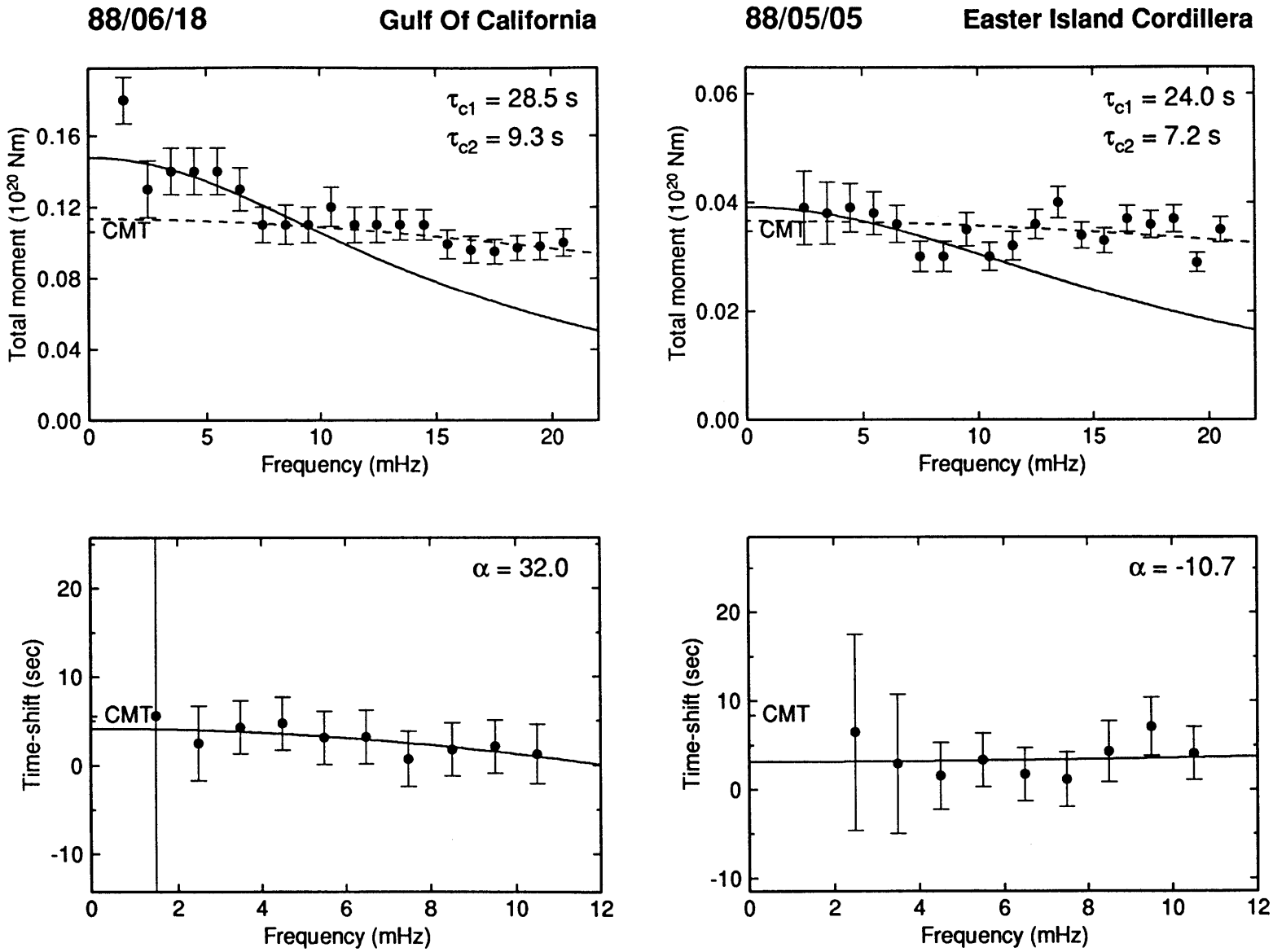
88/06/18
Gulf Of California
88/05/05
Easter Island Cordillera
τc1 = 28.5 s
τc2 = 9.3 s
τc1 = 24.0 s
τc2 = 7.2 s
CMT
Total moment (10^20 Nm)
Frequency (mHz)
α = 32.0
α = -10.7
Time-shift (sec)

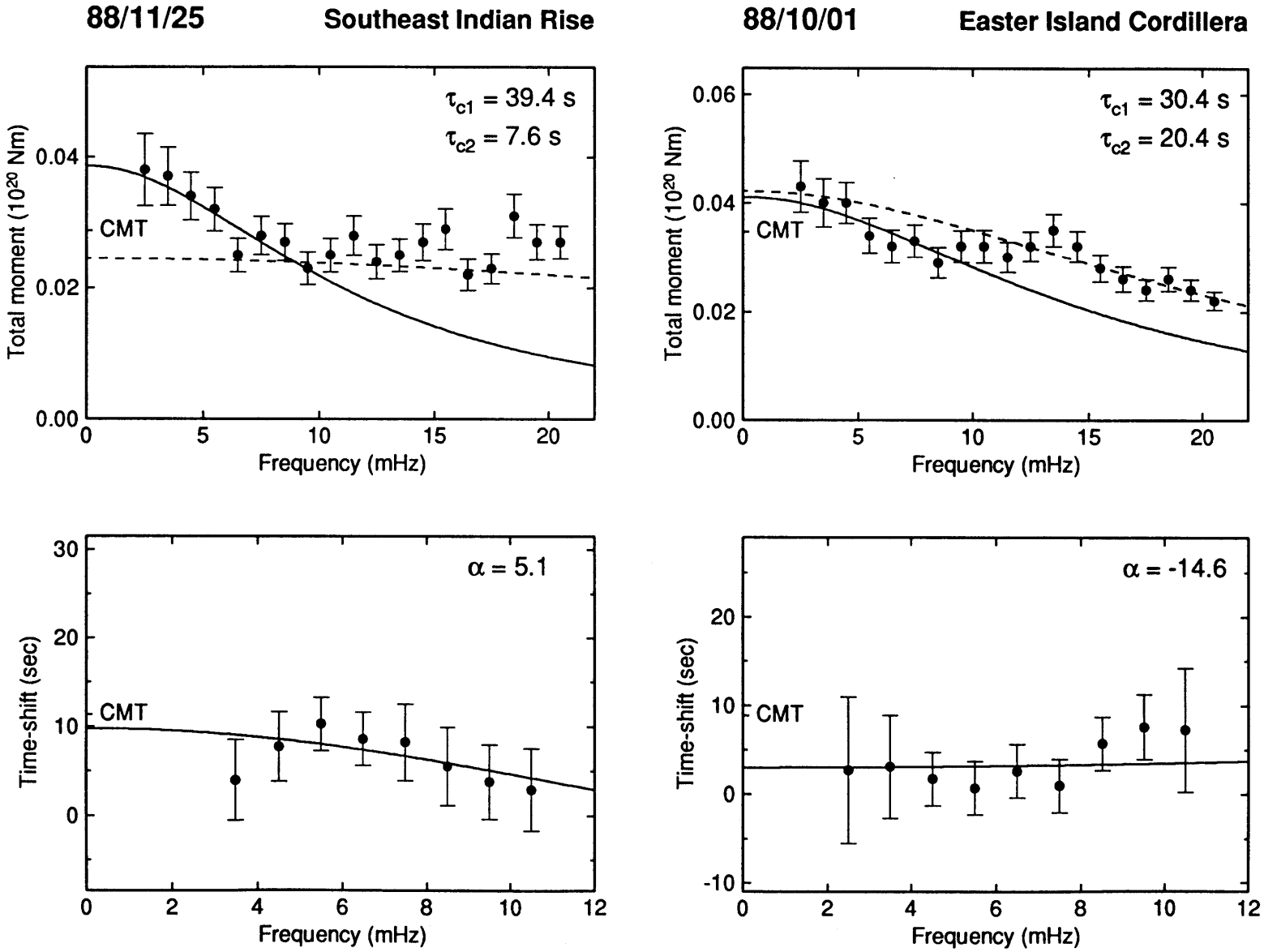
88/11/25
Southeast Indian Rise
88/10/01
Easter Island Cordillera
τc1 = 39.4 s
τc2 = 7.6 s
τc1 = 30.4 s
τc2 = 20.4 s
CMT
Total moment (10^20 Nm)
Frequency (mHz)
α = 5.1
α = -14.6
Time-shift (sec)

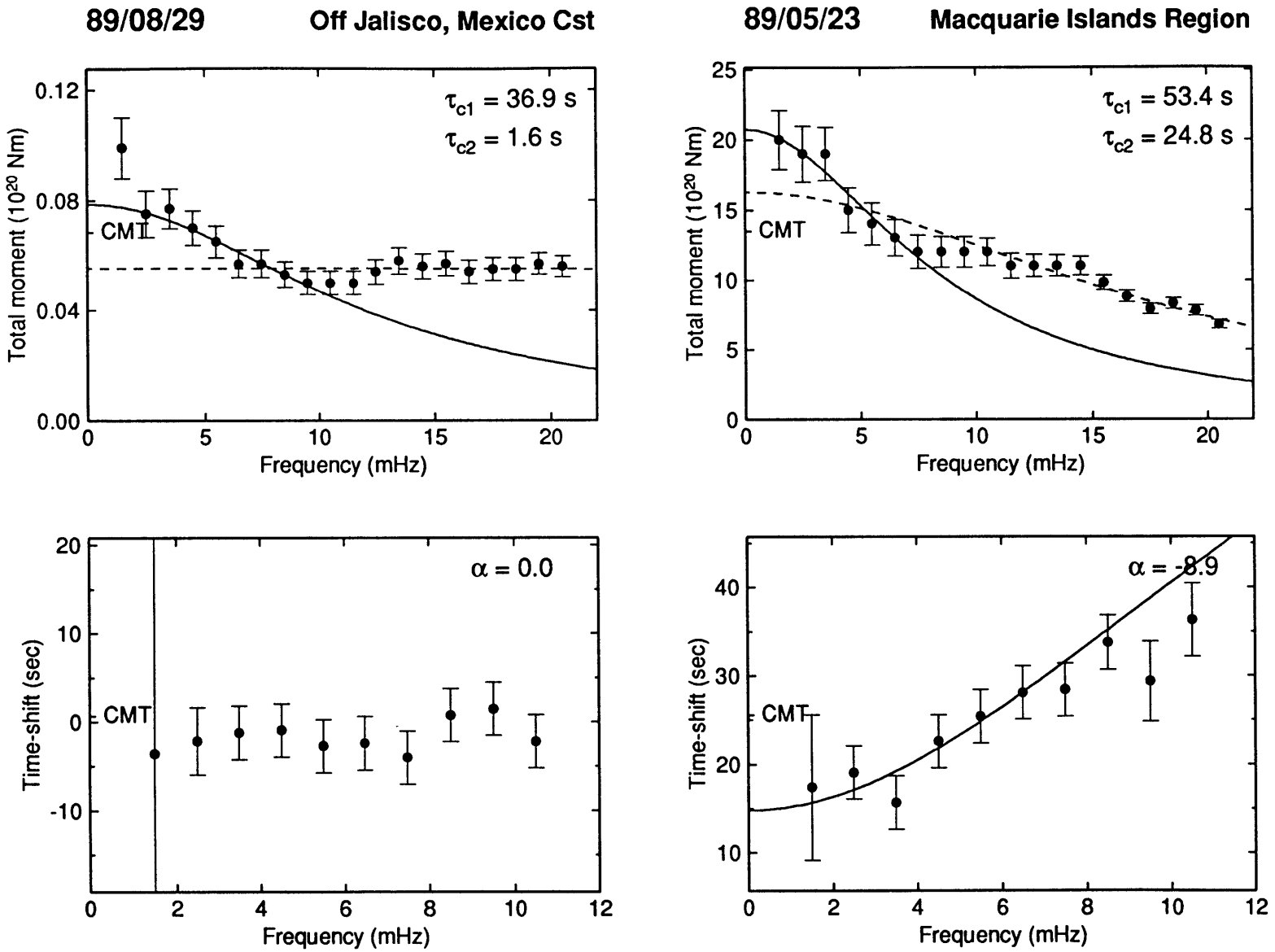
89/08/29
Off Jalisco, Mexico Cst
89/05/23
Macquarie Islands Region
τ_{c1} = 36.9 s
τ_{c2} = 1.6 s
τ_{c1} = 53.4 s
τ_{c2} = 24.8 s
CMT
Total moment (10^{20} Nm)
Frequency (mHz)
α = 0.0
α = -8.9
Time-shift (sec)

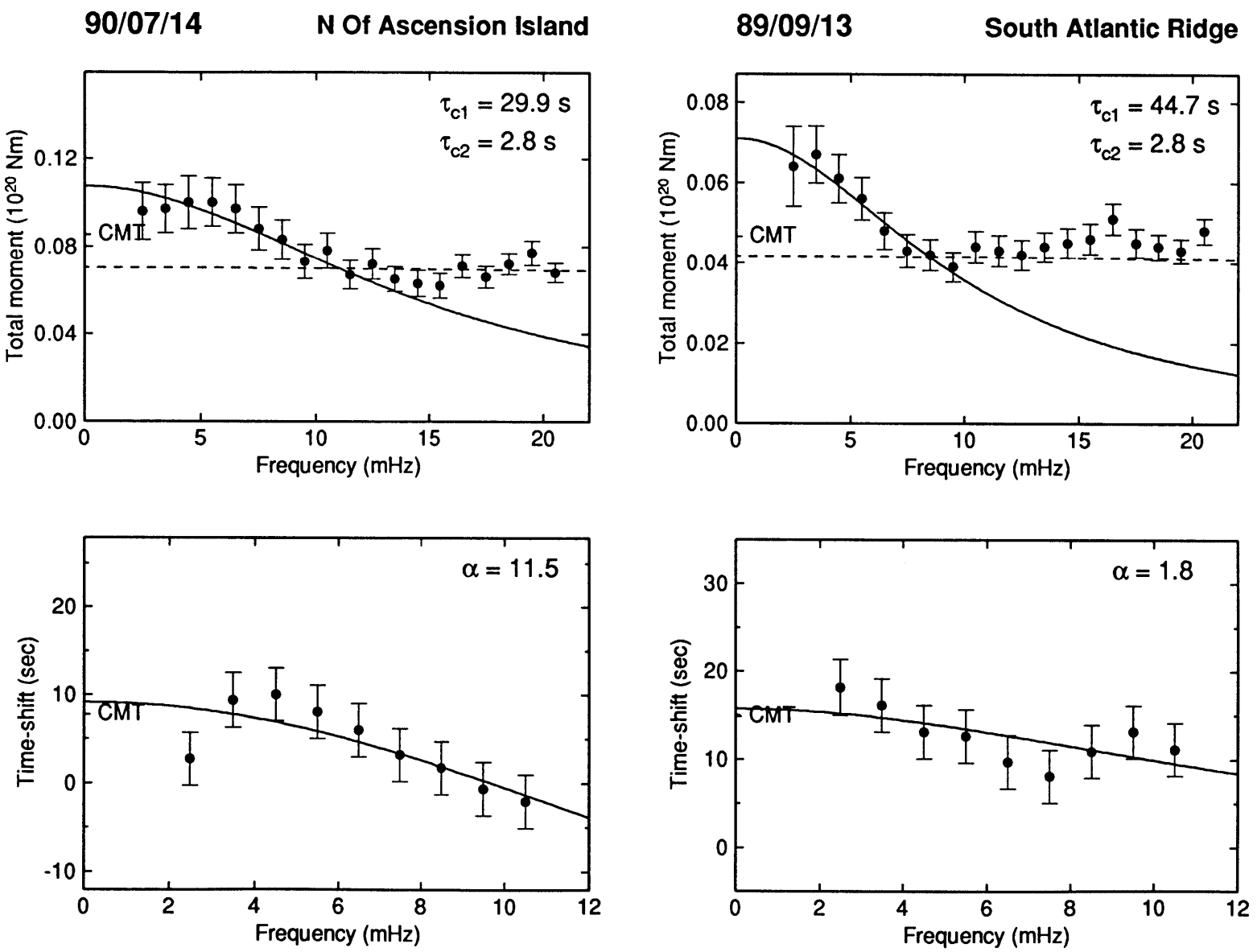
90/07/14
N Of Ascension Island
89/09/13
South Atlantic Ridge
τ_{c1} = 29.9 s
τ_{c2} = 2.8 s
τ_{c1} = 44.7 s
τ_{c2} = 2.8 s
CMT
Total moment (10^{20} Nm)
Frequency (mHz)
α = 11.5
α = 1.8
Time-shift (sec)

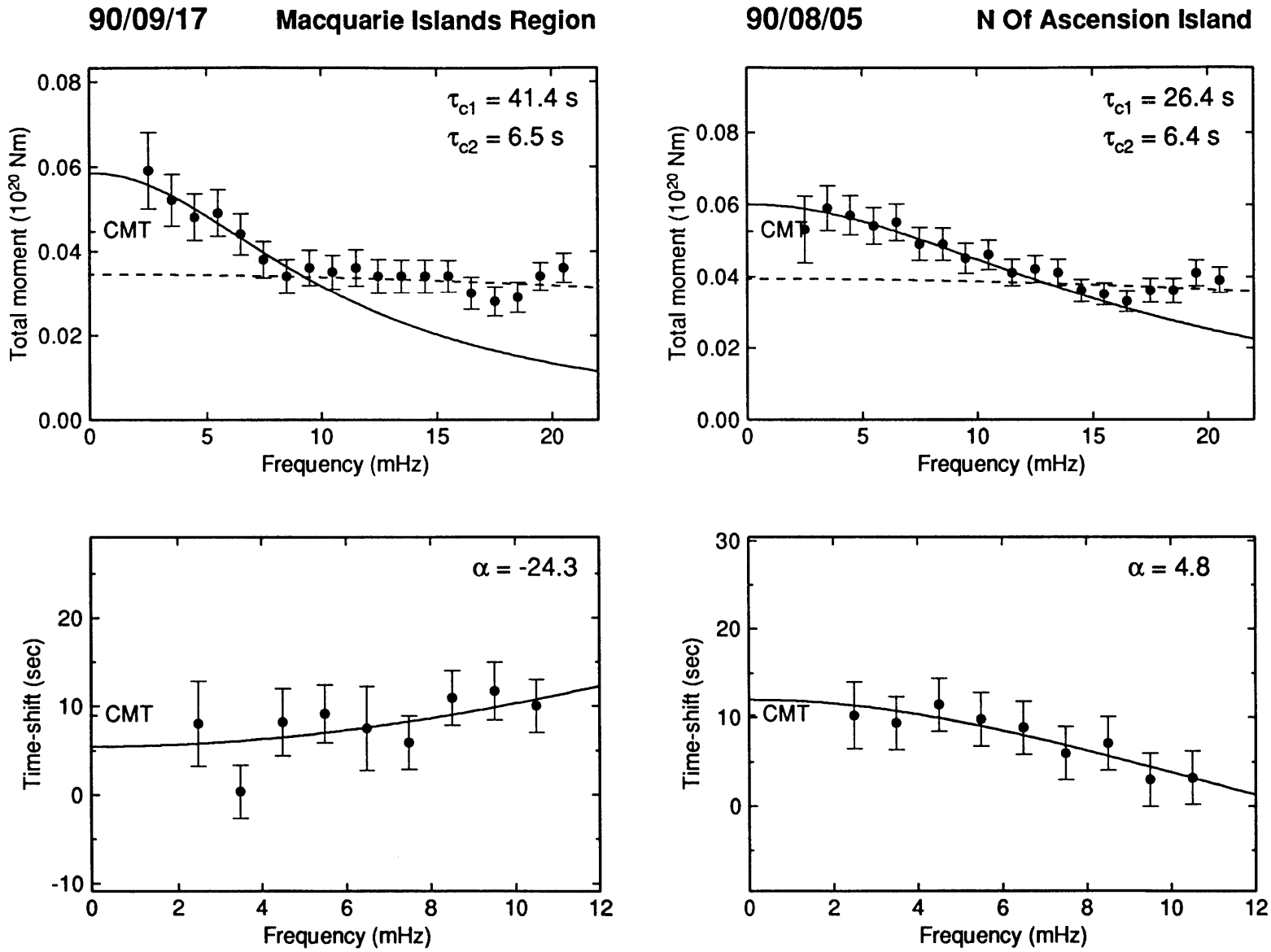
90/09/17
Macquarie Islands Region
τ_{c1} = 41.4 s
τ_{c2} = 6.5 s
CMT
Total moment (10^{20} Nm)
Frequency (mHz)
90/08/05
N Of Ascension Island
τ_{c1} = 26.4 s
τ_{c2} = 6.4 s
CMT
Total moment (10^{20} Nm)
Frequency (mHz)
α = -24.3
CMT
Time-shift (sec)
Frequency (mHz)
α = 4.8
CMT
Time-shift (sec)
Frequency (mHz)

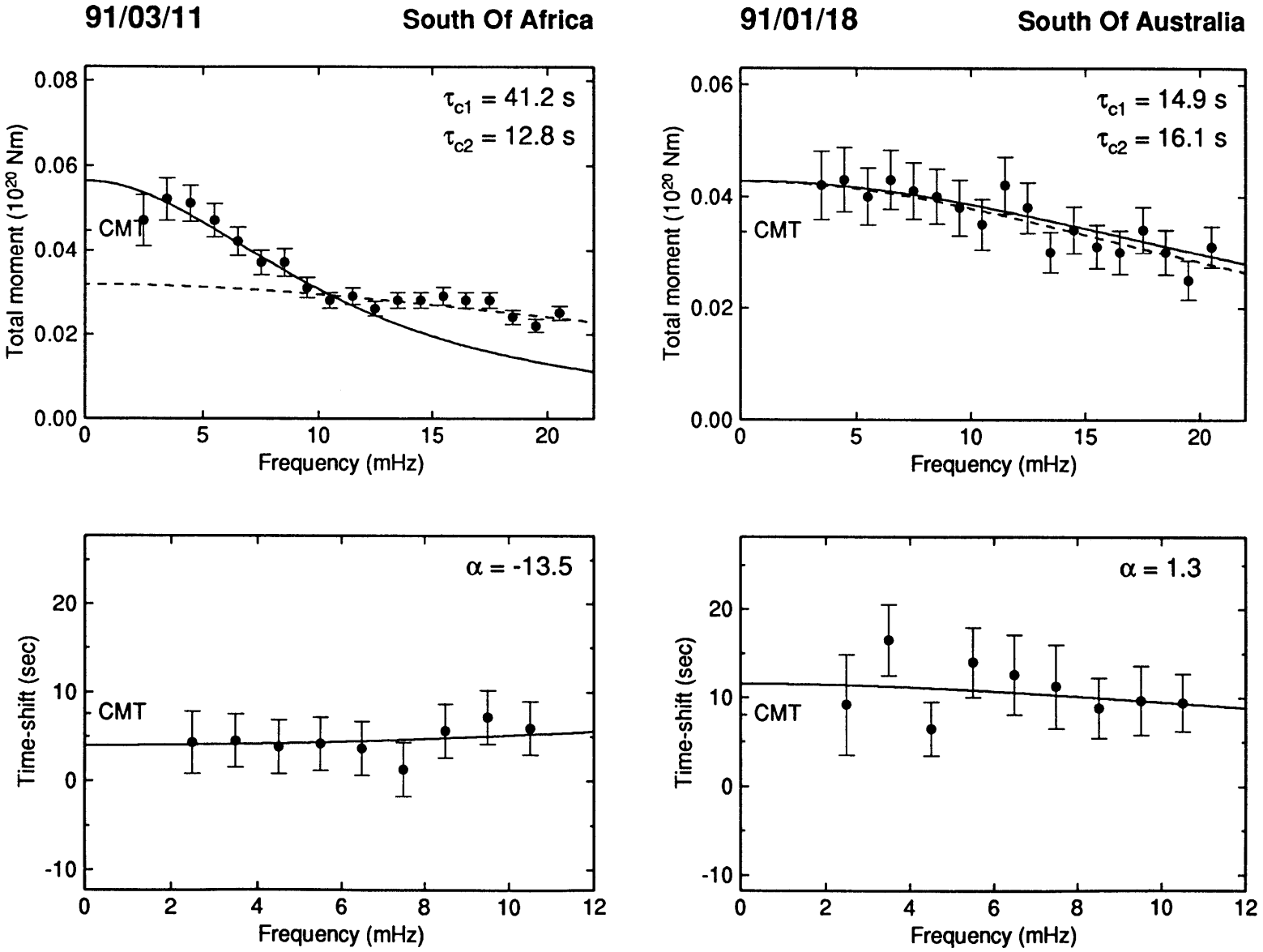
91/03/11
South Of Africa
τ_{c1} = 41.2 s
τ_{c2} = 12.8 s
CMT
Total moment (10^{20} Nm)
Frequency (mHz)
91/01/18
South Of Australia
τ_{c1} = 14.9 s
τ_{c2} = 16.1 s
CMT
Total moment (10^{20} Nm)
Frequency (mHz)
α = -13.5
CMT
Time-shift (sec)
Frequency (mHz)
α = 1.3
CMT
Time-shift (sec)
Frequency (mHz)

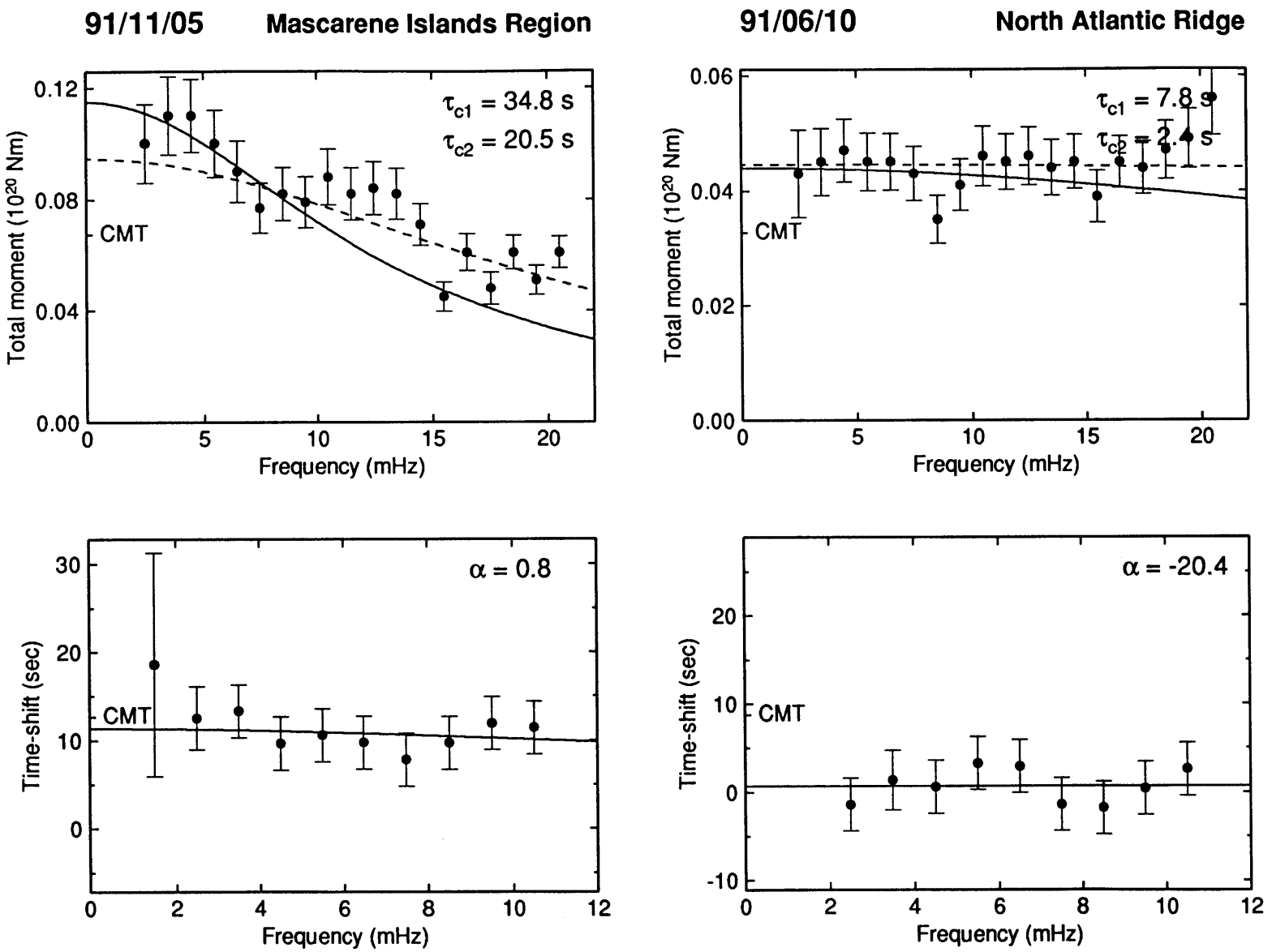
91/11/05
Mascarene Islands Region
91/06/10
North Atlantic Ridge
τ_{c1} = 34.8 s
τ_{c2} = 20.5 s
τ_{c1} = 7.8 s
τ_{c2} = 2.4 s
CMT
CMT
Total moment (10^{20} Nm)
Total moment (10^{20} Nm)
Frequency (mHz)
Frequency (mHz)
α = 0.8
α = -20.4
CMT
CMT
Time-shift (sec)
Time-shift (sec)
Frequency (mHz)
Frequency (mHz)

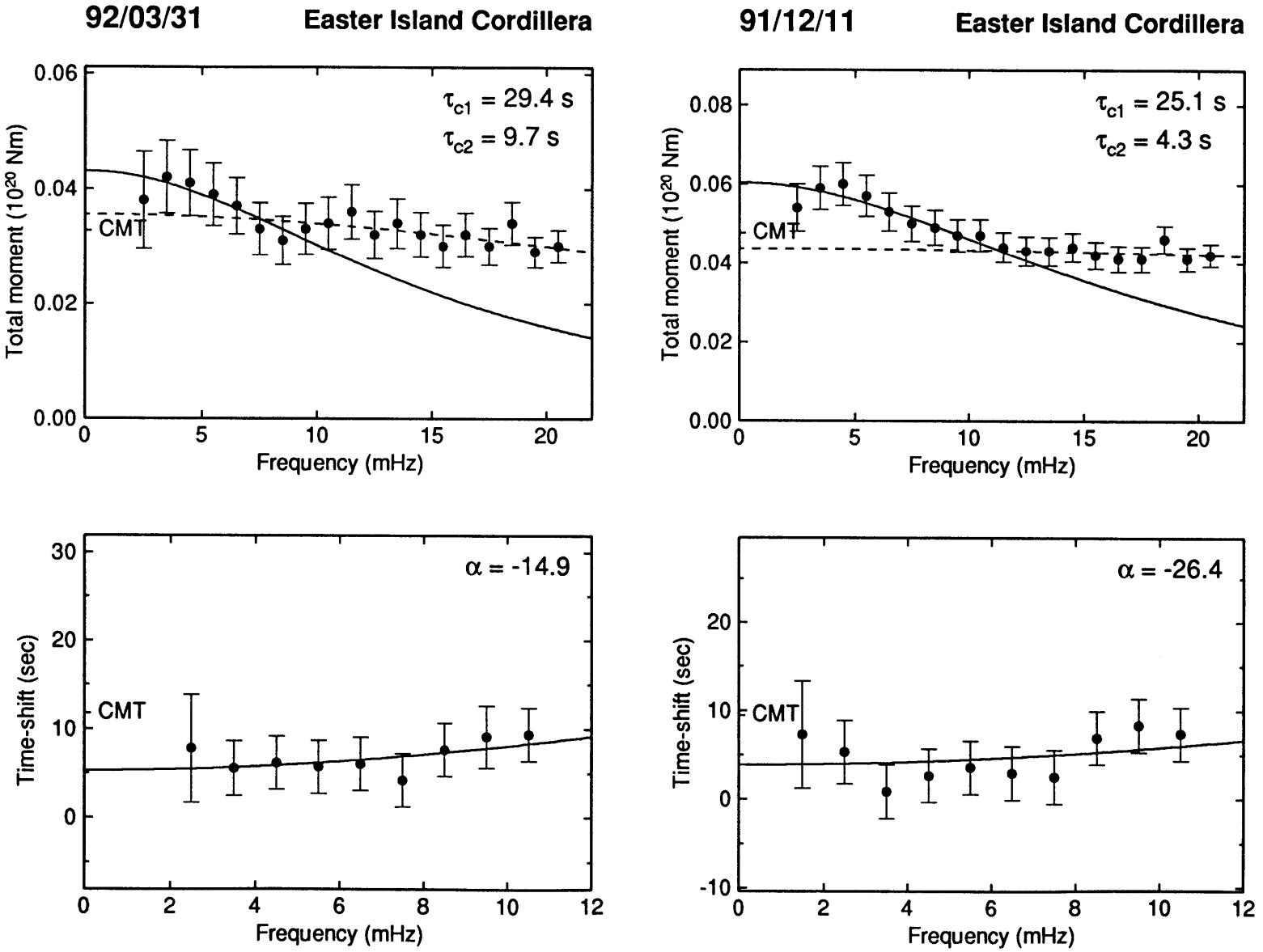
92/03/31
Easter Island Cordillera
τ_{c1} = 29.4 s
τ_{c2} = 9.7 s
CMT
Total moment (10^{20} Nm)
Frequency (mHz)
91/12/11
Easter Island Cordillera
τ_{c1} = 25.1 s
τ_{c2} = 4.3 s
CMT
Total moment (10^{20} Nm)
Frequency (mHz)
α = -14.9
CMT
Time-shift (sec)
Frequency (mHz)
α = -26.4
CMT
Time-shift (sec)
Frequency (mHz)

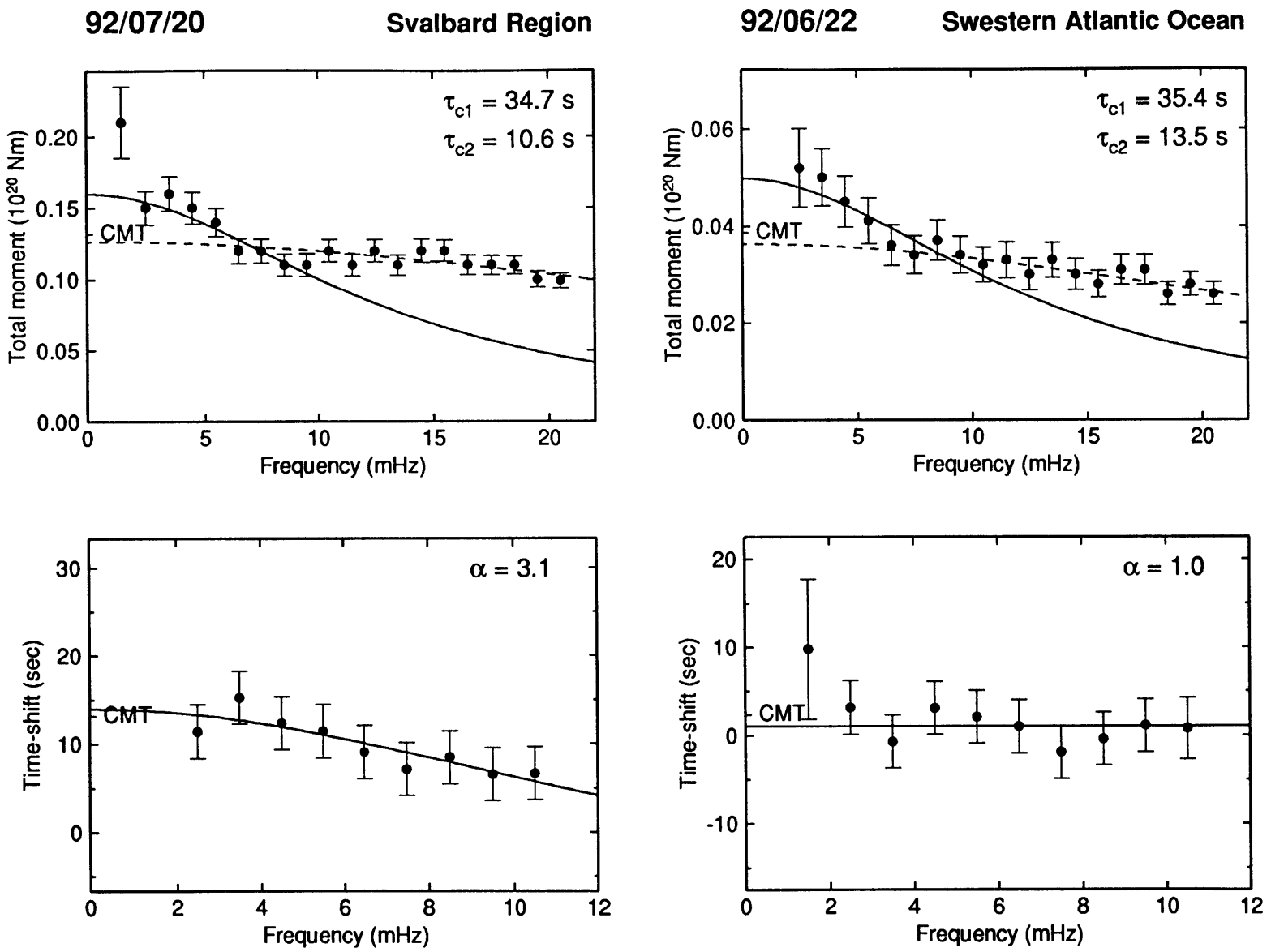
92/07/20
Svalbard Region
92/06/22
Swestern Atlantic Ocean
τ_{c1} = 34.7 s
τ_{c2} = 10.6 s
τ_{c1} = 35.4 s
τ_{c2} = 13.5 s
Total moment (10^{20} Nm)
CMT
Frequency (mHz)
α = 3.1
α = 1.0
Time-shift (sec)

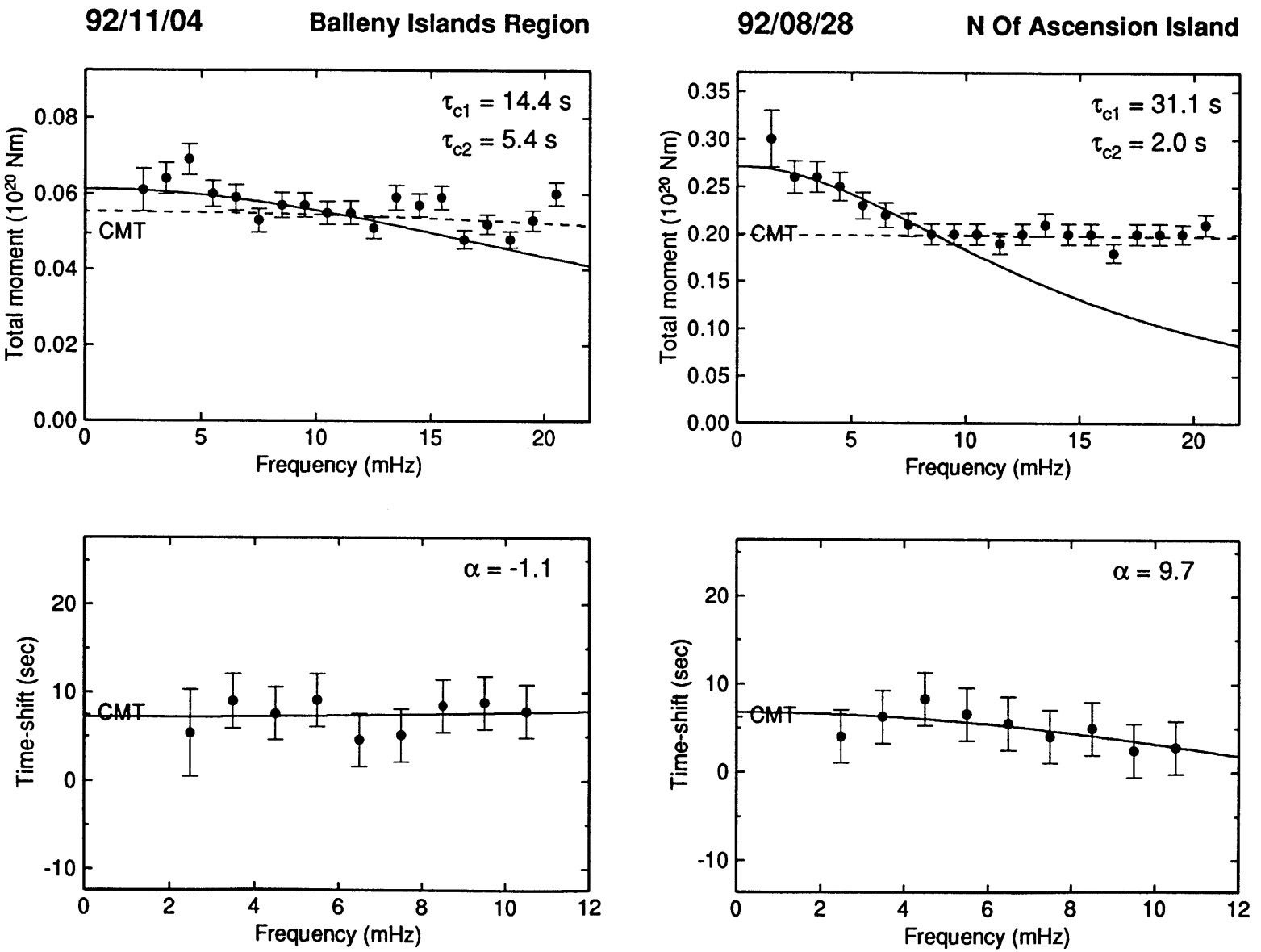
92/11/04
Balleny Islands Region
92/08/28
N Of Ascension Island
Total moment (10^{20} Nm)
τ_{c1} = 14.4 s
τ_{c2} = 5.4 s
CMT
Frequency (mHz)
τ_{c1} = 31.1 s
τ_{c2} = 2.0 s
Time-shift (sec)
α = -1.1
α = 9.7

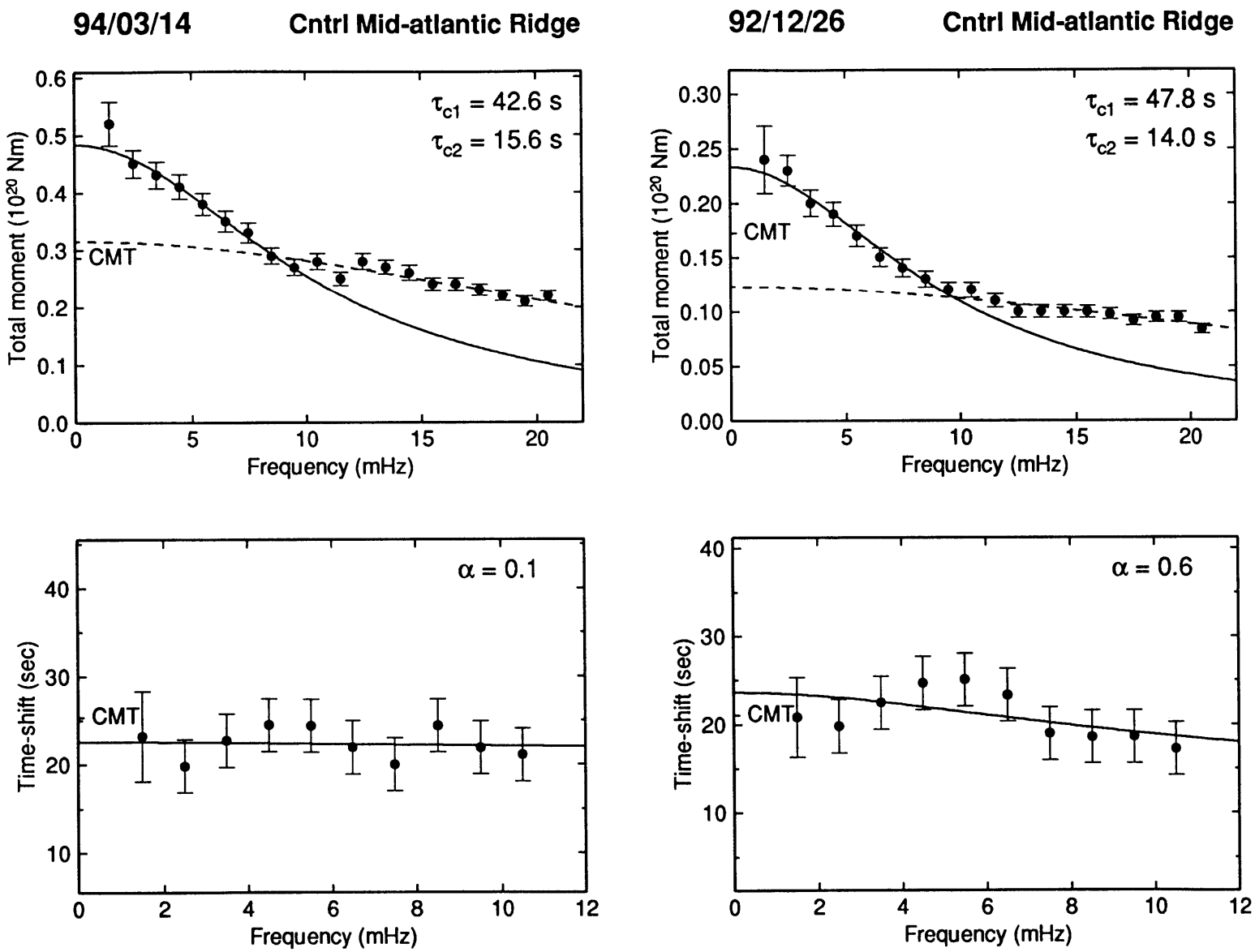
94/03/14
Cntrl Mid-atlantic Ridge
92/12/26
Cntrl Mid-atlantic Ridge
Total moment (10^20 Nm)
τc1 = 42.6 s
τc2 = 15.6 s
CMT
Frequency (mHz)
τc1 = 47.8 s
τc2 = 14.0 s
Time-shift (sec)
α = 0.1
α = 0.6

BIBLIOGRAPHY

Abe, K., Tsunami and mechanism of great earthquakes, *Physics of the Earth and Planetary Interiors*, *7*, 143-153, 1973.

Abercrombie, R. E., J. Mori, and P. C. Leary, Observations of the onset of the 28 June 1992 Landers earthquake: implication for earthquake nucleation and propagation, *Eos Trans AGU*, *73*, 1992.

Agnew, D. C., and J. Berger, Vertical seismic noise at very low frequencies, *J. Geophys. Res.*, 5420-5424, 1978.

Agnew, D. C., J. Berger, R. Bulland, W. E. Farrell, and J. F. Gilbert, International Deployment of Accelerometers: a network for very long period seismology, *Eos Trans. AGU*, *57*, 180-188, 1976.

Agnew, D. C., J. Berger, W. E. Farrell, J. F. Gilbert, G. Masters, and D. Miller, Project IDA: A Decade in Review, *Eos Trans. AGU*, 203-212, 1986.

Aki, K., and P. G. Richards, *Quantitative seismology: Theory and methods*, Freeman, San Francisco, 1980.

Anderson, H. J., The 1989 Macquarie Ridge earthquake and its contribution to regional seismic moment budget, *Geophys. Res. Lett.*, *17*, 1013-1016, 1990.

Anderson, H. J., and J. Zhang, Long-period seismic radiation from the May 23, 1989, Macquarie Ridge earthquake: Evidence for coseismic slip in the mantle?, *J. Geophys. Res.*, *96*, 19853-19863, 1991.

Backus, G., Interpreting the seismic glut moments of total degree two or less, *Geophys. J. R. Astron. Soc.*, *51*, 1-25, 1977.

Backus, G., Seismic sources with observable glut moments of spatial degree two, *Geophys. J. R. Astron. Soc.*, *51*, 27-45, 1977.

Backus, G., and M. Mulcahy, Moment tensors and other phenomenological descriptions of seismic sources - I. Continuous displacements, *Geophys. J. R. Astron. Soc.*, *46*, 341-361, 1976.

Backus, G., and M. Mulcahy, Moment tensors and other phenomenological descriptions of seismic sources - II. Discontinuous displacements, *Geophys. J. R. Astron. Soc.*, *46*, 301-329, 1976.

Bergman, E. A., J. L. Nabelek, and S. C. Solomon, An extensive region of off-ridge normal-faulting earthquakes in the Southern Indian ocean, *J. Geophys. Res.*, *89*, 2425-2443, 1984.

Bergman, E. A., and S. C. Solomon, Transform fault earthquakes in the North Atlantic: Source mechanisms and depth of faulting, *J. Geophys. Res.*, *93*, 9027-9057, 1988.

Beroza, G., and T. H. Jordan, Searching for slow and silent earthquakes using free oscillations, *J. Geophys. Res.*, *95*, 2485-2510, 1990.

Blanpied, M. L., T. E. Tullis, and J. D. Weeks, Frictional behavior of granite at low and high sliding velocities, *Geophys. Res. Let.*, *14*, 554-557, 1987.

Blanpied, M. L., D. A. Lockner, and J. D. Byerlee, Fault stability inferred from granite sliding experiments at hydrothermal conditions, *Geophys. Res. Let.*, *18*, 609-612, 1991.

Bonafede, M., E. Boschi, and M. Dragoni, Mechanical models of slow source processes, in *Earthquakes; Observation, theory and interpretation*, edited by H. Kanamori, and E. Boschi, *International School of Physics "Enrico Fermi"*, pp. 330-344, North-Holland Publ. Co., Amsterdam, 1983.

Bonafede, M., E. Boschi, and M. Dragoni, Viscoelastic stress relaxation on deep fault sections as a possible source of very long period elastic waves, *J. Geophys. Res.*, *88*, 2251-2260, 1983.

Bonafede, M., E. V. Boschi, and M. Dragoni, Slow fracture propagation on a fault surface with an embedded viscous layer, *24*, 3-15, 1982.

Braunmiller, J., and J. Nábelek, Rupture Process of the Macquarie Ridge earthquake of May 23, 1989, *Geophys. Res. Lett.*, *17*, 1017-1020, 1990.

Bryant, A. S., and L. M. Jones, Anomalously deep crustal earthquakes in the Ventura basin, Southern California, *J. Geophys. Res.*, *97*, 437-447, 1992.

Buland, R., and F. Gilbert, Matched filtering for the seismic moment tensor, *Geophys. Res. Letters*, *3*, 205-206, 1976.

Burr, N., and S. Solomon, The relationship of source parameters of oceanic transform earthquakes to plate velocity and transform length, *J. Geophys. Res.*, *83*, 1193-1205, 1978.

Byrne, D. E., D. M. Davis, and L. R. Sykes, Loci and maximum size of thrust earthquakes and the mechanics of the shallow region of subduction zones, *Tectonics*, *7*, 833-857, 1988.

Campillo, M., and R. J. Archuleta, A rupture model for the 28 June 1992 Landers, California, earthquake, *Geophys. Res. Let.*, *20*, 647-650, 1993.

Cifuentes, I. L., The 1960 Chilean earthquake, *J. Geophys. Res.*, *94*, 665-680, 1989.

Cifuentes, I. L., and P. G. Silver, Low-frequency source characteristics of the great 1960 Chilean earthquake, *J. Geophys. Res.*, *94*, 643-663, 1989.

Constable, S. C., R. L. Parker, and C. G. Constable, Occam's Inversion: A pratical algorithm for generating smooth models from electromagnetic sounding data, *Geophysics*, *52*, 289-300, 1987.

Dahlen, F. A., The normal modes of a rotating, elliptical earth, *Geophys. J. Roy. Astron. Soc.*, *16*, 329-367, 1968.

Dahlen, F. A., On the raio of P-wave to S-wave corner frequencies for shallow earthquake sources, *Bull. Seis. Soc. Am.*, *64*, 1159-1180, 1974.

Dahlen, F. A., Reply, *J. Geophys. Res.*, *81*, 4951-4956, 1976.

Dahlen, F. A., The spectra of unresolved split normal modes multiplets, *Geophys. J. R. Astron. Soc.*, *58*, 133, 1979.

Dahlen, F. A., Multiplet coupling and the calculation of synthetic long-period seismograms, *Geophys. J. R. Astr. Soc.*, *91*, 241-254, 1987.

Dahlen, F. A., Single-force representation of shallow landslide sources, *Bull. Seis. Soc. Am.*, *83*, 130-143, 1993.

Das, S., Reactivation of an oceanic fracture by the Macquarie Ridge earthquake of 1989, *Nature*, *357*, 150-153, 1992.

Das, S., The Macquarie Ridge earthquake of 1989, *Geophys. J. Int*, *115*, 778-798, 1993.

Das, S., and B. V. Kostrov, Fracture of a single asperity on a finite fault; A model for slow earthquake?, *Eos Trans AGU*, *66*, 971, 1985.

Das, S., and B. V. Kostrov, Fracture of a single asperity on a finite fault: A model for weak fault?, in *Earthquake Source Mechanism*, edited by S. Das, J. Boatwright, and C. H. Scholz, *Geophysical Monograph 37, Maurice Ewing Volume 6*, pp. 91-96, American Geophysical Union, Washington, D.C., 1986.

Das, S., and B. V. Kostrov, Inversion for seismic slip rate history and distribution with stabilizing constraints: Application to the 1986 Andreanof Islands earthquake, *J. Geophys. Res.*, *95*, 6899-6913, 1990.

Das, S., and B. V. Kostrov, Diversity of solutions of the problem of earthquake faulting inversion. Application to SH waves for the great 1989 Macquarie Ridge earthquake, *Phys. Earth Planet. Int.*, in press.

Das, S., and C. H. Scholz, Subcritical rupture in the Earth, II: Theoretical calculations, *Eos Trans. AGU*, *61*, 305, 1980.

Das, S., and C. H. Scholz, Theory of time-dependent rupture in the earth, *J. Geophys. Res.*, *86*, 6039-6051, 1981.

Davies, G., and J. N. Brune, Global plate motion rates from seismicity data, *Nature*, *229*, 101-107, 1971.

DeMets, C., R. G. Gordon, D. F. Argus, and S. Stein, Current plate motions, *Geophys. J. Int.*, *101*, 425-478, 1990.

Dieterich, J. H., Preseismic fault slip and earthquake prediction, *J. Geophys. Res.*, *83*, 3940-3948, 1978.

Dieterich, J. H., Modeling of rock friction 1. Experimental results and constitutive equations, *J. Geophys. Res.*, *84*, 2161-2168, 1979.

Dieterich, J. H., A model for the nucleation of earthquake slip, in *Earthquake Source Mechanism*, edited by S. Das, J. Boatwright, and C. H. Scholz, *Geophysical Monograph 37, Maurice Ewing Volume 6*, pp. 37-47, American Geophysical Union, Washington, D.C., 1986.

Dieterich, J. H., Earthquake nucleation on faults with rate- and state-dependent strength, *Tectonophysics*, *211*, 115-134, 1992.

Doornbos, D. J., Seismic moment tensors and kinematics source parameters, *Geophys. J. R. astr. Soc.*, *69*, 235-251, 1982.

Doornbos, D. J., Seismic source spectra and moment tensors, *Phys. Earth Planet Int.*, *30*, 214-227, 1982.

Durek, J. J., G. Ekström, and S. Tsuboi, Effect of anelastic heterogeneity on measurements of fundamental mode attenuation, *Eos Trans AGU*, *74*, 439, 1993.

Durek, J. J., M. H. Ritzwoller, and J. H. Woodhouse, Constraining upper mantle anelasticity using surface wave amplitude anomalies, *Geophys. J. Int.*, *114*, 249-272, 1993.

Dziewonski, A. M., and D. L. Anderson, Preliminary reference Earth model, *Physics of the Earth and Planetary Interiors*, *25*, 297-356, 1981.

Dziewonski, A. M., T.-A. Chou, and J. H. Woodhouse, Determination of earthquake source parameters from waveform data for studies of global and regional seismicity, *J. Geophys. Res.*, *86*, 2825-2852, 1981.

Dziewonski, A. M., G. Ekström, J. H. Woodhouse, and G. Zwart, Centroid-moment tensor solutions for April-June 1989, *Physics of the Earth and Planetary Interiors*, *60*, 243-253, 1990.

Dziewonski, A. M., and F. Gilbert, Temporal variation of the seismic moment tensor and the evidence of precursive compression for two deep earthquakes, *Nature*, *247*, 185-188, 1974.

Dziewonski, A. M., and J. M. Steim, Dispersion and attenuation of mantle waves from waveform inversion, *Geophys J. R. Astr. Soc.*, *70*, 503-527, 1982.

Dziewonski, A. M., and J. H. Woodhouse, An experiment in systematic study of global seismicity: centroid-moment tensor solutions for 201 moderate and large earthquakes of 1981, *J. Geophys. Res.*, *88*, 3247-3271, 1983.

Efron, B., and G. Gong, A leisurely look at the bootstrap, the jackknife, and cross-validation, *The American Statistician*, *37*, 36-48, 1983.

Ekström, G., A very broad band inversion method for the recovery of earthquake source parameters, *Tectonophysics*, *166*, 73-100, 1989.

Ekström, G., and A. M. Dziewonski, Evidence of bias in estimations of earthquake size, *Nature*, *332*, 319-323, 1988.

Ekström, G., and B. Romanowicz, The 23 May 1989 Macquarie Ridge earthquake: A very broad band analysis, *Geophys. Res. Lett.*, *17*, 993-996, 1990.

Ekström, G. A., A broad band method of earthquake analysis, thesis, Harvard University, 1987.

Fowler, C. M. R., *The solid earth. An introduction to global geophysics*, pp. 472, Cambridge University Press, Cambridge, 1990.

Fox, P. J., and D. G. Gallo, The geology of North Atlantic transform plate boundaries and their aseismic extensions, in *The Geology of North America, Volume M, The Western North Atlantic Region*, edited by P. R. Vogt, and B. E. Tucholke, pp. 157-172, Geological Society of America, Boulder, Colorado, 1986.

Fox, P. J., and D. G. Gallo, Transforms of the Eastern Central Pacific, in *The Geology of North America, Volume N, The Eastern Pacific Ocean and Hawaii*, edited by E. L. Winterer, D. M. Hussong, and R. W. Decker, pp. 111-124, Geological Society of America, Boulder, Colorado, 1989.

Fuchs, K., and G. Müller, Computation of synthetic seismograms with the reflectivity method and comparison of observations, *Geophys. J. R. Astr. Soc.*, *23*, 417-433, 1971.

Gee, L. S., and T. H. Jordan, Generalized seismological data functionals, *Geophys. J. Int.*, *111*, 363-390, 1992.

Gilbert, F., Excitation of the normal modes of the Earth by earthquake sources, *Geophys. J. R. Astron. Soc.*, *22*, 223- 226, 1970.

Gilbert, F., Derivation of source parameters from low-frequency spectra, *Phil. Trans. R. Soc. London A*, *274*, 369-371, 1973.

Gilbert, F., An introduction to low-frequency seismology, in *Physics of the Earth's interior: Proceedings of the International School of Physics "Enrico Fermi", Course LXXVII*, edited by A. M. Dziewonski, and E. Boschi, pp. 41-126, Soc. Italiana de Fisica, Bologna, 1980.

Gilbert, F., and A. M. Dziewonski, An application of normal mode theory to the retrieval of structural parameters and source mechanisms from seismic spectra, *Phil Trans. R. Soc.*, *278*, 187-269, 1975.

Harabaglia, P., Low-frequency source parameters of twelve large earthquakes, Masters thesis, Massachusetts Institute of Technology, 1993.

Hill, D. P., Seismicity in the Western United States remotely triggered by the M 7.4 Landers, California, earthquake of June 28, 1992, *Science*, *260*, 1617-1623, 1993.

Herrin, E., Introduction to "1968 Seismological tables for P-phases", *Bull. Seismol. Soc. Am.*, *58*, 1193-1195, 1968.

Hobbs, B. E., A. Ord, and C. Teyssier, Earthquakes in the ductile regime?, *Pageoph*, *124*, 309-336, 1986.

Hori, S., Y. Fukao, N. Suda, Y. Ishihara, T. Shibutani, and K. Hirahara, Local network observations of the earth's free oscillations: apparent centroid of the 1989 Macquarie Ridge earthquake, *Geophys. Res. Letters*, *20*, 393-398, 1993.

Houston, H., Broadband source spectrum, seismic energy, and stress drop of the 1989 Macquarie Ridge earthquake, *Geophys. Res. Lett.*, *17*, 1021-1024, 1990.

Huang, P. Y., and S. C. Solomon, Centroid depths of mid-ocean ridge earthquake: Dependence on spreading Rate, *J. Geophys. Res.*, *93*, 13445-13477, 1988.

Hwang, L. J., and H. Kanamori, Rupture process of the 1987-1988 Gulf of Alaska earthquake sequence, *J. Geophys. Res.*, *97*, 19881-19908, 1992.

Ida, Y., Slow-moving deformation pulses along tectonic faults, *Phys. Earth Planet. Inter*, *9*, 328-337, 1975.

Ide, S., F. Imamura, Y. Yoshida, and K. Abe, Source Characteristics of the Nicaragua tsunami earthquake of September 2, 1992, *Geophys. Res. Let.*, *20*, 863-866, 1993.

Ihmlé, P., and T. H. Jordan, Slow earthquakes on transform faults: a global study, *XX General Assembly of the IUGG*, 102, 1991.

Ihmlé, P. F., P. Harabaglia, and T. H. Jordan, Teleseismic detection of a slow precursor to the great 1989 Macquarie ridge earthquake, *Science*, *261*, 1993.

Johnston, M. J. S., A. T. Linde, and M. T. Gladwin, Near-fiel high resolution strain measurements prior to the October 18, 1989, Loma Prieta Ms 7.1 earthquake, *Geophys. Res. Lett.*, *17*, 1777-1182, 1990.

Jordan, T. H., A procedure for estimating lateral variations from low-frequency eigenspectra data, *Geophys. J. R. Astron. Soc.*, *52*, 441-455, 1978.

Jordan, T. H., Dectecting slow precursors to fast seismic ruptures, *Eos Trans. AGU*, *71*, 559, 1990.

Jordan, T. H., Far-Field detection of slow precursors to fast seismic ruptures, *Geophys. Res. Lett.*, 1991.

Jordan, T. H., A. F. Sheehan, and M. A. Riedesel, Detecting slow precursors to fast seismic ruptures, *Eos Trans. AGU, 69*, 1304, 1988.

Jordan, T. H., and K. A. Sverdrup, Teleseismic location techniques and their application to earthquake clusters in the South-Central Pacific, *Bull. Seism. Soc. Am., 71*, 1105-1130, 1981.

Kanamori, H., Mechanism of tsunami earthquakes, *Physics of the Earth and Planetary Interiors, 6*, 346-359, 1972.

Kanamori, H., The energy release in great earthquakes, *J. Geophys. Res., 82*, 2981-2988, 1977.

Kanamori, H., A slow seismic event recorded in Pasadena, *Geophys. Res. Lett., 16*, 1411-1414, 1989.

Kanamori, H., and D. Anderson, Theoretical basis of some empirical relations in seismology, *Bull. Seismol. Soc. Am., 65*, 1073-95, 1976.

Kanamori, H., and D. L. Anderson, Amplitude of the earth's free oscillations and long-period characteristics of the earthquake Source, *J. Geophys. Res., 80*, 1075-1078, 1975.

Kanamori, H., and J. J. Cipar, Focal process of the great Chilean earthquake, *Physics of the Earth and Planetary Interiors, 9*, 128-136, 1974.

Kanamori, H., and J. W. Given, Use of long-period surface waves for rapid determination of earthquake-source parameters, *Physics of the Earth and Planetary Interiors, 27*, 8-31, 1981.

Kanamori, H., and E. Hauksson, A slow earthquake in the Santa Maria basin, California, *Bull. Seism. Soc. Am., 82*, 2087-2096, 1992.

Kanamori, H., and M. Kikuchi, The 1992 Nicaragua earthquake: a slow tsunami earthquake associated with subducted sediments, *Nature, 361*, 714-716, 1993.

Kanamori, H., and J. Mori, Harmonic excitation of mantle Rayleigh waves by the 1991 eruption of Mount Pinatubo, Philippines, *Geophys. Res. Lett., 19*, 721-724, 1992.

Kanamori, H., and G. S. Stewart, Mode of the strain release along the Gibbs fracture-zone, Mid-Atlantic ridge, *Physics of the Earth and Planetary Interiors, 11*, 312-332, 1976.

Kanamori, H., and G. S. Stewart, A slow earthquake, *Physics of the Earth and Planetary Interiors, 18*, 167-175, 1979.

Kanamori, H., H.-K. Thio, D. Dreger, and E. Hauksson, Initial investigation of the Landers, California, earthquake of 28 June 1992 using TERRAscope, *Geophys. Res. Lett., 19*, 2267-2270, 1992.

Kawakatsu, H., Centroid single-force inversion of seismic waves generated by landslides, *J. Geophys. Res., 94*, 12363-12374, 1989.

Kawasaki, I., Y. Kawahara, I. Takata, and N. Kosugi, Mode of seismic moment release at transform faults, *Tectonophysics, 118*, 313-327, 1985.

Kedar, S., and T. Tanimoto, Seismic Moment Estimation from long period free oscillations, *EOS - American Geophysical Union Transactions, 72*, 293, 1990.

Kedar, S., S. Watada, and T. Tanimoto, The 1989 Macquarie Ridge earthquake: seismic moment estimation from long period free oscillations, *J. Geophys. Res.*, in press.

Kennett, B. L. N., *IASPEI 1991 Seismological Tables*, 167 pp., Research School of Earth Sciences, Australian National University, Canberra, 1991.

Kikuchi, M., and H. Kanamori, Inversion of complex body waves, *Bull. Seism. Soc. Am., 72*, 491-506, 1982.

Kikuchi, M., and H. Kanamori, Inversion of complex body waves-II, *Phys. Earth Planet. Int., 43*, 205-222, 1986.

Kikuchi, M., and H. Kanamori, Inversion of complex body waves-III, *Bull. Seism. Soc. Am., 81*, 2335-2350, 1991.

Kikuchi, M., H. Kanamori, and K. Satake, Source complexity of the 1988 Armenian earthquake: evidence for a slow after-slip event, *J. Geophys. Res., 98*, 15797-15808, 1993.

Kilgore, B. D., M. L. Blanpied, and J. D. Dieterich, Velocity dependent friction of granite over a wide range of conditions, *Geophys. Res. Let., 20*, 903-906, 1993.

Kim, W.-Y., O. Kulhanek, and K. Meyer, Source process of the 1981 Gulf of Corinth earthquake sequence from body-wave analysis, *Bull. Seismol. Soc. Am., 74*, 459-477, 1984.

Kostrov, V. V., Seismic moment and energy of earthquakes, and seismic flow of rock, *Izv., Earth Physics, 1*, 23-40, 1974.

Kusznir, N. J., Visco-elastic rebound; A source mechanism for slow and silent earthquakes, *International Union of Geodesy and Geophysics (IUGG), XIX General Assembly, Vancouver, BC, Aug 9-22, 1987, 1*, 38, 1987.

Lawson, C. L., and R. J. Hanson, *Solving least squares problems*, 340 pp., Prentice-Hall, Englewood Cliffs, N.J., 1974.

Levshin, A. L., Effects of lateral inhomogeneities on surface wave amplitude measurements, *Ann. Geophys., 3*, 511-518, 1985.

Linde, A., and P. G. Silver, Elevation changes and the great 1960 Chilean earthquake: support for aseismic slip, *Geophys. Res. Lett., 16*, 1305-1308, 1989.

Lockner, D. A., and J. D. Byerlee, Laboratory measurements of velocity-dependent frictional strength, *USGS, open-file report 86-417*, 1986.

Lognonné, P., Normal modes and seismograms in an anelastic rotating Earth, *J. Geophys. Res., 96*, 20309-20319, 1991.

Marone, C., and B. Kilgore, Scaling of the critical slip distance for seismic faulting with shear strain in fault zones, *Nature, 362*, 618-621, 1993.

Marone, C., and C. H. Scholz, The depth of seismic faulting and the upper transition from stable to unstable slip regimes, *Geophys. Res. Lett., 15*, 621-624, 1988.

Marone, C. J., C. H. Scholz, and R. Bilham, On the mechanics of earthquake afterslip, *J. Geophys. Res., 96*, 8441-8452, 1991.

Masters, T. G., H. Bolton, and P. Shearer, Large-scale 3-D structure of the mantle, *Eos Trans. AGU, 73*, 201, 1992.

Mendiguren, J. A., Inversion of surface wave data in source mechanism studies, *J. Geophys. Res., 82*, 889-894, 1977.

Mendiguren, J. A., Inversion of free oscillation data for an elliptical rotating Earth in source moment tensor studies, *Pageoph, 118*, 1193-1208, 1980.

Menke, W., *Geophysical Data Analysis: discrete inverse theory*, 260 pp., Academic Press, Orlando, 1984.

Mikumo, T., A possible rupture process of slow earthquakes on a frictional fault, *Geophys. J. R. Astronom. Soc., 65*, 129-153, 1981.

Murray, M. H., J. C. Savage, M. Lisowski, and W. K. Gross, Coseismic displacement - 1992 Landers, California, earthquake, *Geophys. Res. Let., 20*, 623-626, 1993.

Nabelek, J. L., Determination of earthquake source parameters from inversion of body waves, thesis, Massachusetts Institute of Technology, 1984.

Ohnaka, M., Y. Kuwahana, K. Yamamoto, and T. Hirasawa, Dynamic breakdown processes and the generating mechanism for high-frequency elastic radiation during stick-slip instabilities, in *Earthquake Source Mechanism, AGU Geophysical Monograph 37*, edited by S. Das, J. Boatwright, and C. Scholz, pp. 13-24, American Geophysical Union, Washington, DC, 1986.

Okal, E., and S. Stein, The 1942 Southwest Indian ocean ridge earthquake; Largest ever recorded on an oceanic transform, *Geophys. Res. Letters, 14*, 147-150, 1987.

Okal, E. A., A physical classification of the Earth's spheroidal modes, *J. Phys. Earth, 26*, 75-103, 1978.

Okal, E. A., and L. M. Stewart, Slow Earthquakes along oceanic fracture zones: evidence for asthenospheric flow away from hotspots?, *Earth Planet. Sci. Lett., 57*, 75-87, 1982.

Pacheco, J. F., and L. R. Sykes, Seismic moment catalog of large shallow earthquakes, 1900 to 1989, *Bull. Seism. Soc. Am, 82*, 1306,1349, 1992.

Park, J., Asymptotic coupled-mode expressions for multiplet amplitude anomalies and frequency shifts on a laterally heterogeneous earth, *Geophys. J. R. Astr. Soc.*, *90*, 129-170, 1987.

Park, J., Synthetic seismograms from coupled free oscillations: effect of lateral structure and rotation, *J. Geophys. Res.*, *91*, 6441-6464, 1987.

Park, J., Radial mode observations from the 5/23/89 Macquarie Ridge earthquake, *Geophys. Res. Lett.*, *17*, 1005-1008, 1990.

Parker, R. L., The inverse problem of electromagnetic induction: Existence and construction of solutions based on incomplete data, *J. Geophys. Res.*, *85*, 4421-4428, 1980.

Parker, R. L., The inverse problem of resistivity sounding, *Geophysics*, *49*, 2143-2158, 1984.

Parsons, B., and J. G. Sclater, An analysis of the variation of ocean floor bathymetry and heat flow with age, *J. Geophys. Res.*, *82*, 803-827, 1977.

Pelayo, A. M., and S. Stein, Variation in source parameters for oceanic ridge, transform and intraplate earthquakes, *Eos Trans. AGU*, *72*, 202, 1991.

Pelayo, A. M., and D. A. Wiens, The November 20, 1960 Peru tsunami earthquake; Source mechanism of a slow event, *Geophys. Res. Lett.*, *17*, 661-664, 1990.

Pelayo, A. M., and D. A. Wiens, Tsunami earthquakes: slow thrust-faulting events in the accretionary wedge, *J. Geophys. Res.*, *97*, 15321-15337, 1992.

Pfulke, J. H., Slow earthquakes and very slow earthquakes, *Fault Mechanics and its Relation to Earthquake Prediction. USGS Open File Report 78-0380,* 447-468, 1978.

Press, W. H., S. A. Teukolsky, W. T. Vetterling, and B. P. Flannery, *Numerical recipes in FORTRAN. The art of scientific computing*, 963 pp., Cambridge University Press, Cambridge, 1992.

Prothero, W. A., and I. D. Reid, Microearthquake on the East Pacific rise at 21 N and the Rivera fracture zone, *J. Geophys. Res.*, *87*, 8509-8518, 1982.

Purdy, G. M., and J. Ewing, Seismic structure of the ocean crust, in *The Geology of North America, Volume M, The Western North Atlantic Region*, edited by P. R. Vogt, and B. E. Tucholke, pp. 313-330, Geological Society of America, Boulder, Colorado, 1986.

Reinen, L. A., T. E. Tullis, and J. D. Weeks, Two-mechanism model for frictional sliding of serpentinite, *Geophys. Res. Lett.*, *19*, 1535-1538, 1992.

Reinen, L. A., J. D. Weeks, and T. E. Tullis, The Effect of normal stress and sliding velocity on the frictional behavior of serpentinite, *Eos Trans AGU*, *71*, 1579, 1990.

Reinen, L. A., J. D. Weeks, and T. E. Tullis, The frictional behavior of serpentinite: implications for aseismic creep on shallow crustal faults, *Geophys. Res. Lett.*, *18*, 1921-1924, 1991.

Reuschle, T., Slow crack growth and aftershock sequences, *Geophys. Res. Lett.*, *17*, 1525-1528, 1990.

Rice, J. R., *Gerlands Beitr. Geophys.*, *88*, 91, 1979.

Rice, J. R., and M. P. Cleary, Some basic stress-diffusion solutions for fluid-saturated elastic porous media with compressible constituents, *Rev. Geophys. Space Phy.*, *14*, 227-241, 1976.

Rice, J. R., and J. C. Gu, Earthquake aftereffects and triggered seismic phenomena, *Pure and Applied Geophysics*, *105*, 343-349, 1983.

Rice, J. R., and D. A. Simons, The stabilization of spreading shear faults by coupled deformation-diffusion effects in fluid-infiltrated porous media, *J. Geophys. Res.*, *81*, 5322-5334, 1976.

Riedesel, M. A., Seismic moment tensor recovery at low frequencies, Ph. D. thesis, University of California, San Diego, 1985.

Riedesel, M. A., and T. H. Jordan, Display and assessment of seismic moment tensors, *Bull. Seismol. Soc. Am.*, *79*, 85-100, 1989.

Riedesel, M. A., T. H. Jordan, A. F. Sheehan, and P. G. Silver, Moment-tensor spectra of the 19 Sept 85 and 21 Sept 85 Michoacan, Mexico, earthquakes, *Geophys. Res. Lett.*, *13*, 609-612, 1986.

Rody, W. L., and J. G. Berryman, Notes on inversion, *Earth Resource Laboratory, MIT*, 1991.

Romanowicz, B., Moment tensor inversion of long period Rayleigh waves: a new approach, *J. Geophys. Res.*, *87*, 5395-5407, 1982.

Romanowicz, B., The upper mantle degree 2: Constraints and Inferences from global mantle wave attenuation measurements, *J. Geophys Res.*, *95*, 11051-11071, 1990.

Romanowicz, B., Strike-slip earthquakes on quasi-vertical transcurrent faults: inferences for general scaling relations, *Geophys. Res. Letters*, *19*, 481-484, 1992.

Romanowicz, B., M. Cara, J. F. Fels, and D. Rouland, GEOSCOPE: A French initiative in long-period three component global seismic networks, *Eos Trans. AGU*, *65*, 753-756, 1984.

Romanowicz, B., and P. Guillemant, An experiment in the retrieval of depth and source mechanism of large earthquakes using very long-period Rayleigh wave data, *Bull. Seism. Soc. Am*, *74*, 417-437, 1984.

Rudnicki, J. W., and C. H. Chen, Stabilization of frictional slip on a weakening fault by dilatant hardening, *J. Geophys. Res.*, *93*, 4745-4757, 1988.

Ruff, L. J., Multi-trace deconvolution with unknown trace scale factors: omnilinear inversion of P and S waves for source time functions, *Geophys. Res. Lett.*, *16*, 1043-1046, 1989.

Ruff, L. J., The Great Macquarie Ridge Earthquake of 1989: Introduction, *Geophys. Res. Lett.*, *17*, 989-991, 1990.

Sacks, I. S., A. Linde, J. A. Snoke, and S. Suyeshiro, A slow earthquake sequence following the Izu-Oshima earthquake of 1978, in *Earthquake Prediction, an International Review*, edited by D. W. Simpson, and P. G. Richard, *Maurice Ewing Series 4*, pp. 617-628, AGU, Washington DC, 1981.

Sacks, I. S., S. Suyehiro, A. T. Linde, and J. A. Snoke, Slow earthquakes and stress redistribution, *Nature*, *275*, 599-602, 1978.

Sacks, I. S., S. Suyehiro, A. T. Linde, and J. A. Snoke, Stress redistribution and slow earthquakes, *Tectonophysics*, *81*, 311-318, 1982.

Satake, K., J. Bourgeois, K. Abe, K. Abe, Y. Tsuji, F. Imamura, Y. Iio, H. Katao, E. Noguera, and F. Estrada, Tsunami field survey of the 1992 Nicaragua earthquake, *Eos Trans. AGU*, *74*, 145, 1993.

Satake, K., and H. Kanamori, Fault parameters and tsunami excitation of the May 23, 1989, Macquarie Ridge earthquake, *Geophys. Res. Lett.*, *17*, 997-1000, 1990.

Satake, K., and K. Shimazaki, Dectability of very slow earthquakes from tide gauge records, *Geophys. Res. Lett.*, *15*, 665-668, 1988.

Scholz, C. H., Scaling laws for large earthquakes: consequences for physical models, *Bull. Seis. Soc. Am.*, *72*, 1-14, 1982.

Scholz, C. H., *The mechanics of earthquakes and faulting*, 439 pp., Cambridge University Press, Cambridge, 1990.

Scholz, C. H., A reappraisal of large earthquake scaling, *Bull. Soc. Seism. Am.*, *84*, 215-218, 1994.

Scholz, C. H., P. Molnar, and T. Johnson, Detailed studies of frictional sliding of granite and implications for earthquake mechanism, *J. Geophys. Res.*, *77*, 6392-6404, 1972.

Shi, Z., Q. Lee, H. Wu, and Y. Yang, A possible historical slow earthquake in eastern China, *Acta Seismologica Sinica*, *7*, 342-347, 1985.

Shimamoto, T., and J. Logan, Velocity-dependent behavior of simulated halite shear zones: an analog for silicates, in *Earthquake source mechanics. AGU Geophys. Mono. 37*, edited by S. Das, J. Boatwright, and C. Scholz, pp. 49-64, American Geophysical Union, Washington, D. C., 1986.

Shimazaki, K., Small and large earthquakes: the effect of the thickness of the seismogenic layer and the free surface, in *Earthquake source mechanics. AGU Geophys. Mono. 37*, edited by S. Das, J. Boatwright, and C. Scholz, pp. 209-216, American Geophysical Union, Washington, D. C., 1986.

Sieh, K., and coworkers, Near-field investigation of the Landers earthquake sequence, April to July, 1992, *Science, 260*, 171-176, 1992.

Silver, P. G., and T. H. Jordan, Fundamental spheroidal mode observations of aspherical heterogeneity, *Geophys. J. R. astr. Soc, 64*, 605-634, 1981.

Silver, P. G., and T. H. Jordan, Optimal estimation of scalar seismic moment, *Geophys. J. R. Astron. Soc., 70*, 755-787, 1982.

Silver, P. G., and T. H. Jordan, Total-moment spectra of fourteen large Earthquakes, *J. Geophys. Res., 88*, 3273-3293, 1983.

Sipkin, S. A., and T. H. Jordan, Regional variation of Qscs, *Bull. Seis. Soc. Am., 70*, 1980.

Smith, S. W., IRIS: a program for the next decade, *Eos Trans. AGU, 67*, 213-219, 1986.

Solomon, S. C., P. Y. Huang, and L. Meinke, The seismic moment budget of slowly spreading ridges, *Nature, 334*, 58-61, 1988.

Spikin, S. A., Estimation of earthquake source parameters by the inversion of waveform data: global seismicity, 1981-1983, *Bull. Seism. Soc. Am., 76*, 1515-1541, 1986.

Stark, P. B., and R. L. Parker, Smooth profiles from $\tau(p)$ and $X(p)$ data, *Geophys. J. R. astr. Soc., 89*, 997-1010, 1987.

Stewart, L., and D. W. Forsyth, Rupture length and duration of a slow earthquake on an Atlantic transform fault, *Eos Trans AGU, 65*, 236, 1984.

Stewart, L. M., and E. A. Okal, Slow earthquakes along oceanic fracture zones; Evidence for Morgan's pipeline structures?, *Eos Trans AGU, 62*, 325, 1981.

Su, W.-j., R. L. Woodward, and A. M. Dziewonski, Degree 12 model of shear velocity heterogeneity in the mantle, *J. Geophys. Res., 99*, 6945-6980, 1994.

Tada, T., K. Shimazaki, and S. Tsuboi, Analysis of short-period P waves from the 1989 Macquarie Ridge earthquake using a broadband array in Japan, *Geophys. Res. Letters, 20*, 269-272, 1993.

Takemoto, S., Some problems on detection of earthquake precursors by means of continuous monitoring of crustal strains and tilts, *J. Geoph. Res., 96*, 10377-10390, 1991.

Thomson, D. J., and A. D. Chave, Jackknifed error estimates for spectra, coherences, and transfer functions, in *Advances in spectrum analysis and array processing*, edited by S. Haykin, *1*, pp. 58-113, Prentice Hall, 1991.

Tichelaar, B. W., and L. J. Ruff, How good are our best models?, *Eos Trans. AGU, 70*, 593-606, 1989.

Tichelaar, B. W., and L. J. Ruff, Rupture process and stress-drop of the Great 1989 Macquarie Ridge earthquake, *Geophys. Res. Lett., 17*, 1001-1004, 1990.

Tikhonov, A. N., and V. Y. Arsenin, *Solutions of ill-posed problems*, pp., V. H. Winston and Sons, Washington, D. C., 1977.

Tromp, J., and F. A. Dahlen, Variational principles for surface wave propagation on a laterally heterogeneous Earth-I. Time-domain JWKB theory, *Geophys. J. Int., 109*, 581-598, 1992.

Tromp, J., and F. A. Dahlen, Variational principles for surface wave propagation on a laterally heterogeneous Earth-II. Frequency-domain JWKB theory, *Geophys. J. Int., 109*, 599-619, 1992.

Tromp, J., and F. A. Dahlen, Variational principles for surface wave propagation on a laterally heterogeneous Earth-III. Potential representation, *Geophys. J. Int., 112*, 195-209, 1992.

Tromp, J., and F. A. Dahlen, Surface wave propagation in a slowly varying anisotropic waveguide, *Geophys. J. Int., 113*, 239-249, 1993.

Tse, S. T., and J. R. Rice, Earthquake instability in relation to the depth variation of frictional slip properties, *J. Geoph. Res*, *91*, 9452-9472, 1986.

Tullis, T. E., Rock friction constitutive behavior from laboratory experiments and its implications for an earthquake prediction field monitoring program, *Pure Appl. Geophys.*, *126*, 555-588, 1988.

Tullis, T. E., and J. D. Weeks, Experiments on rock friction constitutive laws applied to earthquake instability analysis, in 400-403, 1990.

Vidale, J. E., and H. Houston, The depth dependence of earthquake duration and implication for rupture mechanism, *Nature*, *365*, 45-47, 1993.

Wahba, G., *Spline models for observational data*, 169 pp., Society for industrial and applied mathematics, Philadelphia, Pennsylvania, 1990.

Wald, D. J., and T. H. Heaton, Spatial and temporal distribution of slip for the 1992 Landers, California earthquake, *Bull. Seism. Soc. Am.*, in press.

Widmer, R., The large-scale structure of the deep earth as constrained by free oscillation observations, Ph. D. thesis, University of California, San Diego, 1991.

Widmer, R., G. Masters, and F. Gilbert, Spherically symmetric attenuation within the Earth from normal mode data, *Geophys. J. Int.*, *104*, 541-553, 1991.

Widmer, R., and W. Zürn, Bichromatic excitation of long-period Rayleigh and air waves by the Mount Pinatubo and El Chichon volcanic eruptions, *Geophys. Res. Lett.*, *19*, 765-786, 1992.

Widmer, R., W. Zürn, and G. Masters, Observation of low-order toroidal modes from the 1989 Macquarie Rise event, *Geophys. J. Int.*, *111*, 226-236, 1992.

Wielandt, E., and G. Streckeisen, The leaf spring seismometer: design and performance, *Bull. Seis. Soc. Am.*, *72*, 2349-2368, 1982.

Wiens, D. A., and A. M. Pelayo, The 1946 Aleutian and 1960 Peru historic tsunami earthquakes: slow events within the accretionary prism, *Eos Trans AGU*, *72*, 189, 1991.

Wilcock, W. S. D., G. M. Purdy, and S. C. Solomon, Microearthquake evidence for extension across the Kane transform fault, *J. Geophys. Res.*, *95*, 15439-15462, 1990.

Wolfe, C. J., E. A. Bergman, and S. S. Solomon, Oceanic transform earthquakes with unusual mechanisms or locations: Relation to fault geometry and state of stress in the adjacent lithosphere, *J. Geophys. Res.*, *98*, 16187-16211, 1993.

Woodhouse, J. H., and A. M. Dziewonski, Mapping the upper mantle: Three-dimensional modeling of earth structure by inversion of seismic waveform, *J. Geophys. Res.*, *89*, 5953-5986, 1984.

Woodhouse, J. H., and Y. K. Wong, Amplitude, phase and path anomalies of mantle waves, *Geophys. J. R. Astr. Soc.*, *87*, 753-773, 1986.

Woodward, R. L., A. M. Forte, W.-J. Su, and A. M. Dziewonski, Constraints on the large-scale structure of the earth's mantle, *J. Geophys. Res.*, in press.

Yamashita, T., Causes of slow earthquakes and multiple earthquakes, *J. Phys. Earth*, *28*, 169-190, 1980.

Yamashita, T., Quasistatic crack extension in an inhomogeneous viscoelastic medium - a possible mechanism for the occurrence of aseismic faulting, *J. Phys. Earth*, *28*, 309-326, 1980.

Yamashita, T., Stability and instability of interactive shear cracks-generating mechanism for slow earthquakes and fault creep, *J. Phys. Earth*, *30*, 131-154, 1982.

Zhang, J., and T. Lay, Effects of centroid location on determination of earthquake mechanisms using long-period surface waves, *Bull. Seism. Soc. Am.*, *80*, 1205-1231, 1990.